University of Alberta

Optical Detection of Gases and Vacuum with CMOS Microstructures

by

Keith Bradley Brown   Ⓒ

A thesis submitted to the Faculty of Graduate Studies and Research in partial fulfillment

of the requirements for the degree of Doctor of Philosophy

Department of Electrical and Computer Engineering

Edmonton, Alberta

Spring 2003

National Library
of Canada

Bibliothèque nationale
du Canada

Acquisitions and
Bibliographic Services

Acquisisitons et
services bibliographiques

395 Wellington Street
Ottawa ON K1A 0N4
Canada

395, rue Wellington
Ottawa ON K1A 0N4
Canada

The author has granted a non-exclusive licence allowing the National Library of Canada to reproduce, loan, distribute or sell copies of this thesis in microform, paper or electronic formats.

The author retains ownership of the copyright in this thesis. Neither the thesis nor substantial extracts from it may be printed or otherwise reproduced without the author's permission.

L'auteur a accordé une licence non exclusive permettant à la Bibliothèque nationale du Canada de reproduire, prêter, distribuer ou vendre des copies de cette thèse sous la forme de microfiche/film, de reproduction sur papier ou sur format électronique.

L'auteur conserve la propriété du droit d'auteur qui protège cette thèse. Ni la thèse ni des extraits substantiels de celle-ci ne doivent être imprimés ou aturement reproduits sans son autorisation.

Canada

University of Alberta

Library Release Form

Name of Author: Keith Bradley Brown

Title of Thesis: Optical Detection of Gases and Vacuum with CMOS Microstructures

Degree: Doctor of Philosophy

Year this Degree Granted: 2003

Permission is hereby granted to the University of Alberta Library to reproduce single copies of this thesis and to lend or sell such copies for private, scholarly, or scientific research purposes only.

The author reserves all other publication and other rights in association with the copyright in the thesis, and except as hereinbefore provided, neither the thesis nor any substantial portion thereof may be printed or otherwise reproduced in any material form whatever without the author's prior written permission.

Keith B. Brown

(Keith B. Brown)

5 Groveland Avenue
Sherwood Park, Alberta
Canada, T8A 3G1

Date: *April 22, 2003*

University of Alberta

Faculty of Graduate Studies and Research

The undersigned certify that they have read, and recommend to the Faculty of Graduate Studies and Research for acceptance, a thesis entitled **Optical Detection of Gases and Vacuum with CMOS Microstructures** submitted by **Keith Bradley Brown** in partial fulfillment of the requirements for the degree of Doctor of Philosophy.

Dr. C.J. Backhouse, supervisor
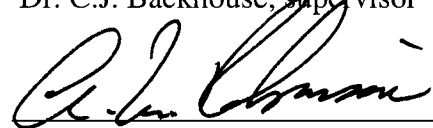
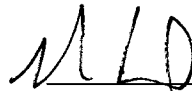Dr. A.M. Robinson, co-supervisor

Dr. F.E. Vermeulen, co-supervisor

Dr. J.C. Sit

Dr. R. DeCorby

Dr. W.A. Moussa

Dr. L.M. Landsberger

Date: _April 16, 2003_

This dissertation is dedicated to the memory of my grandmother

Mabel Sawisky (nee Proskin),

1920 – 2003.

ABSTRACT

A CMOS-compatible micromachined Pirani gauge has been designed, fabricated, and tested for implementation as both a high sensitivity vacuum sensor and a gas analyzer. The Ohmic-heated microstructure emits visible light, and is operated at either constant power or constant response in order to minimize the effect of instability of the electrical resistance of the device. The device is designed to maximize the heat loss due to conduction between the gauge's polysilicon element and the adjacent silicon substrate, through the surrounding gas medium, rather than bulk conduction through the supports.

The amount of heat transferred by conduction through the gas around the heated microstructure will vary as a function of the gas and its pressure. The temperature of the radiator will thus vary with heat transfer, which will affect the radiant energy emitted. By monitoring the visible and near-infrared radiation emitted from the device with a photodiode, it is possible to determine the magnitude of the conductive heat loss, and hence measure the pressure of a particular gas as well as determine the effective thermal conductivity of the gas or gas mixture. The effective thermal conductivity to be used to discriminate between two gases with the aid of calibration curves.

Four different geometries of micro-Pirani gauges have been designed, fabricated, and tested under modes of constant power and constant detector response for pressure ranging from 10^{-3} to 1000 Torr and in the presence of N_2, He, Ar, Kr, or SF_6 (each gas having a large relative difference in thermal conductivity). Transient characteristics were also investigated, as well as variations in device characteristic dimension (etch depth between the device and the underlying substrate). Lastly, an electro-thermal model was developed and a comparison between experiment and finite element simulation performed, and a discussion on device durability and repeatability presented.

ACKNOWLEDGEMENTS

TABLE OF CONTENTS

LIST OF TABLES

LIST OF FIGURES

LIST OF ABBREVIATIONS AND SYMBOLS

α	thermal diffusivity
α_T, β_T	first, second order temperature coefficients of resistance
β	volumetric thermal expansion coefficient
Γ	amplitude reflection coefficient
ε	emissivity
ε_o	permittivity
θ_x	angle 'x'
λ	optical wavelength
λ_{mfp}	molecular mean free path
μ_o	permeability constant
ν	frequency
ν_k	kinematic viscosity
ρ	electrical resistivity
ρ_m	mass density
ρ_o	room temperature resistivity
σ	Stefan-Boltzmann constant
τ	time constant
τ_R	polysilicon rise-time
τ_{V_d}	photodetector fall-time
τ'_{V_d}	photodetector rise-time
Ω	solid angle
∇	del operator
A	area
a	mean molecular collision diameter
b	system response time factor
$\bar{B}$	magnetic field vector
c	speed of light

c_o	speed of light in vacuum
c_p	specific heat
d	system characteristic dimension, etch depth
e	electron charge
$\vec{E}$	electric field vector
$E(T)$	emissive power
g	gravitational acceleration
g_1	electrical conductivity
G_r	Grashof number
h	Planck's constant
h_1	natural convection heat transfer coefficient
H	critical dimension, height
H_x	flux 'x'
i	device current
$\hat{i}, \hat{j}, \hat{k}$	cartesian unit vectors
$I(\lambda, T)$	spectral intensity
I_d	photodetector current
I_x	Intensity 'x'
k	Boltzmann constant
k_1	thermal conductivity
k_g	thermal conductivity of gas
K_n	Knudsen number
L	critical dimension, length
L_1	Lorentz number
m	mass
M_g	molar weight
n_x	index of refraction 'x'
N	moles of substance
p	absolute pressure
p_o	transistion pressure
P	electrical power

P_r	Prandtl number
$\dot{q}$	heat sources or sinks
Q	Quality factor
r_d	detector radius
r, θ, ϕ	spherical coordinates
R	resistance
R'	responsivity
R_a	Rayleigh number
R_e	reflectance
R_o	room temperature resistance
$\Re$	molar gas constant
s_1	device-to-detector distance
$\bar{S}$	Poynting vector
S_{ar}	solid angle ratio
t	time
T	absolute temperature
T_f	fluid ambient temperature
T_s	surface temperature
v	volume
V	voltage
W	critical dimension, width
x, y, z	cartesian coordinates
AC	alternating current
Ar	argon
AsH_3	arsine
BOE	buffered oxide etch
B_2H_6	diborane
BrF_3	bromine trifluoride
CAD	computer-aided-design
CH_3COOH	acetic acid
CE	capillary electrophoresis

CMC	Canadian Microelectronics Corporation
CMOS	complementary metal oxide semiconductor
CVD	chemical vapour deposition
DAQ	data acquisition unit
DC	direct current
DI	de-ionized water
DIP	dual inline package
DRIE	deep reactive ion etching
EDP	ethylene diamine pyrocatechol
FEM	finite element model
GaAs	gallium arsenide
He	helium
HF	hydrofluoric acid
HNA	hydrofluoric nitric acetic acid
HNO_3	nitric acid
ITO	indium tin oxide
KOH	potassium hydroxide
Kr	krypton
LPCVD	low pressure chemical vapour deposition
MEMS	microelectromechanical systems
MST	microsystems technology
N_2	nitrogen
NH_3	ammonia
NEMS	nanoelectromechanical systems
Ni_xFe_y	Permalloy™
NST	nanosystems technology
PCR	polymerase chain reaction
PECVD	plasma enhanced chemical vapour deposition
PH_3	phosphine
RF	radio frequency
RIE	reactive ion etching

SF_6	sulfur hexafluoride
$SiCl_4$	silicon tetrachloride
SiH_4	silane
SiH_2Cl_2	silicon dichlorosilane
SiO_2	silicon dioxide
Si_xN_y	silicon nitride (nonstoichiometric)
SOG	spin on glass
SOI	silicon on insulator
TCR	temperature coefficient of resistance
TEOS	tetraethoxysilane
TMAH	tetra methyl ammonium hydroxide
TO	transistor outline
UV	ultraviolet
XeF_2	xenon difluoride
ZIF	zero insertion force

INTRODUCTION

1.1 BACKGROUND

A gas filled cavity at a pressure below atmospheric is referred to as a vacuum, where the degree of vacuum attained is characterized by the absolute gas pressure in the cavity or system [1]. Units of pressure include the pascal (Pa), equal to one newton of force per square metre, the bar, equivalent to 10^5 pascals, and the Torr, commonly used in vacuum systems and defined as the pressure required to balance 1 mm of mercury at 273 K. Pressure below standard atmosphere (760 Torr) is measured by instruments known as vacuum gauges; however, no gauges presently exist that can measure the full range of pressure from atmospheric to presently attainable vacuum levels ($< 10^{-12}$ Torr). As a result, a vacuum gauge is chosen based on the range of vacuum to be detected, as well as the composition of the gas in the system.

A Pirani gauge is a thermal-conductivity-type vacuum gauge developed by Marcello von Pirani in 1906 [2]. The working principle of these gauges is a result of the fact that heat loss from a hot filament wire via conduction to the surrounding ambient gas is proportional to both the molecular density (pressure) and the thermal conductivity (type) of the gas occupying a given vacuum system. The vacuum system pressure is thus calculated according to the temperature of the filament and is valid only for the specific gas in question. Filling the vacuum system with a gas of significantly different thermal conductivity at the same molecular density would produce a different filament temperature and hence produce an incorrect pressure reading.

The temperature of the filament is obtained by calculating the change in resistance of the heated metal filament operated under conditions of constant current or constant voltage. Conventionally, the filament is made of materials such as tungsten, nickel, or platinum each having high temperature-coefficients-of-resistance (TCR), ensuring good

sensitivity to temperature changes. In terms of a material's TCR, its resistance, R [Ω], at a temperature, T [K], can be expressed as [1]:

$$R = R_o\left(1 + \alpha_T(T - T_o) + \beta_T(T - T_o)^2\right) \qquad (1.1)$$

where R_o [Ω] is the resistance at some initial temperature, T_o, α_T [K^{-1}] is the TCR, and β_T [K^{-2}] is the rarely used second order TCR.

In common practice, the filament forms one arm of a Wheatstone bridge as shown in Figure 1.1, where R3 is the heated filament in the vacuum environment and R4, made from the same material as R3, isolated and subject to a constant reference pressure, provides ambient temperature compensation. The voltage across the bridge, Vs, is thus related to the filament temperature and hence, pressure in the vacuum system.
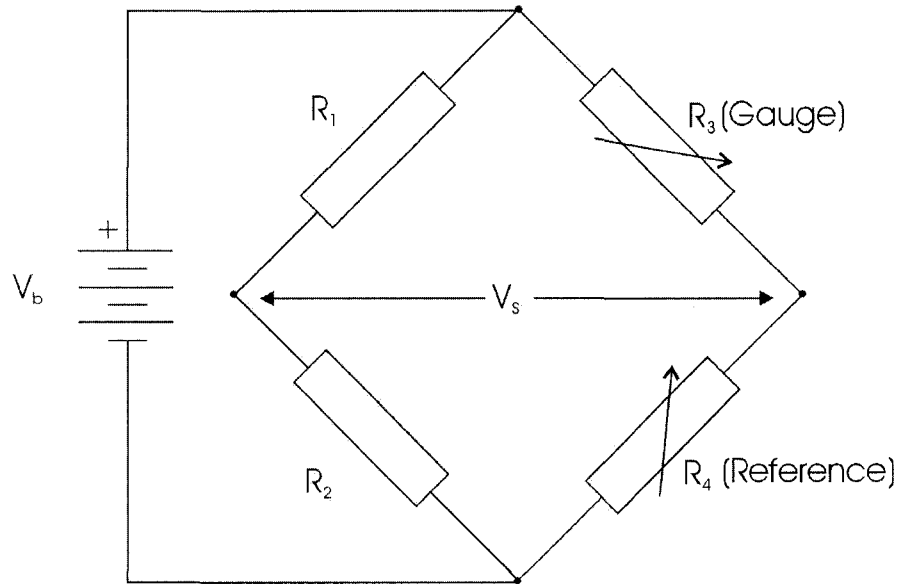
Figure 1.1 Conventional Wheatstone bridge circuit for Pirani gauge readout.

Standard Pirani gauges are bulky and labour intensive to mass-produce, and therefore relatively expensive. Pirani gauge output is also dependent on the type of gas being measured and has a limited useful pressure-sensitive range, typically 0.8×10^{-3} to 20 Torr with an uncertainty of 15 to 20% [3]. Miniaturization of the standard Pirani gauge has been accomplished with the use of semiconductor processing technologies,

commonly referred to as micromachining, where the temperature-dependent resistive filament takes the form of a thermally isolated polysilicon [4-8] or platinum [9,10] thin film. A typical micromachined Pirani gauge is illustrated in Figure 1.2. These micro-Pirani gauges have the advantage of being significantly smaller than conventional Pirani gauges, resulting in two positive effects. These effects are an increase in the upper pressure sensing limit and a smaller instrument load (amount of dead volume) affecting, and easier placement in, the vacuum system. Micromachined Pirani gauges also demonstrate slight improvements in the effective pressure sensing range when used with integrated on-chip electronics [5]. Lastly, they have a reduced unit cost due to the batch fabrication nature of semiconductor production.
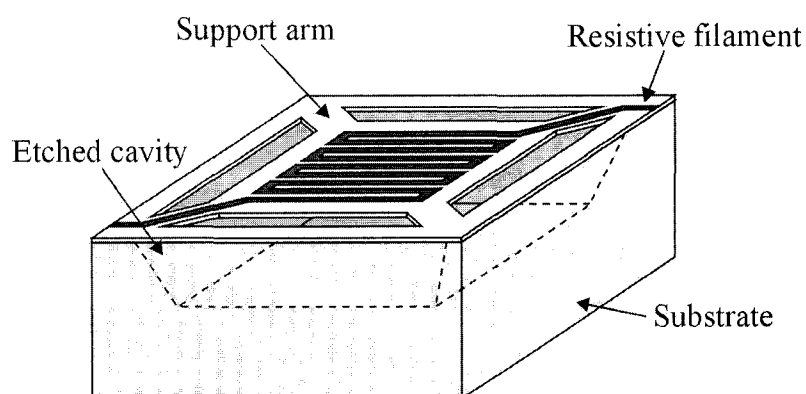
Figure 1.2 Typical micromachined Pirani gauge.

Characterization of the heat transport properties of these micro-Pirani gauge structures, including the development of numerical models, has led to applications such as forced convection gas flow sensing [11-14]. The main method of detection, however, still relies on measuring the change in resistance due to temperature variations in the resistive element of the sensor. Resistive changes due to temperature fluctuations are linear for small fluctuations in temperature and at most quadratic for large fluctuations in temperature, where large temperatures lead to thermal stability problems (phase changes) and eventually device failure [15-17]. Hence, using resistance methods to measure temperature will greatly limit the overall sensitivity of these devices. A solution to increasing the overall sensitivity of a micro-thermal-conductivity-type device was first investigated in [18], in which the amount of radiation emitted from the resistive element

was calculated as a function of dissipated input power at both atmospheric pressure and vacuum. Based on the findings of [18], the true significance of operating a micro-Pirani gauge in "optical" mode was reported in [19] and more recently investigated in detail in [20]. The results showed that by dissipating a selected constant power through the micro-optical-Pirani gauge and monitoring the radiation emitted with a photodetector, the effective pressure sensitive range can be increased by at least two orders of magnitude $(10^{-3}$ to 700 Torr) compared to that of a conventional Pirani gauge, and the measurement uncertainty decreased to less than 8%. In addition, by comparing the micro-optical-Pirani gauge output at a known pressure to calibration curves for various gases of differing thermal conductivities, the constituent gas occupying the vacuum system may be estimated for a binary mixture of known gases. In this role, the micro-optical-Pirani gauge, used in conjunction with a gas-independent pressure gauge, could act as a crude gas analyzer.

1.2 MOTIVATION

Micromachined pressure and gas analyzing sensors are employed in many industries, including, but not limited to, automotive, biomedical, and industrial microelectronics foundries [21-26]. The total market growth of such micromachined pressure and gas analyzing sensors worldwide was predicted to grow by 120% between 1996 to 2002 [27]. The actual worldwide market grew from $603M (US) to $1.34B (US), a gain of 122%, as reported in [28]. For the near future, the same market is expected to continue to grow from $1.34B (US) to $2.8B (US) between 2002 and 2005 (Figure 1.3), an increase of 109% [28]. This growth is partly due to the compact size, increased sensitivity, and lower cost per unit of micro-system technologies (MST). This growth also confirms that there continues to be a strong demand for research and development with respect to pressure and gas analysis sensor systems.
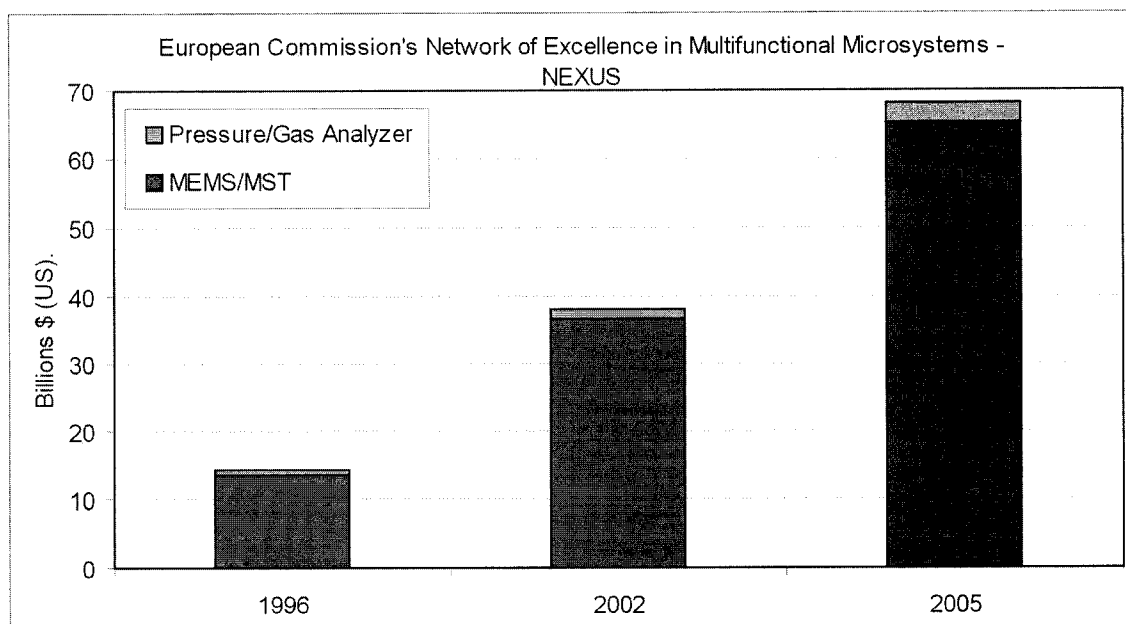
Figure 1.3 Actual and projected microelectromechanical systems (MEMS)/ microsystems technology (MST) total worldwide market growth.

1.3 THESIS ORGANIZATION

This dissertation presents the findings and conclusions obtained from a project that is an expansion of the work performed in [20] with the main objective of extending the application of an optically operated micro-Pirani gauge to include gas analysis. By taking advantage of the gas dependence of the operation of a Pirani gauge it is feasible to not only measure gas pressure, but, when used at a known pressure and in conjunction with calibration curves, also the effective thermal conductivity of the gas present in a vacuum system [29]. The secondary objective of this project has been to refine the overall device operation and simulation models, and improve the device sensitivity through detector-device variations, device geometry variations, and an improvement of the control software.

In Chapter 2, an overview of contemporary micromachining techniques and applications is presented. This overview covers some fundamental definitions related to the micromachining field, followed by a general description of the materials and processes involved in microstructure fabrication. Finally, packaging details and a selection of both present and future applications are discussed.

Chapter 3 of this dissertation discusses the fundamentals of heat transfer as a necessary primer to the understanding of the working principle behind the optically-operated micro-Pirani gauge. Included in this discussion is a brief introduction to the three modes of heat transfer: heat conduction, convection, and radiation, with emphasis on the physics of radiation. A detailed description of the microstructures investigated in this project is given in Chapter 4. Sensor design, an overview of the fabrication process and post-processing specifics are also presented including the effects of post-processing on the room temperature resistance and TCR of polysilicon.

The core material of this treatise is contained in Chapter 5. Experimental configuration and procedure, and a brief comparison between two types of photodetectors used, are described followed by the results from operating the micro-Pirani gauges under constant input power and constant detector response (constant temperature). Transient response properties and the results from varying the etch depth (characteristic dimension) are also investigated and reported here.

Chapter 6 reports on device modeling, simulation results, and a comparison between the experimental results obtained and simulated results generated. Following in Chapter 7 is a discussion on the effectiveness of these optically-operated micro-Pirani gauges when used to sense gas pressure and analyze gases. In addition, a brief discussion regarding the durability and repeatability of using polysilicon for the resistive element is presented.

Lastly, Chapter 8 presents conclusions pertaining to the work completed, as well as suggestions for future research involving optically-operated micro-Pirani devices.

CONTEMPORARY MICROMACHINING TECHNIQUES

2.1 INTRODUCTION

Micromachining is the set of design and fabrication techniques that allows for the precise machining and formation of structures on a scale ranging from millimetres to sub-micrometres (sub-microns). These techniques are the underlying foundation of what is commonly known in North America as microelectromechanical systems (MEMS), or micro systems technology (MST) in Europe and the rest of the world [30-32]. The philosophy driving MEMS/MST is to incorporate microelectronics and micromechanical components in a single chip enabling it to sense, compute, actuate, control, communicate, and power. MEMS-based functional units could facilitate enhanced levels of perception, control, and performance. MEMS/MST is expected to provide the advantages of small size, low power, low mass, low cost (per unit), and high functionality to integrated electromechanical systems both on the micro-, as well as, on the macro-scale [33-37].

Applications of MEMS/MST technology can be loosely categorized (where a specific device may occupy more than one category) as:

- fluid sensing, control, and transport
- optics and imaging
- inertial instruments
- radio frequency components and communication
- sensor and actuator networks or arrays, and
- bio-medical appliances and systems.

Recent advancements in micromachining fabrication techniques have allowed for the scale of micromachined components to reach below 100 nanometres, resulting in the term *nano* replacing *micro*. Arguably, the correct usage of the terms Nanoelectromechanical Systems (NEMS) or Nano Systems Technology (NST) is

achieved when referring to specifically machined structures and features that exist at a scale below 100 nanometres [38,39].

The first micromachined components date back many decades, with the well-established integrated circuit industry playing an important role in fostering an environment suitable for the development and growth of micromachining technologies [40]. Micro-components are typically fabricated by one of two methods commonly known as surface micromachining and bulk micromachining, or a combination of both, and often achieved with the use of complementary metal-oxide semiconductor (CMOS) processes. Surface micromachining involves the deposition of structural and sacrificial layers onto a substrate. These layers, each several microns (1 micron = 10^{-6} m) thick, are etched to create three-dimensional structures that exist solely on the surface of the substrate. In contrast, bulk micromachining involves the removal of large amounts of substrate via the use of an etchant in conjunction with the deposition of one or more structural and/or masking layers. This method of micromachining allows for the creation of several structures such as trenches, pits, and pyramids. Lastly, using CMOS processes to fabricate micromachining components can result in the creation of fully functional integrated circuits in proximity to bulk or surface micromachined devices.

In essence, the characteristics required of a given MEMS design dictate which micromachining method to utilize. Based on the method utilized, the appropriate materials and processes will be chosen to meet the device specifications, production yield, and cost. The result is that the field of MEMS is inherently interdisciplinary, necessitating the understanding of design and fabrication processes, as well as the final application. To this end, the following sections present an overview of the materials and processes involved in the fabrication of micromachined structures. Packaging issues and solutions are discussed, as well as a broad list of current and future applications.

2.2 MATERIALS

There is a very broad selection of substrate materials available to the MEMS designer, with crystalline silicon being the most common. Complementing silicon is a number of materials that can be deposited as thin films. These materials include poly-

silicon, amorphous silicon, silicon dioxides and nitrides, glass, organic polymers, and a selection of metals.

2.2.1 Silicon, Silicon Oxides and Nitrides

The popularity experienced by silicon as the most commonly used substrate is due to the large momentum of the electronic integrated circuit industry and its extensive industrial infrastructure. Silicon is one of only a few materials that can be economically manufactured in single crystal substrates. Impurity doping allows for the precise modulation of electrical conductivity, a property heavily exploited in semiconductor devices. From a mechanical point of view, silicon is an elastic and robust material whose characteristics are well understood and documented.

Silicon exists in any of three solid-state forms: crystalline, polycrystalline, and amorphous. In single crystal form the silicon atoms are periodically arranged in a diamond-like lattice structure, known as face-centered-cubic (fcc), whose primitive unit cell resembles a cube. In describing directions and planes within the unit cell a set of integers, known as Miller indices, are used and designated in reference to the principal axes of the unit cell [41]. An illustration of the fcc structure for crystalline silicon and a few crystallographic planes, and their associated Miller indices are shown in Figure 2.1. Single directions (vectors) are denoted by [abc], where a, b, and c are given by integers, and the notation <def>, where d, e, and f are also integers, represents the family of parallel vectors. Planes are represented in the form (xyz), where x, y, and z are given by integers. The family of planes equivalent under 90° rotation and mirror symmetry are marked as {uvw} (u, v, and w representing integers). For example, the planes (100), (010), and (001) are represented by the family of planes {100}. The angles between {100} and {110} planes and between {100} and {111} planes are 45° and 54.74°, respectively. The angle between {100} and {111} planes is of particular importance to micromachining because many alkaline aqueous solutions selectively etch the {100} plane of silicon but not the {111} plane (known as anisotropic etching, to be discussed in a later section of this chapter). This selective etching is thought to be due to the fact that silicon has a higher packing density along the {111} plane than the other plane orientations [42].

(100)   (110)   (111)
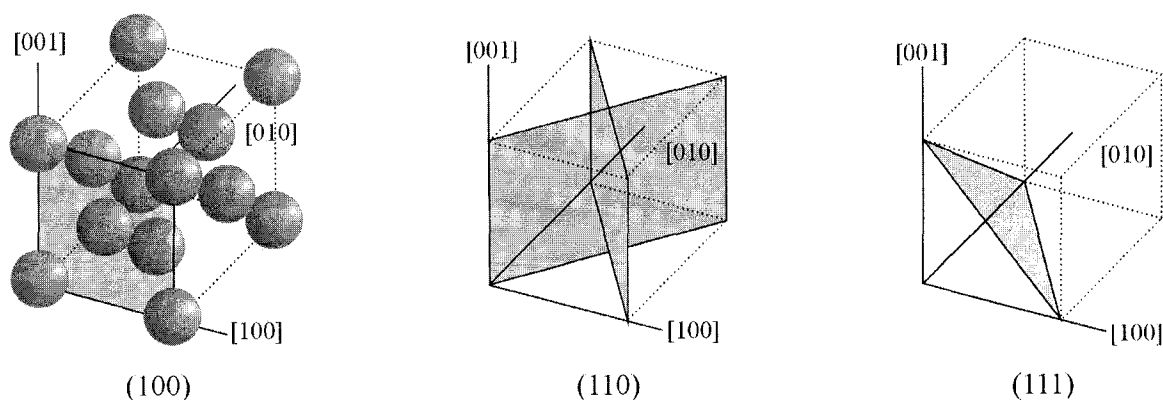
Figure 2.1 Three crystallographic planes and their Miller indices for a silicon crystal. The leftmost illustration depicts a face-centered-cubic structure. In the center illustration two equivalent (110) planes in the {110} family of planes are identified.

Crystalline silicon is commercially available in the form of circular wafers with either 100 or 150 mm diameters and typically 500 to 650 µm in thickness. Larger diameter wafers are at present not economically justified for micromachining fabrication and their use is, therefore, restricted to the integrated circuit industry. To obtain these circular wafers, manufacturers cut thin slices from large silicon boules along specific crystal planes. The cut plane (top surface of the wafer) is known as the orientation cut and is encoded on the wafer in the form of a primary and secondary flat located on the sides of the wafer. The most common wafers are of {100} orientation, which is the preferred orientation for CMOS technology. In addition to the orientation cut, impurity doping type (n or p) and electrical resistivity (in Ω·cm) are also indicated by the supplier. An illustration showing primary and secondary flats and orientation can be seen in Figure 2.2.

Crystalline silicon is free of intrinsic stress, and is a hard and brittle material that deforms elastically until it reaches its yield strength, at which point it breaks by fracture along a crystal plane. Large silicon wafers tend to be fragile, while smaller portions (die) with dimensions on the order of 1 cm x 1 cm or less are robust and can sustain relatively harsh handling conditions. Silicon micromachined actuators have also been shown to be very insensitive to fatigue failure when subjected to a high cyclic loading. Table 2.1 lists some of the electrical, mechanical, and thermal properties for silicon and other micromachining materials.

Polycrystalline silicon (polysilicon) and amorphous silicon are usually deposited

(a)

(b)
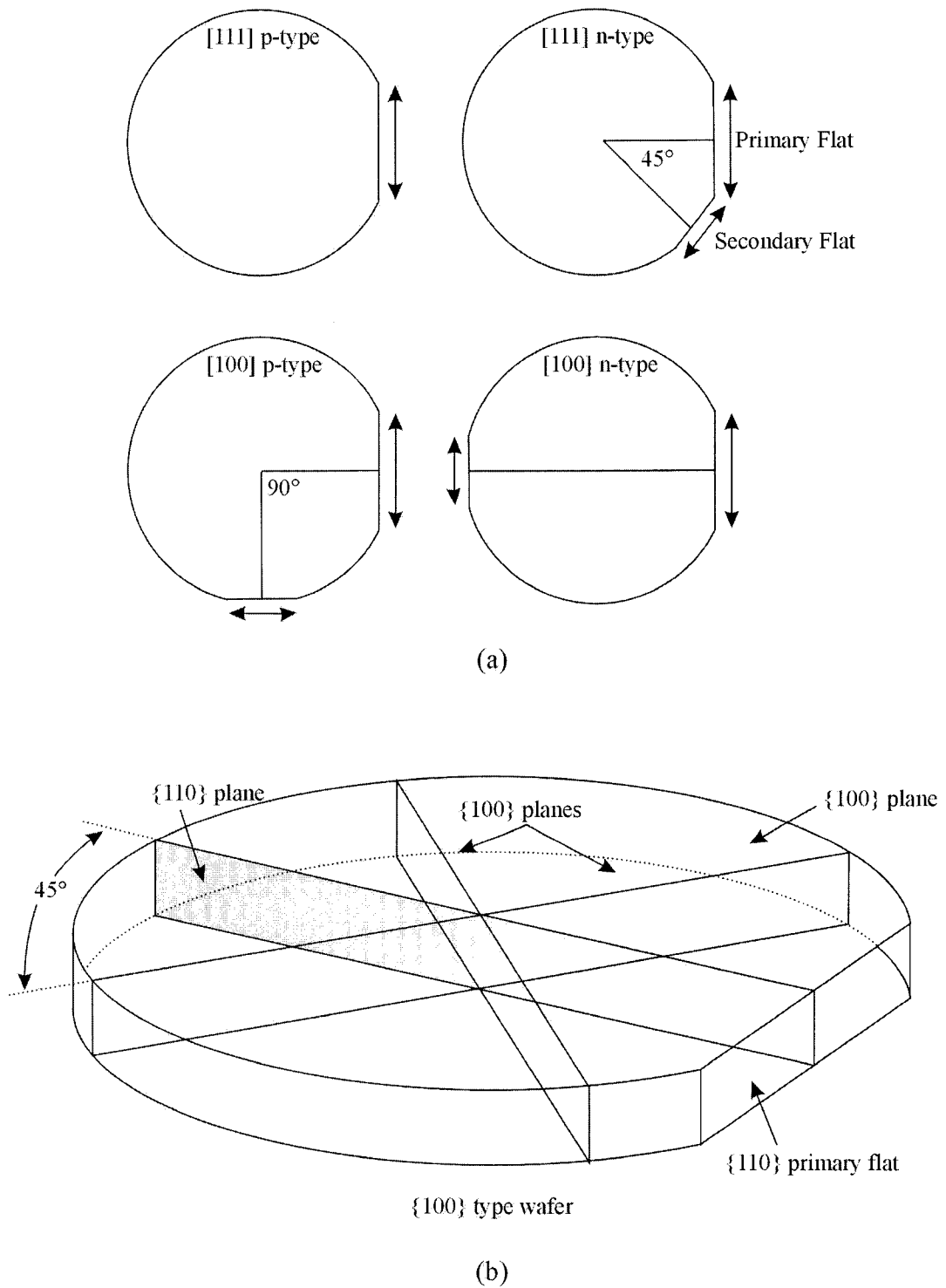
Figure 2.2 (a) Illustration of the primary and secondary flats of {100} and {111} wafers for both n-type and p-type doping. (b) Various planes in a wafer of {100} orientation.

Table 2.1 Electrical, mechanical, and thermal properties of silicon and other micromachining materials [30].

Property	Si	SiO$_2$	Si$_3$N$_4$	Quartz
Relative permittivity, $\varepsilon_r = \varepsilon / \varepsilon_o$	11.8	3.8	4	3.75
Dielectric strength [V·cm^{-1} x 10^{-6}]	3	5-10	5-10	25-40
Resistivity [$\mu\Omega$·cm]	2.3x10^{11}	—	>10^{20}	2x10^{20}
Young's Modulus [GPa]	165	75	380	107
Yield strength [GPa]	7	8.4	14	9
Poisson's ratio	0.22	0.17	0.25	0.16
Density [g·cm^{-3}]	2.33	2.2	2.4	2.65
Coeff. of thermal expansion [10^{-6}·K^{-1}]	2.6	0.55	2.8	0.55
Thermal conductivity [W·cm^{-1}·K^{-1}]	1.48	0.014	0.16	0.0138
Specific heat [J·g^{-1}K^{-1}]	0.712	0.745	0.691	0.787
Melting point [K]	1956	1973	2073	1883

as thin films, each with a typical thickness of less than 5 μm. Each has mechanical and electrical properties that vary with deposition conditions, but for the most part, are similar to those of single crystal silicon [43]. Both polysilicon and amorphous silicon suffer from relatively high levels of intrinsic stress that can be annealed quickly at temperatures greater than 1150 K. Structures made of polysilicon or amorphous silicon have been observed to curl under the effect of intrinsic stress when not properly annealed. The main difference between polysilicon and amorphous silicon is that amorphous silicon produces a high breakdown strength oxide with low leakage currents (compared to low breakdown strength and large leakage currents for polysilicon oxides; the breakdown strength is defined as the electric field at which the molecules break down to allow passage of damaging levels of electric current). For surface micromachining the most commonly used structural material is polysilicon.

Silicon is a good thermal conductor (approximately 100 times that of glass) and a silicon substrate can be used as an efficient heat sink. As for optical properties, silicon is not an active optical material and hence, silicon-based lasers do not exist. At infrared wavelengths longer than 1.1 μm, silicon is transparent, but at wavelengths shorter than 0.4 μm silicon reflects over 60% of incident light. The attenuation depth of light (distance traveled before the intensity decreases to 36% of its initial value) in silicon is 2.7 μm at 633 nm (red) and 0.2 μm at 436 nm (blue). The slight attenuation of transmitted red light relative to other colours is what gives thin silicon membranes their

translucent reddish tint. Silicon also retains its mechanical properties at temperatures up to 750 K, where at higher temperatures it softens appreciably and deforms plastically. Polysilicon, which exhibits similar thermal and mechanical properties as single-crystal silicon, experiences slow-stress annealing effects at temperatures above 520 K. As a result, operation at elevated temperatures will make polysilicon subject to long-term instabilities, resistance drift, and electrical hysteresis effects. Another useful characteristic of crystalline and polycrystalline silicon is that they both exhibit a change in resistance while undergoing strain, a phenomenon known as piezoresistivity.

Interactions of silicon with gases, chemicals, and biological materials remain under investigation, but in general, silicon is considered stable and resistant to many elements and chemicals. Preliminary results indicate that in-vitro silicon is benign and does not release toxic substances when in contact with biological fluids. However, silicon-based surfaces may not be suitable for high-performance polymerase chain reactions (PCR) intended for the amplification of genetic materials due to incompatibility with bio-materials [44-45].

Various forms of silicon oxides such as SiO_2, SiO_x, and silicate glass are widely used in micromachining due to their excellent electrical and thermal insulating properties. Silicon oxides are also used as sacrificial layers in surface micromachining processes because they can be preferentially etched in hydrofluoric (HF) acid with high selectivity to silicon. Silicon dioxide (SiO_2) can be thermally grown by oxidizing silicon at temperatures above 1050 K. Other forms of oxides and glass are deposited by chemical vapour deposition (CVD), sputtering, or even spin-on processes (discussed later in section 2.3). Oxides and glass layers are known to soften and flow when subjected to temperature in excess of 950 K. One problem with oxides is that their relatively large intrinsic stresses are difficult to control or anneal.

Silicon nitride (Si_xN_y) is another widely used insulating thin film that is an effective barrier against mobile ion diffusion, and in particular, the sodium and potassium ions found in biological environments. Silicon nitride is a harder material than silicon and its intrinsic stress can be controlled by the specifics of the deposition process. Silicon nitride is also an effective masking material in many alkaline etch solutions and is commonly used as a passivation layer.

2.2.2 Thin Metal Films

Thin metal films are deposited to create structural features and current paths with the choice of metal depending on the nature of the final application. A list of commonly deposited metals, select bulk properties (usually different from surface properties), and typical applications is shown in Table 2.2. These metal films are deposited by sputtering, evaporation, chemical vapour deposition, or electroplating. Materials in this list that can be electroplated are gold, nickel, and Permalloy™ (Ni_xFe_y).

Table 2.2 Commonly deposited thin metal films for use in micromachining [30].

Metal	Resistivity [$\mu\Omega$·cm]	Density [g·cm^{-3}]	Melting point [K]	Typical application
Al	2.7	2.70	933	Interconnects, optical reflection in visible and infrared
Au	2.4	19.32	1336	High temp. interconnects, optical reflection in infrared, electrochemistry
Cr	12.9	7.19	2130	Adhesion layer
Cu	1.7	8.93	1356	Low resistivity interconnects
ITO	300-3000	7.14	2173	Transparent conductor for liquid crystal displays
Ir	5.1	22.4	2716	Electrochemistry
Ni	6.8	8.9	1725	Magnetic transducing
Pd	10.8	12.02	1825	Electrochemistry
Permalloy™	—	8.74	> 723	Magnetic transducing
Pt	10.6	21.45	2042	Electrochemistry
Ti	42	4.54	1933	Adhesion layer
TiW	75-200	14.58	3203	Adhesion layer, ~0 temperature coefficient of resistance
W	5.5	19.3	3683	High temp. interconnects

For basic electrical interconnections, aluminum is the most predominant material and is easily deposited by sputtering; however, aluminum is limited to use in non-corrosive environments whose temperatures do not exceed 570 K. When there is a requirement for a device to operate at higher temperatures and in harsher environments, gold, titanium, and tungsten are acceptable. Aluminum tends to anneal over time with high temperatures causing changes in its intrinsic stresses. As a result, aluminum is typically deposited away from stress- or strain-sensing elements. Optically, aluminum is highly reflective to visible wavelengths, while gold is highly reflective in the infrared.

Platinum, palladium, gold, and iridium are metals that can be utilized as electrodes for use in electrochemistry and in sensing biopotentials, although the deposition of platinum and palladium is expensive. Chromium, titanium, and tungsten are frequently used as very thin (10 to 100 nm) adhesion layers beneath highly stressed metals with a tendency to peel off, such as sputtered or evaporated nickel, platinum, or palladium.

Recently, thin metal-alloy films with thickness of up to 50 μm have successfully demonstrated shape-memory effects [46]. The shape-memory effect is a property of a special class of alloys, such as titanium nickel, the most common of these alloys, copper-aluminum-nickel, iron-nickel, and iron-platinum, that can be easily deformed into a permanent shape and return to their pre-deformation shape when heated above a critical transition temperature. The transition temperature can be controlled between 173 and 373 K by the addition of impurities during the alloy fabrication. For applications requiring transparent electrodes, such as liquid crystal displays, indium-tin-oxide (ITO) can be used. Lastly, Permalloy™ has been explored as a material to be used for thin magnetic cores and magnetically actuated devices [37].

2.2.3 Other MEMS Materials

Other materials used in the fabrication of microstructures include glass and quartz, organic polymers, metal alloys, and group III-V semiconductor compounds. Micromachining of glass and quartz substrates has been performed where there was a requirement for an electrically insulating or optically transparent substrate. Quartz has a characteristic of being piezoelectric (a property by which a crystalline material produces

an electric field when subjected to an external force), but at present, there are no methods available to deposit crystalline quartz as a thin film over silicon substrates. Glass and silicon can be joined electrostatically by a process referred to as anodic bonding. Unfortunately, glass generally has a higher coefficient of thermal expansion than silicon resulting in interfacial stresses between the bonded silicon and glass substrates. Micromachining of glass or quartz is often limited because chemical etching yields coarsely defined features with poor edge control. Thin metal films can be easily deposited on glass or quartz substrates and patterned via standard lithographic processes, with one popular application being the fabrication of capillary micro-channels in glass substrates with thin metal electrodes for use in miniaturized biochemical assays [47-48].

Polymers, such as photoresist, can be deposited with a varying thickness ranging from a few nanometres to hundreds of microns, with the most common thickness being in the range 1 to 10 μm. Hardening of the photoresist, typically under ultraviolet light, produces rigid structures primarily used to mask underlying regions during etching, but also to sense chemicals and humidity, due to their unique absorption and adsorption properties [49].

Lastly, micromachining using gallium arsenide (GaAs) and other group III-V semiconductor compounds (InP, AlGaAs, and GaN) is proving to be a practical way to integrate radio-frequency (RF) switches, antennas, and other custom high-frequency components with ultra-high-speed devices for use in the wireless telecommunications industry.

2.3 PROCESSES

Many of the processes used to fabricate MEMS structures are derived from the integrated circuit industry, providing a significant advantage in overcoming massive infrastructure requirements, with additional processes having been developed over the years specifically for silicon micromachining. Fundamentally, micromachining combines the deposition of layers over a substrate (usually silicon as discussed in the previous section), followed by the patterning of these layers, and lastly the etching of the substrate to define permanent features. This cycle of deposition, patterning, and etching is then

repeated to complete the microstructure. To clarify this point an illustration of the basic micromachining process flow can be seen in Figure 2.3.

Deposition:
- Epitaxy
- Oxidation
- Sputtering
- Evaporation
- Chemical Vapour
- Spin-on method
- Sol-gel
- Anodic bonding
- Electroplating
- Silicon fusion bonding

Patterning:
- Optical Lithography
- Backside Lithography

Etching:
- Wet Isotropic
- Wet Anisotropic
- Dry/Plasma
- Reactive Ion
- Deep Reactive Ion
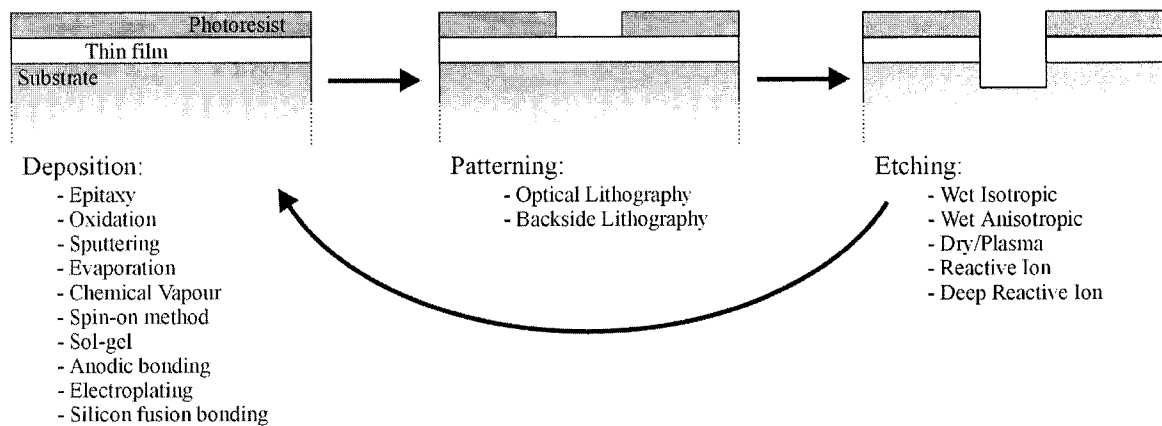
Figure 2.3 Illustration of the basic process flow in micromachining. The process repeats until completion of the microstructure.

2.3.1 Deposition

A list of processes used during the deposition phase of the micromachining fabrication cycle includes epitaxy, oxidation, sputtering, evaporation, chemical vapour deposition, spin-on, sol-gel, anodic bonding, electroplating, and silicon fusion bonding.

Silicon epitaxy is a method by which a layer of crystalline silicon is grown over a silicon wafer. This grown layer exhibits a crystal orientation aligned to that of the underlying substrate, is typically 1 to 20 μm thick, and can have a different dopant type and concentration level than the underlying substrate. The exception to this occurs when growing silicon over an amorphous material such as silicon dioxide, in which case the resulting epitaxial layer is polycrystalline. One method for growing the silicon epitaxial layer results from the dissociation of a silicon source gas, typically silane (SiH_4), silicon dichlorosilane (SiH_2Cl_2), or silicon tetrachloride ($SiCl_4$), at a high temperature (> 1070 K). Growth rates vary between 0.2 and 1.5 μm/min as a function of source gas and temperature. Doping is achieved by the dissociation of a dopant gas concurrent with the silicon deposition.

Oxidation of silicon is obtained in either dry oxygen or steam at temperatures ranging from 1120 to 1420 K. The resulting high-quality silicon dioxide will vary in thickness as a function of temperature, oxidizing environment, and time. Thermal

oxidation of silicon will result in a silicon dioxide film with latent compressive stress due to the oxide molecules occupying a larger volume than silicon molecules and a mismatch between the coefficient of thermal expansion between silicon and silicon dioxide. This compressive stress has been observed in freestanding membranes and suspended cantilevers composed of thermally grown oxides having a tendency to warp or curl.

Sputter deposition is the mechanism by which a target object made of a material to be deposited is physically bombarded by a flux of noble gas ions (e.g., argon, helium) in a vacuum chamber. This ion flux results in material particles being ejected from the target and deposited onto the substrate. The noble gas ion flux is propagated by either a direct current (DC) field between the target and substrate, an RF excitation applied to the target, or an applied magnetic field near the target in conjunction with the DC or RF excitations. Sputtering is a popular method in the MEMS community as deposition can occur at relatively low temperatures (< 420 K). The deposited film has a fine granular structure and is frequently under stress: compressive stress for low vacuum system pressures (10^{-3} to 10^{-2} Torr) and tensile stress for high pressures (10^{-2} to 10^{-1} Torr). Controlling the stress is difficult, as the transition pressure between tensile and compressive stress is often only a few thousandths of a Torr; however, increasing the substrate temperature during sputtering will usually result in a decrease in film stress.

Evaporation involves the localized heating of a source material to the point at which a vapour is generated and deposited. The main issue is to adjust the vacuum chamber pressure such that the vapour pressure of the evaporated material is greater than the surrounding vacuum chamber pressure. Source heating is accomplished either electrically by Joule heating or by scanning an electron beam over the target. Evaporation is a directional process where the majority of material deposits at a specific angle to the substrate. The angle of deposition results in a shadowing effect that can be exploited to selectively deposit material on only one side of a step or trench, otherwise, rotation of the substrate during deposition will reduce the shadowing effect and produce a more conformal coverage. Evaporated films exhibit high tensile stresses that can be reduced, as in sputtering, by increasing the substrate temperature during deposition.

Chemical vapour deposition (CVD) works on the principle of combining two gases that undergo a chemical reaction resulting in a reacted species that deposits onto a

heated substrate. Unlike sputtering, CVD is a high temperature process (> 570 K). Typical thin films generated in this manner include polysilicon, silicon oxides and nitrides, titanium, titanium nitrides, and copper. Related CVD processes include low pressure (LPCVD) and plasma-enhanced (PECVD), where LPCVD operates at even higher temperatures (770 to 1070 K) and PECVD operates at approximately 570 K with the application of a RF excitation to enhance the plasma. Polysilicon is deposited by the decomposition of silane into silicon and hydrogen in a LPCVD reaction. The same reaction in PECVD results in amorphous silicon being deposited. Doping of the deposited polysilicon and amorphous silicon is achieved by introducing dopant source gases such as arsine (AsH_3), phosphine (PH_3), or diborane (B_2H_6). Likewise, silicon dioxide is generally deposited by reacting silane and oxygen in a CVD, LPCVD, or PECVD reactor at temperatures below 770 K. Other techniques exist for depositing silicon dioxides at higher temperatures and with various dopants and are described in [30,32-34]. Silicon nitride, used mainly for passivation in integrated circuits, is also an effective masking layer in micromachining for use in selective etching of silicon in alkaline solutions. Stoichiometric silicon nitride (Si_3N_4) is deposited at atmospheric pressure by reacting silane and ammonia (NH_3), or at low pressure by reacting dichlorosilane and ammonia. Typical deposition temperatures vary between 970 and 1170 K. At temperatures below 670 K, non-stoichiometric silicon nitride (Si_xN_y) is created by reacting silane with ammonia in a PECVD system.

Spin-on deposition is simply a process of depositing organic materials and dielectric insulators via a spinning chuck upon which a substrate resides. An amount of material is dispensed in liquid form onto the center of the 500 to 5000 rpm (revolutions-per-minute) spinning wafer and inertial forces spread the material in a uniform manner. Spin-on glass (SOG) has the ability to uniformly coat surfaces in layers ranging from 5 to 100 μm in thickness. Thinner layers of SOG (0.1 to 0.5 μm) have been investigated for use as an inter-metal dielectric insulting material; however, the electrical properties of SOG are poor compared with thermally grown or CVD silicon oxides [32, 48].

Sol-gel deposition, while similar to the spin-on method, is a process where a chemical reaction between solid particles in colloidal suspension within a solvent (a sol) forms a gelatinous network (a gel) that is transformed to a solid upon removal of the

solvent. The most common application of sol-gel processing is in the coating of surfaces with optically absorptive materials. An example of a sol-gel process is where tetraethoxysilane (TEOS) in suspension in water is spun onto a surface. The TEOS is then converted into a silica gel by hydrolysis and condensation using hydrochloric acid as a catalyst. Heating the sample to temperatures between 470 and 870 K results in the transition of the gel into glass, and then into silicon dioxide [50].

Anodic bonding, also known as electrostatic bonding, is the process by which a bare silicon wafer is joined to a sodium-containing glass substrate. This process is fundamental to the fabrication of a wide variety of micromachined components, namely pressure sensors, because it provides the relatively fragile silicon wafer with a rigid support (the glass substrate). The bonding can be performed in a vacuum, in air, or in an inert gas environment and requires temperatures from 470 to 770 K. A large voltage of 500 to 1500 V is applied across the two substrates, with the glass at the negative (cathode) potential. Mobile positive ions (Na^+) in the glass then migrate towards the cathode and away from the silicon-glass interface, leaving behind fixed negative charges. The bonding is complete when the ion current being externally measured reduces to zero, indicating that all mobile ions have reached the cathode. The bond is thus created by both the electrostatic attraction between the fixed negative charges in the glass and the positive charges in the silicon, and the silicon-glass chemical bond created by the elevated temperature. Two issues to consider when performing anodic bonding are the careful matching of thermal expansion coefficients for the glass and silicon, and the presence of thin ($<$ 100 nm) silicon oxides on the silicon surface that can disturb the current flow and hence the bond.

Electroplating is a mature industrial method, adapted to micromachining, of depositing metal films. In order for electroplating to take place, a conductive base must be present on the target substrate. The substrate is then immersed in a metal-ion-rich solution and a current path created between the solution and the immersed substrate. Some metals that have been successfully electroplated onto silicon substrates include gold, nickel, copper, and nickel-iron alloys (Permalloy™).

Silicon-fusion bonding, commonly known as direct wafer bonding, is a method for joining two silicon substrates and was an important step in the development of

silicon-on-insulator (SOI) technology [30, 32-34]. The bonding mechanism is not well understood, but is believed to occur at the molecular level between silicon and oxygen atoms at the interface. Both surfaces must be very smooth, planar, and clean to ensure a uniform and void-free bond. The two wafers are immersed in an ammonium hydroxide solution at approximately 370 K, carefully brought into contact, and held together by van der Waals forces. A temperature anneal at 1070 to 1370 K strengthens the bond. A thin polysilicon film can also be fusion-bonded to a silicon wafer or to a silicon dioxide layer under similar conditions. Wafer bonding can be then be repeated arbitrarily to form multi-wafer stacks.

2.3.2 Patterning

The most important process in micromachining is the patterning of deposited materials, more commonly known as lithography. Without the lithography process, it is doubtful that integrated circuit technology, let alone micromachining, would be at the level of sophistication that it is at today. Photolithography involves three sequential steps that are often repeated many times during a complete microfabrication process: photoresist application, pattern transfer from a mask to the photoresist by optical exposure, and development of the photoresist.

Photoresist is applied using the spin-on method described earlier in section 2.3.1 and can be classified as either positive photoresist or negative photoresist. Positive photoresist is an organic resin material containing a sensitizer that prevents the dissolution of unexposed resin during immersion in a developer solution. Exposure to ultraviolet radiation in the 200 to 400 nm range breaks down the sensitizer causing any exposed regions of photoresist to dissolve in the developer solution. For a negative photoresist, the opposite process occurs – exposed regions remain intact and unexposed regions are dissolved by the developer. Typically, photoresists are applied with a thickness ranging from 0.5 to 10 μm; however, thicker applications of up to 100 μm have been deposited for specific applications and not without difficulty [30, 32-34].

The mask used for the pattern transfer is itself often a patterned opaque chromium layer on a transparent quartz glass substrate. The pattern is generated by using a computer-aided-design (CAD) tool and transferred to the thin chromium layer using a

pattern generator system.

Optical exposure is accomplished by contact, proximity, or projection methods. The contact method of lithography consists of the mask coming into direct contact with the wafer, eliminating diffraction effects but reducing the life of the mask and leaving undesired residue on both the mask and the wafer. Proximity lithography is similar to the contact method with the exception being that the mask is only brought to within 25 to 50 μm of the photoresist surface. This method preserves the mask from wear, eliminates undesired residues, but is limited due to near-field (Fresnel) diffraction. Lastly, projection lithography uses complex optics to project an image of the mask onto the wafer, resulting in greater resolution, but limited by far-field (Frauhoffer) diffraction and the quality of the optics. Typical peak wavelengths for optical lithographic systems used in micromachining are 400 nm (UV) and 248 nm (Deep UV) with the resolution defined as the minimum feature resolved and as being proportional to the wavelength divided by the numerical aperture of the optics. The depth of field, defined as being proportional to the wavelength divided by the square of the numerical aperture, becomes important especially when dealing with thick photoresists or when topographical height variations exceed 10 μm.

Backside lithography is used when both sides of the wafer are required to have features. An example of this is in the fabrication of pressure sensors where the front-side of the wafer contains the sensing membrane and the backside of the wafer contains the cavity. Alignment of the front- and back-side features is the main challenge for this process and various solutions have been marketed, with a specialized infrared (IR) mask aligner being the most common [30, 32-34].

2.3.3 Etching

The object of etching is to selectively remove material (silicon, for example) with the use of a differing material or materials as a masking template. For a successful etch to occur there must be sufficient selectivity between the mask material(s) and the material being etched. Etch processes for MEMS device fabrication have many scientific underpinnings, but for a large part remain an art. The etchant medium is classified as either wet (aqueous solutions) or dry (reactant gases), and the etch type as either isotropic

or anisotropic.

Isotropic etchants remove material uniformly in all directions, resulting in rounded cross-sectional features. Anisotropic etchants, in contrast, etch in one direction preferentially over others. The direction of the preferential etch is determined by the orientation of the crystal planes, the result being trenches or cavities delineated by flat and well-defined surfaces. Hence, anisotropically etched surfaces need not be perpendicular to the surface of the wafer. The etch medium (wet or dry) also creates some variation even when comparing the same isotropy, as illustrated in Figure 2.4. Dry etchants often produce higher yields than wet etchants at the cost of a decrease in throughput and increase in cost/unit due to the specialized equipment required.

	Wet etch	Dry/Plasma etch
Isotropic		
Anisotropic		
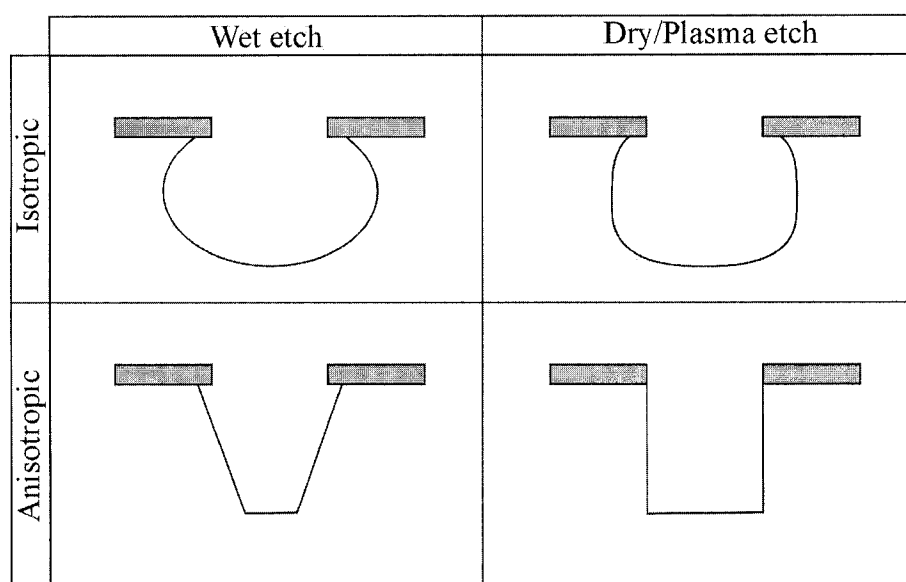
Figure 2.4 Illustration of cross-sectional trench profiles resulting from different etch types and mediums.

Isotropic wet etching of silicon is achieved with the use of highly reactive acids or bases, the most common being HNA. HNA is a mixture of hydrofluoric (HF), nitric (HNO_3), and acetic (CH_3COOH) acids [51]. Typical etch rates vary from 1 to 5 μm/min and can increase up to 20 μm/min with agitation. The nitric acid oxidizes the silicon, which is then removed by the hydrofluoric acid. Further details of the reaction are very complex and are discussed in [35, 51-52].

Wet anisotropic etching of silicon can be accomplished by a number of aqueous

solutions. Hydroxides of alkali metals (NaOH, KOH, CsOH,...), simple and quaternary ammonium hydroxides (NH$_4$OH, (CH$_3$)$_4$NOH), and ethylenediamine mixed with pyrocatechol in water (EDP) form a list of the major silicon anisotropic etch solutions. From these groups the most common etchants are potassium hydroxide (KOH), tetramethyl ammonium hydroxide (TMAH - (CH$_3$)$_4$NOH), and EDP.

KOH typically etches silicon at rates of 8.5 μm/min at 370 K with a selectivity ratio of 100:1 for the {100}:{111} planes, with heavily boron-doped regions (in p-type silicon) acting as effective etch stops. The preferred mask for this etchant is silicon nitride (10 nm/min etch rate in KOH) with silicon dioxide not recommended since KOH etches silicon dioxide faster than it etches silicon. Photoresist is not always an effective masking layer as it is often etched in alkaline solutions. Alkali hydroxides are extremely corrosive and as such, aluminum bond pads are quickly damaged when exposed. CMOS fabrication facilities are often reluctant to use such etchants, or even accept wafers previously exposed to alkali hydroxides for fear of contamination by potassium or sodium, two ions detrimental to the operation of CMOS integrated circuits. In terms of safety, KOH is a poison by ingestion, a skin irritant, and very corrosive to the eyes and mucous membranes.

EDP is another wet etchant with selectivity to {111} planes and heavily boron-doped silicon. A common mix for EDP is 750 mL of ethylene diamine (NH$_2$-CH$_2$-CH$_2$-NH$_2$), 240 g pyrocatechol (C$_6$H$_4$(OH)$_2$), 240 mL de-ionized water (DI), and 6 g pyrazine (C$_4$H$_4$N$_2$) [53]. EDP will not etch gold, chromium, silver, copper, or tantulum. Etch rates for silicon are 1.4 to 1.6 μm/min at 392 K in the (100) direction with an anisotropy ratio of 40:1 for the {100} to {111} planes. Aluminum and silicon dioxide and nitride etch rates are typically 10 nm/min, 10 nm/hr, and 10 nm/hr, respectively, making the latter excellent masking layers. EDP is a highly dangerous nerve toxin and carcinogenic etchant that has now been banned in most commercial fabrication facilities. It should be kept in a pure nitrogen environment as exposure to oxygen forms benzoquinone, which will cause uncontrollable etch rate increases and a darkening of the solution. In addition, after etching with EDP, the wafers should be rinsed in DI water for at least 24 hours to prevent the forming of a benzoquinone residue on the substrate and hence further etching.

TMAH exhibits similar etching properties as KOH. Etching parameters for

TMAH are a silicon etch rate of 1.0 μm/min at 363 K for 25 wt.% solutions, selectivity ratios of 50:1 for the {100} to {111} planes, and etch-stop for heavily p-doped silicon regions. Silicon dioxide and nitride make excellent masking layers for TMAH etching and the reduction of pH due to the dissolving of silicon powder has been reported to significantly reduce the etch rate of aluminum while lowering the silicon etch rate only slightly [36]. A disadvantage of TMAH commonly associated to a reduced pH is the occasional formation of pyramidal hillocks along the {100} plane resulting in undesirable surface roughness. These hillocks are believed to be a result of the surface attachment of hydrogen bubbles produced during the dissolution reaction and deposition of insoluble material [42]. Surface roughness has been noticeably reduced and the silicon etch rate increased by the addition of oxidizers to the TMAH solution [36]. TMAH is a strong base that is both stable and colourless, can cause severe irritation to skin, eyes, and mucous membranes, and is poisonous when absorbed through the skin.

Exploiting the orientation dependence of the anisotropic etchant yields a variety of fabricated shapes. A typical profile of a wet anisotropic etch is illustrated in Figure 2.5. Truncated pyramidal cavities may be created by the careful alignment of a specified mask shape with a given surface orientation and stopping the etching before the {111} planes are completely exposed [54]. For example, a truncated pyramidal pit is created with a square mask aligned to the {100} surface plane. Table 2.3 indicates the relationship between mask shape, surface orientation, and the anisotropic etch structure.
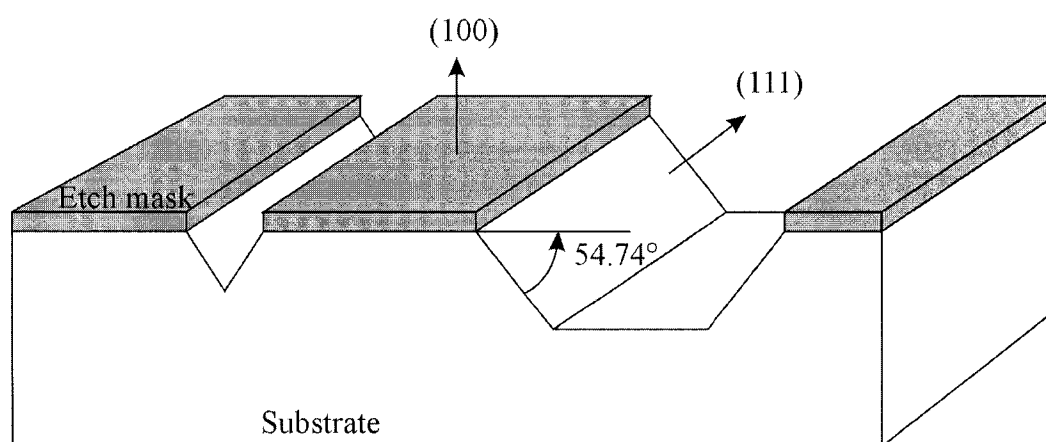
Figure 2.5 Illustration of a typical wet anisotropic etch profile.

Table 2.3 Relationship between mask shape, surface orientation, and etch structure for anisotropic etch processes.

Mask shape	Surface orientation	Etch structure
Square	{100}	Pyramidal or truncated pyramidal pit
Rectangle	{100}	Rectangular pit (trench)
Circle	{100}	Pyramidal pit
Arbitrary shape	{100}	Rectangular pit
Square	{110}	Pit with vertical side walls
Rectangle	{110}	Pit with vertical side walls

Gas-phase or dry etching of silicon is isotropic by nature and achieved by the spontaneous chemical reaction of a gas with silicon. The etching mechanism is believed to begin with the non-dissociative adsorption of gas-phase species at the silicon surface. The adsorbed gas then dissociates and reacts with the silicon surface forming adsorbed product molecules. Lastly, the product molecules are desorbed into the gas-phase.

In terms of dry etching, two chemically reactive compounds in use today are xenon difluoride (XeF_2) and bromine trifluoride (BrF_3) [55,56]. Both etch silicon isotropically and demonstrate superb selectivity over silicon dioxide, silicon nitride, and photoresist. In the case of most metals, such as aluminum, copper, gold, and nickel, a passivated non-volatile metal fluoride layer is formed on the metal surface effectively preventing further reaction. The selectivity over these metals has been reported at greater than 1000 to 1. Under standard room conditions, XeF_2 exists as a white granular crystal that sublimates into a vapour when subjected to pressures below its vapour pressure of approximately 4 Torr. In similar fashion, BrF_3 exists as a colourless to grey-yellow liquid at room temperature and pressure with a vapour pressure of approximately 7 Torr. The etching reaction for XeF_2 can be expressed as:

$$XeF_{2(g)} + \tfrac{1}{2}Si_{(s)} \rightarrow Xe_{(g)} + \tfrac{1}{2}SiF_{4(g)} + 839 \text{ kJ/mol,} \tag{2.1}$$
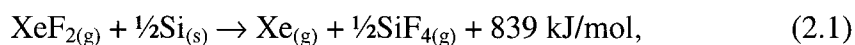
while the etching reaction for BrF_3 can be written in the form:

$$BrF_{3(g)} + \tfrac{3}{4}Si_{(s)} \rightarrow \tfrac{1}{2}Br_{2(g)} + \tfrac{3}{4}SiF_{4(g)} + 2036 \text{ kJ/mol.} \tag{2.2}$$
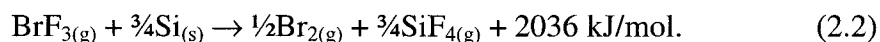
From (2.1) and (2.2) it can be seen that both reactions are quite exothermic and as such

care must be taken when etching thermally insulated structures (to be discussed in more detail later in Section 4.3.1 and Section 7.2.1).

The apparatus required to efficiently perform gas-phase silicon etching with either XeF_2 or BrF_3 consists of an etching/reaction chamber, an etchant source, an expansion reservoir, nitrogen purge, and a vacuum subsystem. A schematic diagram of a generic XeF_2/BrF_3 etching system is depicted in Figure 2.6. The construction materials should be stainless steel and, for safety reasons, the system should be housed inside a fume hood with ample ventilation. The main safety concern is any exposure of XeF_2 or BrF_3 to water or water vapour results in the formation of HF, a reactive acid.
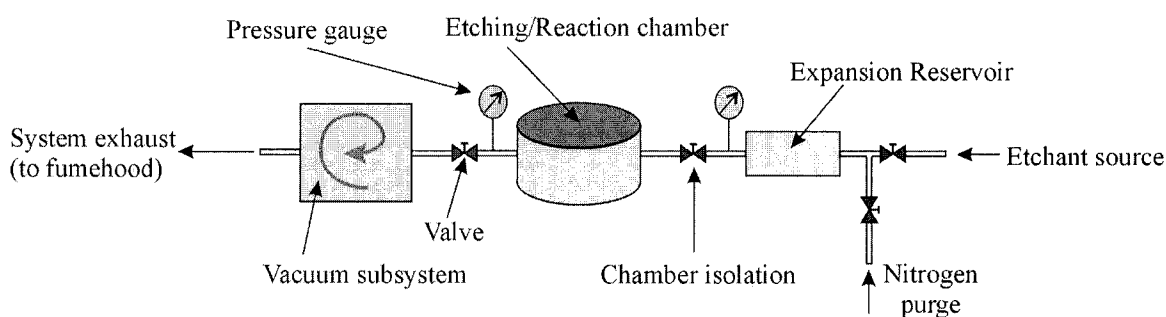
Figure 2.6 Schematic diagram of a generic XeF_2/BrF_3 etching system.

The samples to be etched are loaded into the etching chamber and both the etching chamber and expansion reservoir are pumped below 10 mTorr. The pump-down is followed by a nitrogen purge to aid in the removal of water vapour adsorbed to the inner surfaces of the etching chamber and expansion reservoir. The system is again pumped to below 10 mTorr, the chamber isolation valve is then closed, and a fixed amount of etchant vapour is introduced into the expansion reservoir. The chamber isolation valve is then opened to allow the etchant vapour to enter the etching chamber. Enough time is given to ensure the majority of etchant has been consumed by the etching reaction. The above procedures define one pulse of the etching, with as many as four etch pulses occurring consecutively. The chamber isolation valve is then opened; both the expansion reservoir and etching chamber are pumped down, followed by a nitrogen purge and another pump down. The etch rates for silicon will be dependent on the surface area of silicon exposed, the amount of vapour in each pulse, and the length of time the vapour is allowed to react with the silicon.

Plasma-phase etching of silicon occurs when the reactive gas that is used for dry etching is first bombarded with electrons excited by an RF field [30]. The electron interaction causes the reactive gas to dissociate into chemically reactive neutrals and ions before adsorbing and reacting with the silicon surface. The plasma-phase is a mixture of electrons, ions, and neutrals and results in an increased density of ions and neutral species that can participate in the chemical reaction, thus accelerating the reaction rate. If, after generating the plasma, the ions are accelerated towards the targeted substrate by the application of an electric field and this bombardment plays a synergistic role in the chemical etch reaction, the process is then referred to a reactive ion etching (RIE). The directionality of the accelerated ions and the unique properties of the plasma chemistry then result in the ability to control the degree of anisotropy during an RIE etch process. Plasma-phase etching and RIE are used to etch shallow cavities in silicon and etch polysilicon in surface micromachining.

A relatively new tool for etching very deep trenches (up to 500 μm) in silicon with nearly vertical sidewalls is known as deep reactive ion etching (DRIE). DRIE evolved from the need within the micromachining community for an etch process capable of anisotropically etching high aspect ratio (ratio of depth to width) trenches at rates substantially larger than those for traditional plasma-phase and RIE etch processes. One method of DRIE consists of cooling the wafer to cryogenic temperatures. Condensation of the reactant gases protects the sidewalls from etching by the reactive fluorine atoms; however, difficulties arise as the cooling can be difficult to maintain locally, and may result in undesirable thermal stresses. Another method of DRIE, referred to as the Bosch process (patented by Robert Bosch of Germany), consists of alternating deposition and etching cycles. The etch cycle, lasting five to fifteen seconds, uses SF_6 to etch the silicon. In the next cycle, a fluorocarbon polymer (made of a chain of CF_2 molecules in similar composition to Teflon™) about 10 nm thick is plasma deposited using C_4F_8 as a source gas. In the subsequent etch cycle the energetic ions (SF_x^+) remove the passivating polymer at the bottom of the trench as a result of the ions' directionality, leaving the polymer film relatively intact along the sidewalls. Alternating the etch and deposition cycles in a repetitive manner results in a very directional etch at a rate as high as 4 μm/min.

A limitation of DRIE is the decrease in etch rate as the aspect ratio increases, known as lag. In addition, the high selectivity to silicon dioxide makes it possible to etch deep trenches and stop on a buried layer of silicon dioxide, as in the case of etching SOI wafers. However, when the etch reaches the buried silicon dioxide layer, the concentration of reactive fluorine species increases dramatically, resulting in an undesirable lateral undercut confined to the silicon-silicon dioxide interface. The solution to this problem when etching deep trenches in SOI wafers is to use a fast etching process followed by a slow etching process as soon as the buried silicon dioxide layer is detected.

2.4 PACKAGING

The process of housing microelectromechanical components and systems inside a protective container is called packaging. The main goal of packaging is to convert the micromachined system into a useful assembly that can safely and reliably interact with its surroundings. Unlike the integrated circuit industry, where packaging need only provide reliable, dense interconnections for high-frequency electrical signals, MEMS packaging is very broad in scope and must account for a complex and diverse set of parameters, since each application is unique. Standards for MEMS packaging are lacking and successful designs often remain proprietary. Package design is responsible for 75 to 95% of the overall cost of a microelectromechanical component or system [57].

This section presents a brief overview of the packaging process, some of the main issues to consider when designing a MEMS package, and a few packaging solutions. To begin, a simplified process flow for MEMS packaging is illustrated in Figure 2.7.

After inspection, testing, and dicing of the wafer each individual die is separated and any additional processing, known as post-processing, is performed as required. The individual die is then mounted inside a package and attached onto a platform made of metal, ceramic, or plastic. Generally, die-attach processes employ metal alloys (solders) or organic adhesives (silicones and epoxies). Organic adhesives are attractive because they are inexpensive, easy to automate, and cure at low temperatures.

The process of establishing interconnects follows the die attachment and for

1. Inspect and test wafer   2. Dice wafer   3. Separate dice   4. Post-process
                                                                          (optional)

Wire bond

Flip chip

7. Calibration and test   6. Package seal   5. Attach die and interconnects
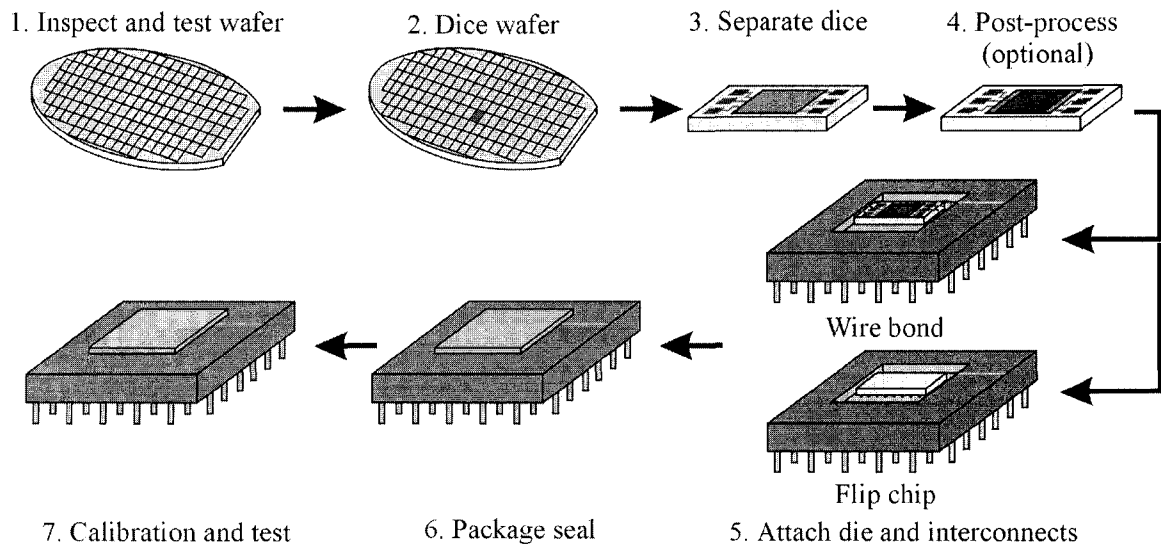
Figure 2.7 Illustration of a simplified process flow for MEMS packaging.

MEMS can include both electrical and fluid connectivity. Electrical connectivity addresses the task of providing electrical wiring between the die and the package, while fluid connectivity ensures the reliable transport of liquids and gases between the die and external fluid control units. Two methods of establishing electrical interconnects are wire bonding and flip-chip bonding.

Wire bonding is the most popular technique to electrically connect the die to the package. A short length of gold or aluminum wire forms a low resistance contact between the aluminum bond pads on the die and the package leads. The free ends of the wire are attached by either thermosonic (for gold wire), or ultrasonic (for aluminum wire) bonding. Thermosonic gold bonding is the simultaneous combination of heat (420 K), pressure, and ultrasonic energy to the bond area, whereas ultrasonic bonding is the combination of only pressure and ultrasonic energy.

Flip-chip bonding involves bonding the die, top-face-down, on a package substrate. Electrical contacts are made by means of plated solder bumps between bond pads on the die and metal pads on the package substrate. The attachment has a relatively small die-to-package spacing of 50 to 200 μm and, unlike wire bonding, which requires bond pads positioned peripherally to avoid crossing wires, flip-chip allows bond pad placement over the entire die resulting in a significant increase in interconnect density. More details regarding wire and flip-chip bonding can be found in [30, 32, 34].

With regard to fluid interconnect technology no standards exist for packaging microfluidic devices such as micropumps and microvalves simply because the field remains in its infancy and few microfluidic devices are commercially available. Most microfluidic interconnect schemes remain at the level of manually inserting a capillary into a silicon cavity or via-hole, and sealing the assembly with silicone or epoxy.

Lastly, the package is sealed and a final calibration and test is performed prior to the component being put into service.

2.4.1 Packaging Issues

Some of the factors and considerations frequently encountered in MEMS packaging that need to be addressed are:

- wafer thickness and wafer dicing
- thermal management and stress isolation
- protective coatings and media isolation
- hermetic packaging

In terms of wafer thickness, standards in the integrated circuit industry dictate silicon wafer thickness, depending on their diameters. Often, in the case of micro-machining, a stack of bonded silicon or glass wafers can have a total thickness exceeding 1 mm. This thickness, significantly greater than the standard 500 to 650 μm, can pose a challenge for packaging facilities due to incompatibility with standard packages.

Wafer dicing is a harsh process where a high speed, water-cooled diamond or carbide saw blade cuts through the wafer to separate the dice, subjecting free-standing microstructures to strong vibrations. Protecting these sensitive components from particulates, liquids, and vibrations requires the application of unique design approaches. One approach consists of forming shallow dimples in wafer tape and mounting the wafer upside down prior to dicing. Another approach is to perform the final etch process (post-processing), that yields the freestanding structures, after dicing. This variation in process sequence ensures that there are no free structures during dicing, but has the disadvantage of sacrificing the batch fabrication process and hence, results in an increase in cost/unit.

The role of thermal management in MEMS includes the cooling of heat-dissipating devices, especially thermal actuators, and the controlling of sources of

temperature fluctuations that can adversely affect sensor or actuator performance. Thermal management is performed at two levels: the die level, and the package level. At the die level the nature of the application severely influences thermal management. For example, in a typical pressure sensor that dissipates a few tens of milliwatts over an area of several square millimetres, the role of thermal management is to ensure the long-term thermal stability of the piezoresistive sense elements. In terms of packaging materials, ceramics and metals are excellent because of their high thermal conductivities. Careful selection of the die-attach material in terms of thermal performance is also a factor to consider.

As for stress isolation, it is important that any piezoresistive or piezoelectric elements are not subject to mechanical stress of undesirable origin and extrinsic to the parameter being sensed. An example of extrinsic stress would be a piezoresistive pressure sensor producing incorrect readings because of stresses on the silicon die originating with the package housing. Another serious effect of packaging on stress-sensitive sensors is long-term drift resulting from creep in the adhesive used to attach the die to the package housing.

Micromechanical structures in direct contact with external media must be protected against adverse environmental effects, especially if the devices are subject to long-term reliability requirements. One example is that sensors designed for automotive applications must be able to withstand salt water and acid rain pollutants. In instances of mildly aggressive environments, a thin coating, such as parylene, is sufficient protection [58-59]. For extreme environments, such as applications in heavy industries, aerospace, or oil drilling, thin coatings are unable to provide adequate protection for silicon microstructures, hence special media isolation packaging is necessary. One such media isolation scheme for pressure sensors involves immersing the silicon microstructure in special silicone oil, with the entire assembly contained within a heavy-duty steel housing.

A hermetic package is defined as one that prevents the diffusion of helium. In practice, it is understood that a hermetic package also prevents the diffusion of water vapour. A hermetic package significantly increases the long-term reliability of electronic components by shielding against moisture and other contaminants, thus eliminating many common failure mechanisms, such as corrosion. A hermetic package must be made from

metal, ceramic, millimetre-thick glass, or silicon, and is typically evacuated or filled with an inert gas. Plastics, though passing the strict helium leak-rate test, are generally not considered hermetic in practice, as they allow the infusion of moisture into the package interior.

2.4.2 Packaging Solutions

There are three general categories of widely adopted packaging approaches in MEMS, each representing the constituent material used in the die housing. The three approaches are ceramic, metal, and plastic, each with its own merits and limitations. A list of some of the diversity of MEMS packaging requirements is presented in Table 2.4. Ceramics are hard and brittle materials made by shaping a nonmetallic mineral and then firing at a high temperature for densification. Most ceramics are electrically insulating, some are good thermal conductors, and all are completely customizable, allowing for the formation of through-ports and manifolds. Unfortunately, ceramics usually suffer from shrinkage (13 to 15%) during firing and compared with plastic packaging, are significantly more expensive. Due to their ease in shaping, reliability, and favorable material properties, ceramic packages are the mainstay in electronic packaging, despite the relatively high cost. Figure 2.8 shows some photographs from a collection of ceramic packages used for MEMS applications.

Metal packages are attractive to MEMS for the same reasons the integrated circuit industry adopted the technology over 30 years ago. Metal packages are robust and easy to assemble, they satisfy the small pin-count requirements of most MEMS applications, they can be prototyped in small volumes with rather short turnaround periods, and they can be hermetically sealed. A major drawback of metal packaging is the relatively large expense of metal headers and caps, at least ten times higher than an equivalent plastic package. The standard family of transistor outline (TO) –type packages, covering a wide variety of shapes, accommodating as many as ten electrical pins, and made from either stainless steel or Kovar® alloy, are the commonly adopted form of metal packages for MEMS applications. Other metal package types, in dual-inline-package (DIP) form, are used strictly for RF MEMS applications where there is a requirement for significant noise reduction that can only be accommodated by an enclosing metal structure. Photographs

Table 2.4 List showing some of the diversity of MEMS packaging requirements [30].

Application	Electrical contacts	Fluid ports[1]	Media contact	Stress isolation	Thermal isolation	Package type[2]
Sensors						
Pressure	Yes	Yes	Yes	Yes	No	P, M, C
Flow	Yes	Yes	Yes	No	Yes	P, M, C
Acceleration	Yes	No	No	Possibly	No	P, M, C
Yaw-rate	Yes	No	No	Possibly	No	P, M, C
Microphone	Yes	Yes	Yes	No	No	P, M, C
Hydrophone	Yes	Yes	Yes	No	No	M, C
Actuators						
Optical switch	Yes	No	No	No	No	C
Display	Yes	No	No	No	Possibly	C
Valve	Yes	Yes	Yes	No	Possibly	M, C
Pump	Yes	Yes	Yes	No	No	M, C
PCR & CE	Yes	Yes	Yes	No	Yes	P, M, C
Passive						
Nozzles	No	Yes	Yes	No	No	P, M, C
Fluid mixer	No	Yes	Yes	No	No	P, M, C
Fluid amplifier	No	Yes	Yes	No	No	M, C

[1] fluid includes liquid or gas, [2] P: Plastic, M: Metal, C: Ceramic

(a) (b) (c)

(d) (e) (f) (g)
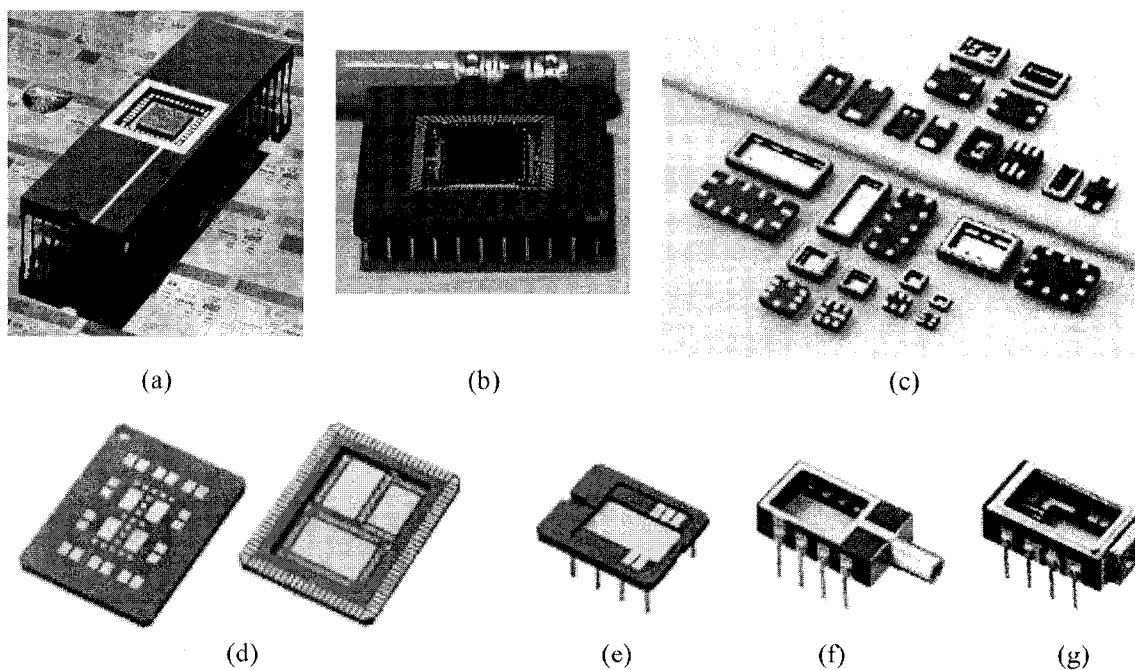
Figure 2.8 Photographs showing a collection of ceramic packages used for MEMS applications: (a) 40 pin dual-inline, (b) 84 pin gate array, (c) various surface mount, (d) multi-chip, (e) optoelectronic for passive alignment, (f) optoelectronic for fiber input, and (g) optoelectronic with ball lens.

of two types of metal packages are presented in Figure 2.9.

Unlike metal or ceramic packages, molded plastic packages are not considered hermetic; however, they are cost-effective solutions and advances in plastic packaging have further improved reliability to high levels, resulting in their domination in the packaging of integrated circuits. Photographs of some plastic packages are shown in Figure 2.10.

(a)   (b)
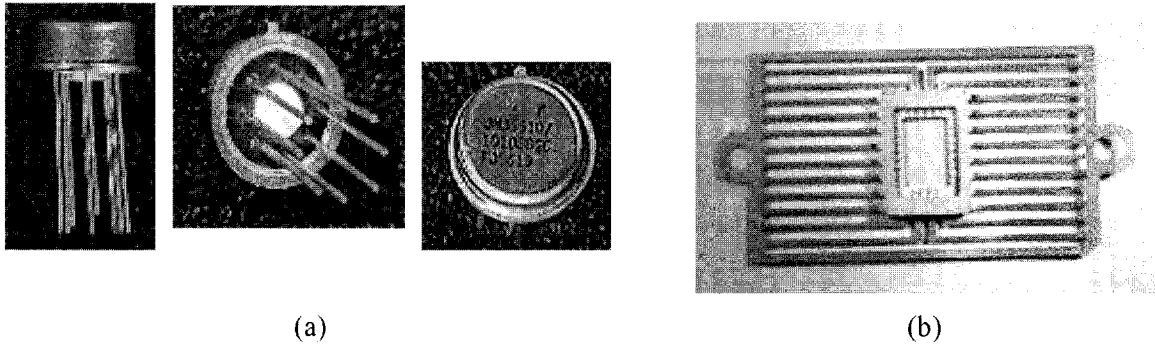
Figure 2.9 Photographs depicting two types of metal packages used for MEMS applications: (a) 8 pin transistor outline, (b) 24 pin dual-inline for RF applications.
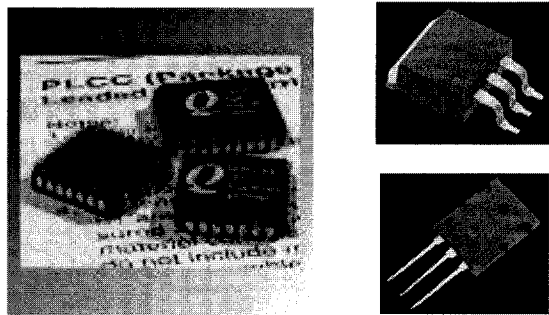
Figure 2.10 Photographs showing plastic packages.

2.5 APPLICATIONS

The list of MEMS structures and devices continues to grow as more applications prove to benefit from miniaturization [60-63]. However, economics ultimately determines the commercial success of a particular micromachined design or technology. The design process begins with specifications leading to the identification of general operating principles and structural elements. This is followed by analysis and simulation, and finally the outlining of the fabrication process steps. The design process is iterative,

often involving continuous adjustments in the progression from idea to product and may rely on economic considerations or ease of manufacturing rather than performance.

MEMS applications can be categorized into two broad categories: sensors and actuators. Sensors are transducers that convert a specific physical parameter, such as mechanical, thermal, or other forms of energy, to the exclusion of other interfering parameters, into a signal. Actuators behave exactly opposite to sensors in that actuators convert electrical energy into mechanical, thermal, and other forms of energy [64].

Perhaps the most common sensing technique is temperature measurement using the dependence of various material properties on temperature. For example, the temperature coefficient of resistance (TCR) property common to many metals can range from 10 to 100 parts per million per degree celsius. Both piezoresistivity and piezoelectricity are also often used sensing techniques. Piezoresistivity is the phenomenon by which an electrical resistance changes in response to mechanical strain. Likewise, piezoelectricity exhibits a change in electrical potential in response to mechanical strain. Another sensing technique is capacitive sensing that relies on an external physical parameter changing either the spacing or the relative dielectric constant between two plates of a capacitor. Electromagnetic sensing techniques include the Hall effect, where a magnetic field induces a voltage in a direction orthogonal to current flow, and Faraday's law of induction, where a current is generated by the motion of a conductor through a magnetic field.

In terms of actuation methods, the most common are electrostatic, piezoelectric, thermal, and magnetic techniques. Electrostatic actuation relies on the attractive force between two conductors carrying opposite charge. Piezoelectric actuation is the opposite of piezoelectric sensing in that an applied voltage creates a mechanical strain. Thermal actuation occurs when a heated material expands. Another method of thermal actuation, termed thermo pneumatic, consists of heating a fluid inside a sealed cavity. Pressure from evaporation exerts a force on the cavity walls, which bend if made sufficiently compliant. Lastly, the dominant magnetic actuation mechanism is the Lorentz force, that is, the force generated by a current-carrying conductor located within a magnetic field. The following section is a brief description of some of the sensors and actuators presently

under production, as well as a look into some future applications for MEMS presently under development.

2.5.1 Sensors

An incomplete list of micromachined sensors currently under mass production includes: pressure sensors, acceleration sensors, mass flow sensors, angular rate sensors and gyroscopes, and micromachined microphones. This list is incomplete because it does not include any designs presently under development and only describes some of those sensors that have reached a certain level of popularity due to their success.

The first high-volume production of a micromachined pressure sensor began in 1974 by National Semiconductor Corporation. For the majority of today's pressure sensors, the fabrication method is bulk micromachining. The two largest applications are manifold absolute pressure [65] and disposable blood pressure [66] sensing. These pressure sensors utilize a silicon diaphragm that deflects in response to a pressure load; the deflection is usually measured by piezoresistive or capacitive methods.

It took nearly 15 years since their first demonstration at Stanford University in 1979 for micromachined accelerometers to become accepted mainstream products. All accelerometers share a basic structure where an inertial mass is suspended from a spring. They differ, however, in the method of sensing the relative position of the inertial mass as it is displaced under externally applied acceleration forces. Capacitive sensing is a common method, where the mass is used as one side of a two-plate capacitor. Another sensing method uses piezoresistors to sense the internal strain induced in the spring. Finally, in yet another method, the spring is fabricated with piezoelectric properties to provide a potential in direct proportion to the displacement [30, 32, 34].

Flow sensors operate on the principle that the flow of gas over a surface of a heated element will produce convective heat loss at a rate proportional to the mass flow. Another name for devices of this nature is "hot-wire anemometers", and they all share a basic structure consisting of a thin-film heating element and a temperature-measuring device, both on a thin thermally isolating membrane suspended over an etch cavity [12-14].

The gyroscope is a critical navigational instrument used for maintaining a fixed orientation with great accuracy, regardless of position and earth rotation. A classical gyroscope consists of a flywheel mounted in gimbal rings, where the angular momentum of the flywheel counteracts externally applied torques, and thus maintains the orientation of the spin-axis. Micromachined sensors that detect angular rotation are often incorrectly referred to as gyroscopes, since miniaturization of the flywheel leads to a miniscule angular momentum that is easily influenced by small externally applied torques. Such micromachined sensors detect angular rotation via the Coriolis effect. The Coriolis effect is a direct consequence of a body's motion in a rotating frame of reference and manifests itself in weather phenomena, such as hurricanes and tornadoes for example. Micromachined angular-rate sensors (gyroscopes) all consist of an oscillating element at their core (the moving body) where rotation of the sensor body produces a Coriolis acceleration proportional to the cross product of angular velocity and the velocity of core oscillation [67-68]. The resulting core deformations from the Coriolis acceleration are subsequently detected by capacitive methods.

Finally, a micromachined capacitive microphone is designed to measure very small pressure fluctuations that arise from the transmission of acoustic energy through air. The basic structure of this MEMS device consists of a diaphragm suspended over a back plate that together form a capacitor. Holes through the diaphragm ensure that there is no static pressure build up, otherwise, variations in atmospheric pressure would overload the sensor's output. In operation, the diaphragm vibrates in response to dynamic acoustical pressure waves, that is, the microphone detects changes in pressure rather than the pressure magnitude. To further improve the frequency response, a micromachined resonance cavity is etched in the underlying substrate beneath the back plate [30].

2.5.2 Actuators

Like the preceding section on sensors, this section describes several micromachined actuators that have been successful enough to enter mass production and achieve some level of acceptance. These actuators include: digital micro-mirror devices,

micromachined valves, and, while not by strict definition an actuator, nozzles that play an important role in the inkjet printer and microfluidic industry.

The Digital Micromirror Device™ (DMD) is a trademark of Texas Instruments, which developed and commercialized this projection display technology [69]. The DMD consists of a two-dimensional array of optical switching pixels, each pixel being a reflective micro-mirror supported from a central post, residing on a silicon substrate. The central post, in turn, resides on an electrostatically actuated metal platform, which, supported by torsional hinges, exhibits two degrees of freedom motion.

The field of micromachined valves is relatively nascent and continues to show promise despite the strong competition from more mature, traditional valve technologies. Miniature valves demonstrate their developmental importance in the control of fluid-flow functions of small-scale applications such as portable biochemical analysis systems [70]. Typically, micromachined valves operate on the principle of a vertical fluid port that is blocked by a silicon plug suspended from a spring that is displaced under actuation.

Lastly, nozzles are among the simplest microstructures to fabricate and are common features in the design of atomizers, medical inhalers, and fluid spray systems. The thermal inkjet print head, used in inkjet printers for personal computers, receives frequent mention as a premier success story of MEMS technology [71]. In operation, a thin ink layer is superheated by a thin-film resistor residing at the bottom of an ink cavity, at the top of which is the exit nozzle. The super-heated ink layer quickly produces a bubble that forces the expulsion of ink out of the nozzle within 24 μs of the initiation of the heating. After the ink is expelled, the bubble collapses and the ink cavity refills with ink.

2.5.3 Future Applications

This section describes an overview of the role of MEMS in a number of emerging applications. The structures described are under development at industrial companies, organizations, and academic institutions and cover such applications as hinge mechanisms, miniature biochemical reaction chambers, micro-resonators and high-frequency filters, "grating light valve" displays, optical switches, micropumps, and thermo-mechanical data storage devices.

Hinges are very useful structures that, at the microscopic scale, extend the utility of inherently two-dimensional surface-micromachining technology into the third dimension. A potential future commercial application that may benefit from hinge structures is an assembly of microlenses, mirrors, and other optical components [72]. The micro-hinge structure consists of a plate, a support arm, and a staple residing over the support arm and anchored to the substrate. Assembly has mainly been done by manual probing with mechanical levers that lock into positions on the plate to permanently hold the hinge in an upright position.

Commercial instruments for biochemical and genetic analysis, such as those available from Perkin-Elmer, perform a broad range of analytical functions, but are generally desktop in size. MEMS technology, as evidenced by the high level of activity in the scientific community, promises to miniaturize these instruments [73]. Two important analytical tools presently under investigation are DNA amplification by polymerase chain reaction (PCR) and DNA separations via a process known as capillary electrophoresis (CE). Several demonstrations of PCR and CE on a silicon chip have been done but have failed to out-perform the existing, inexpensive plastic cartridges thus delaying mass commercialization [30].

In response to the demand for small portable telephones, MEMS technology promises to deliver miniature oscillators, filters, switches, and tunable capacitors to replace conventional discrete components such as quartz crystals. Aggressive price requirements, however, will ultimately determine what level of success MEMS technology will achieve in wireless systems. The specifications required of a micro-resonator are a high resonant frequency and a very high quality factor (Q). One design, incorporating two electrostatic comb structures connected to a shuttle plate and suspended from a double folded spring, has demonstrated resonant frequencies up to 70 MHz with Q values in excess of 20,000 [74]. Linking two similar devices in a linear chain can result in a high-frequency narrow bandpass filter. Similar phenomena have been observed at much lower frequencies in [36].

The grating light valve is a novel light-switching concept that relies on closely spaced parallel rows of reflective ribbons suspended over a substrate [75]. The separation gap between the ribbons and the substrate is approximately one-quarter the

wavelength of visible light. In their rest state, the ribbons appear as a continuous surface to incident light and normal reflection occurs. When an electrostatic voltage pulls down alternate rows of ribbons, the light reflecting from the deflected ribbons travels an additional one-half of a wavelength and thus becomes 180° out-of-phase with respect to the light from the stationary ribbons. The effect is that of a phase grating, diffracting the incident light into higher orders. A full colour display is created by combining three sets of ribbons together to create a single pixel, one for each of the three primary colours. The main advantage of this system is its fast switching speed on the order of 20 ns, approximately 1000 times faster than the DMD™ mentioned in Section 2.5.2.

Miniature optical switches are to optical communications and light transmission what the transistor is to electronic signaling. Two general application areas have emerged, one in fibre optic communications and another in data storage. In data storage applications, miniature optical switches can steer light pulses to appropriate locations on the platter of a magneto-optical disk. In fibre optic communications, arrays of optical switches allow the rapid (tens of milliseconds) reconfiguration of optical networks by altering the light path of intersecting fibres. One demonstration from the University of Neuchâtel, Switzerland illustrates the basic structure of one implementation of a 2 x 2 optical switch [76]. It consists of an electrostatic comb actuator that controls the position of a vertical mirror at the intersection of two perpendicular grooves; within each lie two optical fibres. If the mirror is retracted, light passes unobstructed. If the mirror is positioned in the middle of the intersection, light is reflected 90° thereby altering the data path. This device was fabricated on SOI wafers that had a 75 μm thick top silicon layer and relied extensively on the DRIE etching process.

Micropumps are likely to be used for the automated handling of fluids for chemical analysis and drug-delivery systems and can have a significant advantage over conventional systems if they can be integrated with other fluid-handling components. One demonstration of an efficient micropump that exhibits bi-directional flow consists of a stack of four wafers each etched separately before bonding together [77]. The bottom two wafers define two check valves at the inlet and outlet, while the top two wafers form the electrostatic actuation unit. An applied AC voltage electrostatically actuates the pump diaphragm in conjunction with check valves to allow fluid flow in one direction

only. Increasing the driving frequency beyond the response time of the check valves results in an operation lag that can change the direction of fluid flow, thus enabling bi-directional pumping.

The use of micromachined cantilevers for data storage has been demonstrated in [78]. The write operation is done by long, thin cantilevers embedded with heaters at their tips to locally melt the surface of a spinning polycarbonate disk. The read operation is achieved by sensing the surface topography with a piezoresistive cantilever. Both read and write cantilevers remain in light contact with the surface of the spinning disk sufficiently apart to avoid wear. This method of data storage has the potential to increase storage densities by at least one order of magnitude compared to present storage densities and the disadvantage of only being able to write data once to the surface (though read many times).

2.6 SUMMARY

This chapter has presented an overview of micromachining materials, processes, packaging techniques, present applications, and future applications. Continued refinement of MEMS/MST technology and the aforementioned is being achieved daily, resulting in new commercial products and new possibilities. Due to these continuous advancements, it has been predicted that micromachining technology will someday become as common in everyday life as integrated circuit technologies are today.

Chapter
THREE
HEAT TRANSFER FUNDAMENTALS

3.1 INTRODUCTION

Thermodynamics states that energy can be transferred by interactions of a system with its surroundings. The nature of these interactions take the form of a combination of one, or more, of three basic heat transfer modes: heat conduction, convection, and thermal radiation [79]. In this chapter, a brief overview of these modes is presented, with emphasis on introducing the physics involved in the transfer of heat by thermal radiation.

For thermal-conductivity-type vacuum gauges the heat loss from a heated filament to the surrounding environment occurs via the three aforementioned modes in four ways: thermal radiation, convection, heat conduction through the gas to the surrounding walls and substrate, and heat conduction through the filament supports. These four heat loss means are illustrated in Figure 3.1. The contribution from each of these four transfer mechanisms varies as a function of the system pressure. This variation is represented by the Knudsen number, K_n, which is defined as the ratio of the mean free path, λ_{mfp}, of the gas molecules to the characteristic dimension, d, of the system [80]. An illustration of the variation in heat transfer mechanism versus Knudsen number is shown in Figure 3.2.
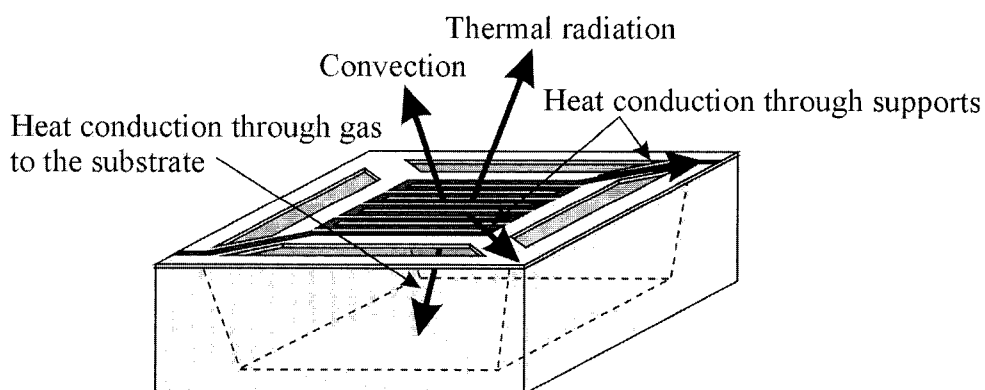
Figure 3.1 Typical micromachined Pirani gauge showing the heat loss mechanisms.
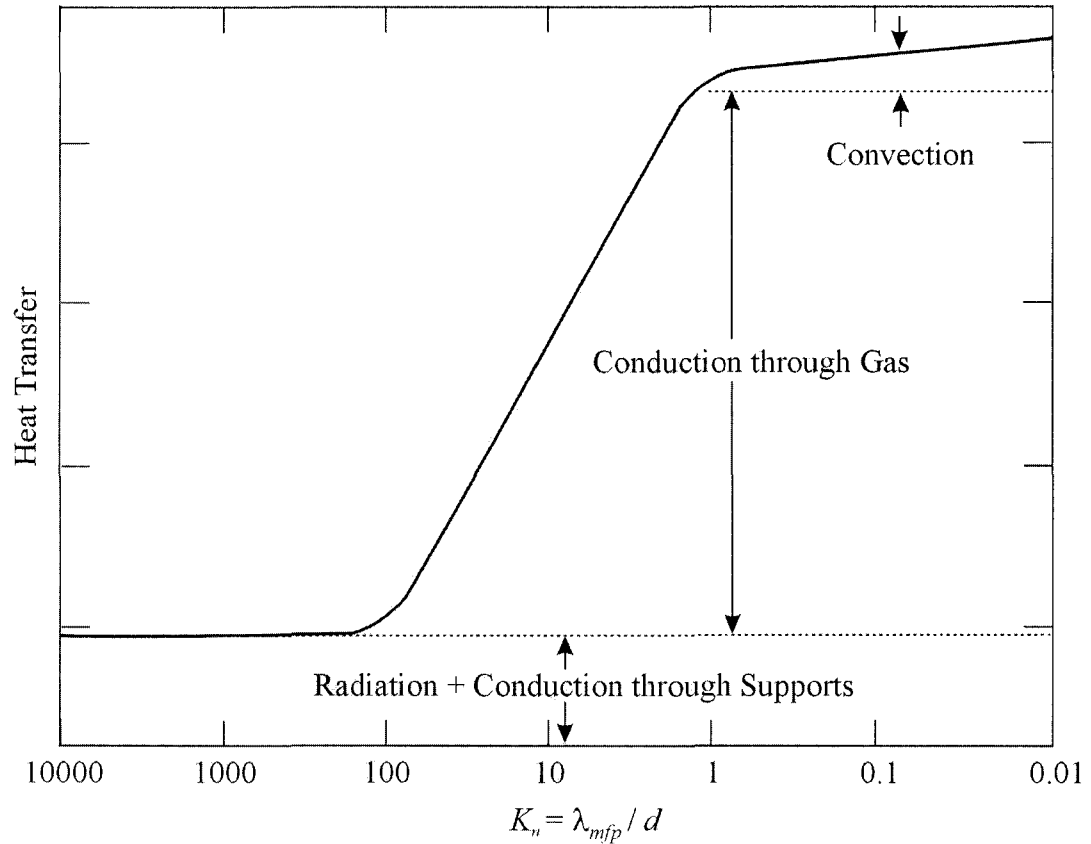
Figure 3.2 Heat transfer variation for a thermal-conductivity-type vacuum gauge.

The mean free path of a gas is defined as the mean distance traveled by its constituent molecules between collisions, these collisions occurring with other gas molecules or with the walls of the enclosing vessel. In terms of gas pressure, p [Pa], the mean free path is expressed by [81]:

$$\lambda_{mfp} = \frac{kT}{\sqrt{2}\pi a^2 p},$$

(3.1)

where k is the Boltzmann constant [1.3805×10^{-23} J·K^{-1}], T [K] is the absolute temperature of the gas, and a [m] is the mean collision diameter of the gas molecule. From (3.1) it can be understood that molecular collisions become more frequent (decrease in mean free path) by increasing the pressure (density) of the gas and less frequent by decreasing the pressure of the gas. The characteristic dimension is the shortest distance between the

heated filament and its enclosure for conventional thermal-conductivity-type gauges and the cavity depth below the heated platform (Figure 3.1) for micro-Pirani-type gauges.

At pressures near atmospheric where $K_n < 1$, the heat flow is independent of gas pressure except for a small convection effect. Decreasing the gas pressure so that $1 < K_n < 100$ results in conductive heat loss through the surrounding gas molecules becoming the dominant heat transfer mechanism, a mechanism that is also pressure dependent. Thermal-conductivity-type vacuum gauges are based upon this effect. Continuing to decrease the pressure to a region where $K_n > 100$ causes the heat flow to again become pressure-independent (infrequent collisions) and to be predominantly a result of thermal radiation and heat conduction through the supports. Assuming the heated filament is kept at a constant average temperature for pressure where $K_n > 100$, the thermal radiation and heat conduction to the supports will establish a constant loss. The magnitude and stability of this background will determine the lowest useful operating pressure of the vacuum gauge.

3.2 HEAT CONDUCTION

Heat conduction is the transfer of energy by particles (e.g. phonons, electrons, and molecules) in a substance due to molecular collisions between particles, where such a transfer requires the presence of a temperature gradient. Consider, for example, a long insulated bar of copper lying on the x-axis, and heated to a known temperature at one end and kept at a constant, lower temperature at the other end. Due to the conductive transfer of heat, the temperature along the bar will stabilize given sufficient time, a condition known as steady-state. The rate of heat flowing per unit area, or heat flux, at steady-state in the one-dimensional case can be written as

$$H_{conduction} = -k_1 \frac{dT}{dx},$$ (3.2)

where k_1 [$W \cdot m^{-1} K^{-1}$] is the thermal conductivity constant, dependent on material properties and somewhat on material temperature, and dT/dx is the temperature gradient

in the x-direction, the direction of heat flow. Note that in (3.2) the negative sign is a consequence of the fact that heat is transferred in the direction of decreasing temperature. The fact that heat is transferred in the direction of decreasing temperature derives directly from the definition of the second law of thermodynamics [82]. An illustration of the steady-state one-dimensional heat flux in (3.2) can be seen below in Figure 3.3.
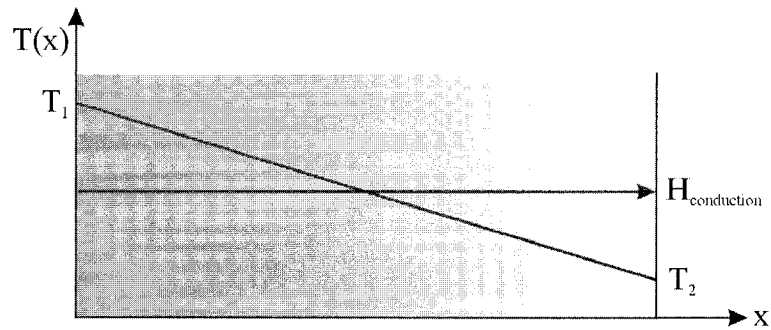
Figure 3.3 Illustration of steady-state one-dimensional heat conduction.

In general form, the three-dimensional heat flux can be expressed in vector format, known as Fourier's law, as [79]:

$$\vec{H}_{conduction} = -k_1 \nabla T(x, y, z) = -k_1 (\hat{i} \frac{\partial T}{\partial x} + \hat{j} \frac{\partial T}{\partial y} + \hat{k} \frac{\partial T}{\partial z}), \quad (3.3)$$

where ∇ is the three-dimensional del operator and $T(x,y,z)$ is the scalar temperature field in terms of the Cartesian coordinates, x, y, and z. Taking into account transient effects and heat sources or sinks per unit volume, the result is known as the heat diffusion, or more simply the general heat equation [79]:

$$\nabla \cdot k_1 \nabla T(x, y, z) + \dot{q} = \frac{\partial}{\partial x}(k_1 \frac{\partial T}{\partial x}) + \frac{\partial}{\partial y}(k_1 \frac{\partial T}{\partial y}) + \frac{\partial}{\partial z}(k_1 \frac{\partial T}{\partial z}) + \dot{q} = \rho_m c_p \frac{\partial T}{\partial t}, \quad (3.4)$$

where $\dot{q}$ [W·m^{-3}], ρ_m [kg·m^{-3}], and c_p [J·kg^{-1}K^{-1}] represent heat sources or sinks, density, and specific heat, respectively. Solving (3.4) provides both the spatial and temporal temperature distribution for a given system.

The parameters k_1, ρ_m, c_p, and $\dot{q}$ in the above equation can be both space- and temperature-dependent. In the case where k_1 is constant, (3.4) reduces to:

$$k_1 \nabla^2 T(x, y, z) + \dot{q} = \frac{\partial^2 T}{\partial x^2} + \frac{\partial^2 T}{\partial y^2} + \frac{\partial^2 T}{\partial z^2} + \frac{\dot{q}}{k_1} = \frac{1}{\alpha} \frac{\partial T}{\partial t}, \qquad (3.5)$$

where $\alpha = k_1/\rho_m c_p$ [$m^2 \cdot s^{-1}$] is the thermal diffusivity, a measure of the speed of propagation of heat within the solid when temperature changes over time. When no sources or sinks are present, (3.5) reduces to the Biot-Fourier equation [83]:

$$\frac{\partial^2 T}{\partial x^2} + \frac{\partial^2 T}{\partial y^2} + \frac{\partial^2 T}{\partial z^2} = \frac{1}{\alpha} \frac{\partial T}{\partial t}. \qquad (3.6)$$

Under steady-state conditions, (3.5) reduces to Poisson's equation:

$$\frac{\partial^2 T}{\partial x^2} + \frac{\partial^2 T}{\partial y^2} + \frac{\partial^2 T}{\partial z^2} + \frac{\dot{q}}{k_1} = 0, \qquad (3.7)$$

and, under steady-state conditions with $\dot{q} = 0$, (3.5) reduces to the well known Laplace equation [84]:

$$\frac{\partial^2 T}{\partial x^2} + \frac{\partial^2 T}{\partial y^2} + \frac{\partial^2 T}{\partial z^2} = 0. \qquad (3.8)$$

For gases, the thermal conductivity, k_1 is both temperature and pressure dependent. For temperature fluctuations on the order of a few hundred degrees, the thermal conductivity of a gas can be accurately described as being solely pressure dependent. When the gas is not at standard pressure, the following expression derived from empirical gas thermal conductivity versus pressure data, is used to approximate the pressure dependence of the thermal conductivity [6]:

$$k_g(p) \cong k_g^{atm}\left(\frac{p/p_o}{(1+p/p_o)}\right), \tag{3.9}$$

where k_g^{atm} is the thermal conductivity at atmospheric pressure and p_o is the pressure of transition between molecular and viscous flow for a particular gas. This transition pressure is loosely defined as the pressure at which $K_n \approx 1$ (the mean free path approximately equals the characteristic dimension) and is subsequently determined by [80, 85]:

$$p_o \cong \frac{kT}{\sqrt{2}\pi a^2 d}, \tag{3.10}$$

an equation similar to that for the mean free path, (3.1), but utilizing the characteristic dimension, d, rather than λ_{mfp}. In addition, and like the mean free path, the transition pressure is proportional to the temperature. Therefore, the transition pressure will increase for either an increase in temperature or a decrease in characteristic dimension.

3.3 CONVECTION

Convection as a mode of heat transfer consists of two mechanisms. The first mechanism is energy transfer due to diffusion or random molecular motion. The second mechanism is energy transfer due to the bulk motion of the fluid. That is, at any instant, large numbers of molecules are moving collectively. Convective heat transfer occurs between a fluid and a bounding surface and, like conduction, where a temperature gradient is required between the two for the transfer to occur. The total heat transferred by convection is the sum of the diffusion and bulk motion mechanisms.

The rate of one-dimensional steady-state natural convective heat transfer per unit area is known as Newton's law of cooling and can be expressed as [79]:

$$H_{convection} = h_1(T_s - T_f), \tag{3.11}$$

where: h_1 [W·m^{-2}K^{-1}] is the convection heat transfer coefficient, dependent on boundary layer conditions, fluid properties, temperature, and pressure; T_s [K] is the surface temperature; and T_f [K] is the fluid temperature at a distance far from the heated surface.

Convective heat transfer can be classified as forced, free (natural), or mixed, depending on the nature of the flow. Forced convection is the result of external means causing the movement of the fluid near a surface, such as, for example, atmospheric winds. Free or natural convection results from buoyancy forces exceeding the fluid's own viscous and gravitational forces. Finally, mixed convection, as the name implies, is the result of a combination of both forced and free convection.

The likelihood of free convection occurring is determined in terms of the Rayleigh number, R_a, defined as the product of the Prandtl and Grashof numbers, P_r and G_r, respectively:

$$R_a = G_r \times P_r$$

$$= \frac{g\beta(T_s - T_f)L^3}{v_k^2} \times \frac{v_k}{\alpha}$$

$$= \frac{g\beta(T_s - T_f)L^3}{\alpha v_k},$$

(3.12)

where g is the gravitational acceleration [9.81 m·s^{-2}], β is the volumetric thermal expansion coefficient [K^{-1}], v_k is the kinematic viscosity [m^2·s^{-1}], α, T_s, and T_f have their usual meanings as previously stated in (3.5) and (3.11), and L is the critical dimension. For the case of a horizontal heated plate, the buoyancy force is normal to the plate surface and does not act exclusively to induce fluid motion. Trapped gas beneath the plate results in a reduction in fluid velocities along the plate and can be accounted for by defining the critical dimension as the ratio of the surface area of the plate to its perimeter [79].

The Prandtl number, equal to the ratio of kinematic viscosity to thermal diffusivity, provides a measure of the relative effectiveness of the fluid to momentum and energy transport by diffusion. The value for P_r in air at temperatures ranging from 300 to

1000 K is approximately 0.72 at atmospheric pressure and decreases as pressure decreases.

The Grashof number is defined as the ratio of the buoyancy to viscous forces and is directly proportional to pressure. Under the same conditions of gas, pressure, and temperature as those used for calculating the Prandtl number, and using a square heated platform of 120 μm per side (typical micro-Pirani gauge dimensions) results in $G_r \cong 2 \times 10^{-5}$. Combining these values for G_r and P_r yields a Rayleigh number of approximately 10^{-5}. Typically, a Rayleigh number less than 10^3 indicates that any heat transfer due to free convection is very weak because of the buoyancy forces being unable to overcome the resistance imposed by the viscous forces [79]. Hence, this indicates that it is reasonable to assume that free convection does not contribute in a significant way to the transfer of heat within the operation of a micro-Pirani gauge. Furthermore, to confirm this assumption, experiments with micro-Pirani gauges have demonstrated the device response to be independent of device orientation [15]. Changing the device orientation in the presence of natural convection should produce a variation in device response.

3.4 THERMAL RADIATION

Radiation is energy emitted by matter, where the emission is governed by the temperature of the matter. The emission is attributed to changes in electron configurations of the constituent atoms or molecules. Energy emitted from this process takes the form of electromagnetic waves or photons and does not require the presence of a material medium for transport. For radiation propagating in a particular medium, the standard wave properties of frequency, v [s^{-1}] and wavelength, λ [m] are related by:

$$\lambda = \frac{c}{v} , \qquad (3.13)$$

where c [m·s^{-1}] is the speed of light in the medium. For propagation of light in the absence of a medium (that is, in a vacuum), $c = c_o \cong 2.998 \times 10^8$ m·s^{-1}. Thermal radiation is generally considered to encompass those wavelengths associated with the intermediate

portion of the electromagnetic spectrum. Such wavelengths include the near ultraviolet (0.1 to 0.4 μm), the visible (0.4 to 0.7 μm), and the infrared (0.7 to 100 μm) portions of the electromagnetic spectrum.

The rate of radiative energy flux emitted from a surface in all directions at a temperature, T_s, over all wavelengths is known as the Stefan-Boltzmann law. This law is described as follows [86-87]:

$$E(T) = \varepsilon \sigma T_s^4, \tag{3.14}$$

where $E(T)$ is known as the emissive power per unit of emitting surface area [W·m^{-2}], σ is the Stefan-Boltzmann constant [5.67x10^{-8} W·m^{-2}K^{-4}], and ε is the emissivity, dependent on the surface material and finish, wavelength, and somewhat on temperature, with values in the range $0 \le \varepsilon \le 1$. Surfaces with $\varepsilon = 1$ are known as blackbodies or ideal radiators; surfaces with $\varepsilon < 1$ are commonly referred to as gray bodies. A blackbody or ideal radiator can be described as having the following properties:

(a) a blackbody absorbs all incident radiation, regardless of wavelength and temperature;

(b) no surface can emit more energy than a blackbody at a prescribed temperature and wavelength; and

(c) radiation is emitted from a blackbody surface equally in all directions, this characteristic defining what is called a diffuse emitter.

The origin of (3.14) was found experimentally by Stefan in 1879 and later, in 1900, associated with Planck's law for the spectral intensity, $I(\lambda,T)$ [W·m^{-3}], over all wavelengths by [88]:

$$E(T) = \int_0^\infty I(\lambda,T)d\lambda = \int_0^\infty \frac{2\pi h c_o^2}{\lambda^5 (e^{hc_o/\lambda kT_s} - 1)} d\lambda, \tag{3.15}$$

where h is Planck's constant [6.626x10^{-34} J·s]. A plot of Planck's law, $I(\lambda,T)$, known as the Planck distribution, is shown in Figure 3.4. The Planck distribution shows how a

blackbody emits at a peak wavelength that shifts to shorter wavelengths as the temperature of the emitting body increases. The wavelength, λ_{max} [μm], at which the maximum intensity of blackbody radiation is emitted at temperature T, that is, the peak of the Planck distribution, is expressed by Wien's displacement law [87]:

$$\lambda_{max} = \frac{2898\ \mu m \cdot K}{T}.$$

(3.16)
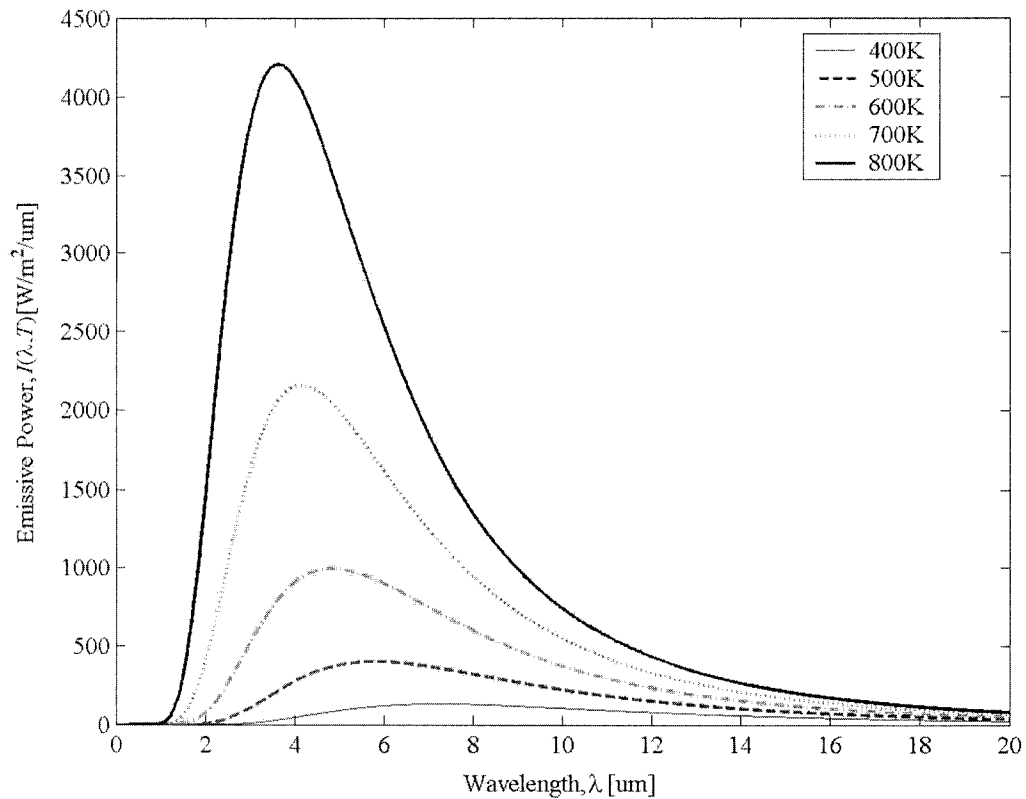
Figure 3.4 Planck distribution showing the emissive power per unit area per wavelength for various surface temperatures ranging from 400 to 800 K.

A special case of (3.14) occurs when the radiating surface is enclosed by an absorbing surface, for example, a very small incandescent light bulb with surface area, A_s, and surface temperature, T_s, enclosed within a large metal sphere at temperature T_∞ [79]. The resulting rate of thermal radiation transfer can be expressed in the form:

$$H_{radiation} = \varepsilon\sigma A_s (T_s^4 - T_\infty^4),$$
(3.17)

where the units of $H_{radiation}$ are Watts and the light is emitted from the source equally in all directions (diffuse emitter).

The solid angle of the emitted radiation is defined as the area of the spherical surface where the radiation is intercepted, divided by the radius squared of the surface, or in mathematical terms:

$$\Delta\Omega = \frac{\Delta A}{r^2}.$$
(3.18)

Substituting the surface area of a sphere, $\Delta A = 4\pi r^2$, into (3.18) results in a solid angle of 4π sr or steradians, a steradian being the dimensionless unit of solid angle.

Suppose now that the absorbing surface is of differentially small area, dA, specified in terms of a spherical coordinate system and illustrated in Figure 3.5. The area, dA, can then be represented in terms of the zenith and azimuthal angles, θ and ϕ, respectively by:

$$dA = r^2 \sin\theta \, d\theta \, d\phi.$$
(3.19)

Substituting (3.19) into (3.18) results in a solid angle of:

$$d\Omega = \sin\theta \, d\theta \, d\phi,$$
(3.20)

where, for a completely enclosing surface:

$$\Omega = \int_0^{2\pi} \int_0^{\pi} \sin\theta \, d\theta \, d\phi = 4\pi.$$
(3.21)
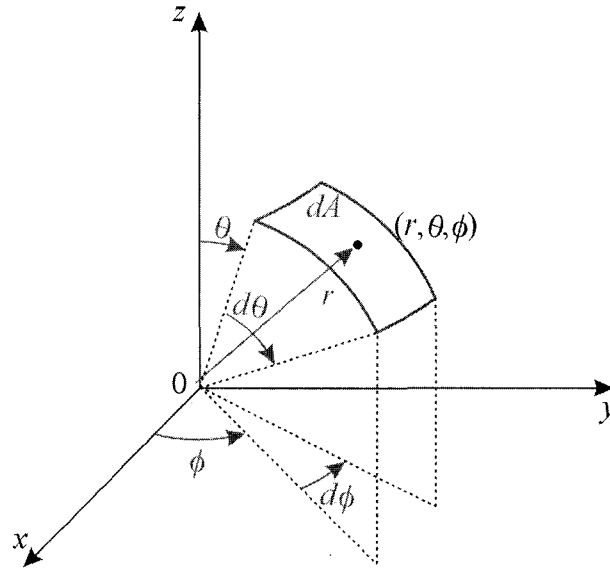
Figure 3.5 The spherical coordinate system showing the differentially small surface, dA.

In the case of a point source radiative emitter placed at the origin and a flat, circular absorbing surface (photodetector) placed normal to and at a distance, s_1, from the emitter (Figure 3.6), the solid angle is calculated from the projected shadow of the flat surface onto an equivalent spherical surface. The projection results in a solid angle of:

$$\Omega = \int_0^{2\pi} \int_0^{\theta} \sin\theta \, d\theta \, d\phi$$

$$= 2\pi(1 - \cos\theta) \qquad . \qquad (3.22)$$

$$= 2\pi\left(1 - \frac{s_1}{\sqrt{s_1^2 + r_d^2}}\right)$$

The case described by (3.22) leads to the development of what is called the solid angle ratio, S_{ar}, defined as the ratio of radiation absorbed (3.22) to radiation emitted (3.21):

$$S_{ar} = \frac{\Omega}{4\pi}, \qquad (3.23)$$

where in the case of a flat, circular absorbing surface normal to the origin, substituting (3.22) into (3.23), results in:

$$S_{ar} = \frac{1}{2}\left(1 - \frac{s_1}{\sqrt{s_1^2 + r_d^2}}\right).$$

(3.24)

$$\cos\theta = s_1/r$$

$$r^2 = s_1^2 + r_d^2$$
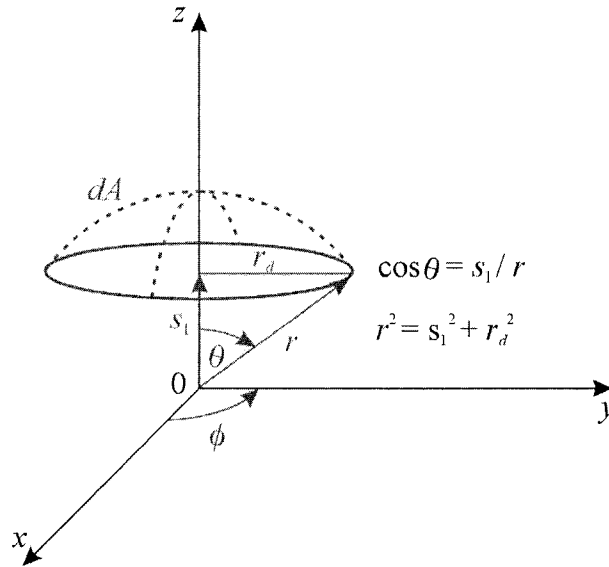
Figure 3.6 Illustration showing a flat, circular absorbing surface normal to the origin and the equivalent spherical surface for calculation of the solid angle.

Finally, combining the solid angle ratio of (3.24) with (3.17) allows for the determination of the radiative emitter's temperature, T_s, by sampling the emitted power over a small area and takes the form:

$$T_s = \left[T_\infty^4 + \frac{H_{radiation}}{\varepsilon\sigma A_s} \cdot \frac{1}{S_{ar}}\right]^{\frac{1}{4}},$$

(3.25)

where A_s is the surface area of the radiative emitter, and the other variables have their usual meanings as defined previously in this chapter.

3.5 SUMMARY

The preceding sections have presented a brief summary of the operating principles and equations that govern heat conduction, natural convection, and thermal

radiation. The direct application of (3.24) and (3.25) are the principle by which simulations of the operating micro-optical Pirani gauge device can be generated. That is, a mean device temperature can be determined by knowing the solid angle ratio of the detector and the amount of radiation collected. Additional equations such as (3.2), (3.4), (3.9), (3.10), and (3.15) will be utilized and further refined in Chapter 6, where a mathematical model of the structures examined in this project is presented and computer-generated simulations produced.

MICRO-OPTICAL PIRANI SENSORS

4.1 INTRODUCTION

The micro-optical Pirani sensors studied during this project are intended for use as absolute gas pressure sensors and for gas analysis/detection based on each gas having a markedly different thermal conductivity. Each sensor consists of a thermally isolated silicon dioxide platform with dimensions on the order of one hundred microns that resides over a cavity etched in a silicon substrate. Embedded inside the platform is an electrically heated, resistive polycrystalline silicon (polysilicon) filament that emits broadband radiation primarily in the visible to the infrared wavelengths as a function of the device mean temperature. For a given amount of dissipated power in the polysilicon the mean temperature of the platform will vary as a function of the thermal conductivity of the surrounding medium either from a change in the medium pressure (molecular density) or a change in the medium composition (constituent gas or gases).

In this chapter, the design and fabrication of the micro-Pirani devices investigated in this project is presented along with foundry yield statistics. An outline of the post-processing preformed to thermally isolate the microstructures by selective etching of the silicon substrate is also presented. Included in the post-processing section are the summarized results of the effect of the chosen etching process on the final fabrication yield and the thermo-physical properties of the polysilicon.

4.2 SENSOR DESIGN AND FABRICATION

The devices used in this study were fabricated by the MITEL Corporation 1.5 μm CMOS process [89]. This process incorporates multiple silicon dioxide (oxide) insulating layers, a silicon nitride (nitride) passivation layer, two aluminum metal layers (metal1 and metal2) for interconnects, and two polysilicon layers (poly1 and poly2)

typically used for fabrication of transistor gates and resistors. A cross sectional schematic diagram of the deposited layers incorporated in the MITEL 1.5 μm CMOS process is shown in Figure 4.1. All thickness dimensions are specified by the CMOS manufacturer. The opportunity to access this commercial foundry was made possible by the Canadian Microelectronics Corporation (CMC) who sponsored nine square millimetres of fabrication space on the multi-project masks, from which a number of die were made.
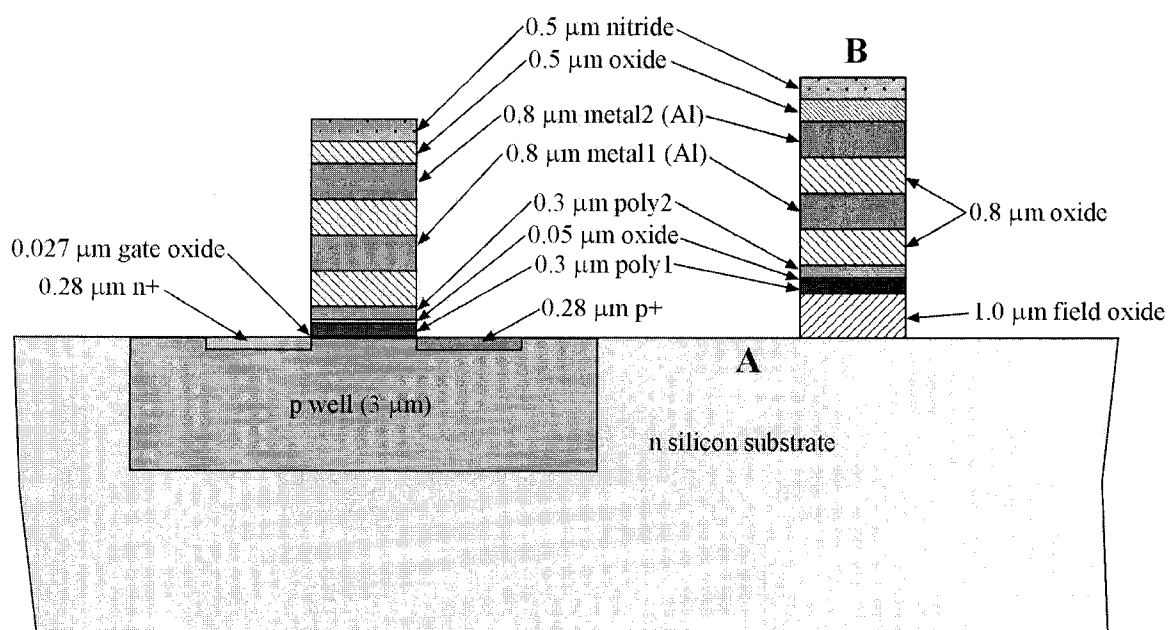
Figure 4.1 Cross-sectional schematic of the MITEL 1.5 μm CMOS process. Region A is exposed substrate, while region B is a typical micromachine profile.

Before the fabrication process begins, a graphical layout of the device geometry is drawn using a computer-aided design (CAD) software package, such as L-Edit™ or Cadence™. Following the graphical layout step, each design layer is associated with a number that corresponds to a specific fabrication step. A file in a format known as gdsII, containing the graphical data for each layer, is then generated from the CAD software. The gds file, independent of the originating design software, is then sent to the foundry for fabrication via CMC.

The CAD output for the submitted micro-optical Pirani sensor die is shown in Figure 4.2. All devices studied for this work were created through Cadence™. This
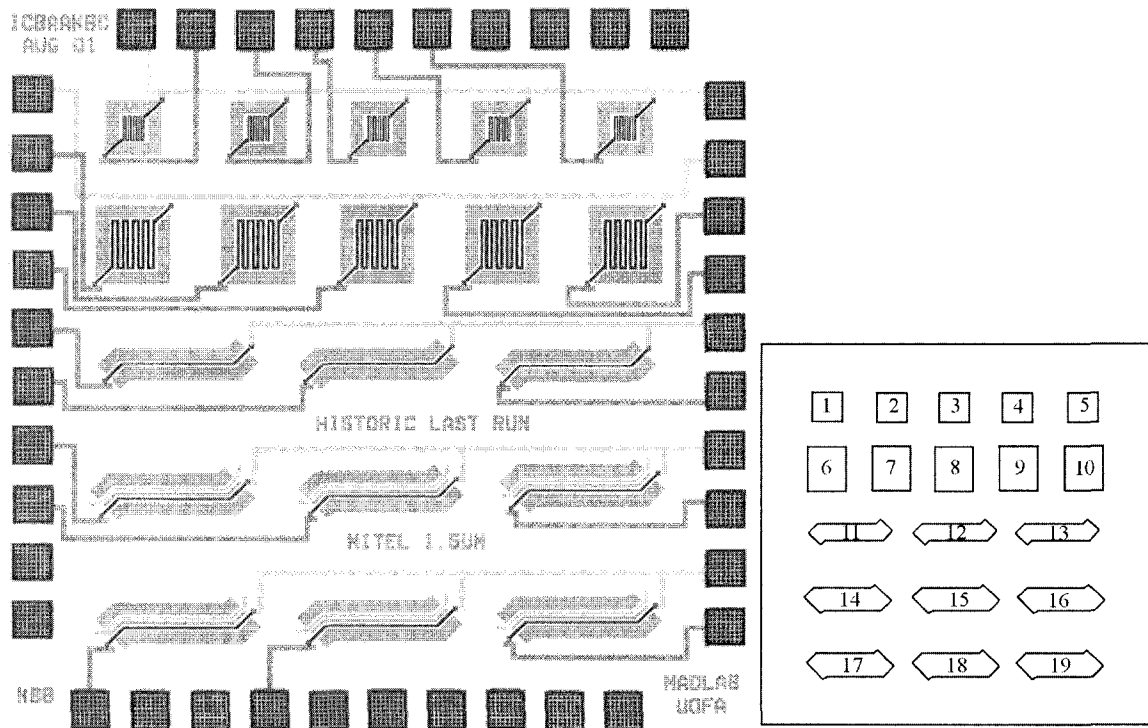
Figure 4.2 CAD output of the submitted die design generated using Cadence™. Device labeling scheme is shown to the right.

design consists of four different sensor devices. The first set of devices, numbered 1 to 5 in Figure 4.2, are termed small square. Similarly, devices numbered 6 to 10, 11 to 13, and 14 to 19 are referred to as large square, single bridge, and double bridge, respectively. Throughout this dissertation, the device numbering scheme shown in Figure 4.2 is maintained. A microphotograph of the fabricated chip as received from the foundry is shown in Figure 4.3 for comparison.

Microphotographs of the small and large square devices are shown in Figure 4.4 (a) and (b), respectively. For the small square, the silicon dioxide/silicon nitride platform is approximately 120 μm x 120 μm. Two supporting arms, each 21.5 μm wide and 69 μm in length, connect the platform to the surrounding CMOS layers. Areas of exposed n-silicon substrate surface (region A in Figure 4.1), roughly 50 μm wide, surround the platform and arms and are referred to as open regions. In Mitel, the open regions are specified by selecting regions where the silicon dioxide and silicon nitride layers are to be removed. The polysilicon layer, in contrast, is deposited only in regions that are specified by the designer. The open regions are required in subsequent
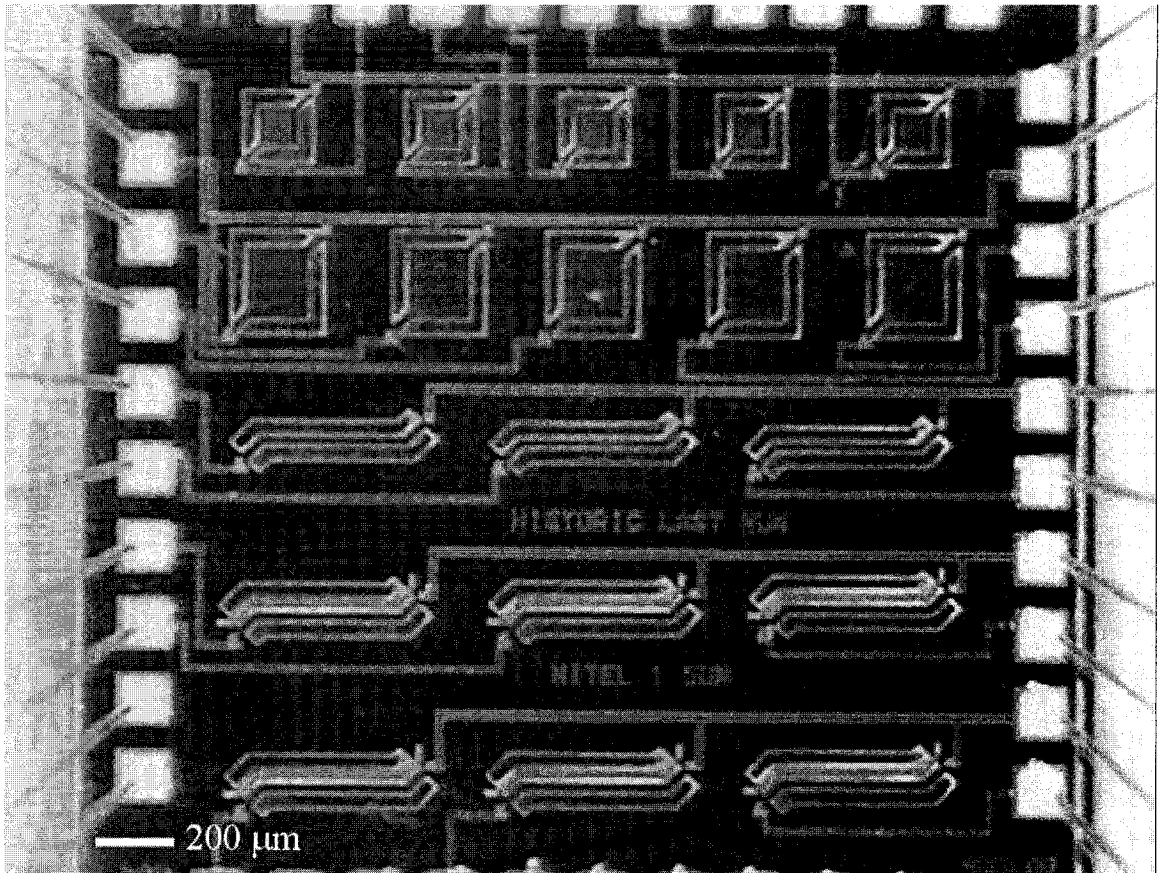
Figure 4.3 Microphotograph of the fabricated design as received from the foundry.

(a)   (b)
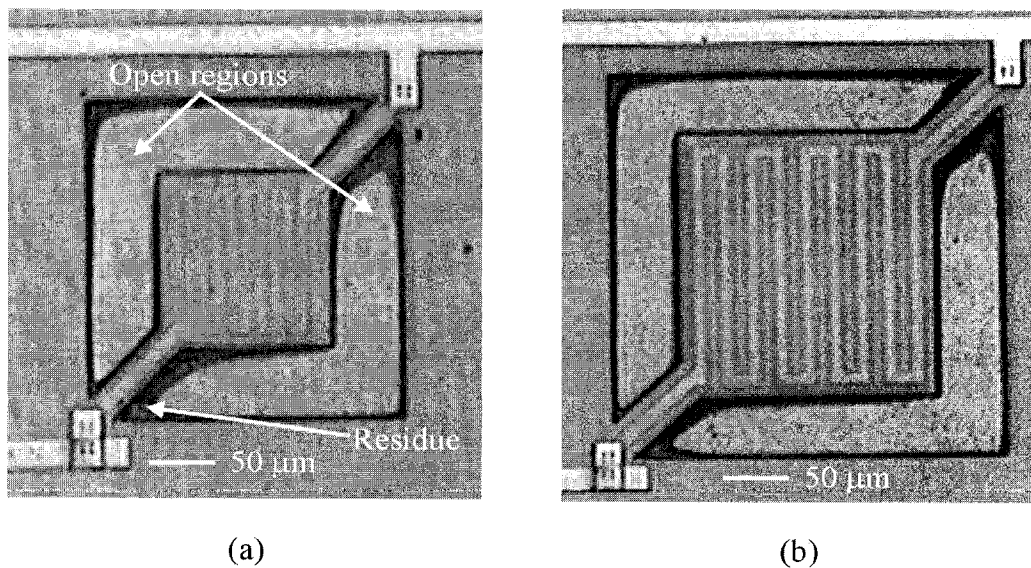
Figure 4.4 Microphotograph layout of (a) small square, and (b) large square
as received from foundry and prior to post-processing.

processing steps to allow access of silicon etchant to the substrate. The use of a silicon etchant realizes the release of the platform and arms from the substrate by the removal of silicon directly below the open regions and device, thus creating a thermally isolated structure. The reader is referred to Figure 3.1 in Chapter 3 for visualization of the removal of silicon substrate below the device. Also seen in the figure is what is termed residue, present in the corners of the open regions. The residue is composed of silicon dioxide and nitride layers resulting from non-conformal coverage of the photoresist during fabrication – a side effect of violating design rules to create the open regions. The overall small square device, including open regions, measures approximately 200 μm x 200 μm. From a cross-sectional point of reference, the platform and arms are approximately 3.9 μm thick, consisting of 1.0 μm of field silicon dioxide below a 0.3 μm thick polysilicon layer, 2.1 μm of silicon dioxide above the polysilicon, and 0.5 μm of silicon nitride on top for protection from rapid oxidation and contamination. The silicon dioxide and nitride layers were used as masking layers for the silicon etchant (region B in Figure 4.1). In regions of the platform and arms where the polysilicon is not present, the overall thickness tapers to 3.6 μm. The polysilicon layer, embedded inside the silicon dioxide platform and arms, consists of three continuous areas. The first two areas, each 11.5 μm wide, extend down the entire length of each supporting arm. The last area, created in a serpentine shape to increase the amount of heat generated on the platform and thus radiation emitted, is 5 μm wide and 935 μm long. At the outer ends of the supporting arms, the polysilicon layers are joined to an aluminum interconnect layer by contact holes etched in the inter-polysilicon-aluminum silicon dioxide layer. The interconnect layer is, in turn, connected to a bonding pad at the perimeter of the die, thus providing the electrical connection between the bonding pads and the devices.

The large square design (Figure 4.4 (b)) has an identical layout as that of the small square, but with a polysilicon serpentine width that is increased by a factor of two. The result is a silicon dioxide platform of 220 μm x 220 μm, supporting arms 32 μm wide by 71 μm long, 50 μm wide open regions, and an overall large square device size of 320 μm x 320 μm. The polysilicon areas in the supporting arms remain 11.5 μm wide; however, the polysilicon serpentine is 10 μm wide and approximately 1870 μm in length. The

overall resistance of the polysilicon for both the small and large square devices is approximately the same despite the difference in size. This can be accounted for by taking into consideration the semiconductor definition of resistance [90]:

$$R = \rho \frac{L}{H \cdot W} = R_\square \frac{L}{W}$$
(4.1)

where ρ [$\Omega \cdot \mu m$] is the material resistivity, L [μm] is the resistor length, W [μm] is the resistor width, H [μm] is the resistor height, and $R_\square$ [$\Omega/\square$], called the resistance per square, is the ratio of resistivity to thickness (since the polysilicon film is a constant thickness). For the Mitel 1.5 μm process, $R_\square = 20\pm5$ $\Omega/\square$ [89]. For both the large and small squares the ratio of length to width equals 187, hence both devices are expected to have the same resistance values. The actual resistance values for these devices will be discussed later in this section.

Microphotographs of the layouts for the single and double bridge devices are shown in Figure 4.5 (a) and (b), respectively. The single bridge is similar in concept to the small square; however, the square silicon dioxide platform has been replaced by a 441 μm x 26 μm bridge. The bridge is fixed at both ends by support arms each 31 μm wide and 76 μm long, and both bridge and support arms are surrounded by 50 μm-wide open regions. The overall structure measures approximately 640 μm x 200 μm. Inside the length of the support arms, the polysilicon layer is 11.5 μm wide, while the polysilicon within the center section of the bridge is only 8 μm wide.

The double bridge design has an identical geometry to the single bridge but with the addition of a second, parallel silicon dioxide bridge separated 10 μm from the first bridge. Inside the second bridge is an 8 μm wide trace of aluminum that is placed in direct contact with the silicon substrate at both ends using a pair of contact holes. In addition, the thickness of the bridge in the aluminum areas is approximately 4.4 μm, tapering to 3.6 μm in areas where only silicon dioxide and silicon nitride reside. The second bridge was designed to function as a heat sink fixed at a constant distance from the heated polysilicon trace. The overall dimensions of the double bridge structure are
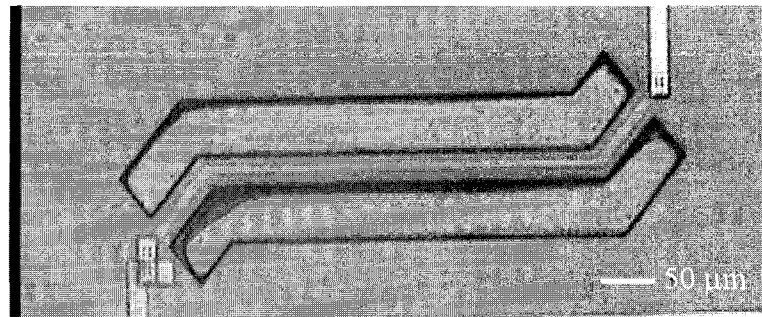
(a)
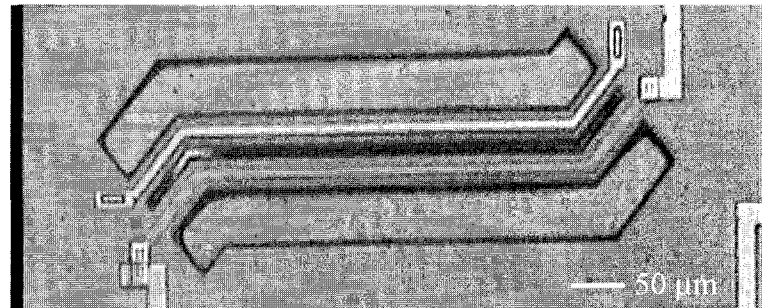
(b)

Figure 4.5 Microphotograph layout of (a) single bridge, and (b) double bridge as received from foundry and prior to post-processing.

approximately 640 μm x 240 μm.

Fifteen packaged and bonded die (in 40 pin DIPs), and an additional 35 loose die were received from the foundry. Six of the loose die were subsequently packaged and bonded in 40 pin DIPs. A continuity test was performed on each device on all packaged die (21 total) at room temperature to determine the mean device resistance, the variation in device resistance, and fabrication yield. The continuity test was performed using a Hewlett Packard 34401A digital multimeter with internal impedance of 10 MΩ and a sensing current of 100 μA when measuring resistances in the 10 kΩ range. Table 4.1 lists a summary of the results from the continuity test showing the minimum, mean, and maximum device resistances measured in Ohms. Also shown in Table 4.1 is the standard error or standard deviation in Ohms and as a percentage of the mean resistance. The overall fabrication yield prior to post-process etch was determined to be 98.2%.

As the micro-Pirani devices are operated under conditions of constant power, it is necessary to know the TCR value of each device for input into the control software, to be discussed in the next chapter. TCR measurements were performed by placing the chip

Table 4.1 Summary of room temperature continuity test prior to etching showing the minimum, mean, and maximum device resistances, the standard deviation and yield.

Device Type	Minimum R_o [Ω]	Mean R_o [Ω]	Maximum R_o [Ω]	Std Error δR_o [Ω]	Yield
Small Square	3964	3996	4042	20 (0.5%)	100/105
Large Square	3891	3916	3954	13 (0.3%)	104/105
Single Bridge	1423	1433	1447	6 (0.4%)	63/63
Double Bridge	1425	1434	1446	5 (0.3%)	125/126
				Total	392/399 (98.2%)

under test in an Omegalux™ LMF 6525 furnace programmed to heat at a rate of 1°C/minute to a temperature of 150°C (423 K). During the course of testing, the devices were held at the test temperature for 12 minutes and then allowed to cool over a 12-hour period. During this period the device resistance and temperature were measured every 60 seconds with a Fluke Hydra 2620A data acquisition unit (DAQ) and the values recorded to a text file on a computer via an RS-232 communication cable. The DAQ implemented a J-type thermocouple to sense temperature, and measured resistance with an internal impedance of 10 MΩ and a sensing current of 13 µA (set to a resistance range of 30 kΩ). To calculate the TCR value a linear fit to a plot of resistance versus temperature for the cooling data was performed. From (1.1), ignoring β_T and setting $T_o = 0$, the resistance is:

$$R = R_o(1 + \alpha_T(T - 0))$$
$$\Rightarrow R = R_o + R_o\alpha_T T$$

(4.2)

Hence, to calculate the value for α_T, the slope of the linear fit is divided by the intercept. This method is used solely for determining the TCR, and R_o here should not be confused with the room temperature resistance where $T_o \neq 0$. Four separate chips were tested in the furnace to determine the mean and deviation in TCR from the foundry, yielding a mean value of 1.13×10^{-3} K^{-1} and a standard deviation of 2×10^{-5} K^{-1} (1.8%). Each device on a chip is considered to have the same TCR value since the polysilicon layer for each device was fabricated during the same CMOS process step and all devices were equally

subjected to any subsequent process steps.

4.3 POST-PROCESSING

As received from the foundry, the devices are not thermally isolated from the substrate and require what is referred to as post-processing, processing performed after the completion of the main CMOS fabrication run. These additional process steps are necessary to create three-dimensional structures.

In the case of the micro-Pirani gauges investigated, selective portions of the silicon substrate were removed from each die by etching with tetra-methylammonium hydroxide (TMAH) and/or by etching with xenon difluoride (XeF_2). In total, six chips were etched in XeF_2, one chip by TMAH, and three chips by TMAH followed by XeF_2.

4.3.1 XeF$_2$ Etching

The isotropic gas-phase etching of the silicon substrate was accomplished by XeF_2 in the manner described previously in Section 2.3.3 of Chapter 2. The XeF_2 etching system used for this phase of the project and shown in Figure 4.6 was operated in the same manner as that described in Chapter 2. As mentioned in Chapter 2, XeF_2 etching is exothermic and as such, the heat generated at the site of etching can be significant and detrimental to microstructures as they become thermally isolated [91]. For this reason, measurements of pre- and post-etch room temperature resistance, TCR, and yield where performed as well as in-situ resistance measurements during etching to determine the effect of etching on the micro-Pirani gauge structures.

To prevent lateral etching of the edges of the die and subsequent undesirable undercutting of the bonding pads, the exposed silicon sides of the die were covered with a protective film. A UV-curable polymer (Norland optical adhesive #81: viscosity 300 cps, cure at 320 to 400 nm) was applied to the inside of the package cavity surrounding the packaged substrate. The choice of polymer used was governed by required viscosity (for control of application) and potential for emission of vapours (out-gassing) when subjected to vacuum. For the tested die, applying polymer to the die edges reduced the area of exposed silicon by approximately 90% and hence reduced the undercutting of the
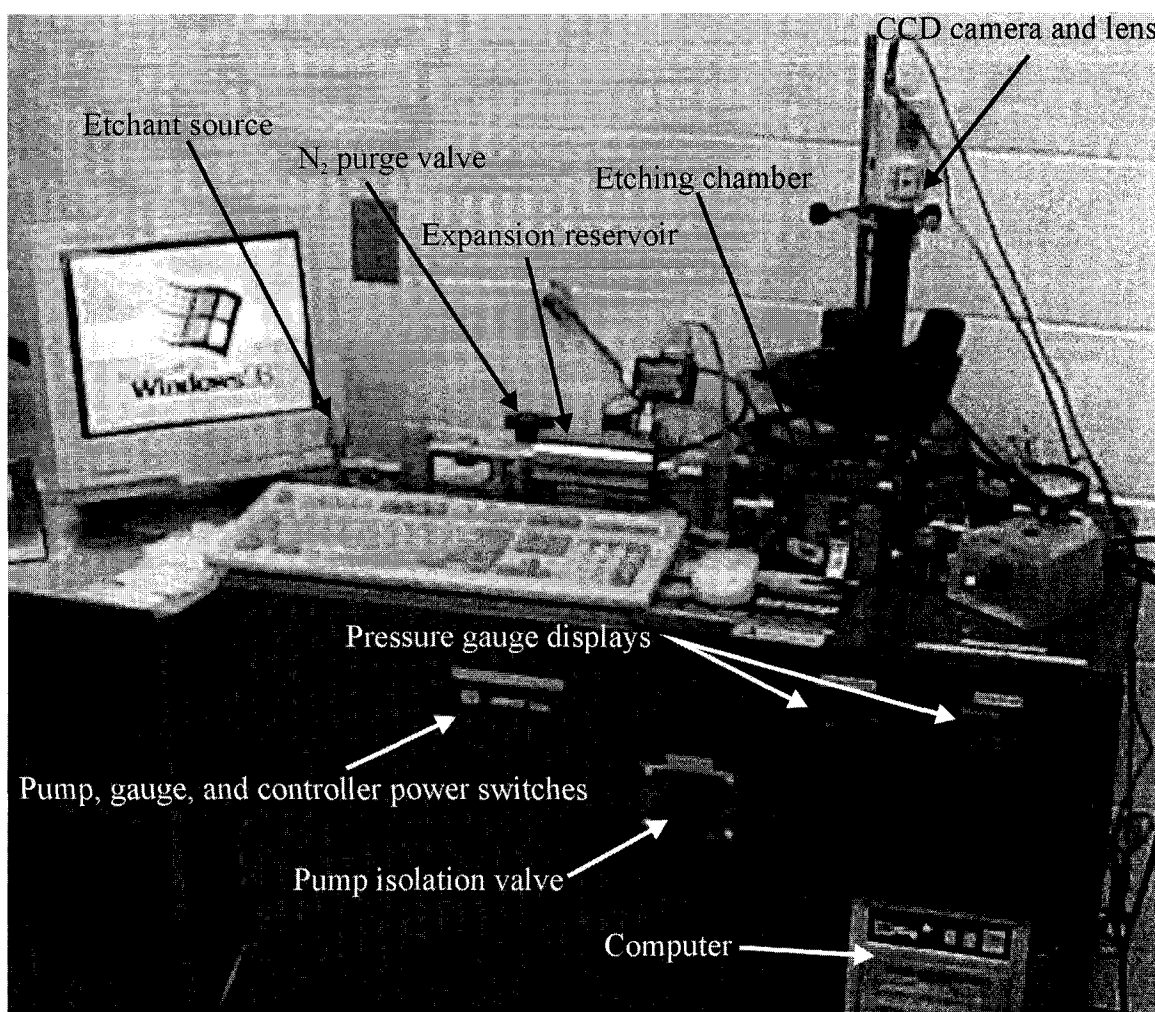
Figure 4.6 XeF₂ etching system. Pump and vacuum subsystem not shown.

silicon dioxide layers beneath the bonding pads (which could lead to a reduction in yield).

The results from etching one of the polymer-protected die in XeF₂ for 18 minutes can be seen in Figures 4.7 and 4.8. The outer dark oval-shaped regions seen in the figures are the edges of the undercutting, while the inner oval regions are SiF$_x$-deposited debris resulting from the etch reaction. Also, the left-hand-side of the bridges in Figure 4.8 appear dark as a result of intrinsic stresses causing the bridges to bend away from the plane of the die once released. The oval-shaped nature of the undercut illustrates the isotropic nature of XeF₂ etching. The etch depth was estimated using the change in focal point between the device platform and the bottom of the etched cavity using an optical microscope and is considered accurate to within ±5 µm. Release of the devices from the

(a)   (b)
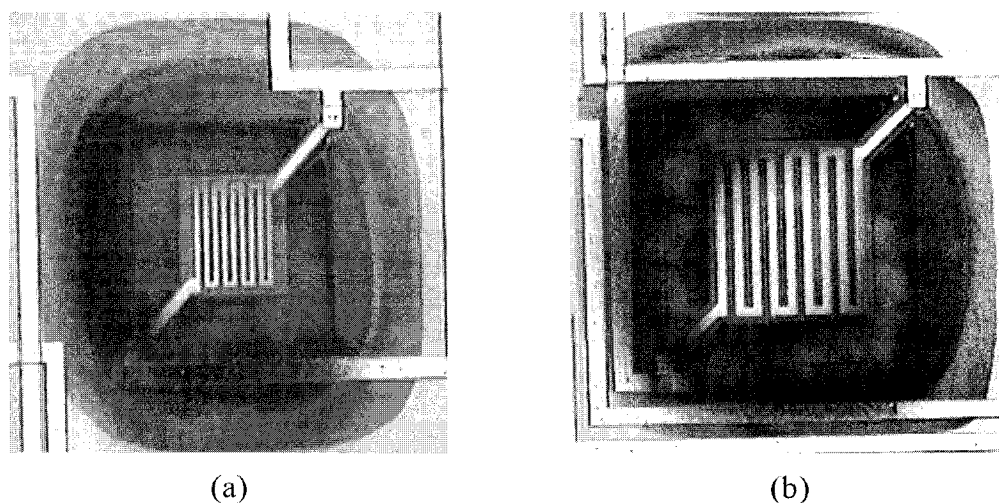
Figure 4.7 Microphotograph of (a) small square, and (b) large square after 18 minutes of XeF_2 etching. Undercut is about 100 μm, seen as the outer dark oval. The inner dark oval is deposited SiF_x debris from the etch reaction. Estimated etch depth is 110 μm.

(a)

(b)
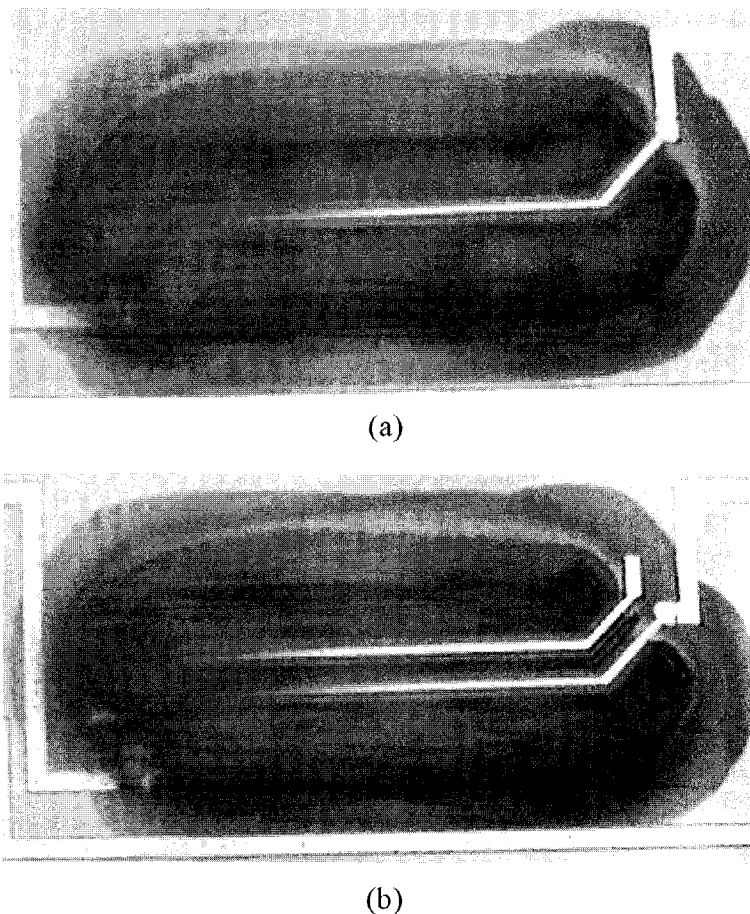
Figure 4.8 Microphotograph of (a) single bridge, and (b) double bridge after 18 minutes of XeF_2 etching. Undercut is about 100 μm, seen as the outer dark oval. The inner dark oval is deposited SiF_x debris from the etch reaction. Estimated etch depth is 110 μm.

substrate typically required etch times of 14 to 19 minutes and produced etch depths of approximately 100 μm. Subjecting the die, prior to XeF_2 etching, to a 30 second etch by 10:1 BOE to remove the native silicon dioxide layer, a thin layer known to reside on any oxidizing surface in the presence of atmospheric air and humidity, reduced the amount of time required to achieve device release and 100 μm etch depths to 10 minutes.

Table 4.2 lists the summary of the post-etching continuity test showing the pre- and post-etching device mean resistances and standard errors in Ohms for a sample of the device population from Table 4.1. The standard error is also shown as a percentage of the mean. The difference in mean is calculated as the percentage difference between the pre- and post-etch device mean resistance and shows that the mean room temperature resistance value of each of the four micro-optical Pirani devices has decreased due to etching. Also, and more importantly, device failure due to fracturing of the support arms resulted in a 28% decrease in yield after etching. Fracture is believed to be the result of residual stresses in and between the silicon dioxide and silicon nitride layers (see Section 2.2.1 in Chapter 2).

For the single and double bridge devices, the post-etching mean resistance lies within one standard deviation of the pre-etching mean resistance and hence, it is reasonable to conclude that the etching had little or no significant effect on the single and double bridge structures. This may be the result of the bridge geometry requiring only a few minutes of exposure to the etchant to achieve complete release. For the small and large square devices, the percent difference between the pre- and post-etching mean is

Table 4.2 Summary of room temperature continuity test after etching with XeF_2 showing the pre- and post-etching device mean resistance and standard error in Ohms, and yield.

Device Type	Pre-etch			Post XeF_2-etch			Difference in Mean
	Mean R_o [Ω]	Std Error δR_o [Ω]	Yield	Mean R_o [Ω]	Std Error δR_o [Ω]	Yield	
Small Square	3989	12 (0.3%)	30/30	3881	13 (0.3%)	22/30	-2.7%
Large Square	3913	8 (0.2%)	29/30	3816	13 (0.3%)	7/30	-2.5%
Single Bridge	1431	4 (0.3%)	18/18	1428	11 (0.8%)	18/18	-0.2%
Double Bridge	1431	3 (0.2%)	36/36	1427	9 (0.6%)	34/36	-0.3%
		Total	99.1%		**Total**	71.1%	

almost ten times greater than the standard deviation and hence, it should be concluded that the XeF_2 etching had a significant effect on the thermal properties of these structures. To support these conclusions, a single die with one of the small square devices covered with polymer to prevent etching was etched until the other, exposed, devices were released from the substrate. The resistance value for the protected device following etching was 3984 Ω, essentially unchanged within the pre-etch standard error. Therefore, the temperature increase as a result of the heat generated by XeF_2 etching must be a local effect, restricted to areas where etching occurs and where the local temperature is determined by the thermal properties of the surrounding materials.

Table 4.3 lists the summary for the post-XeF_2 etch TCR measurements conducted in the same manner as the pre-etch TCR measurements. Since the four device designs were subjected to differing amounts of etching, the TCR value for each device type was measured. The results in Table 4.3 show that within the error in determining the TCR value, there is essentially no change in the TCR of any device resulting from XeF_2 etching.

Table 4.3 Summary of TCR measurements after etching with XeF_2.

| Device Type | Pre-etch | | Post XeF_2-etch | | |
	Mean α_T [x10^{-3} K^{-1}]	Std Error $\delta\alpha_T$ [x10^{-3} K^{-1}]	Mean α_T [x10^{-3} K^{-1}]	Std Error $\delta\alpha_T$ [x10^{-3} K^{-1}]	Difference in Mean
Small Square			1.12	0.10 (8.9%)	-0.9%
Large Square	1.13	0.02 (1.8%)	1.12	0.10 (8.9%)	-0.9%
Single Bridge			1.10	0.03 (2.7%)	-2.7%
Double Bridge			1.11	0.05 (4.5%)	-1.8%

Changes in polysilicon resistance with temperature have been investigated and reported; the change in resistance of the polysilicon is reversible for temperatures less than some critical temperature [89, 92-94]. Exposing polysilicon to temperatures in excess of the critical temperature causes changes in grain boundaries and sizes, which leads to permanent changes in resistance and TCR. Specifically, exceeding the critical

temperature of polysilicon by annealing produces localized melting and re-crystallization of grains that results in larger grain sizes. Resistance is largely dependent on the inverse of the grain size [92]. Resistance changes have also been reported when the annealing time is of sufficient duration (>> 1 minute at temperatures on the order of 700 K) to promote outdiffusion of dopant into the surrounding silicon dioxide layer, leading to reliability issues [92]. For the polysilicon in the present micro-optical Pirani devices, the critical temperature has been reported to be approximately 600 K [89].

Since the resistance values of the large and small square devices have been reduced significantly by the etching process and since the XeF_2 etch reaction is known to be exothermic, it must be concluded that significant heating of the microstructures is taking place during etching. To confirm this conclusion, in-situ resistance measurements during XeF_2 etching were taken, with the results from one of the etched die presented in Figure 4.9. In the figure, the first temperature increase seen is from the fourth pulse of the first set of four pulses. The first three pulses of this set have not produced enough etching to reach and heat the polysilicon. The top two curves (Figure 4.9) show the resistance versus time for the square devices and whose values are associated to the left vertical axis, while the bottom two curves show the resistance versus time for the bridge devices whose resistances correspond to the right vertical axis. During a one-minute etch cycle, the resistance of each device increased by approximately 1% (40 Ω for the square devices, 14 Ω for the beam devices) in 16 seconds, which corresponds to a mean device temperature increase of 10 K. Between each of the etch cycles (expansion cycle) the resistance for the square devices decreased by slightly more than 1% until structural release, after which the resistance increased and decreased the same amount (about 1%) during the etching and expansion cycles. The result is a permanent decrease in room temperature resistance of about 100 Ω for the square devices. For the bridge structures, between etch cycles, the resistance decreased the same amount (about 1%) as it increased during etching cycles resulting in no permanent change in room temperature resistance.

The permanent change in resistance is unlikely to be the result of dopant outdiffusion, a slow process, since the duration of etching (heating) lasts only one minute. Hence, the mechanism responsible for the resistance shift is probably due to the resizing of polysilicon grains and changing of grain boundaries despite a mean device temperature
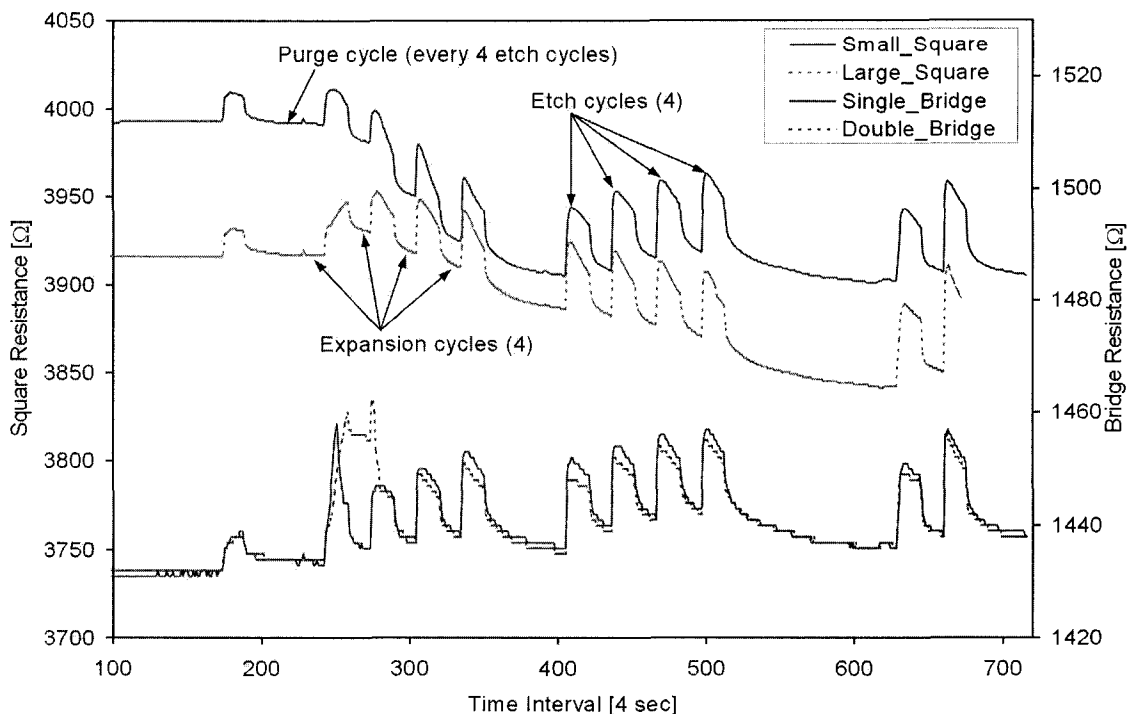
Figure 4.9 Graph of in-situ resistance versus time for XeF_2 etching. The top two curves correspond to the square devices and the left vertical axis. The bottom two curves correspond to the bridge devices and the right vertical axis.

during an etch cycle of much less than the required 600 K. However, until structural release has occurred a portion of the platform remains in direct contact with the silicon substrate acting as a heat sink at room temperature. Also, only the area of polysilicon in proximity to the etch reaction is expected to experience heating. Therefore, in the immediate micro-region of etching, temperatures in excess of 600 K are assumed to occur with the mean polysilicon resistance resulting from the sum of hot areas under etch and cool areas not under etch.

To support the hypothesis that excessive localized heating of the polysilicon is occurring during etching, we assume a small length of polysilicon, Δl [μm], is being heated by the etching reaction. We also assume that the rest of the polysilicon of length, $L' = L_{eff} - \Delta l$ [μm], remains at room temperature, where L_{eff} [μm] is the effective length of polysilicon (since the polysilicon in the arms is of different width than that in the platform) equal to the total plan view area of polysilicon divided by 5 μm. We ignore the polysilicon thickness, as it is uniform throughout the device. The measured mean

resistance, $\overline{R}$ [Ω], in terms of the room temperature resistance, R_o [Ω] and the increase in resistance of the portion of polysilicon subjected to localized heating, referred to here as etching resistance, $R_{etching}$ [Ω] is then:

$$\overline{R} = R_o + R_{etching}.$$ (4.3)

Substituting the resistivity as defined in (4.1) for the resistance in (4.3) (using an effective cross-sectional area equal to the total polysilicon volume divided by the effective length) and eliminating common terms produces:

$$\overline{\rho}L_{eff} = \rho_o L' + \rho_{etching}\Delta l.$$ (4.4)

In (4.4), we have made the simplifying assumption that all polysilicon in length L' has resistivity ρ_o, whereas in fact that region of the polysilicon that has been heated by the etching has a resistivity which is reduced by approximately 4%. This simplification does not significantly affect our estimates of the resulting temperature increase. Replacing the etching resistivity, $\rho_{etching}$ [$\Omega \cdot \mu m$] with its equivalent form (ignoring thermal expansion which can be considered negligible for temperature changes of a few hundred degrees) as in (4.2); that is, $\rho_{etching} = \rho_o(1+\alpha_T \cdot \Delta T)$ where ΔT [K] denotes the temperature increase above room temperature, and replacing L' with $L_{eff} - \Delta l$, yields:

$$\overline{\rho}L_{eff} = \rho_o(L_{eff} - \Delta l) + \rho_o(1 + \alpha_T \cdot \Delta T)\Delta l.$$ (4.5)

Finally, solving for ΔT gives:

$$\Delta T = \frac{L_{eff}}{\alpha_T \cdot \Delta l}\left(1 - \frac{\overline{\rho}}{\rho_o}\right).$$ (4.6)

Substituting in values for $L_{eff} = 1252$ μm, $\alpha_T = 1.13 \times 10^{-3}$ K^{-1}, $\rho_o = 4.652$ $\Omega \cdot \mu m$,

and $\overline{\rho}$ = 4.835 Ω·µm (taken from Figure 4.9 at time interval 400) produces a graph of localized polysilicon heating as a function of etching length, Δ*l*, that is shown in Figure 4.10.
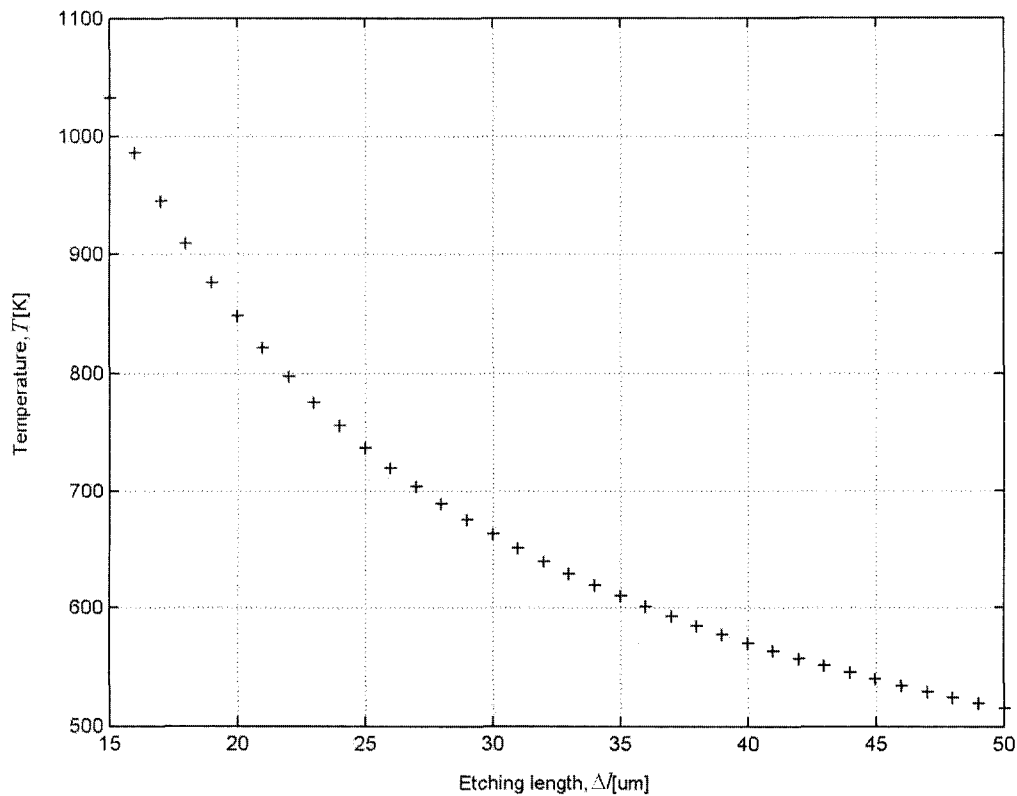
Figure 4.10 Plot of localized polysilicon temperature versus proximity equivalent etching length.

To determine the length of the etching region at a steady state interval (about 16 seconds in Figure 4.9), an estimate of the lateral etch was calculated to be approximately 2.6 µm. Assuming a circular etch commencing at the perimeter of the small square platform and proceeding inwards for 2.6 µm results in an exposed polysilicon length of roughly 19 µm. This etching length corresponds to a localized temperature of almost 870 K – more than sufficient to permanently affect the polysilicon grain size and hence, resistance. From Figure 4.10 the minimum temperature of 600 K required to affect the polysilicon relates to an etching length of 40 µm or less, which corresponds to 3.2% of the entire polysilicon area. That is, if 3.2% or less of the polysilicon surface is

simultaneously exposed to XeF$_2$ etching, then localized temperatures in excess of 600 K are likely to occur.

4.3.2 TMAH Etching

TMAH, briefly discussed earlier in Section 2.3.3 of Chapter 2, is a wet anisotropic silicon etchant used here to produce structures that are thermally isolated from the substrate. For this project, it was necessary to passivate the TMAH solution against aluminum etching due to the presence of aluminum bonding pads and bonding wires. This passivation was achieved by lowering the pH of the solution from 14 to between 12.0 and 12.5 [36]. Lowering the pH of the TMAH solution has the disadvantage of decreasing the silicon etch rate; however, increasing the etch rate can be achieved by increasing the temperature of the solution and by decreasing the concentration of the TMAH. Increasing the temperature of solution above 90°C (363 K) produces a large rate of evaporation and hence a solution whose pH and concentration are hard to control. Decreasing concentrations of TMAH produce an increase in the surface attachment of hydrogen bubbles (produced during the dissolution reaction) and hence an increase in surface roughness and hillocks, eventually leading to a decrease in silicon etch rate. In order to counter the increase in surface roughness an oxidizer is added that will suppress the formation of hydrogen bubbles and hence, also maintain the silicon etch rate.

Four packaged die were etched for 45 minutes in a 5 to 6 wt.% TMAH solution using the setup shown in Figure 4.11. The recipe developed for passivating the TMAH solution while maximizing the silicon etch rate and minimizing the surface roughness was composed of 200 ml of 25 wt.% TMAH added to 700 ml DI water, 40 g of silicic acid (SiO$_2$-5H$_2$O), and 3 g of potassium persulfate (K$_2$S$_2$O$_8$) [76]. After dissolving the acid and oxidizer, the solution was left on the magnetic stirrer at room temperature for at least 24 hours. When ready to etch, the pH was adjusted as needed by either adding a small amount of TMAH or silicic acid, and the solution heated to 80°C (353 K). The solution was replenished every 30 minutes during etching by adding 5 ml of 25 wt.% TMAH and 3 g of K$_2$S$_2$O$_8$.

Preceding the TMAH etch, each of the packaged die was subjected to 30 seconds
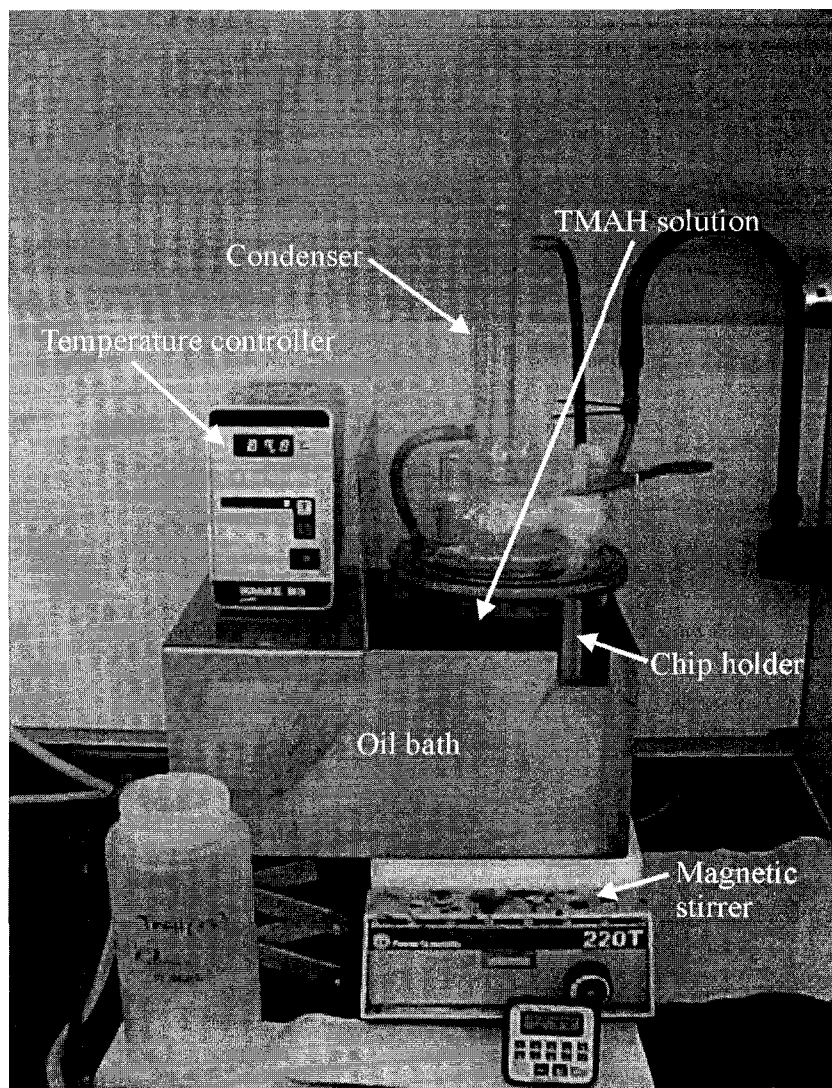
Figure 4.11 TMAH etching setup housed in a fumehood.

of etching by 10:1 BOE to remove any native silicon dioxide growth. At the completion of the TMAH etch, the die were rinsed in DI water and dried with compressed dry nitrogen gas. A microphotograph showing typical results after etching in TMAH at 80°C (353 K) for 45 minutes is shown in Figure 4.12. Observed in the figure is no undercut outwards from the open regions, illustrating the anisotropic nature of the etching.

Post-etching room temperature resistance measurements were conducted on the four TMAH-etched chips with the same equipment and in the same manner as the post-XeF$_2$ etching continuity test, the results of which are shown in Table 4.4. All of the changes in resistance after etching remained within the uncertainty in measuring resistance, suggesting that the TMAH etching had no detectable effect on the polysilicon.
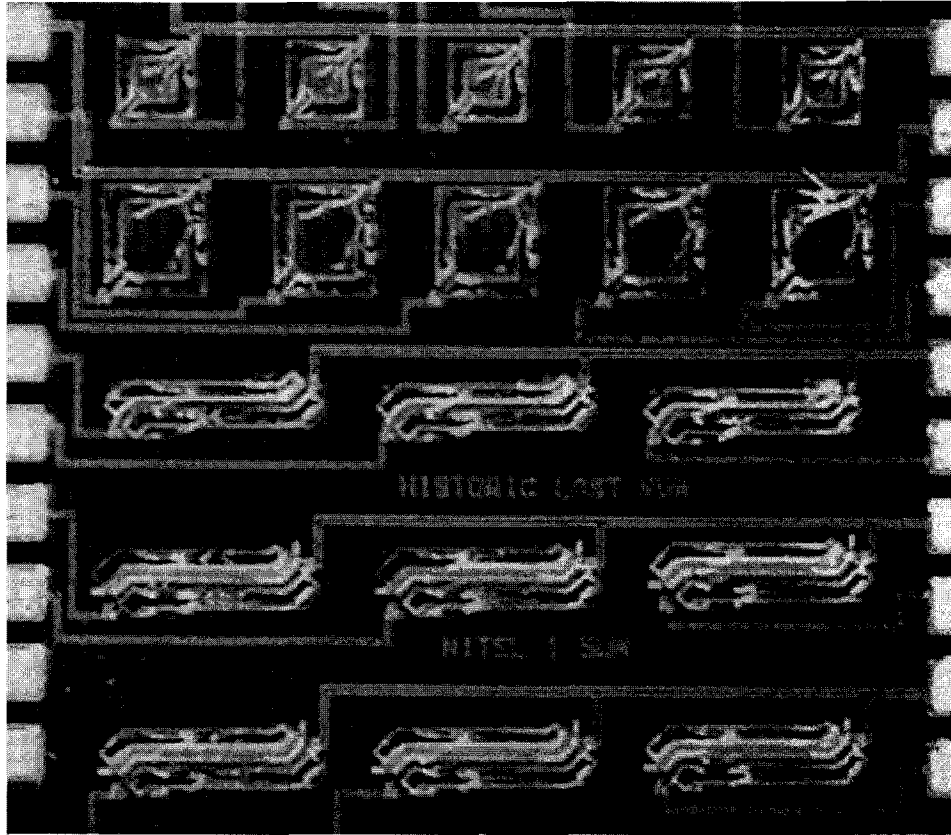
Figure 4.12 Micro-photograph showing the results of TMAH etching for 45 minutes at 80°C (353 K) and the anisotropy of the TMAH etching. Estimated etch depth is 35 µm.

Table 4.4 Summary of room temperature continuity test after etching with TMAH.

Device Type	Pre-etch			Post TMAH-etch			Difference in Mean
	Mean R_o [Ω]	Std Error δR_o [Ω]	Yield	Mean R_o [Ω]	Std Error δR_o [Ω]	Yield	
Small Square	3984	13 (0.3%)	20/20	3966	22 (0.6%)	20/20	-0.4%
Large Square	3908	7 (0.2%)	20/20	3896	10 (0.3%)	16/20	-0.3%
Single Bridge	1430	4 (0.3%)	12/12	1427	4 (0.3%)	9/12	-0.2%
Double Bridge	1430	4 (0.3%)	24/24	1426	4 (0.3%)	19/24	-0.3%
		Total	100%		**Total**	84.2%	

The table also shows a uniform decrease in mean resistance, which may be due to a slight decrease in room temperature between tests. Specifically, the changes listed in Table 4.4 correspond to a room temperature change of between 2 and 4 K. Since the room temperature resistance was essentially unchanged after etching with TMAH, it was

assumed the TCR would also remain unchanged. In addition, none of the devices etched by TMAH achieved structural release. The amount of time exposed to TMAH was limited because of the uncertainty in the effectiveness of the solution passivation towards aluminum. Lastly, a 15.8% decrease in device yield due to the TMAH etching, significantly less than the 28% decrease in XeF_2 etching yield, was observed with the expectation that the yield may continue to decrease with further TMAH etching until the devices are released.

4.3.3 Combination TMAH and XeF_2 Etching

Perhaps the best possible results can be produced by etching with both TMAH and XeF_2, especially when requiring significant amounts of undercutting to achieve structural release and control over the etch profile [36]. Three of the die that had been previously etched by TMAH were subsequently etched with XeF_2 for 4 or 6 minutes to achieve structural release. The resulting etch depths are approximately 55 μm for the dice etched for 4 minutes and 80 μm for the single die etched for 6 minutes. The amount of undercutting is estimated at 50 μm for all combination-etched die in contrast to at least 100 μm of undercutting for the XeF_2-only etched die. Table 4.5 lists the summary of the continuity tests for the three combination etched die, while a microphotograph of one of the combination etched die can be seen in Figure 4.13. Note that the mean pre-etch resistance in the table corresponds only to the three devices subjected to both TMAH and XeF_2 etching. The resulting permanent change in room temperature resistance after

Table 4.5 Summary of room temperature continuity test after TMAH and XeF_2 etching.

Device Type	Pre TMAH-etch			Post XeF_2-etch			Difference in Mean
	Mean R_o [Ω]	Std Error δR_o [Ω]	Yield	Mean R_o [Ω]	Std Error δR_o [Ω]	Yield	
Small Square	3983	14 (0.4%)	15/15	3876	28 (0.7%)	10/15	-2.7%
Large Square	3909	8 (0.2%)	15/15	3831	7 (0.2%)	15/15	-2.0%
Single Bridge	1429	4 (0.3%)	9/9	1425	4 (0.3%)	8/9	-0.3%
Double Bridge	1432	4 (0.3%)	18/18	1424	4 (0.3%)	18/18	-0.5%
		Total	**100%**		**Total**	**89.5%**	
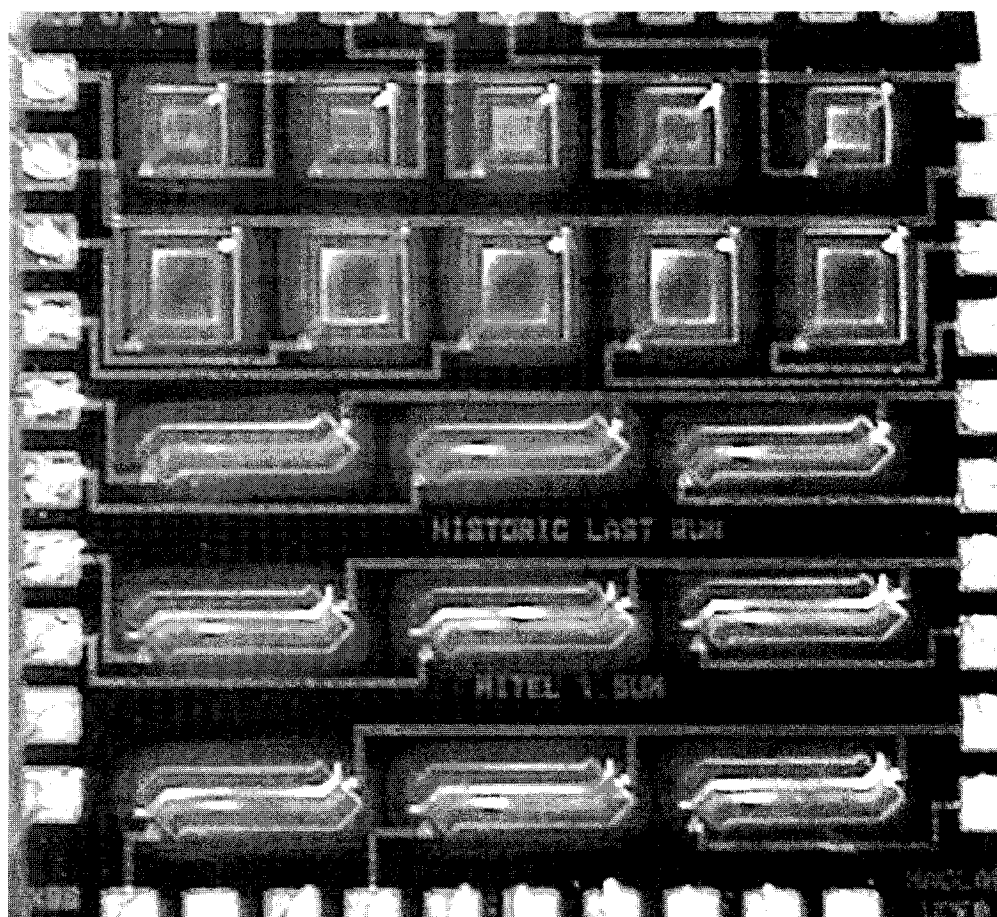
Figure 4.13 Microphotograph showing the result of combination etching with TMAH and XeF_2.

combination etching was roughly the same as that of the XeF_2-only etched die. The most important result from the combination etching is the improvement in yield, being 89.5% when compared to a yield of only 71.1% for the XeF_2-only etched die.

4.4 SUMMARY

This chapter has presented a detailed description of the devices designed and fabricated for use as micro-optical Pirani gauges. The post-processing performed to achieve structural release from the substrate has been included. Yield statistics and post-processing effects on the room temperature resistance and TCR of the polysilicon have also been presented and discussed. The next chapter deals with the operation of these devices when employed as gas pressure sensors and gas analyzers.

FIVE
VACUUM MEASUREMENT AND GAS ANALYSIS

5.1 INTRODUCTION

In this chapter, the results obtained from utilizing the post-processed micro-optical Pirani sensors for vacuum measurement and gas analysis are presented. A description of the experimental layout and procedures followed for collecting the data is first discussed. Results include a comparison between the use of silicon and germanium photodetectors/diodes, and direct current source measurements for devices under two operating modes: constant power and constant detector signal, for use in pressure sensing in a nitrogen environment. When utilized for gas analysis, the devices were operated under both modes while sourcing direct and pulsed currents. The gases used during gas analysis experiments were nitrogen (N_2), argon (Ar), helium (He), krypton (Kr), and sulfur hexafluoride (SF_6). In addition, results from a transient response investigation are included. Lastly, the effects of variations in characteristic dimension (etch depth) were experimentally investigated.

5.2 EXPERIMENTAL LAYOUT

To detect the radiation from the micro-Pirani gauges during operation, a fixture housing a pair of silicon (Si) and germanium (Ge) photodiodes and a test socket was assembled. This fixture is shown in Figure 5.1, where (a) illustrates the two photodetectors, of which only one detector can be used during any given course of testing. The separation distance between the packaged die and the detector in use can be varied from approximately 2 to 20 mm, as shown in (b). The entire assembly is placed in the vacuum test chamber of the experimental test system depicted in Figure 5.2. The system consists of a vacuum test chamber with an internal volume of 5580 cm^3 and was designed to prevent the intrusion of visible light from external sources. The test chamber
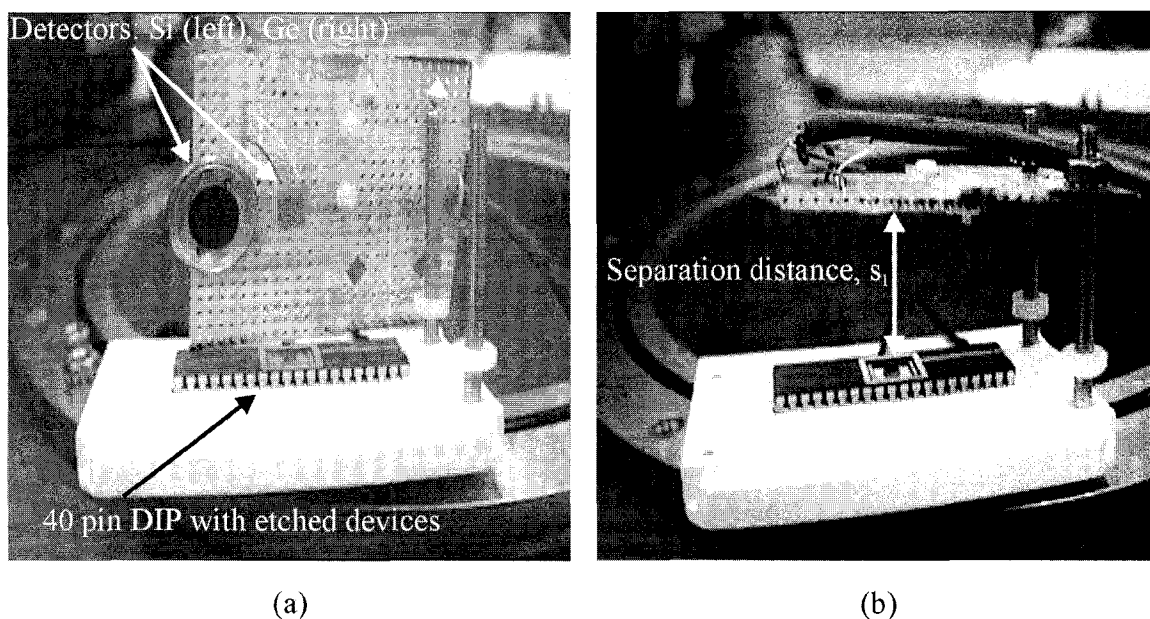
Figure 5.1 Detector-device configuration showing (a) silicon and germanium photodetectors, packaged design, and (b) adjustable detector-radiator separation.

is evacuated by two vacuum pumps comprised of an Alcatel I Series rotary vane (roughing) pump that reduces the system pressure from atmosphere to 100 mTorr, and a BOC Edwards EXT 70 water-cooled turbo-molecular pump that further reduces the pressure of the chamber below 0.1 mTorr. Determination of the system base pressure was not possible due to the limit of the attached pressure gauges, but it is sufficiently below 0.1 mTorr as to not affect our measurements. Venting of the test chamber is achieved via a needle valve. Measuring of the test chamber pressure was performed by a pair of MKS Baratron® capacitance manometers connected to an MKS PR4000 pressure gauge controller. A manometer is a sealed and evacuated chamber separated by a diaphragm from the vacuum pressure to be measured. As pressure changes, the diaphragm deflects; measuring the amount of deflection allows the determination of pressure. For a capacitance manometer, deflection of the diaphragm is measured by changes in capacitance in the plate capacitor formed by the diaphragm and a fixed electrode residing behind the diaphragm. Capacitance manometers were chosen for the ability to measure absolute, gas-independent pressure with high sensitivity. The combined gauges can measure pressures from 1000 to 10^{-4} Torr. The resulting output from the gauge controller was input to a computer via the RS232 communication bus for data acquisition.
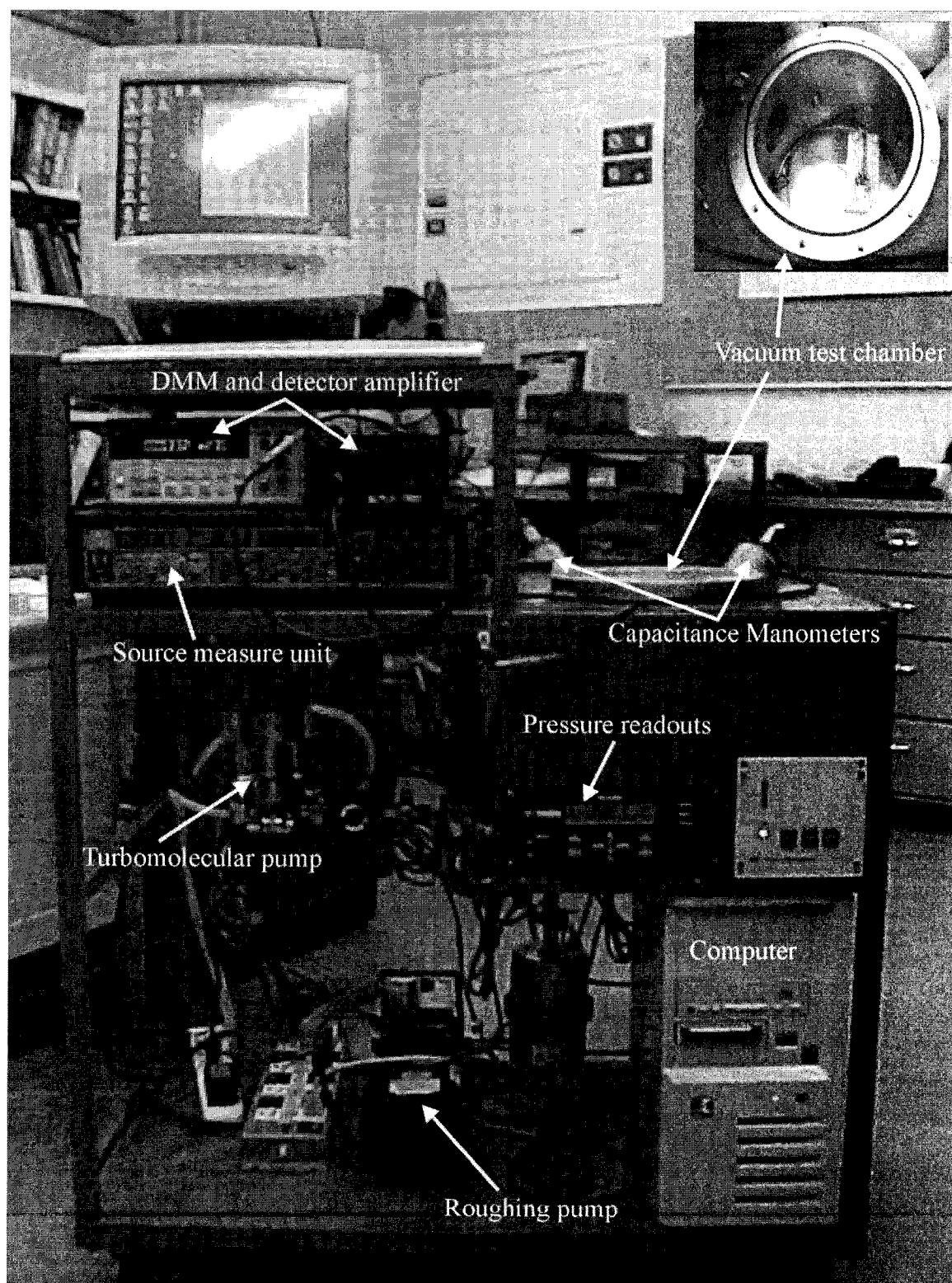
Figure 5.2 Vacuum test and automated data acquisition system.

The power dissipated by the devices under test was provided by a Keithley 236 source measure unit (SMU). The SMU was configured to source current through, and simultaneously measure the voltage across, its output leads. Control of the SMU was provided by computer via an IEEE 488 communication bus. Output from the photodetector was collected and amplified by a Melles Griot Large Dynamic Range Amplifier set to the 200 μA scale with an associated transimpedance gain of 10 000. The output from the amplifier was further measured by an HP 34401A digital multimeter (DMM), which was also controlled by computer over an IEEE 488 bus.

The coordination and control of the communications to the SMU, DMM, and gauge controller were performed by in-house-written software using LabVIEW™ 'G'. 'G' is an object-oriented, graphically-based, programming language designed for controlling physical instrumentation via a user-created virtual instrument console. The virtual instrument console provides a window for all user-specified parameters to be entered, while at the same time displaying all user-specified results and outputs. In addition, the programmer can specify which parameters and results are written to file for ease of analysis.

5.3 DETECTOR COMPARISON

Two photodetectors were used with this research project, a silicon and a germanium photodiode, both manufactured by Melles Griot, Ltd. To determine which of these detectors provided the best response and sensitivity, a comparison was performed.

The silicon detector is 11.4 mm in diameter, while the germanium detector is 5.0 mm in diameter. Responsivity data for both detectors provided by the manufacturers was plotted and is shown in Figure 5.3. The figure shows silicon sensitive to wavelengths ranging from 400 to 1100 nm with peak sensitivity at 1000 nm. Germanium is sensitive from 800 to 1800 nm with peak sensitivity at 1512 nm. It is intuitive that the germanium detector will be more sensitive to the output of the Pirani-sensors as its peak sensitivity occurs at a longer wavelength; however, the germanium detector area is only 19.2% that of the silicon detector and a quantitative value for the effectiveness per unit area of the germanium when compared to silicon is desired.
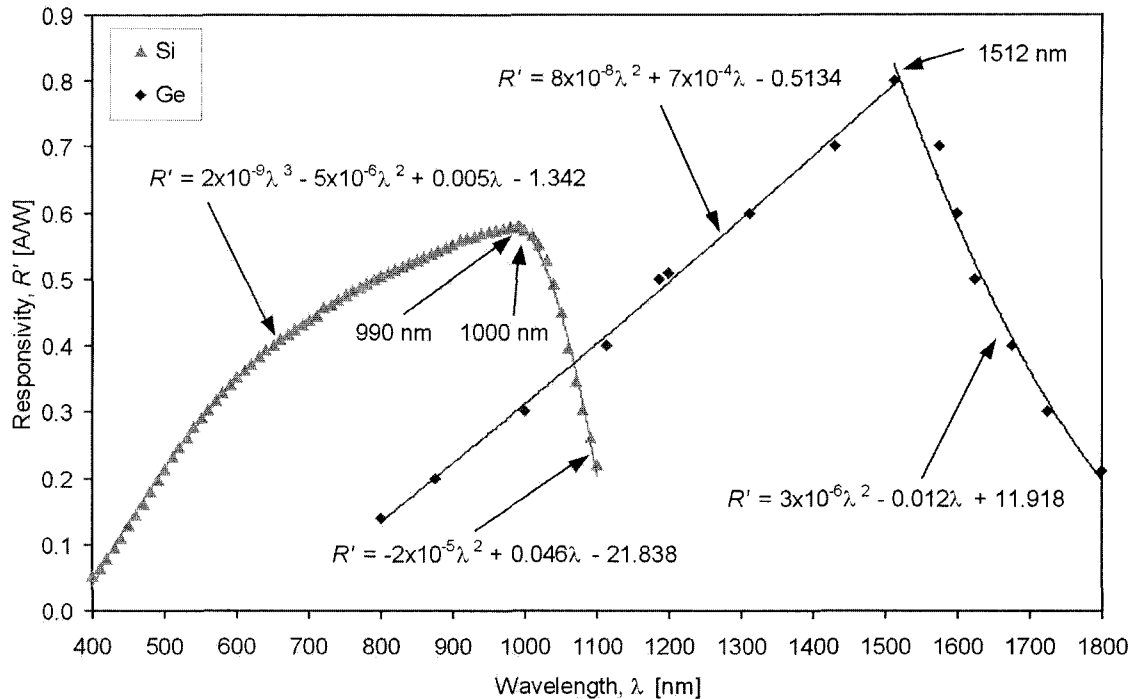
Figure 5.3 Manufacturer responsivity data for silicon and germanium photodiodes.

The comparison of the two photodetectors consisted of varying the distance, s_1, between the operating micro-Pirani device and the individual detectors from 2.0 to 20 mm under identical operating conditions of gas, pressure, micro-Pirani device, and operating power. The experiments were conducted by first pumping out the vacuum test chamber to below 50 mTorr and zeroing the high-pressure manometer to eliminate DC drift as specified by the operating manual. Next, the large dynamic range photodetector amplifier was zeroed. The test chamber was then vented with pure, dry nitrogen until a pressure of 20 Torr was achieved as displayed by one of the capacitance manometers. A small square device was operated at an empirically determined constant power of 18 mW, chosen such that a sufficiently large signal was produced. The corresponding detector current was then measured and written to file. The system was then vented to atmosphere, the detector-device separation distance, s_1, varied, and the experiment repeated. Upon completing testing of the silicon detector, the same experimental method was applied to the germanium detector. The results for both detectors are shown in Figure 5.4. The error in measuring the detector-device separation distance was determined to be ±0.5 mm. Curve fitting to the data points in Figure 5.4 was performed
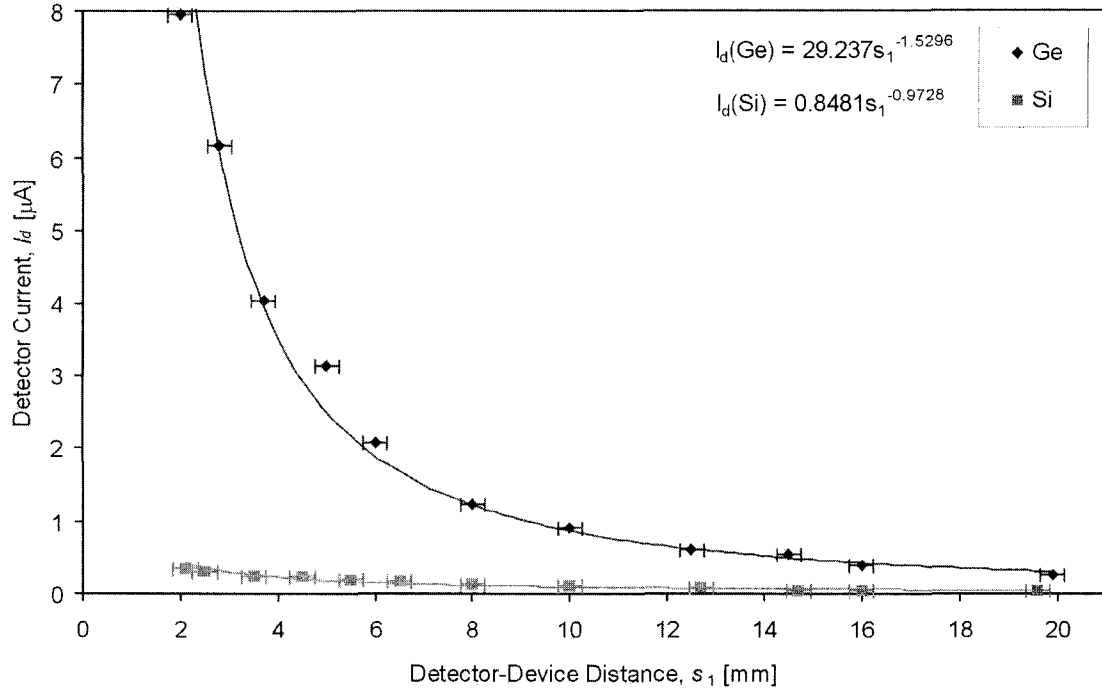
Figure 5.4 Plot of germanium and silicon detector current versus separation distance for a small square device in nitrogen, operated at 18mW.

with the exponential form, which provided the highest correlation, and the relevant formulas are provided.

From Figure 5.4 it is evident that despite the smaller size of the germanium detector, it provides a larger response compared to the silicon detector under identical operating conditions, especially for separation distances below 10 mm. To account for the differences in detector size the results were divided by the solid angle ratio as defined in (3.24). In addition, since the two detectors are dissimilar not only in size but in material, a correction for reflectance was also applied, as described below.

When a light beam intercepts a surface, a portion of the beam is reflected from the surface and the remainder transmitted through the surface [95]. The transmitted beam is bent or refracted as it passes into the material. A diagram showing the reflection and refraction of a light beam can be seen in Figure 5.5. The law of reflection states that the reflected angle, θ_r, is equal to the incident angle, θ_i, as shown in (5.1). Snell's law relates the refracted angle, θ_t, to the incident ray as shown in (5.2).

$$\theta_i = \theta_r \tag{5.1}$$

$$n_1 \sin\theta_i = n_2 \sin\theta_t, \tag{5.2}$$

where n_1 is the index of refraction, a dimensionless quantity equal to the speed of light in free space divided by the speed of light in the substance in question, of the incident medium, and n_2 is the index of refraction of the transmission medium. The index of refraction is not constant for a substance, but varies with the wavelength of the incident light beam.
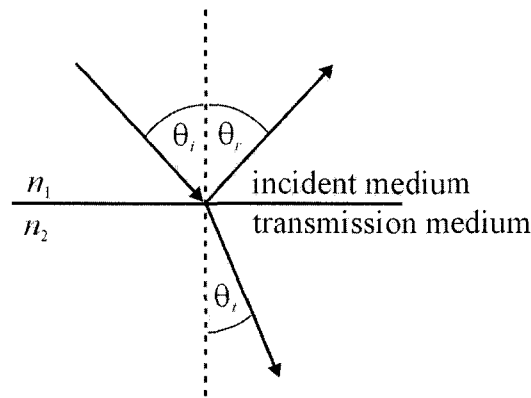
Figure 5.5 Reflection and refraction of light.

Light can be described as a traveling electromagnetic wave whose rate of energy transport per unit area or flux in the direction of propagation is given by the Poynting vector, $\bar{S}$ [W·m^{-2}] defined as

$$\bar{S} = \frac{1}{\mu_o} \bar{E} \times \bar{B}, \tag{5.3}$$

where $\bar{E}$ [N·C^{-1}] and $\bar{B}$ [T] are the corresponding time-varying electric and magnetic field vectors. For non-magnetic materials the average value of the time-varying magnitude of $\bar{S}$ is known as the intensity, I [W·m^{-2}] and is determined by

$$I = \left|\overline{\bar{S}}\right| = \frac{1}{c_o \mu_o} E_{rms}^2, \tag{5.4}$$

where c_o is the speed of light in vacuum, μ_o is the permeability constant [$4\pi \cdot 10^{-7}$ H/m], and E_{rms} is the root-mean-square of the magnitude of the time-varying electric field. The reflectance is defined as the ratio of energy of reflected light to incident light from a dielectric and can be expressed as

$$R_e = \Gamma^2 = \frac{I_r}{I_i} = \left(\frac{E_{rms,r}}{E_{rms,i}}\right)^2 .$$

(5.5)

The unitless variable, Γ, is called the amplitude reflection coefficient and is equal to the ratio of reflected to incident electric field amplitudes. For reflectance normal to a surface and incident from air ($n_1 = 1$), the reflectance is

$$R_e = \left(\frac{n_2 - 1}{n_2 + 1}\right)^2 .$$

(5.6)

In the case of germanium, with index of refraction 4.1 at a wavelength of 2.0 μm, (5.6) produces a reflectance value of 37.0%. That is, 37% of the light (at wavelengths near 2 μm) arriving perpendicular to the germanium surface is reflected. For silicon whose index of refraction is 3.5 at a wavelength of 1.4 μm, the reflectance for incident light normal to the surface is 30.8%. For the wavelengths of interest (Figure 5.3) both indices of refraction are assumed constant and without a complex component [96]. This is an approximation in which the semiconductor is taken to be a dielectric.

For light that is not incident normal to the reflecting surface, the reflectance is calculated in terms of the incident angle and the orientation of the electric field. The orientation of the electric field can be either perpendicular (s-polarized light) to the plane of incidence or parallel (p-polarized light) to the plane of incidence. In terms of incident angle and s- and p-polarized light, the reflectance is described by (5.7) and (5.8) below:

$$
R_{e,\perp} = \Gamma_{\perp}^2 = \left\{ \frac{\cos\theta_i - \sqrt{\dfrac{n_2^2}{n_1^2} - \sin^2\theta_i}}{\cos\theta_i + \sqrt{\dfrac{n_2^2}{n_1^2} - \sin^2\theta_i}} \right\}^2 , \tag{5.7}
$$

$$
R_{e,//} = \Gamma_{//}^2 = \left\{ \frac{\dfrac{n_2^2}{n_1^2}\cos\theta_i - \sqrt{\dfrac{n_2^2}{n_1^2} - \sin^2\theta_i}}{\dfrac{n_2^2}{n_1^2}\cos\theta_i + \sqrt{\dfrac{n_2^2}{n_1^2} - \sin^2\theta_i}} \right\}^2 . \tag{5.8}
$$

A plot of the reflectance versus incident angle is shown in Figure 5.6 for (a) the germanium, and (b) the silicon detectors, respectively. The curve labeled "un-polarized" is the mean value of the s- and p-polarized curves and represents the overall reflectance of light incident on each of the detectors surfaces. Also shown in Figure 5.6 is that for p-polarized light there is an angle, called the Brewster angle, at which no reflection occurs.

For the detector-device separation experiment, assuming the detector's center is aligned directly above the device, the incident angle increases from $0°$ at the center of the detector surface to some maximum angle at the edge of the detector surface at each separation distance. This maximum angle is at its largest when the detector-separation distance is at its smallest, which was 2.0 mm for the germanium detector and 2.1 mm for the silicon detector. These minimum separation distances correspond to a maximum edge angle and un-polarized reflectance of $51.3°$ and 37.0% (unchanged from $0°$ incidence) for the germanium detector, and $72.5°$ and 35.0% (an increase of less than 5 percentage points) for the silicon detector, respectively. Assuming the device is a diffuse point source emitter, an effective reflectance, $R_{e,effective}$, can then be calculated that represents the mean fraction of light reflected from the surface of the detector at each separation distance, s_1, and over all incident angles, θ:

$$R_{e,effective} = \frac{\int_0^{r_d} R_{unpolarized} (\sin^{-1}(\frac{r}{(s_1^2 + r^2)^{1/2}})) \cdot \frac{r^2}{(s_1^2 + r^2)^{3/2}} dr}{\int_0^{r_d} \frac{r^2}{(s_1^2 + r^2)^{3/2}} dr} , \qquad (5.9)$$

where a detailed derivation of (5.9) is presented in Appendix A. In our case, as seen in Figure 5.6, the effective reflectance can be considered constant for incident angles of less than 73° for either detector. For un-polarized light or incident angles greater than 73°, however, a numerical solution to (5.9) then becomes necessary.

After determination of the effective reflectance. the detector current was then divided by $(1 - R_{e,effective})$ at each separation distance to produce a value for the total emitted radiation. A plot of the detector current corrected for solid angle and reflectance versus separation distance is shown in Figure 5.7. The curve fitting of the corrected data points in Figure 5.7 now shows a linear fit with both silicon and germanium data. Notable in the figure is that each detector displays similar results where the higher detector current is associated with large separation distances, with the detector current decreasing as the separation distance decreases.

However, the curves in Figure 5.7 do not display zero slope as expected, which means that more processes than the solid angle and reflectance must be accounted for. An experiment to determine if each detector surface exhibited uniform sensitivity across the surface area was then performed. A broadband light source was placed 2.5 mm from each detector with a pinhole aperture, less than 0.5 mm diameter, placed between them. The aperture was then moved across the centerline of each detector and the photocurrent measured. Results showed that for each detector, the outer one millimetre edge, when compared to the rest of the detector surface, was 33.3% less sensitive for germanium, and 8% less sensitive for silicon. The separation results were then corrected for the non-uniform surface sensitivity by normalizing the sensitivity results, multiplying by the percentage area and determining a mean signal factor. This mean signal factor was then applied to the separation results and is shown in Figure 5.8. The curves fitted to the results in Figure 5.8 are observed to have decreased, but still non-zero slopes are exhibited. One possible explanation for this behaviour is that the treatment up to now has
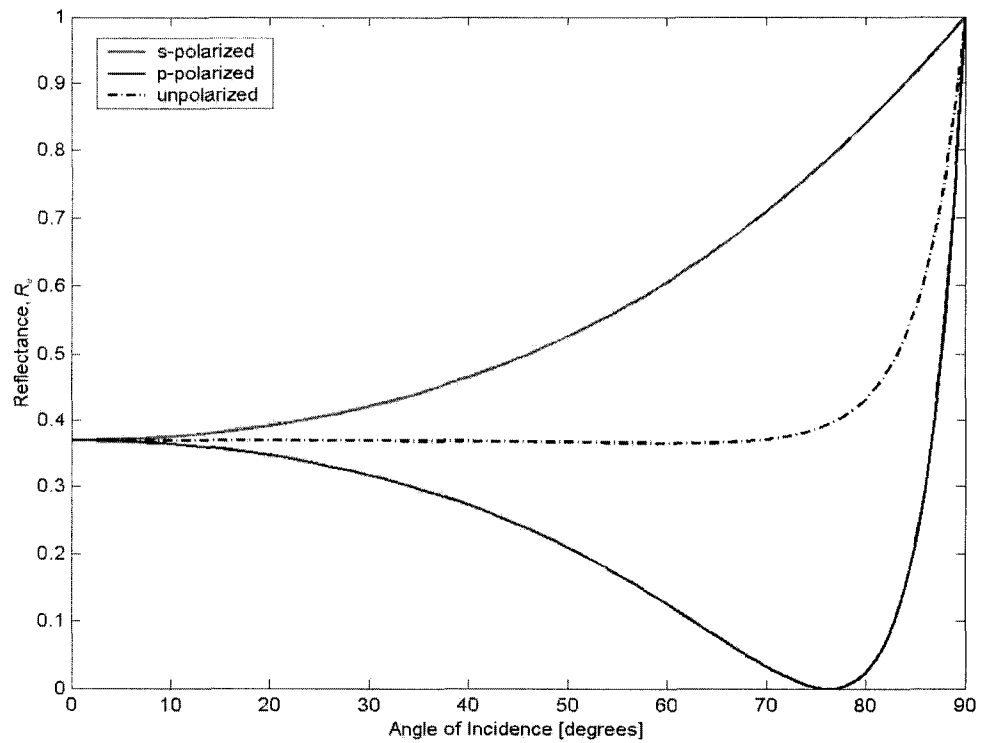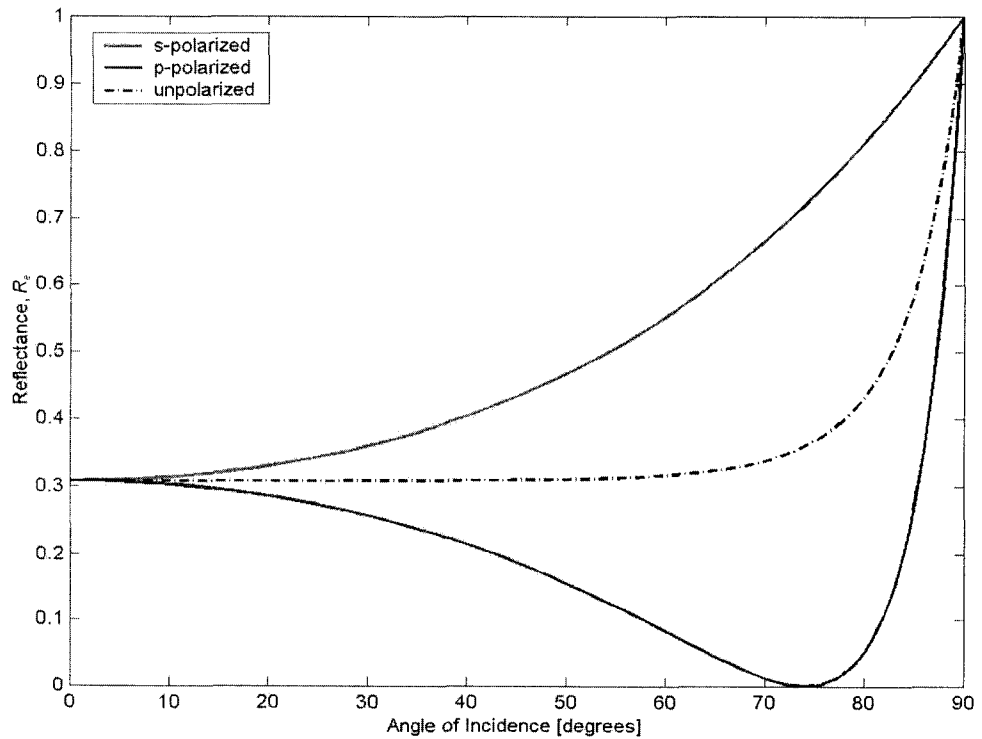
Figure 5.6 Plot of reflectance versus incident angle for (a) germanium, and (b) silicon. The curve labeled "un-polarized" is the mean of the s- and p-polarized curves.
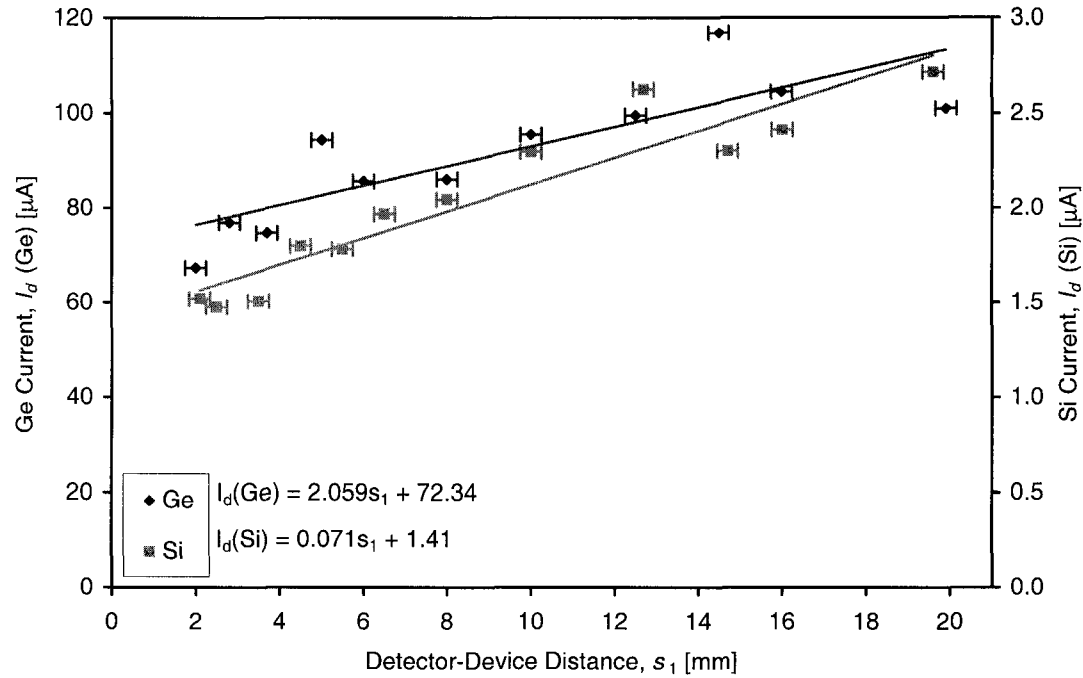
Figure 5.7 Plot of corrected (solid angle and reflectance) detector current versus detector separation. The left and right vertical axes correspond to the germanium and silicon detector current, respectively.

assumed the device to be a point source emitting equally in all directions, when in fact, the device is a planar light source with size on the order of 0.1 mm which results in a non-diffuse emitter. Non-diffuse emitters are characterized by a non-trivial form factor that varies as a function of emitter-detector separation distance and the respective geometry of the emitter and detector [79]. However, we felt that further correction of the data would not be warranted.

The important point is that the comparison between the germanium and silicon photodetectors shows that germanium is roughly 40 times more effective at detecting broadband thermal radiation than silicon, for this particular micro-Pirani gauge, under the conditions stated above. Thus, all further measurements were performed using the germanium detector.

$I_d(Ge) = 0.564s_1 + 93.63$

$I_d(Si) = 0.031s_1 + 2.08$
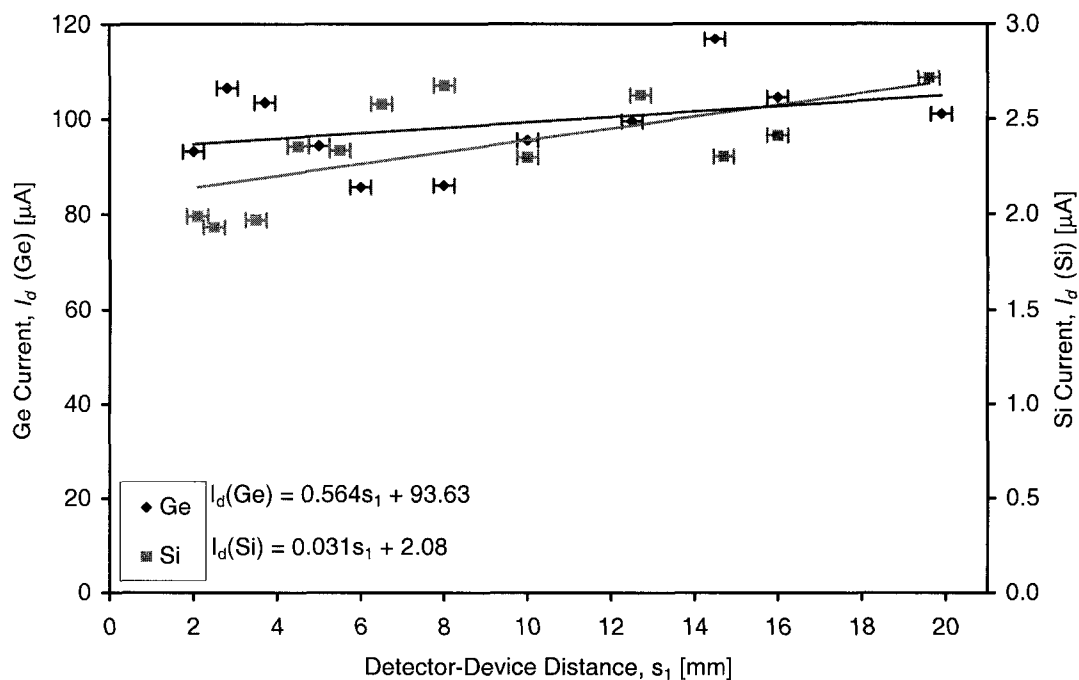
Figure 5.8 Plot of corrected (solid angle, reflectance, and detector surface sensitivity effects) detector current versus detector separation. The left and right vertical axes correspond to the germanium and silicon detector current, respectively.

5.4 VACUUM MEASUREMENT

One of the possible applications for the micro-Pirani devices is use as a pressure gauge. Each of the four device geometries was tested at various pressures in a nitrogen atmosphere and the detector current measured. Two modes of device operation were employed. The first mode of operation, referred to as constant power, consists of adjusting the current through while simultaneously measuring the voltage across the polysilicon element such that the power being dissipated by the structure is maintained constant. The resultant detector current is then measured and all parameters recorded to file; the detector current determines the pressure upon calibration. The second mode, referred to as constant response, adjusts the amount of current through the polysilicon element to maintain the resultant detector current constant. The voltage across the device is measured, the power calculated, and all parameters also written to file; the device power determines the pressure upon calibration. Flowcharts of the two modes are shown in Figure 5.9 (a) and (b), respectively. For both cases, direct current was sourced through

the polysilicon, data written to file every tenth loop of execution (the execution time between loops being approximately 80 ms).
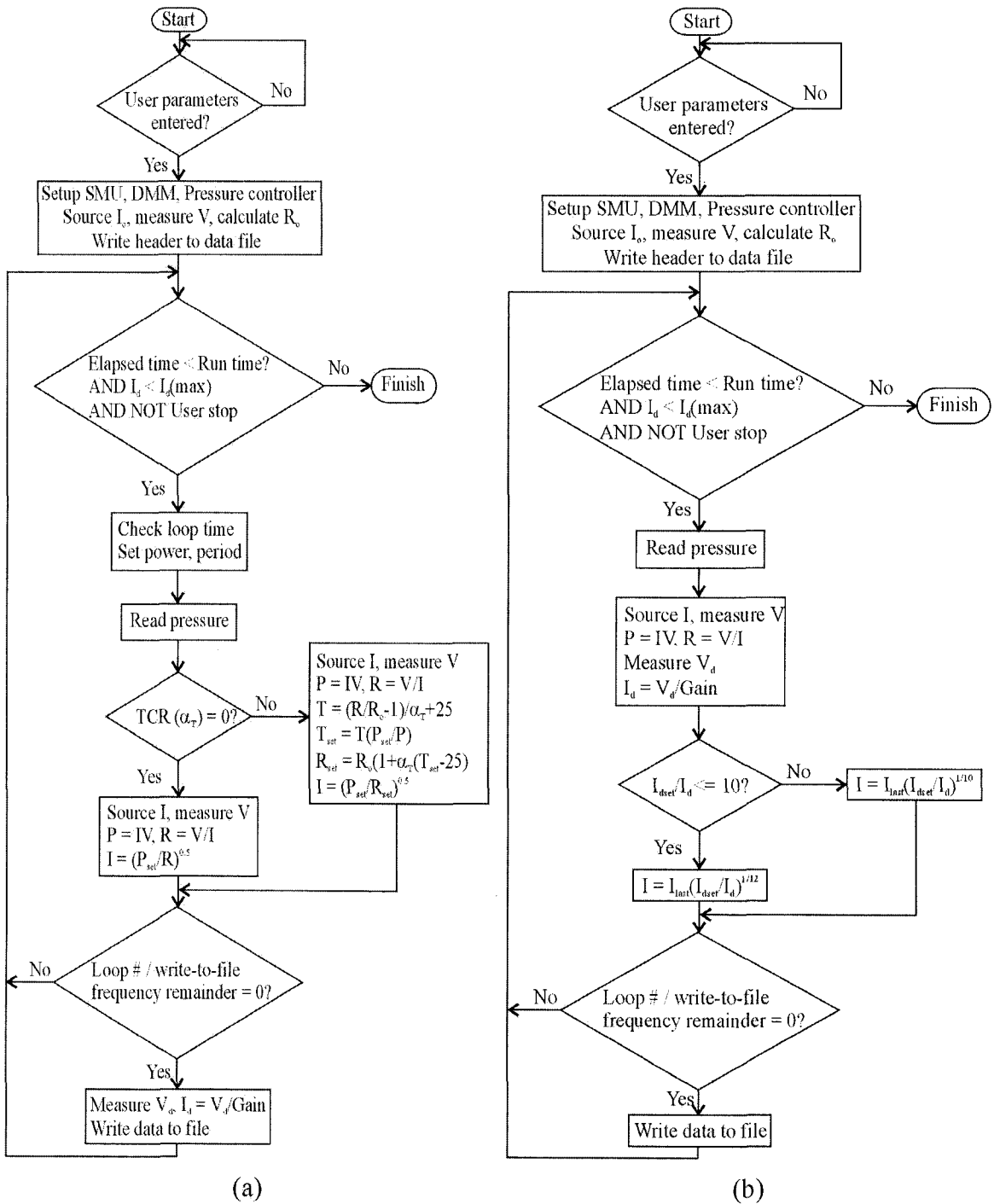
Figure 5.9 Flowchart for (a) constant power, and (b) constant response operation with direct current source.

5.4.1 Constant Power

The results from testing two small square-type devices can be seen in Figure 5.10. The vacuum test chamber was first evacuated to a pressure below 1 mTorr before being vented with dry, pure nitrogen to atmospheric pressure. The error in measuring pressure was ±0.1 Torr for pressures greater than 1 Torr and ±0.2 mTorr for pressures less than or equal to 1 Torr, each pressure range corresponding to one of the capacitance manometers. At each power tested, the device was operated first at atmospheric pressure and then the pressure decreased until either the pressure became less than 1 mTorr or a preset maximum detector current, of 30 μA, was measured. The error in measuring detector current was conservatively estimated at ±0.1 μA. To calculate the room temperature resistance, a small current of 10 μA, sufficiently small enough to prevent self-heating, was sourced through and the voltage measured across the device. The detector current measured during the sourcing of the 10 μA was assumed due to thermal noise and detector dark current, this background detector current was subtracted from every subsequent data point for that particular run.

The powers maintained through each device as the pressure was varied from atmospheric to below 1 mTorr were, within ±1%: 4, 6, 8, 10, 12, 15, 20, and 30 mW, respectively. For the results shown in Figure 5.10, all devices resided on die 13 which has an etch depth of 80 ± 5 μm. The data points corresponding to powers of 4 to 10 mW were obtained from device 4, while the powers of 12 to 30 mW were obtained from device 3. The results were not taken from the same device due to the problem of low device durability. After completing the first four power runs, device 4 failed; the polysilicon trace became open-circuited. Further discussion on the durability of the micro-Pirani gauges is presented in Chapter 7. From Figure 5.10 it can be observed that for increasing power dissipated through the device, detector current increases, indicating a higher device temperature; the pressure at which the large increase in response occurs also increases. For application as a vacuum sensor, this leads to the conclusion that pressure over a wide range can be measured with sufficient sensitivity by dissipating an appropriate amount of power through the structures. This concept of power-switching is discussed in detail in [20].
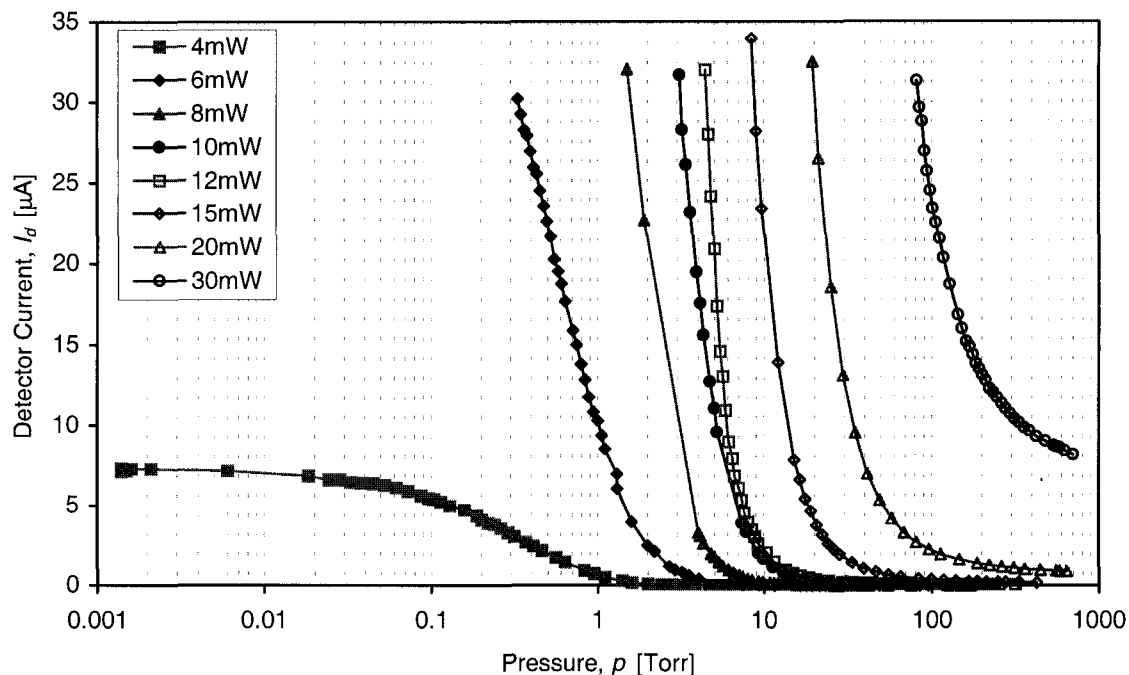
Figure 5.10 Detector current versus pressure for small square devices 4 (solid points) and 3 (hollow points) residing on die 13 at various powers in nitrogen.

Experiments were also conducted for the large square, single bridge, and double bridge devices in nitrogen for the aforementioned variation in pressure and powers, with the results shown in Figures 5.11 to 5.13. Again, because of low device durability, not all tests were achieved with a single device from each type. The sole exception to this are the results shown in Figure 5.12 in which only single bridge device 13, residing on die 12 and with approximately the same etch depth as die 13, was used. Die 12 was also used for obtaining the results for the large square and double bridge structures, devices 6 and 14 for powers of 4 to 10 mW, and devices 10 and 15 for powers of 12 to 30 mW. Additional plots are included in Appendix B. The results for the large square, single bridge, and double bridge devices appear very similar to those of the small square device. As the pressure decreases, the detector current increases from less than 1 μA to over 30 μA, and as the power is increased, the pressure at which the large increase in detector current is observed on the linear-log plot increases.
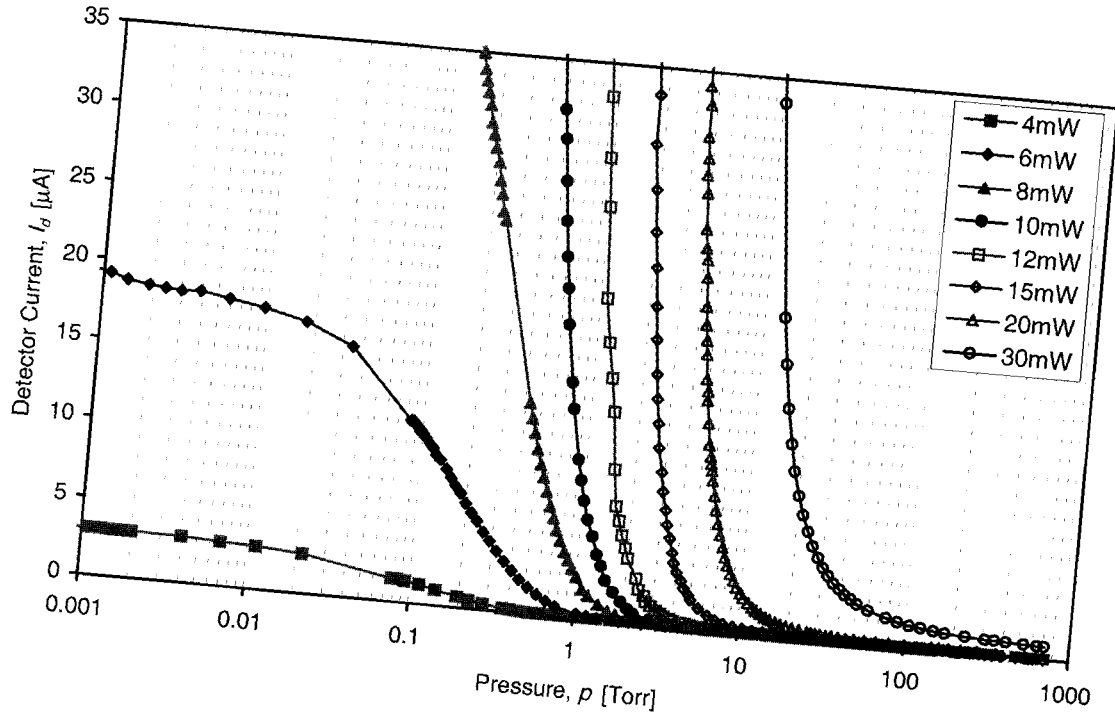
Figure 5.11 Detector current versus pressure for large square devices 6 (solid points) and 10 (hollow points) residing on die 12 at various powers in nitrogen.
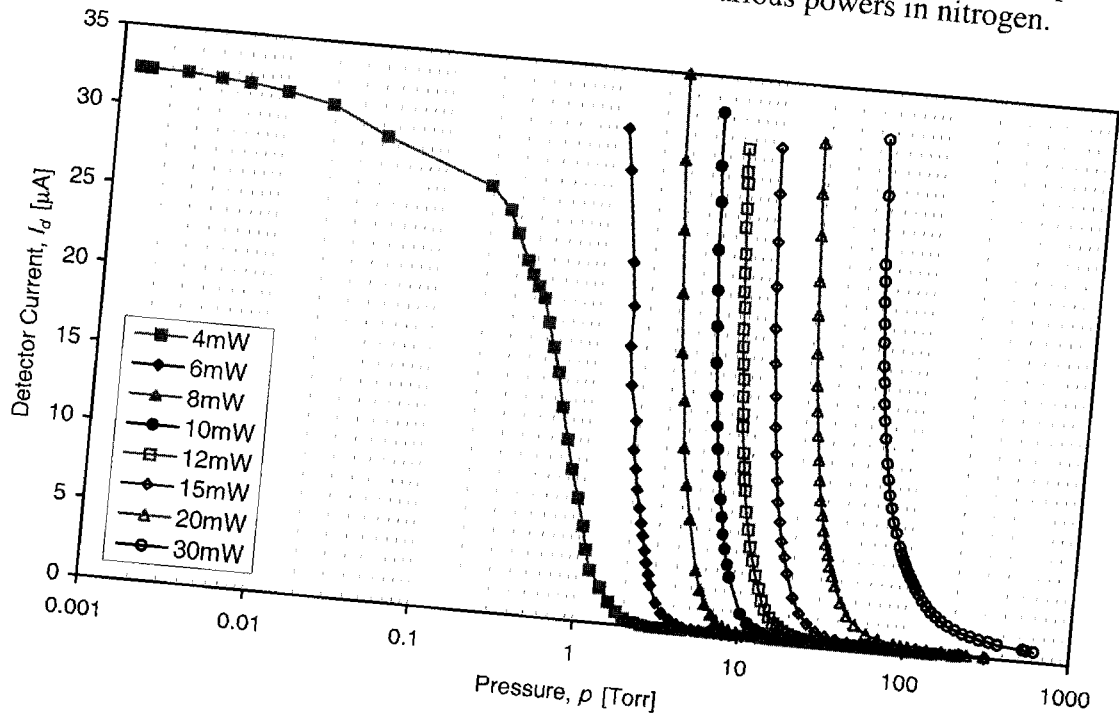
Figure 5.12 Detector current versus pressure for single bridge device 13 residing on die 12 at various powers in nitrogen.
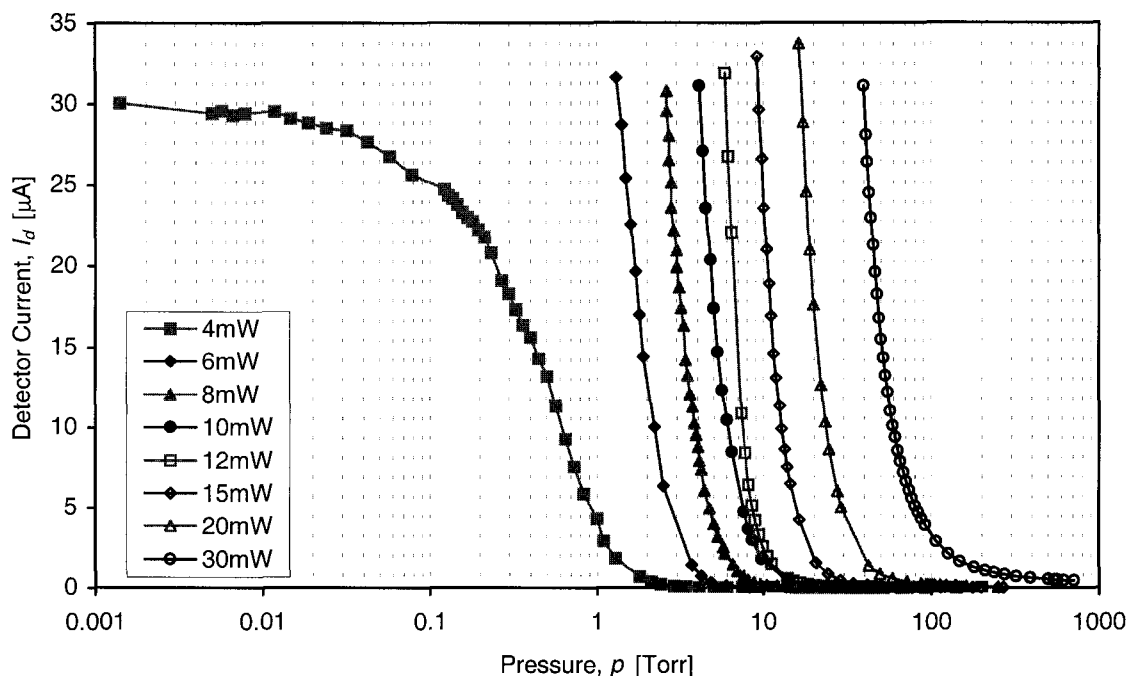
Figure 5.13 Detector current versus pressure for double bridge devices 14 (solid points) and 15 (hollow points) residing on die 12 at various powers in nitrogen.

To compare the four device types, the data from one run, namely 10 mW, was plotted and is shown in Figure 5.14. As stated, each device produces similar results, except for the large square whose detector response curve enters the large increase in response region at approximately 1 Torr as compared to the other devices whose response curves exhibit the same large response increase at approximately 10 Torr. This appears reasonable as the large square is dissipating the same power over a larger surface, and hence, would operate at a much cooler temperature when compared to the other three device types. This cooler temperature would manifest itself as a response curve shifted towards a lower pressure since the higher temperatures would not be achieved until the density (pressure) of the conducting gas medium was further decreased. In addition, the double bridge devices consistently produce an equivalent response occurring at a slightly lower pressure when compared to single bridge devices under similar operating conditions. This result is expected as the aluminum bridge was designed to act as a heat sink, thus cooling the polysilicon bridge and requiring a lower pressure to produce the same device temperature (and subsequent detector response) as for the single bridge.
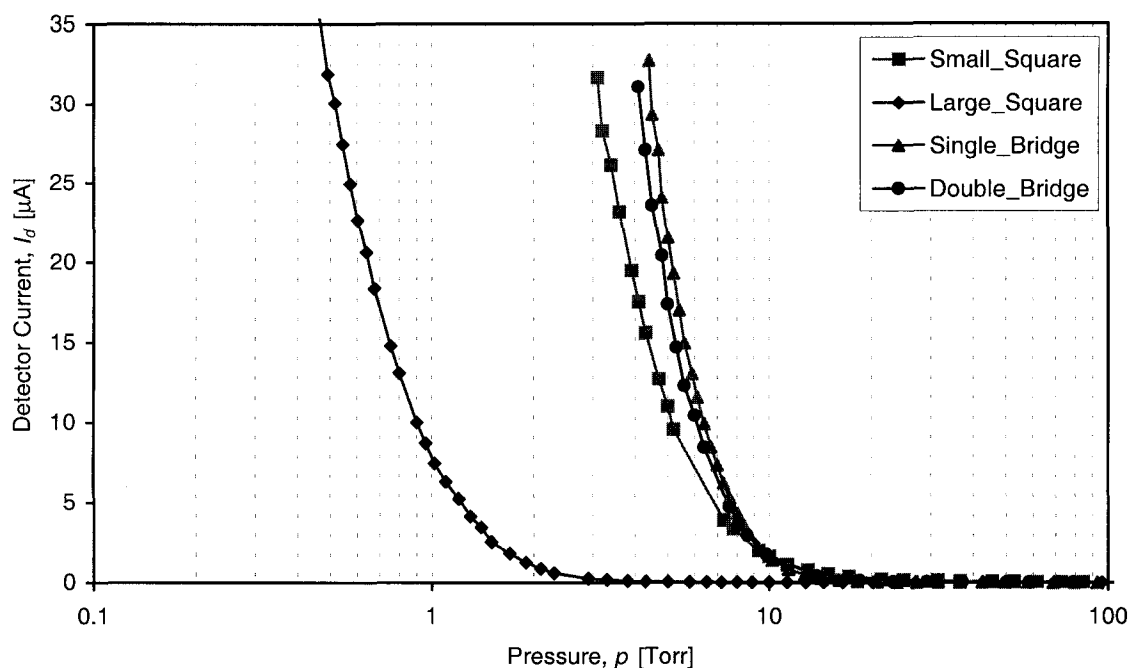
Figure 5.14 Detector current versus pressure for all four device types at
10 mW power in nitrogen.

Compared to a standard Pirani gauge device, the curves shown in Figures 5.10 to
5.14 exhibit a similar shape of response, with the standard Pirani gauge producing a much
smaller change in response as a function of pressure. Further discussion on the pressure
measurement sensitivity and repeatability is presented in Chapter 7.

5.4.2 Constant Response

Results from large square device 6 residing on die 13, operated under various
constant detector responses are shown in Figure 5.15. The plot shows the power required
to maintain a detector response of 0.5, 5, 10, and 50 μA as the pressure is varied from
1000 Torr to below 1 mTorr. The uncertainty in measuring power is conservatively
estimated at $\pm$0.1 mW. As expected, higher powers were required at higher pressures due
to the heat loss to the surrounding relatively dense gas medium. Decreasing the pressure
(density) of the gas reduced the heat loss, resulting in less power needed to generate the
same device mean temperature (detector response). Only the large square device was
tested for four constant responses due to durability issues arising with the other devices;
however, all device types were tested in nitrogen while maintaining constant responses of

5 and 10 μA with the data for 10 μA only plotted in Figure 5.16. The data resulting from the 5 μA runs (all devices) produced similar curves as those shown in Figure 5.15; this plot is included in Appendix B. All of these devices resided on die 13, and consisted of devices 4 (tested first under constant response, followed by constant power during which it failed as detailed in the previous section), 6, 13, and 15 for the small square, large square, single bridge, and double bridge, respectively. Figure 5.16 shows that at 100 Torr, the large square and bridge devices required approximately 50 mW of power to maintain a constant detector response of 10 μA. The small square, however, required only about 30 mW or 40% less power at the same pressure to produce the same detector response. Again, this is likely due to the relative smaller area of the small square device where the heat loss through the gas is less than that of the other devices, hence producing a larger mean device temperature (response) for a given power. Also seen in Figure 5.16 is that the single bridge device failed as the pressure was decreased below 10 Torr. This result, in part, was responsible for the limited testing of constant responses performed on the devices.
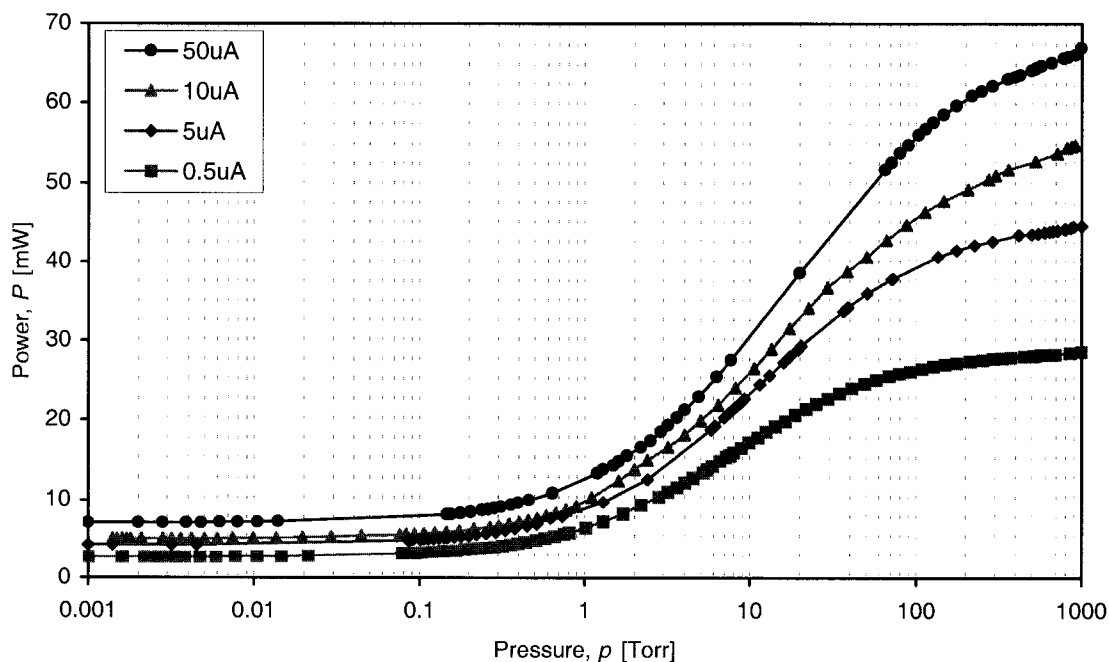
Figure 5.15 Power versus pressure for large square device 6 residing on die 13 at various responses in nitrogen.
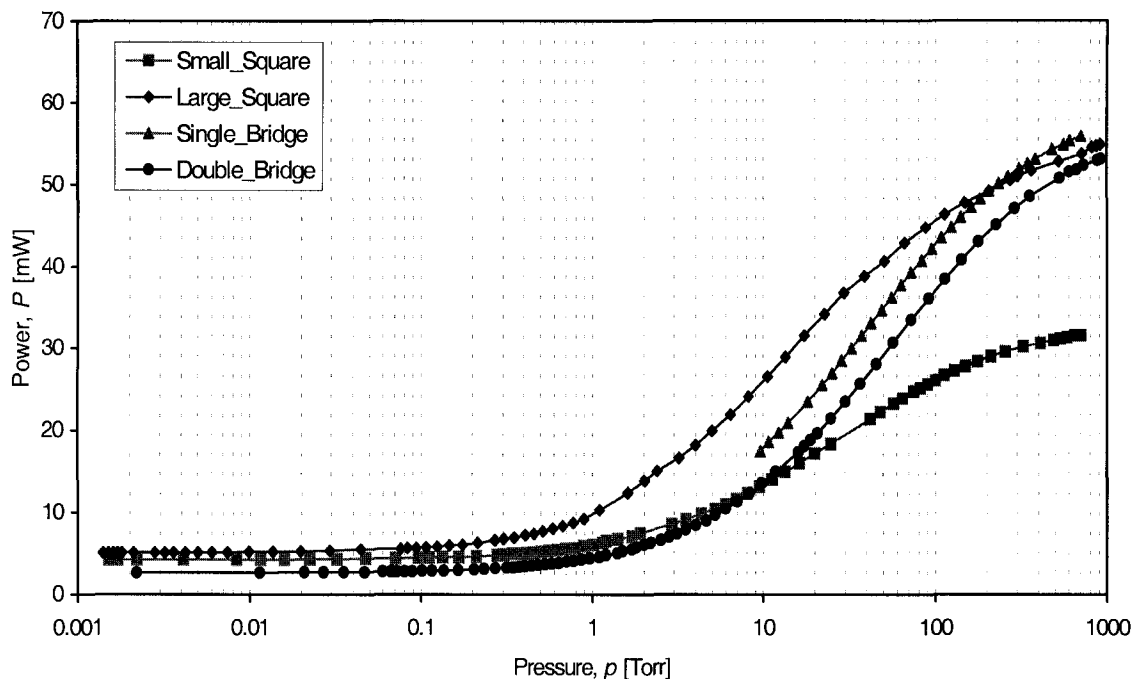
Figure 5.16 Power versus pressure for all four device types at 10 μA response in nitrogen.

Lastly, the curves in Figure 5.16 are observed to cross each other at various pressures. No significance should be placed on the fact that the curves cross as each represents a separate device. Chapter 7 discusses the implications of using the constant detector response mode of operation as a means of measuring vacuum.

5.5 GAS ANALYSIS

The main emphasis for this project was to validate the use of the micro-Pirani structures as gas analyzers, that is, at a known pressure a constituent gas in the vicinity of the sensor could be identified. To determine the feasibility of this goal, the four device types were tested under constant power and constant response modes of operation in presence of nitrogen (N_2), argon (Ar), helium (He), krypton (Kr), and sulfur hexafluoride (SF_6). The tests were conducted for two modes of operation where the devices were initially sourced with direct current and then with alternating current in the form of a square wave with an 80% duty cycle.

5.5.1 Constant Power

5.5.1.1 Direct Current Source

Initially, all device types were to be tested at both 4 mW and 15 mW in each of the five gases of interest (N_2, Kr, Ar, He, and SF_6) for pressures ranging from 1000 to 10^{-4} Torr. Due to poor durability and a low number of available devices, however, not all device types were tested in all five gases and at the two separate powers. It was also observed that when any devices were operated in the presence of SF_6, conditions producing a detector output in excess of a 10 μA caused the devices to either fail during operation or fail shortly after operation. Further investigation indicated that SF_6 is known to decompose for temperatures in excess of 700 K. Furthermore, the presence of water in a high temperature SF_6 environment causes the formation of HF, a known etchant of silicon dioxides [97]. The test chamber was evacuated for only seconds before filling with any particular gas, so it is not unreasonable to assume the presence of water molecules adhering to the inner chamber surfaces. However, microphotographs taken after device failure in the presence of SF_6 did not show any observable etching or related effects. Nonetheless, since testing in the presence of SF_6 produced a negative effect on device durability, testing in this gas was halted. More discussion with regards to SF_6 and device failure mechanisms is presented in Chapter 7.

Plots of detector current versus pressure for large square devices 7 and 9 residing on die 13 and tested in the five separate gases at 15 mW and 4 mW constant power (direct current source) are shown in Figures 5.17 and 5.18, respectively. Plots of the results from testing of the other device types under similar conditions have been included in Appendix C. The figures follow a similar pattern as observed for the vacuum measurement tests in nitrogen. That is, as the pressure decreases, the detector current increases from essentially 0 μA to over 30 μA at 15 mW power, and from 0 to 2.7 μA at 4 mW power. At the higher power, measurements were limited to approximately 30 μA, to avoid device failure. The pressure at which the detector current for each curve increases is different not only for each power, but for each gas. In both cases, krypton is observed to cause the largest detector current at the highest pressure, followed by argon. In the case of nitrogen and helium, initially the nitrogen produces the larger response, and then the helium crosses the nitrogen curve to produce the larger response as the pressure
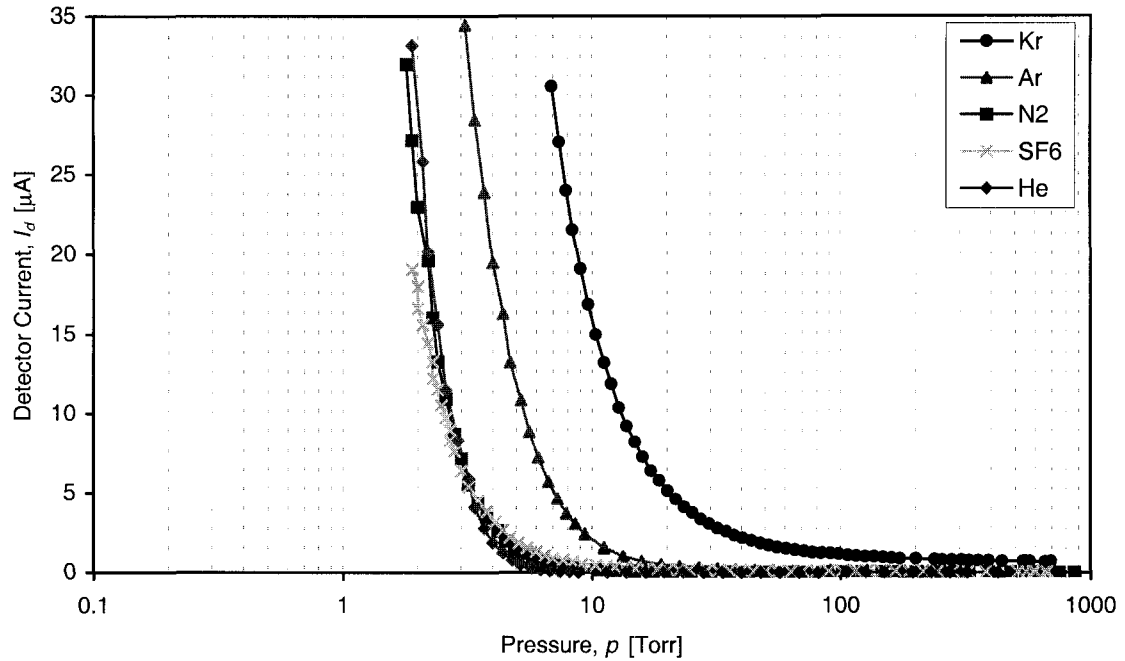
Figure 5.17 Detector current versus pressure for large square devices 7 (Kr, Ar, N_2, He) and 9 (SF_6) residing on die 13 at 15 mW power, DC source, and for various gases.
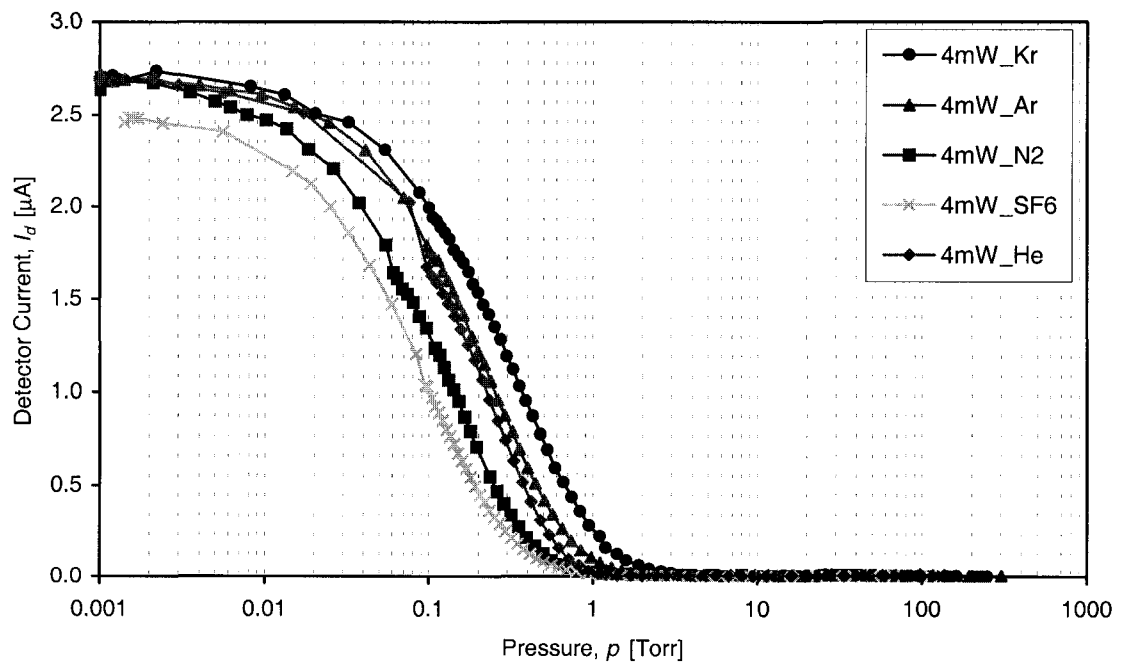
Figure 5.18 Detector current versus pressure for large square devices 7 (Kr, Ar, N_2, He) and 9 (SF_6) residing on die 13 at 4 mW power, DC source, and for various gases.

decreases. However, in Figure 5.17, the nitrogen and helium curves are virtually identical. This is the only observed case of this result. The pressure at which the crossing between the helium and nitrogen curves occurs is approximately 3 Torr for 15 mW operation and 1 Torr (not observable in the figure) for 4 mW operation. In both the 15 and 4 mW cases, the sulfur hexafluoride curves do not produce an increasing detector current until essentially the lowest pressures. The position of the SF_6 curves is interesting in that the thermal conductivity value for SF_6 is between that of Kr and Ar, leading us to believe the SF_6 line should occur between the Ar and Kr lines. The fact that the SF_6 curve does not behave in this way could be the result of the decomposition of SF_6.

Improved device reliability was achieved by not only ceasing device testing in SF_6, but also by further limiting the maximum allowed detector current to 10 μA. As a result, the rest of the constant power DC tests were recorded with the use of only one device of each type. A single power of 8 mW was arbitrarily chosen as representative of the various powers for the purpose of illustrating sensitivity to the constituent gas under test. A plot of the detector response versus pressure for small square device 1, residing on die 5 (85 μm estimated etch depth) for Kr, Ar, He, and N_2 is shown in Figure 5.19. From Figure 5.19 it is observed that the small square response at 8 mW is in a manner consistent with the response for the large square devices at 15 and 4 mW, as seen in Figures 5.17 and 5.18. Further, the crossover between the helium and nitrogen curves (not easily apparent in the figure) is also consistent with Figure 5.17 in that the event occurs at approximately 3 Torr. The reason for this is a cross-over in gas thermal conductivity, as discussed later in Chapter 7. Results for large square device 6, single bridge device 11, and double bridge device 14, all residing on die 5, are shown in Figures 5.20 to 5.22, respectively. In each of the figures, the behaviour of the devices is consistent with previous results noting that the large square device produces increasing detector currents at the lowest pressure as expected, and the pressure at which the nitrogen and helium lines cross is approximately 2 Torr for the large square and 6 Torr each for the single and double bridge devices.

A comparison between each of the four device types in nitrogen was made and the results were plotted and are shown in Figure 5.23. As with previous results, the small square, and bridge-type devices produce detector current versus pressure curves that are

very similar under like conditions with the double bridge device consistently producing an increasing detector response at a slightly lower pressure than that for the single bridge device. Likewise, as per previous results, the large square device produces no large detector response until pressures are below those shown for the other devices. Comparing the results in Figure 5.23 (8 mW) with those of Figure 5.14 (10 mW), the shape and relative position of the curves is similar with each of the 10 mW curves occurring at a slightly higher pressure than their respective 8 mW responses.
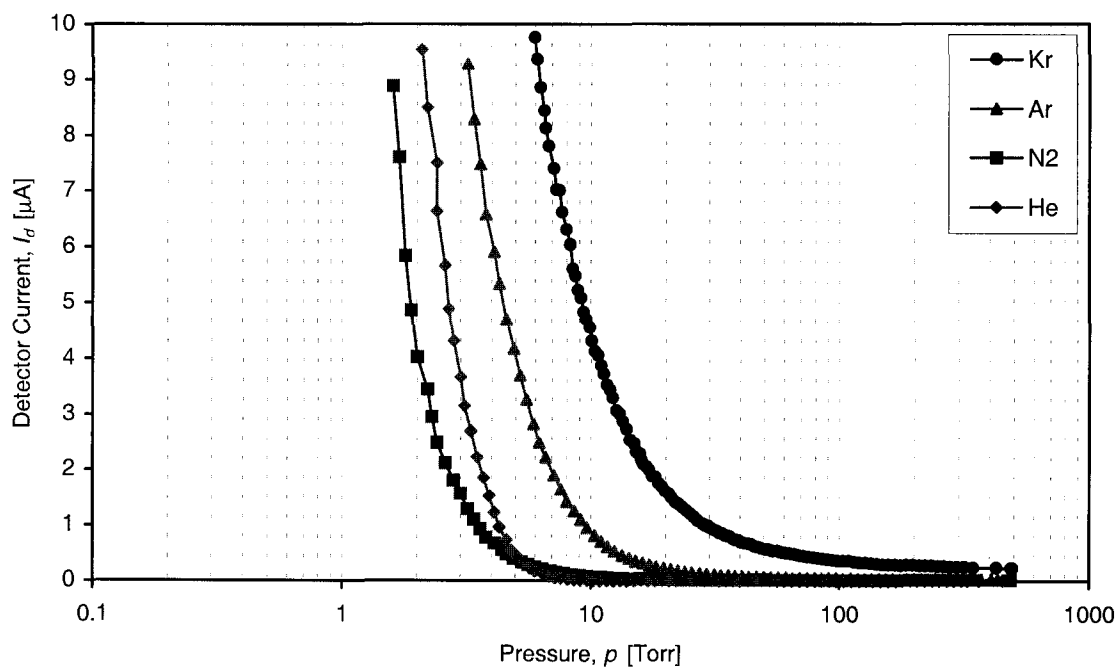
Figure 5.19 Detector current versus pressure for small square device 1 residing on die 5 at 8 mW power, DC source for various gases.
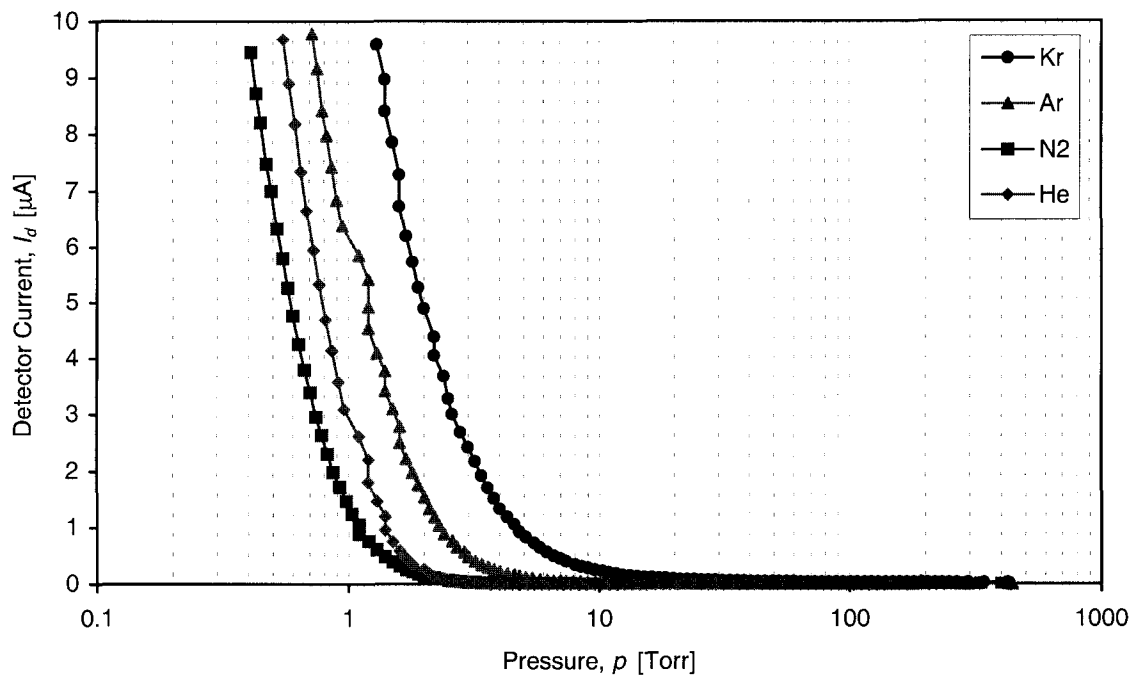
Figure 5.20 Detector current versus pressure for large square device 6 residing on die 5 at 8 mW power, DC source for various gases.

Figure 5.21 Detector current versus pressure for single bridge device 11 residing on die 5 at 8 mW power, DC source for various gases.

Figure 5.22 Detector current versus pressure for double bridge device 14 residing on die 5 at 8 mW power, DC source for various gases.

Figure 5.23 Detector current versus pressure for each device type residing on die 5 at 8 mW power, DC source in nitrogen.

5.5.1.2 Alternating Current Source

Testing of the micro-Pirani gauge devices under an alternating current (AC) source was done to observe the transient characteristics under various operating conditions. The AC tests were also performed to determine if there were any observable differences with the DC results due to a reduction of the duty cycle below 100%, thus slightly increasing the power consumption efficiency.

To produce the alternating current, the original computer control code was modified to measure the detector current immediately after sourcing the device current and measuring the voltage. On completion of the detector current measurement, the source current was turned off until all ancillary functions were completed and the program loop execution was completed. For both modes of operation, the smallest waveform period attainable to capture steady-state at all pressures, measured by oscilloscope, was 150 ms, with a non-zero current on-time of 120 ms, and a zero current off-time of 30 ms, for an overall duty cycle of 80%. Increasing the current off-time to lower the duty cycle was not done since doing so would increase the program loop execution time resulting in an unsatisfactory system response time to pressure variations. The relatively long on-time for the current pulse was required, as it was observed by oscilloscope that the polysilicon resistance exhibited a rise-time, defined as the time for the signal to change from 0 to 95% of its steady-state value, of as much as 100 ms when the devices were operating at high temperatures. An example of a typical waveform produced by constant power operation with pulsed current can be seen in Figure 5.24. The waveform shown in the figure was displayed on an HP 54600A digital oscilloscope and captured to computer via an RS-232 communication bus. The voltage across the polysilicon is displayed as channel one and the voltage across the detector amplifier output is shown as channel two. The data was produced from small square device 1 residing on die 5 (measured etch depth of 85 μm), operated at 8 mW in nitrogen at a pressure of 3 Torr.

From Figure 5.24 it is observed that the polysilicon rise-time (0 to 95%) is 102 ms, and the detector current rise- and fall-times are 117 ms and 9.6 ms, respectively. The detector rise-time is larger than the polysilicon rise-time since the detector does not begin to show an increase in response until the device is sufficiently heated above room
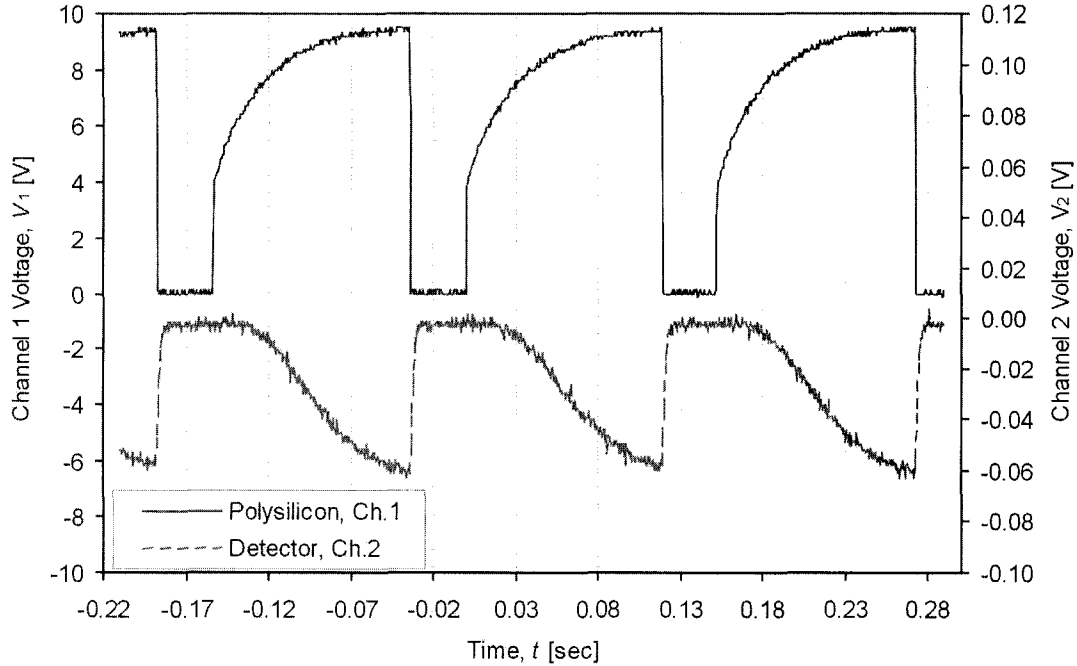
Figure 5.24 Typical waveform for pulsed current operation using small square device 1, residing on die 5, at 8 mW in nitrogen, and at 3 Torr.

temperature to produce radiation of the appropriate wavelengths and intensities to be within the bandwidth and sensitivity of the detector. When the current is turned off in a step-wise fashion, the detector output decreases rapidly. An empirical relation describing the coupling between the rise-time of the polysilicon resistance, τ_R [ms], the fall-time of the detector output, τ_{V_d} [ms], and the rise-time of the detector output, τ'_{V_d} [ms], is:

$$\tau'_{V_d} = b \cdot \left[\frac{1}{\tau_{V_d}} + \frac{1}{\tau_R} \right]^{-2}, \tag{5.10}$$

where b has a value of 1.52 ms^{-1} for nitrogen taken from the measured rise- and fall-times in the figure. It must be stressed that (5.10) was found empirically as an attempt to determine the relation between the temperature changes of the polysilicon and the resulting changes in detected thermal radiation. Further analysis of the transient response for various gases and at different pressures is presented in Section 5.5.3.

Testing under constant power with a pulsed current (AC) source was performed with the same four devices analyzed in Section 5.5.1.1, in the same four gases, and at the same operating power of 8 mW to allow for comparison with the DC results. Plots of detector current versus pressure for the respective small and large square, and single and double bridge devices are shown in Figures 5.25 to 5.28. Again, the resulting curves are consistent with those of the DC-sourced power of the previous section. A comparison between each of the four device types in nitrogen is shown in Figure 5.29. From the figure, it can be seen that the two bridge devices produce near identical curves. The small square device also produces a detector current versus pressure curve near that of the bridge devices, and the large square device produced the expected curve at lower pressures starting at approximately 1 Torr.

A comparison between the AC and DC sourced responses for the small and large square, and single and double bridge devices is shown in Figure 5.30. The figure demonstrates no significant difference in response between the same device operated by DC or AC current sourcing. Any difference in the figure is attributed to the uncertainty in device repeatability and the difference in system response time between the DC and AC software programs. The advantages to utilizing an AC source is mainly in the added ability to observe transient behaviour (investigated in Section 5.5.3), and marginally in the approximate 30% reduction of device power consumption. The reduction in power consumption is more than 20% (suggested by the duty cycle) since the power dissipated in the device does not follow a step-wise function (see Figure 5.24). The main disadvantage to utilizing the present AC setup is the large system response time required, preventing the accurate operation of the devices during large dynamic changes in pressure.
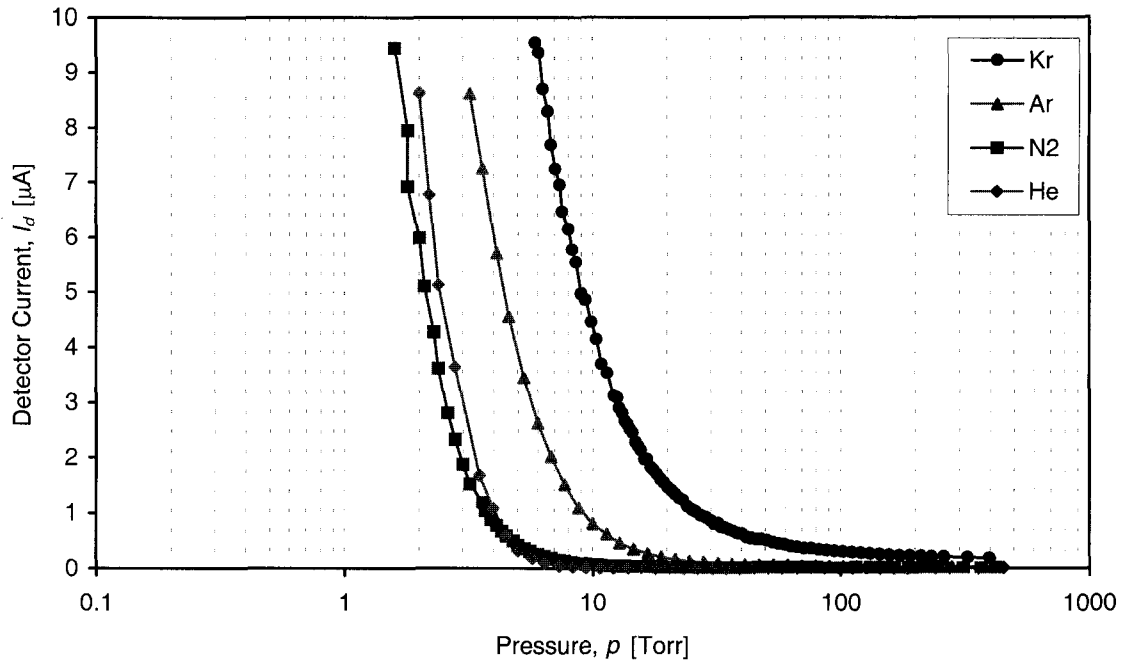
Figure 5.25 Detector current versus pressure for small square device 1 residing on die 5 at 8 mW power, AC source in various gases.
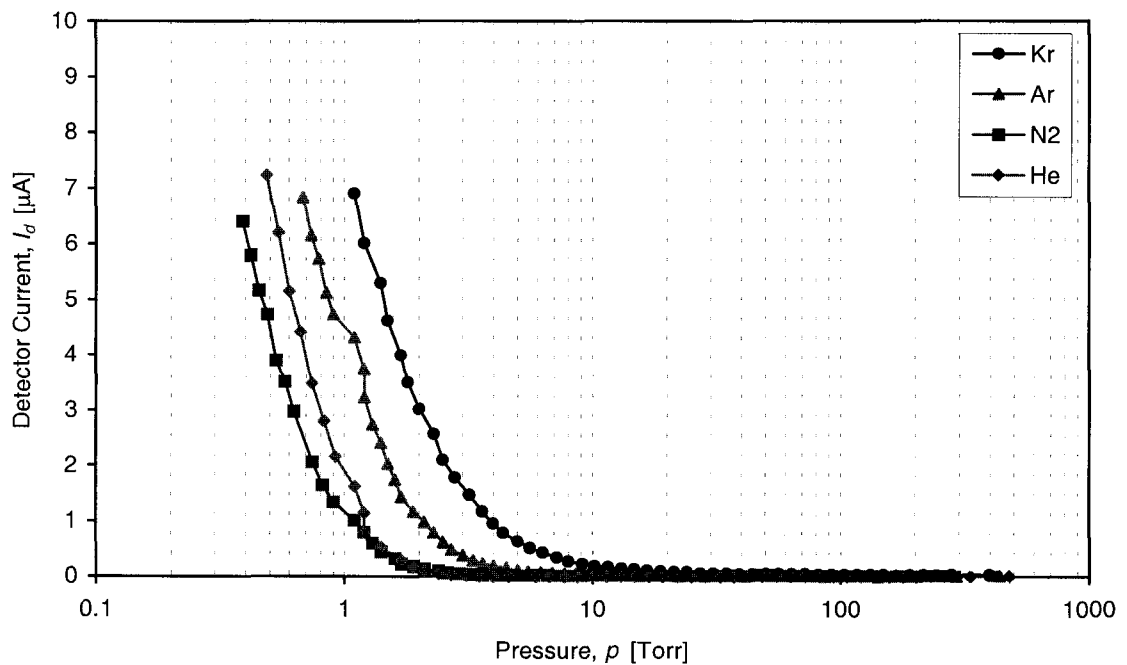
Figure 5.26 Detector current versus pressure for large square device 6 residing on die 5 at 8 mW power, AC source in various gases.
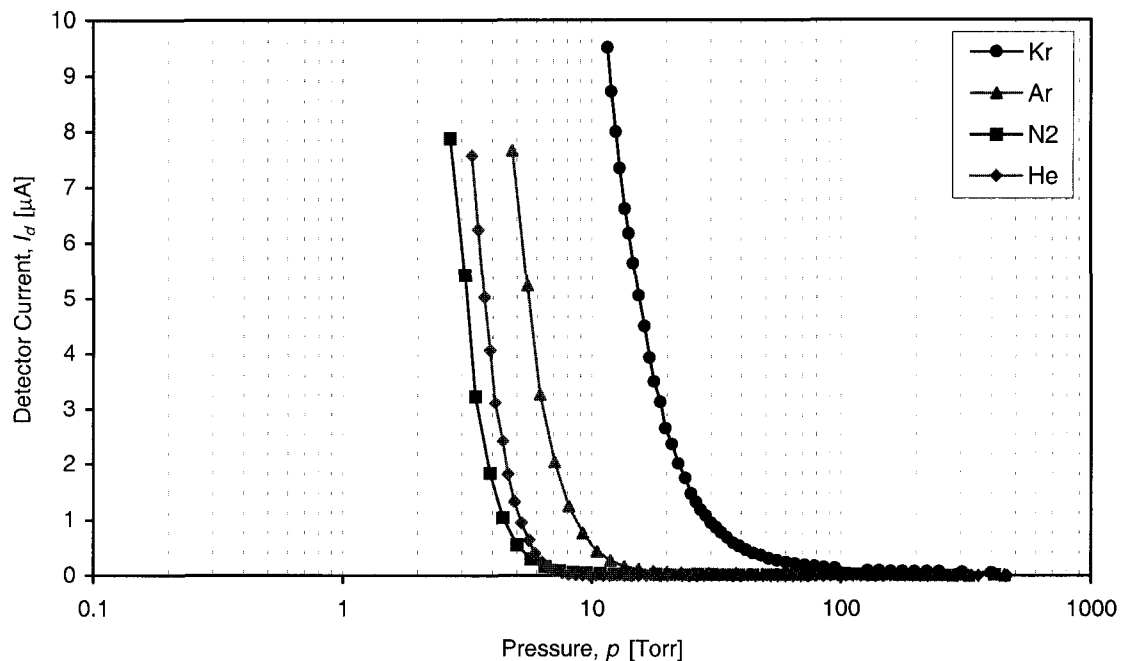
Figure 5.27 Detector current versus pressure for single bridge device 11 residing on die 5 at 8 mW power, AC source in various gases.
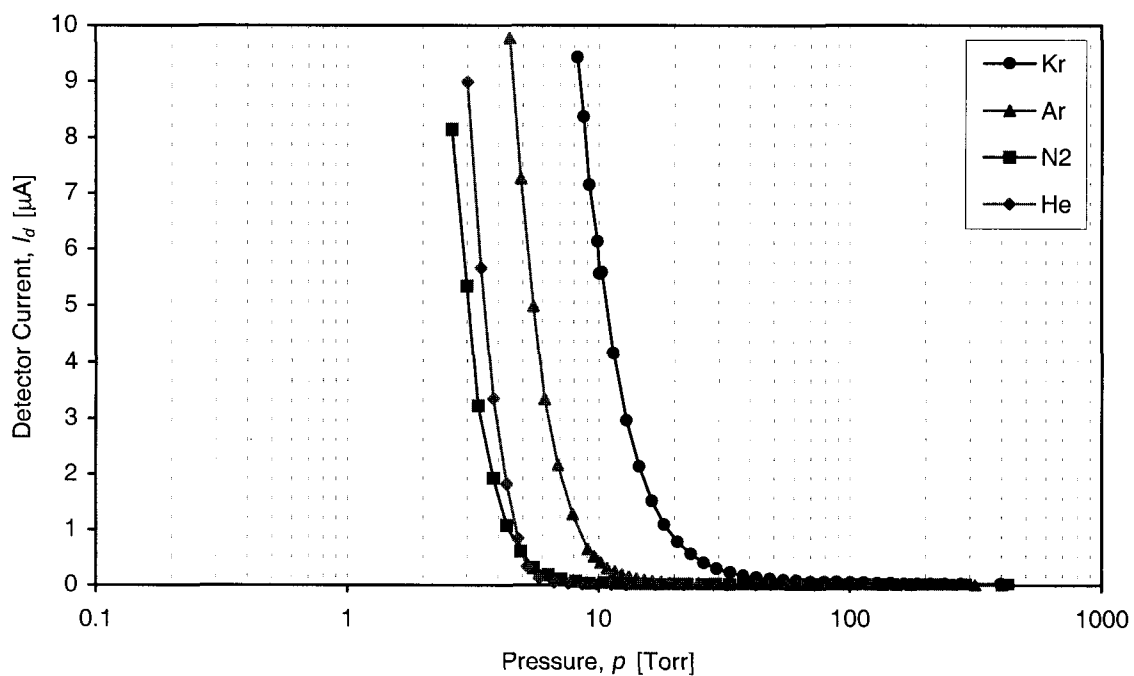
Figure 5.28 Detector current versus pressure for double bridge device 14 residing on die 5 at 8 mW power, AC source in various gases.

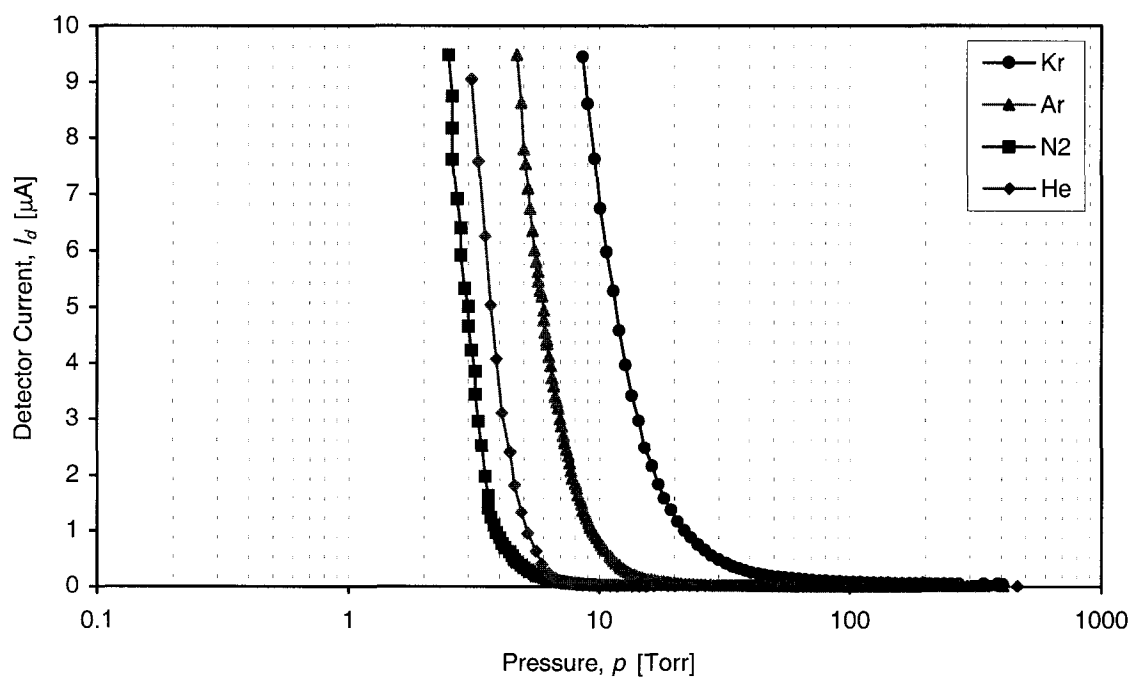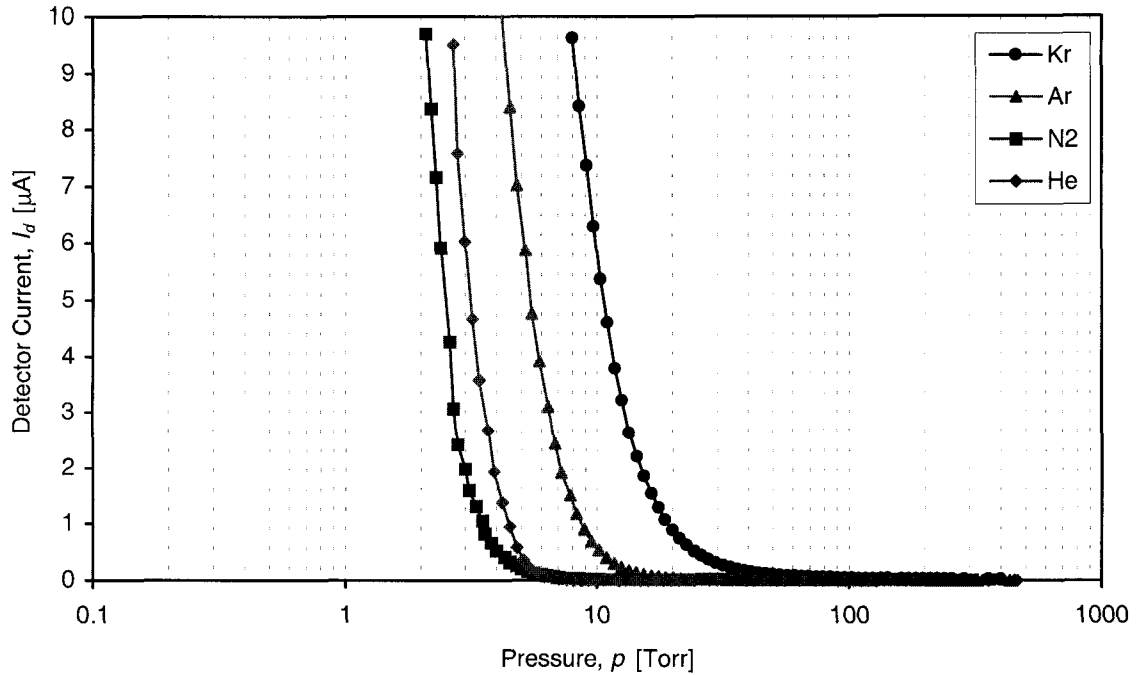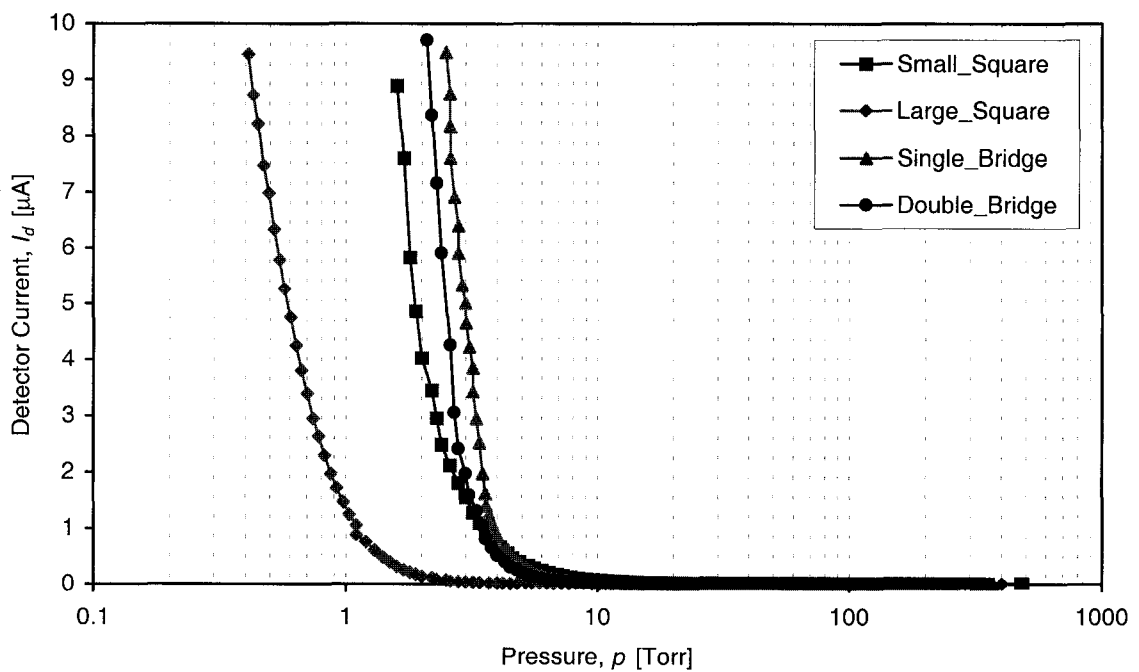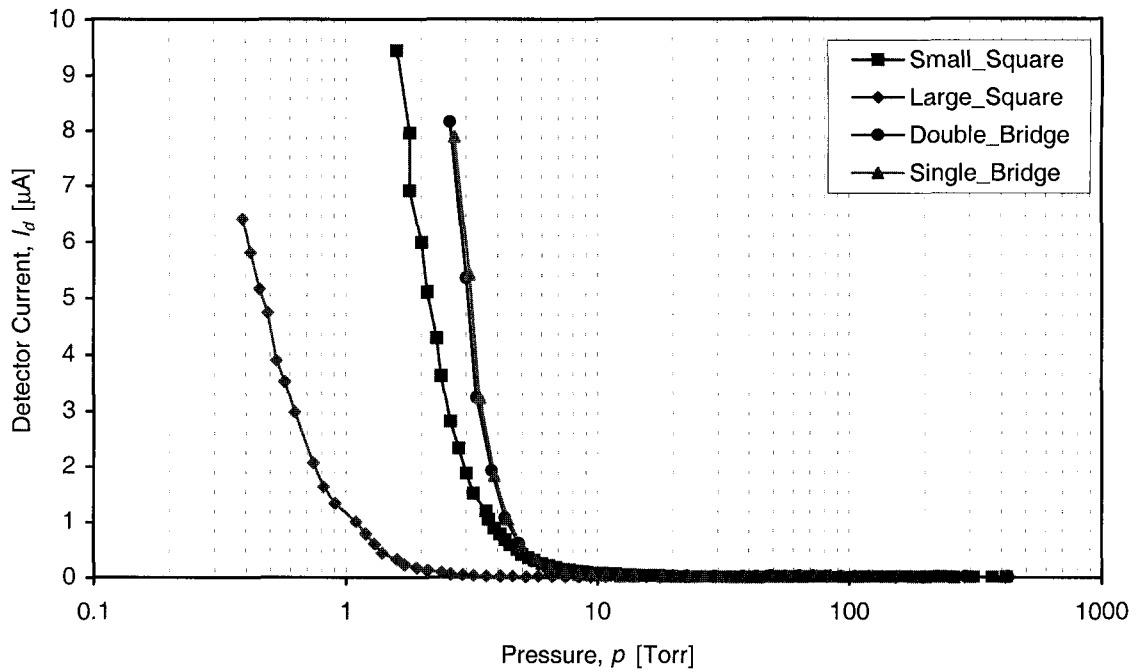**Figure 5.29** Detector current versus pressure for each device type residing on die 5 at 8 mW power, AC source in nitrogen.
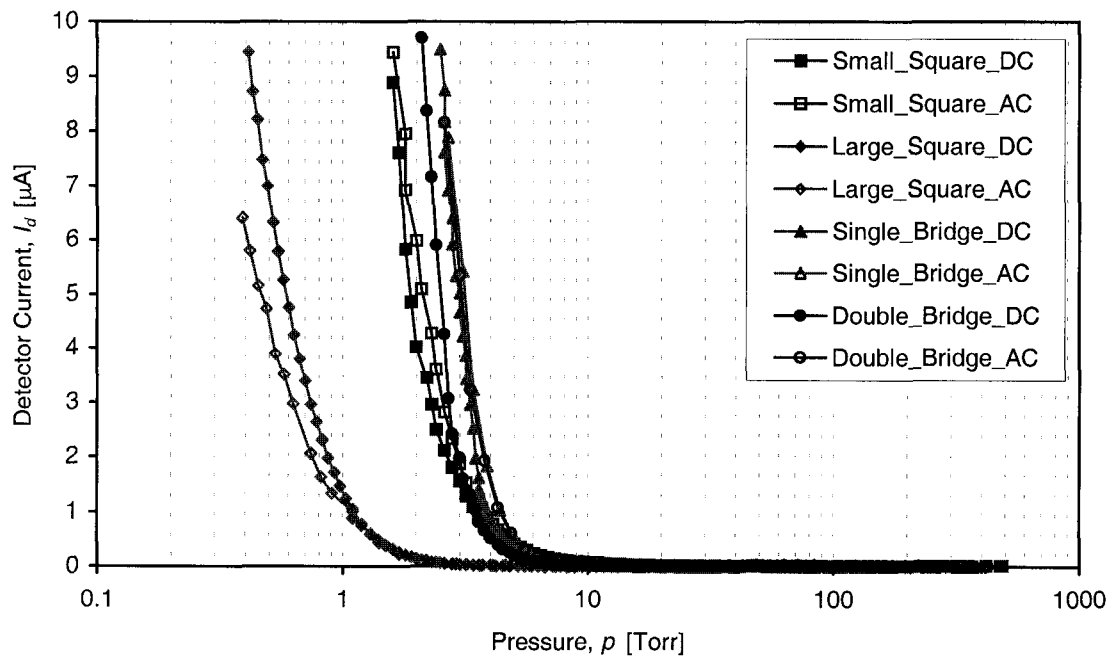
Figure 5.30 Detector current versus pressure for comparison between AC and DC sourced power for all device-types on die 5 at 8 mW power in nitrogen.

5.5.2 Constant Response

5.5.2.1 Direct Current Source

A plot of power versus pressure for two double bridge devices, residing on die 12 and operated at a constant detector response (with DC source) of 10 μA in the five gases of interest, is shown in Figure 5.31. All results shown in the figure were collected using device 15 with the exception of the data for SF_6, which were collected using device 14. The variation in response between devices is shown later in Chapter 7 to be marginal. As seen in the figure, each of the gases produces a unique power versus pressure curve with He requiring the most power, followed by SF_6, N_2, Ar, and Kr. Also, although not apparent in the figure, the He and N_2 cross over at approximately 3 Torr. Finally, seen in the figure is the close proximity between the SF_6 and the N_2 curves. For reasons presented in Section 5.5.1, testing in SF_6 was not extensively performed. Complete results are given in the form of plots from various devices and are shown in Appendix C. Note that the goal here was to perform the constant power and constant response tests, each with AC and DC sources and in various gases, with the exact same four devices – one from each geometry.

Sourcing direct current through the same four devices as used in the constant power trials (Section 5.5.1) and operating at a constant detector response of 5 μA, plots of power versus pressure were created and are displayed in Figures 5.32 to 5.35. From each figure, it is observed that the order of the curves with respect to each gas is preserved, including the crossover point between He and N_2 (at approximately 3 Torr), as a result of a crossing in thermal conductivity value. From the results of Figures 5.32 to 5.35, the pressure at which the largest difference in required power between each gas is 700 Torr, the maximum pressure used for the constant response trials. Extrapolating from the curves suggests that an even larger difference would be achieved at pressure above 700 Torr, with the large square results (Figure 5.33) suggesting an eventual saturation of the power, even for the He. That is, the power required to maintain a constant detector response increases with pressure, but not indefinitely.

For comparison, Figure 5.36 shows a plot of the nitrogen curve from each device type (taken from Figures 5.32 to 5.35). The bridge devices exhibit similar behaviour for all pressures, while at high pressure, the bridge devices and large square require a similar

amount of power. At 700 Torr, the small square requires, as a result of its geometry and smaller area, approximately 55% of the power required by the other devices to produce the same detector response. At pressures below 10 Torr, the bridge and small square devices behave in a similar manner, with power to each device type remaining constant at pressures below 0.1 Torr. Further discussion on the device behaviour is presented in Chapter 7.
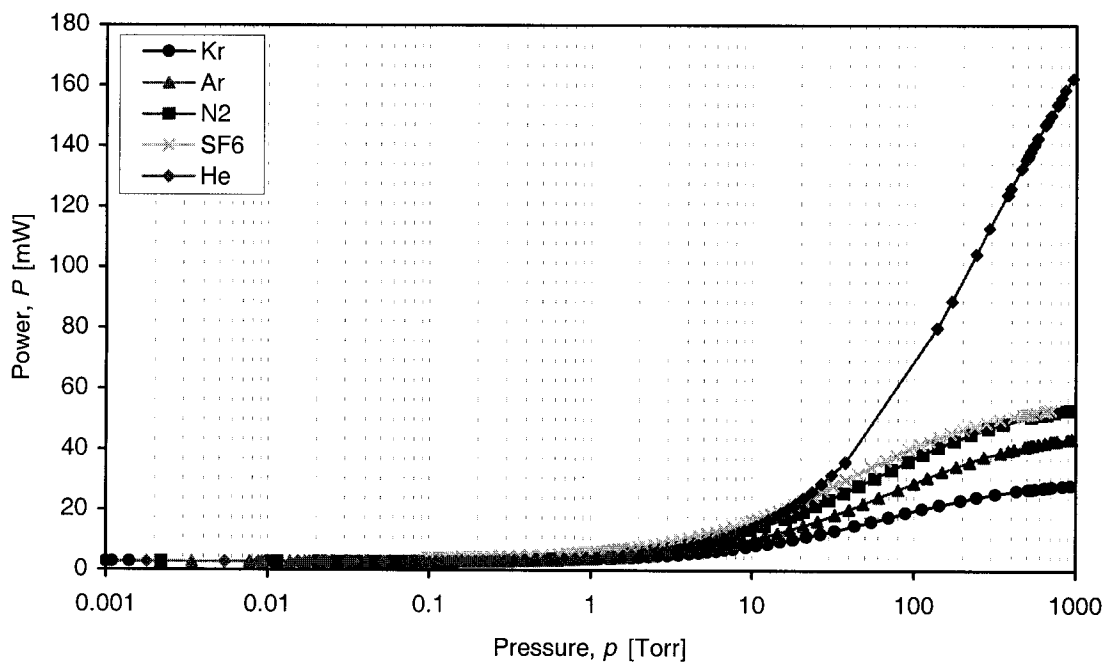
Figure 5.31 Power versus pressure for double bridge devices 15 (Kr, Ar, N_2, He) and 14 (SF_6) residing on die 12 at 10 μA response, DC source in various gases.
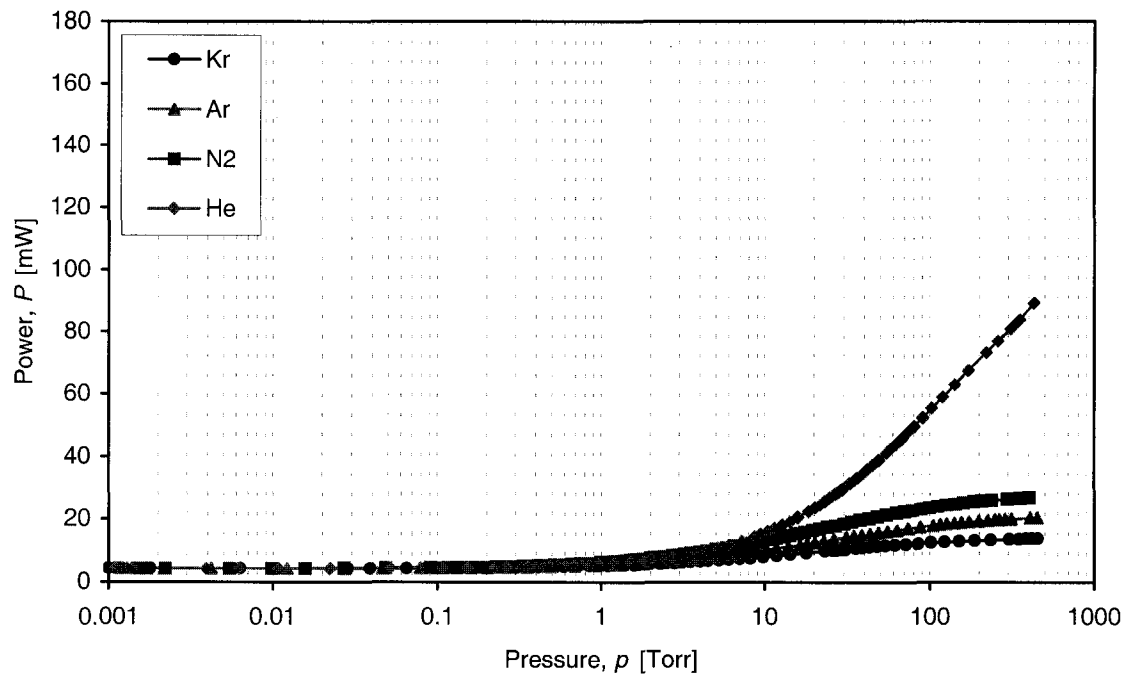
Figure 5.32 Power versus pressure for small square device 1 residing on die 5 at 5 μA response, DC source in various gases.
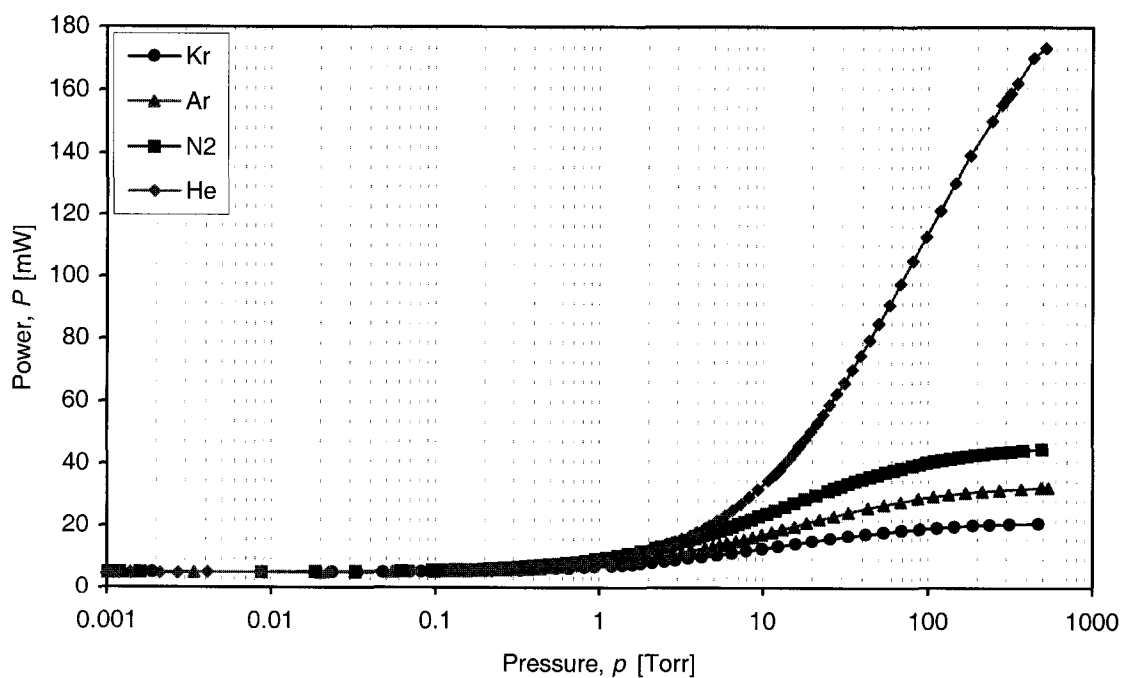
Figure 5.33 Power versus pressure for large square device 6 residing on die 5 at 5 μA response, DC source in various gases.
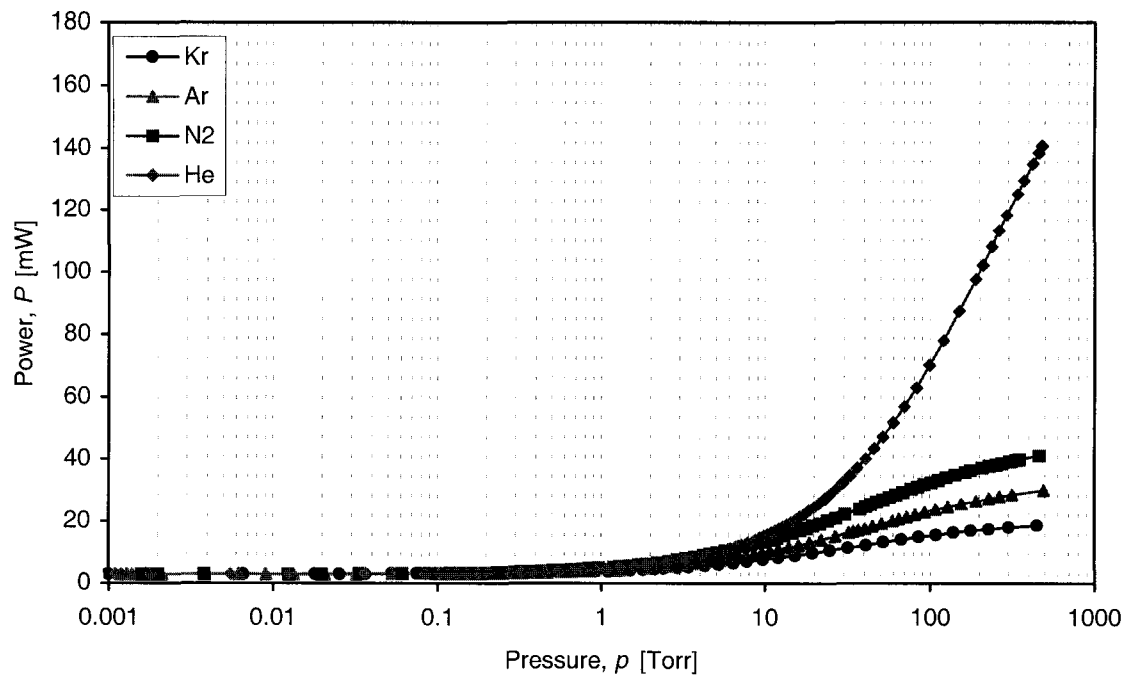
Figure 5.34 Power versus pressure for single bridge device 11 residing on die 5 at 5 μA response, DC source in various gases.
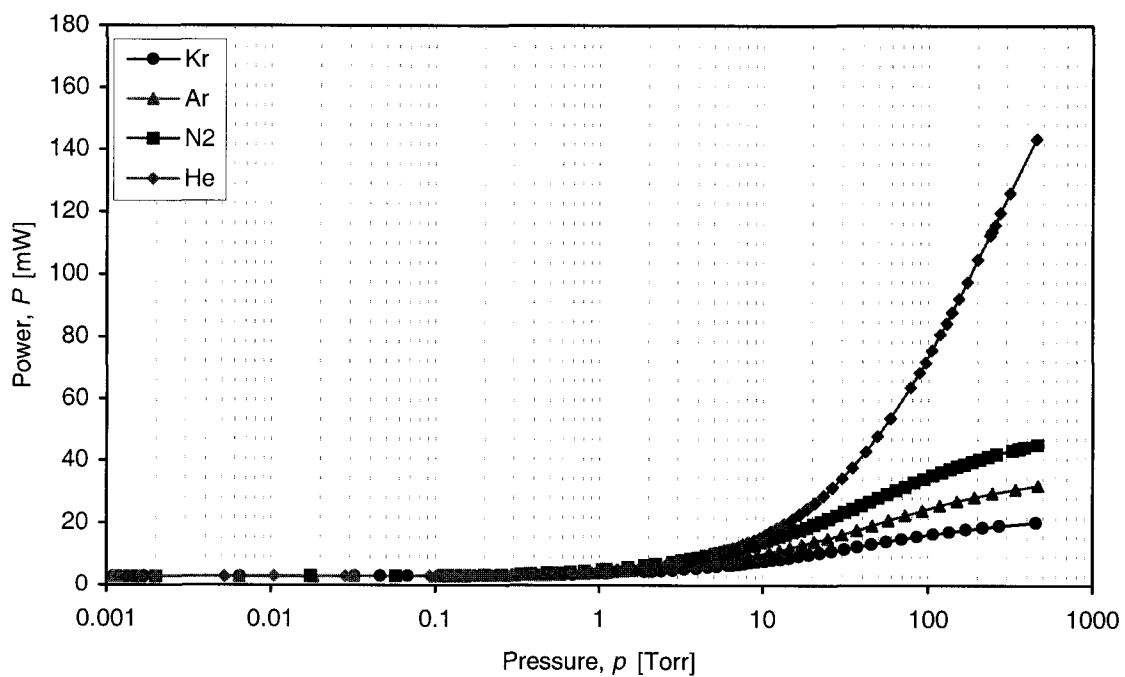
Figure 5.35 Power versus pressure for double bridge device 14 residing on die 5 at 5 μA response, DC source in various gases.
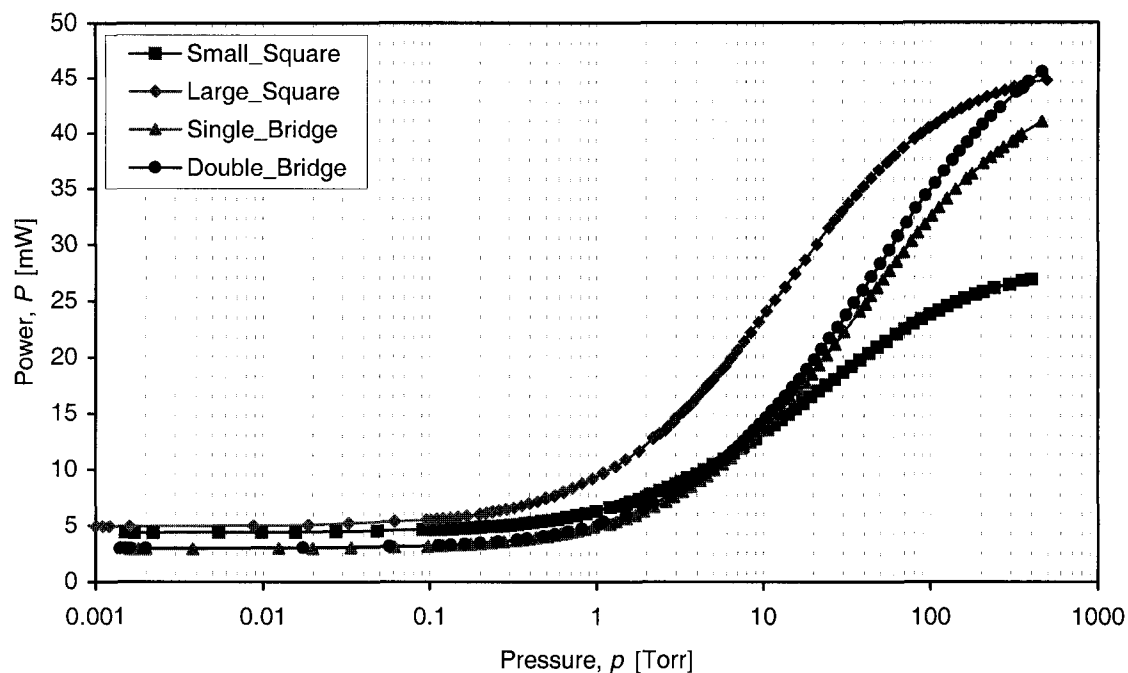
Figure 5.36 Power versus pressure for each device type residing on die 5 at 5 μA response, DC source in nitrogen.

5.5.2.2 Alternating Current Source

As with the constant power alternating current source testing, the constant response code was modified to produce a current pulse of 120 ms, with a period of 150 ms. Testing with the same four devices used throughout the previous tests was performed with the modified response code while maintaining a constant detector response of 5 μA in the four gases of interest. Plots of power versus pressure for the single square, large square, single bridge, and double bridge devices are shown in Figures 5.37 to 5.40. Consistent with the DC source results of Section 5.5.2.1, the order of curve appearance for each gas is maintained along with the 3 Torr, He-N_2 crossover point. Also, as in the previous section, a plot of each device in nitrogen was generated for comparison and is shown in Figure 5.41. The behaviour depicted in Figure 5.41 is of the same shape as that described by the DC source results of Figure 5.36.

Finally, a comparison between the AC and DC sourced results for each device in nitrogen is shown in Figure 5.42. The figure depicts no significant difference in power required to maintain a constant detector response between the same device operated by

AC or DC sourcing. As stated earlier, any differences in the figure are attributed to device repeatability variation. Like the constant power AC and DC comparisons, utilizing an AC source provides the advantages of a marginal approximate 30% reduction in power consumption and the ability to observe transient behaviour, and the disadvantage of a long system response time. As with the constant power AC results, the reduction in power consumption is more than 20% (suggested by the duty cycle) since the power dissipated in the device does not follow a step-wise function.
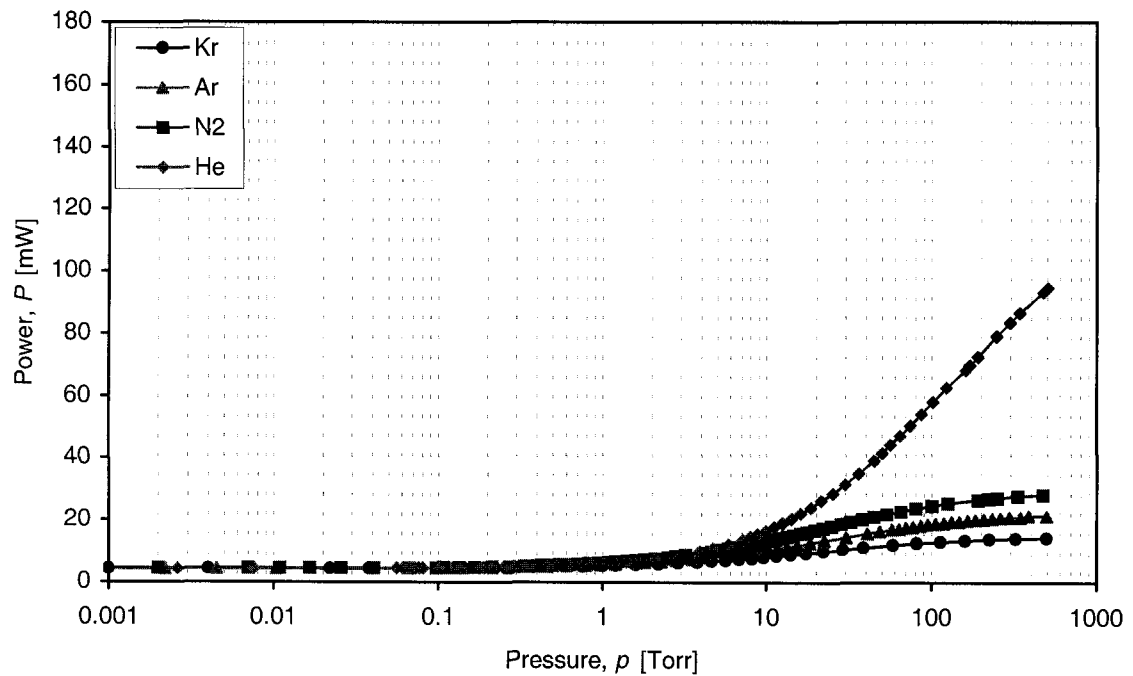
Figure 5.37 Power versus pressure for small square device 1 residing on die 5 at 5 μA response, AC source in various gases.
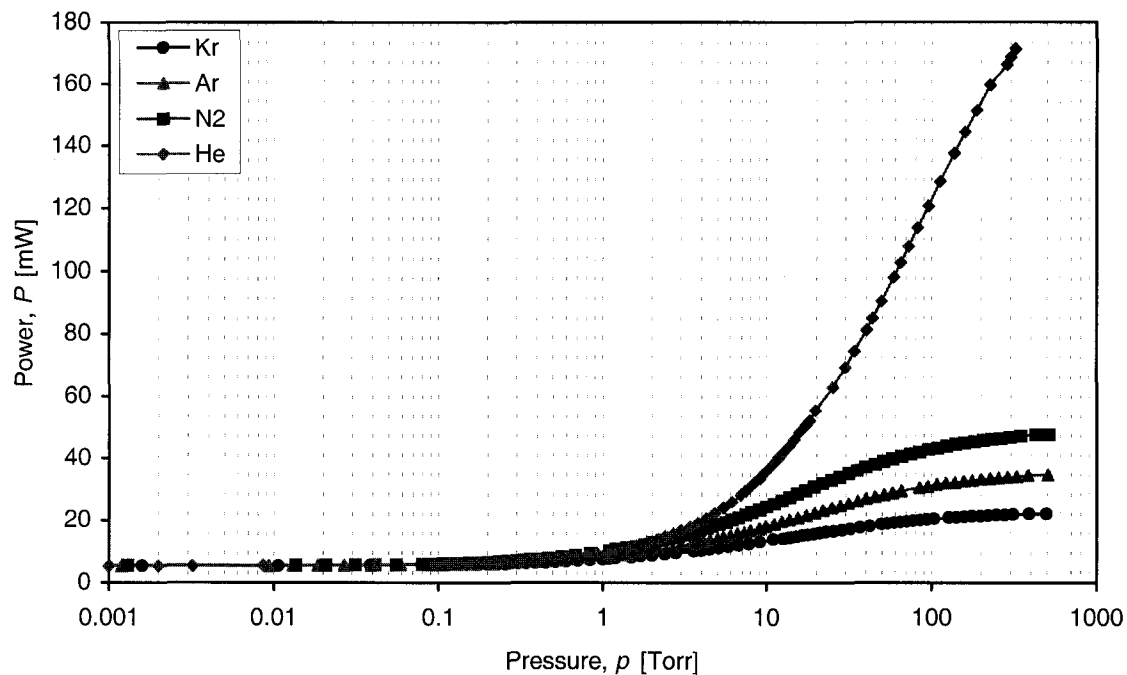
Figure 5.38 Power versus pressure for large square device 6 residing on die 5 at 5 μA response, AC source in various gases.
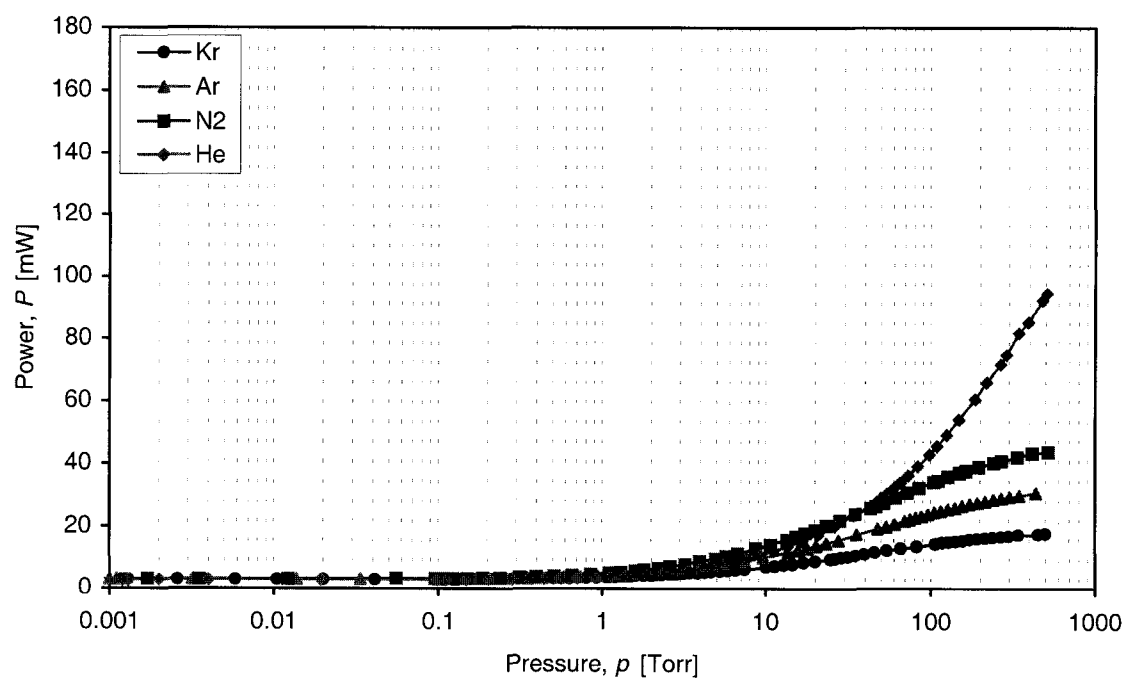
Figure 5.39 Power versus pressure for single bridge device 11 residing on die 5 at 5 μA response, AC source in various gases.
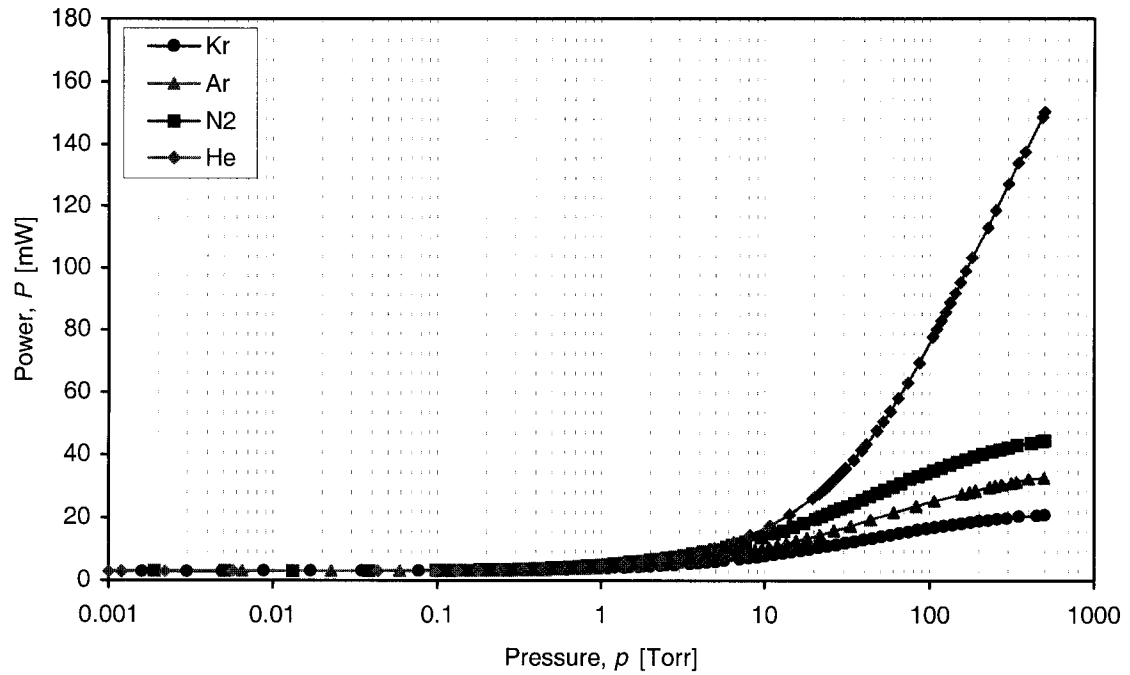
Figure 5.40 Power versus pressure for double bridge device 14 residing on die 5 at 5 μA response, AC source in various gases.
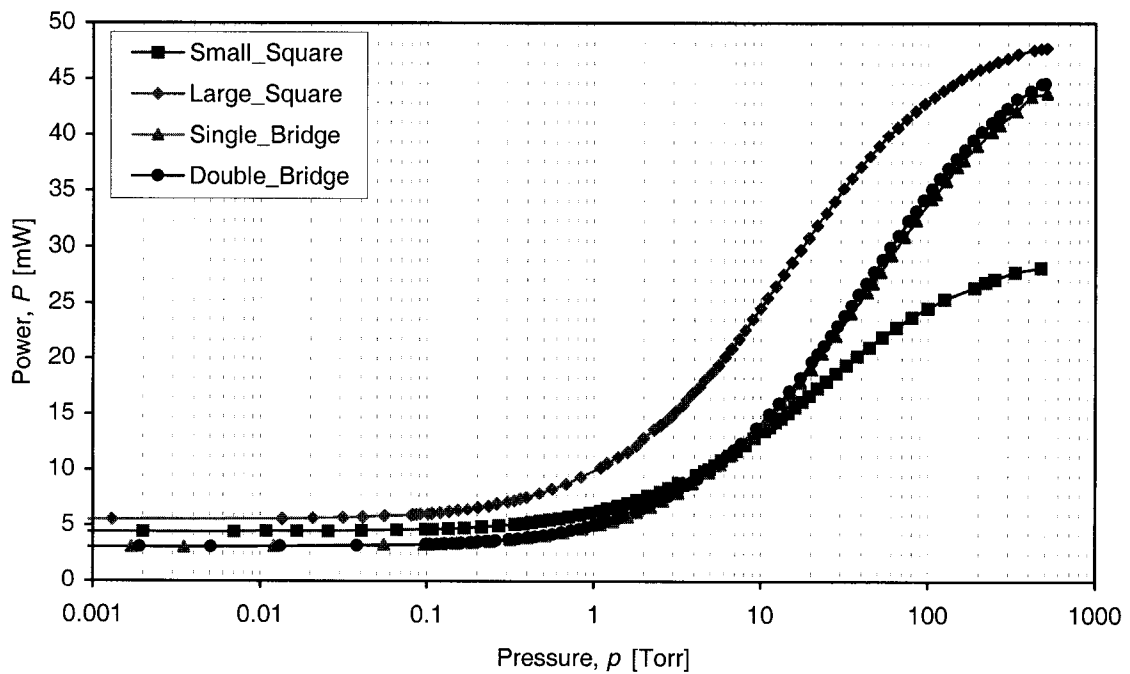
Figure 5.41 Power versus pressure for each device type residing on die 5 at 5 μA response, AC source in nitrogen.
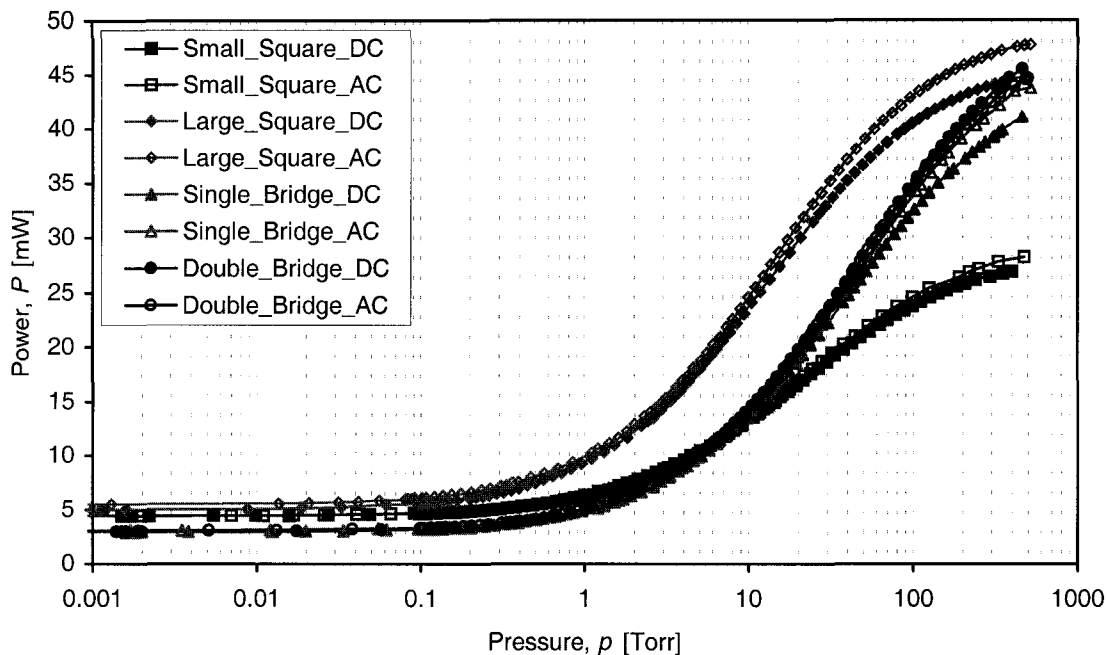
Figure 5.42 Power versus pressure for comparison between AC and DC sourced detector response for all device-types on die 5 at 5 μA in nitrogen.

5.5.3 Transient Response

To measure the device transient response for variations in pressure and gas, a small square device was operated under 8 mW constant power with AC source. The voltage across the polysilicon element and the photodetector response were output to an HP 54600A digital oscilloscope and the waveform captured to computer via an RS-232 communication bus. An example of this waveform was displayed previously in Figure 5.24. Waveforms were captured at a pressure of 700, 100, 50, 20, 10, 5, and 3 Torr each in N_2, Ar, Kr, and He. Pressure below 3 Torr was not measured due to concerns over exceeding the maximum safe detector response and thus destroying the devices.

A plot of the polysilicon resistance rise-time, τ_R, is shown in Figure 5.43. As pressure decreases the polysilicon rise-time increases. At 10 Torr, the lowest pressure at which a rise-time for all four gases was obtained, the longest measured time occurring in krypton, followed by argon, nitrogen, and lastly, helium. It is observed in the figure that at each pressure, the individual gases have a different polysilicon resistance rise-time, with the difference increasing as the pressure decreases, noting that the helium and

nitrogen rise-times converge at approximately 3 Torr, the crossover pressure for the previous results. It is believed that at lower pressure, the difference between the helium and nitrogen rise-times will increase. This belief is based on the change in thermal conductivity of the gases with pressure as described later in Section 6.3.2.2 of Chapter 6.
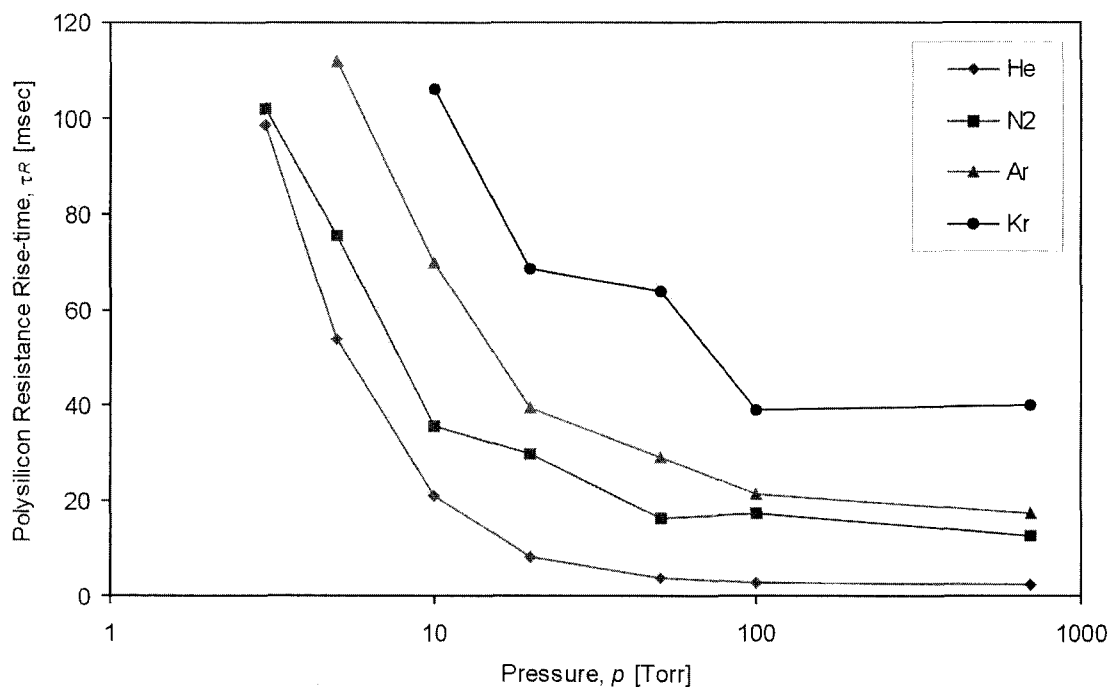
Figure 5.43 Polysilicon resistance rise-time versus pressure in various gases.

Measured at each pressure and for each gas were the rise- and fall-times (in milliseconds) of the photodetector signal, τ'_{V_d} and τ_{V_d}, respectively, the results of which are displayed in Tables 5.1 to 5.4. For each pressure, where possible, the factor, b, in (5.10) was calculated and included in the tables. At each pressure, the polysilicon rise-time was easily measured, while the photodetector rise- and fall-times were not measurable until the pressure was significantly reduced. Rise- and fall-times for the detector would be observed at higher pressures with higher powers; however, no signal would be detected at lower pressures due to the device exceeding the set maximum safe detector signal. As a result, it is likely that only a few data points would be gathered for the detector signal no matter what power was used. Since the number of detector data points was limited, no significant meaning is associated to the factor, b, and measuring

the change in detector rise-and fall-time is not an effective means of detecting a gas with the present setup. Construction of a faster AC current source and feedback circuitry would likely allow for a more detailed investigation of the device radiative response times.

Table 5.1 Transient rise- and fall-times for nitrogen.

Pressure, p [Torr]	Polysilicon resistance rise-time, τ_R [ms]	Photodetector rise-time, τ'_{V_d} [ms]	Photodetector fall-time, τ_{V_d} [ms]	b [ms^{-1}]
700	12.4	-	-	-
100	17.4	-	-	-
50	16.2	-	-	-
20	29.8	-	-	-
10	35.6	-	-	-
5	75.8	104	4.8	5.10
3	102.0	117	9.6	1.52

Table 5.2 Transient rise- and fall-times for argon.

Pressure, p [Torr]	Polysilicon resistance rise-time, τ_R [ms]	Photodetector rise-time, τ'_{V_d} [ms]	Photodetector fall-time, τ_{V_d} [ms]	b [ms^{-1}]
700	17.2	-	-	-
100	21.4	-	-	-
50	29.2	-	-	-
20	39.2	-	-	-
10	70.0	111	6.0	3.63
5	112	116	10	1.38
3	-	-	-	-

Table 5.3 Transient rise- and fall-times for krypton.

Pressure, p [Torr]	Polysilicon resistance rise-time, τ_R [ms]	Photodetector rise-time, τ'_{V_d} [ms]	Photodetector fall-time, τ_{V_d} [ms]	b [ms^{-1}]
700	40.0	-	-	-
100	38.8	-	-	-
50	64.0	74.8	5.0	3.48
20	68.6	109	6.2	3.37
10	106	115	9.8	1.43
5	-	-	-	-
3	-	-	-	-

Table 5.4 Transient rise- and fall-times for helium.

Pressure, p [Torr]	Polysilicon resistance rise-time, τ_R [ms]	Photodetector rise-time, τ'_{V_d} [ms]	Photodetector fall-time, τ_{V_d} [ms]	b [ms^{-1}]
700	2.4	-	-	-
100	2.8	-	-	-
50	3.6	-	-	-
20	8.0	-	-	-
10	21.0	-	-	-
5	53.8	74.0	4.0	5.34
3	98.6	113	8.2	1.97

5.6 CHARACTERISTIC DIMENSION

The characteristic dimension of a thermal-conductivity-type gauge will affect the upper limit of the pressure-sensitive range. As described previously in Chapter 3, decreasing the characteristic dimension results in an increase in the pressure at which conductive heat loss to the surrounding gas molecules becomes the dominant heat transfer mechanism. For this project, the distance between the polysilicon/silicon dioxide platform and the bottom of the silicon etched pit is considered the characteristic dimension.

To measure the effect of varying the etch depth or characteristic dimension, a single, unetched small square device was utilized. Initially, the die containing the device under test was subjected to a 20 second etch by 10:1 BOE to remove any native silicon dioxide layer. Next, a constant power run at 8 mW with DC source was conducted from 700 to 0.1 Torr, after which the die was etched by XeF$_2$ for 4 minutes, and the etch depth and undercut measured. Another constant power run at 8 mW was then conducted. At this point the device was etched for an additional minute bringing the total etch time to 5 minutes, the etch depth and undercut measured, and a constant power run at 8 mW performed. This process of etching for 1 minute, measuring the etch depth and undercut, and performing a constant power run at 8 mW was repeated until the device had experienced a total of 8 minutes of etching. Also, at the end of 6, 7, and 8 minutes of etching, a constant response run at 5 μA was also performed over the same pressure range as that for the constant power runs. Table 5.5 lists the measured etch depth, undercut, and the status of device release at each etching instance (the reader is referred

to Figures 4.7 or 4.8 in Chapter 4, depicting XeF_2 etch characteristics and undercut). Plots of the detector current versus pressure and power versus pressure for each etching instance are shown in Figures 5.44 and 5.45, respectively. The figures show that increasing the etch depth leads to an increase in mean device temperature and thus larger responses.

Table 5.5 Device etch depth, undercut, and release status for each etching interval.

Etch time [min]	Etch depth ±2.5 [μm]	Undercut ±5 [μm]	Device released?	Maximum photo-detector response [μA]
0	0	0	No	0.012
4	37	~ 40	No	0.007
5	48	~ 50	No, almost	0.021
6	62	~ 60	Yes	8.193
7	72	~ 70	Yes	8.850
8	77	~ 80	Yes	9.326
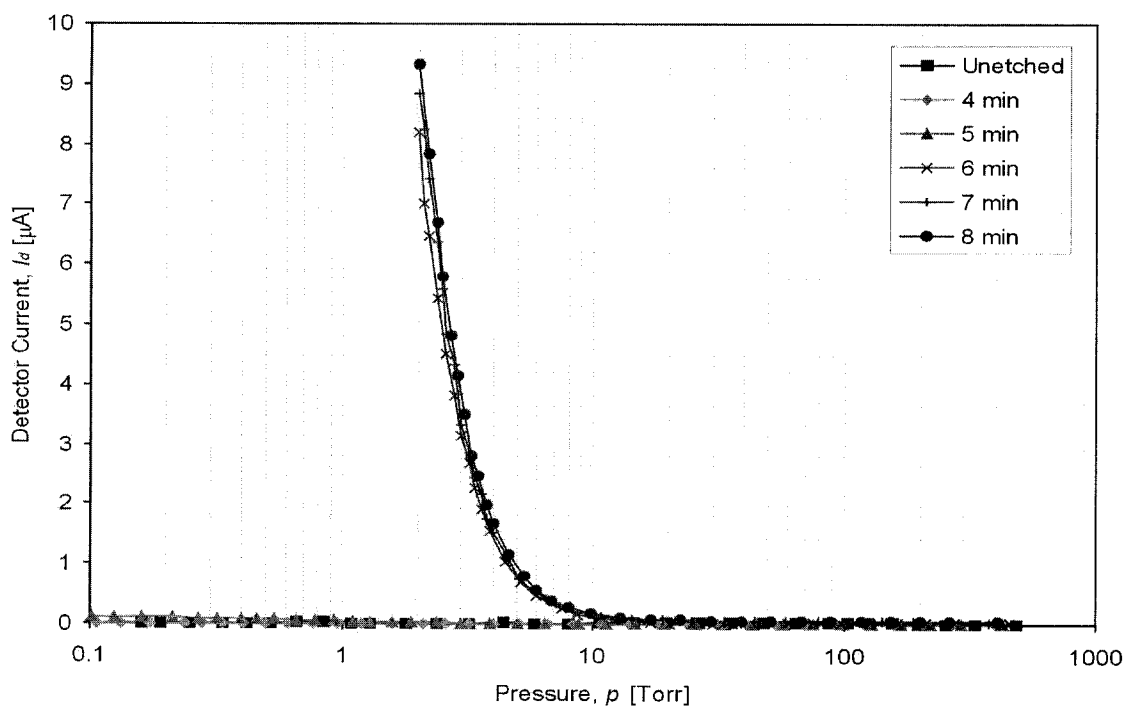
Figure 5.44 Detector current versus pressure for a small square device under 8 mW constant power in nitrogen for various etching times.
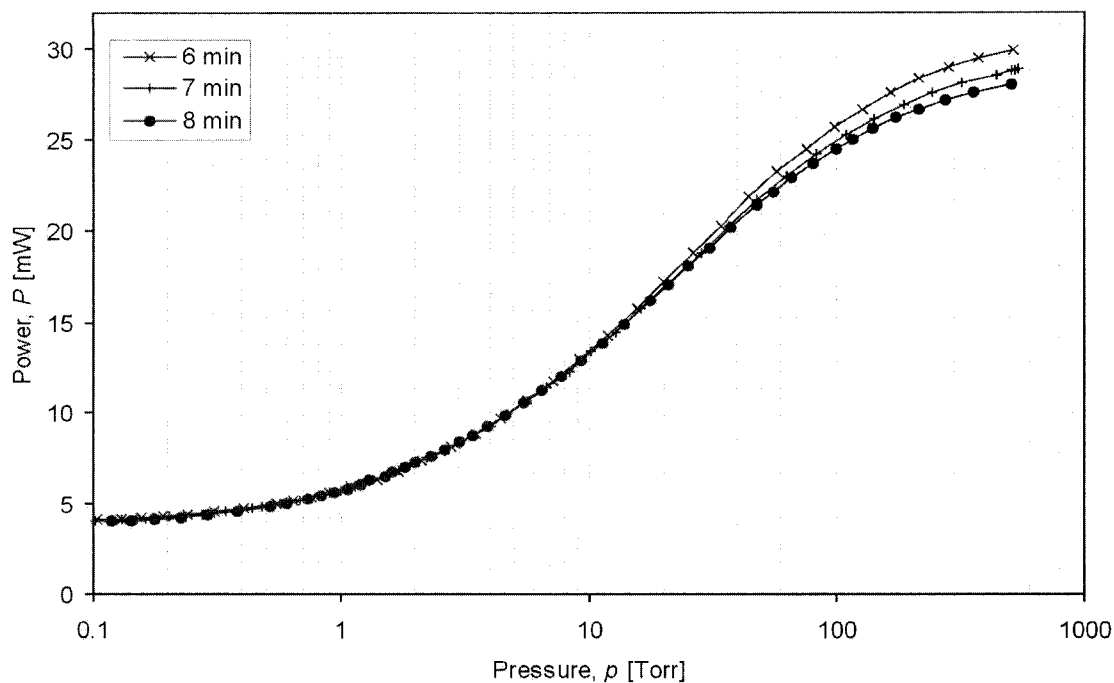
Figure 5.45 Power versus pressure for a small square device under 5 μA constant detector response in nitrogen for various etching times.

Figure 5.44 shows that until the device is released, there is essentially no change in detector signal with pressure. After release, the detector response varies with pressure in a manner consistent with previous results from released devices, but shows no appreciable difference in response as the etch depth is increased. This is likely due to the small percentage change in the etched cavity volume between the three released etch times, a result of the significant undercutting required to achieve device release initially. The difference in response between etch times would be more pronounced, for example, if it was possible to achieve device release with only a 10 μm etch depth. Figure 5.45 shows that as the etch depth increases the amount of power required to maintain a constant detector response of 5 μA decreases. This effect, albeit not as dramatic as hoped for, produces results consistent with those expected from physical considerations.

The effect of the etch depth is more readily seen in Figure 5.46, a plot of detector current and power versus etch depth, taken from the data of Figures 5.44 and 5.45. The figure shows that at 2 Torr and under a constant power of 8 mW, as the etch depth increases the detector response also increases. The figure also shows that at 508 Torr, as

the etch depth increases, the amount of power required to maintain a constant response of 5 μA decreases. These results agree when considering the etch depth to be related to conductive heat transfer through the gas between the substrate and the heated platform. As the density (pressure) of the gas decreases, the effective heat transfer decreases, resulting in an increase in mean device temperature – which is the manner in which the micro-Pirani gauges are designed to operate.
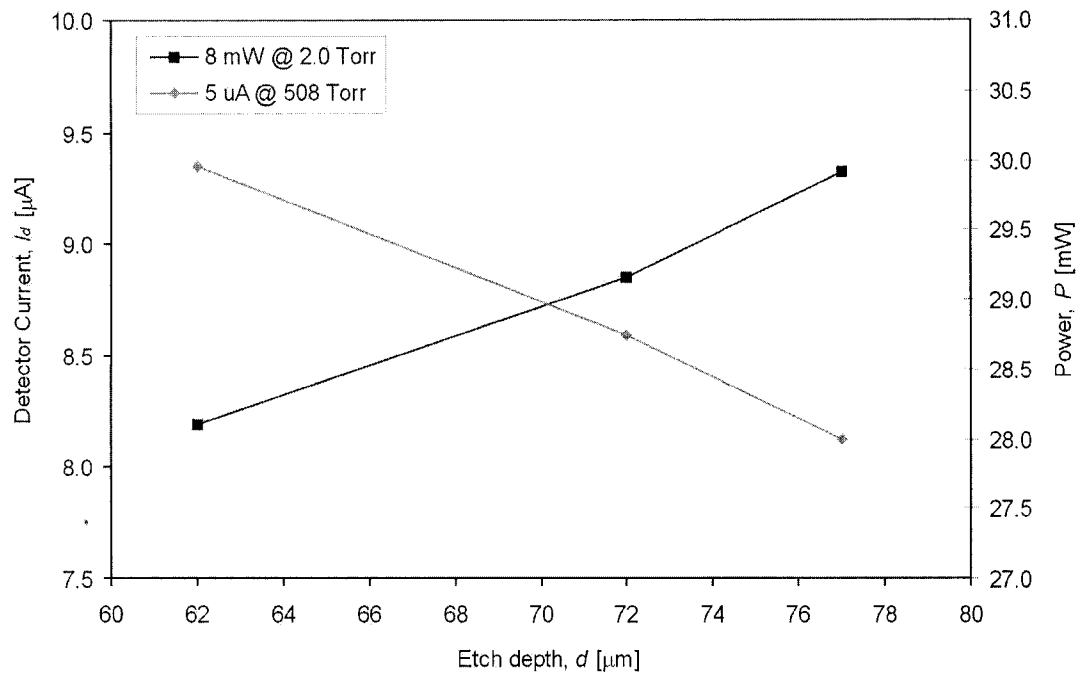
Figure 5.46 Detector current versus etch depth for a small square device for both constant power and constant response modes in nitrogen.

5.7 SUMMARY

The results obtained from testing various post-processed micro-Pirani sensors have been presented. These sensors were tested for application as both vacuum sensors and in the detection of various gases. A description of the apparatus used and procedures followed have been discussed. The devices were tested for constant power and constant response modes of operation when sourcing first direct current and then alternating (pulsed) current.

Varying the power dissipated in the devices allows for the measuring of vacuum, as does maintaining a constant detector response. At a given power or detector response, each of the gases tested displayed a distinguishable response. Low device durability was observed when operating the devices in a manner that produced a photodetector response in excess of 10 μA. Testing in one of the gases, SF_6, was halted after it was observed that devices failed during or shortly after testing in a SF_6 environment. Comparisons between the four device geometries used and between the responses for AC and DC sources were investigated, the results showing that all devices displayed similar trends, and no significant difference was observed between the AC and DC source results.

Lastly, an examination of the transient response as a function of pressure and gas, as well as the effect of varying the etch depth (characteristic dimension) on device response were completed. Testing indicates that measuring the time for the polysilicon resistor to reach steady-state can be used to distinguish the constituent gas and the system pressure. Increasing the characteristic dimension leads to a higher device response with little change in the pressure observed at which the response occurs, the change in pressure suggested by Figure 3.2.

In the next chapter, a heat transfer model describing the operation of the micro-Pirani devices and finite element simulations are presented. A comparison between the experimental results compiled and the results of finite element simulation are also included.

DEVICE MODELING

6.1 INTRODUCTION

In order to maximize the sensitivity of the micro-Pirani devices to variations in the surrounding gas medium an understanding of the heat transfer mechanisms present during device operation is required. Such an understanding allows for the development of a mathematical model to both explain and predict device behaviour.

This chapter expands upon the heat transfer principles introduced in Chapter 3 by adapting these principles to the operation of the micro-Pirani gauges investigated, and presents an electro-thermal model describing device behaviour. A solution to the electro-thermal model is obtained by numerical modeling using the finite element method. Finally, numerical modeling results are compared to experimental results and the validity of the electro-thermal model is established.

6.2 ELECTRO-THERMAL MODEL

When electrical power, P, is dissipated into the micro-Pirani device, the temperature of the structure increases. Since the device is thermally isolated from the substrate, a modest input power will result in a temperature increase of several hundred degrees relative to the substrate. The degree of thermal isolation, and hence heating, for a given input power results from the separation of the device from the substrate, referred to as the characteristic dimension, d, and varies as a function of the density, thermal conductivity, and specific heat of the gas medium surrounding the structure.

Representing a simplified micro-Pirani gauge platform as a differential volume, $\Delta v = \Delta x \Delta y \Delta z$, as shown in Figure 6.1 at a distance, d, above the substrate, the net rate of heat transfer is expressed as

$$H_{total} = P + \sum_{i=1}^{N} H_i , \qquad\qquad (6.1)$$

where H_{total} is the net rate of change of the internal energy of the platform in Watts, P [W] is the electric power dissipated inside the platform, and H_i [W] are the heat gain or loss mechanisms acting on the differential volume. In the figure, the substrate temperature is represented by T_{Si} [K], the gas medium temperature by T_f [K], and the mean temperature of the element by $\bar{T}$ [K]. For this case, we assume $\bar{T} > T_{Si}$ and $\bar{T} > T_f$.
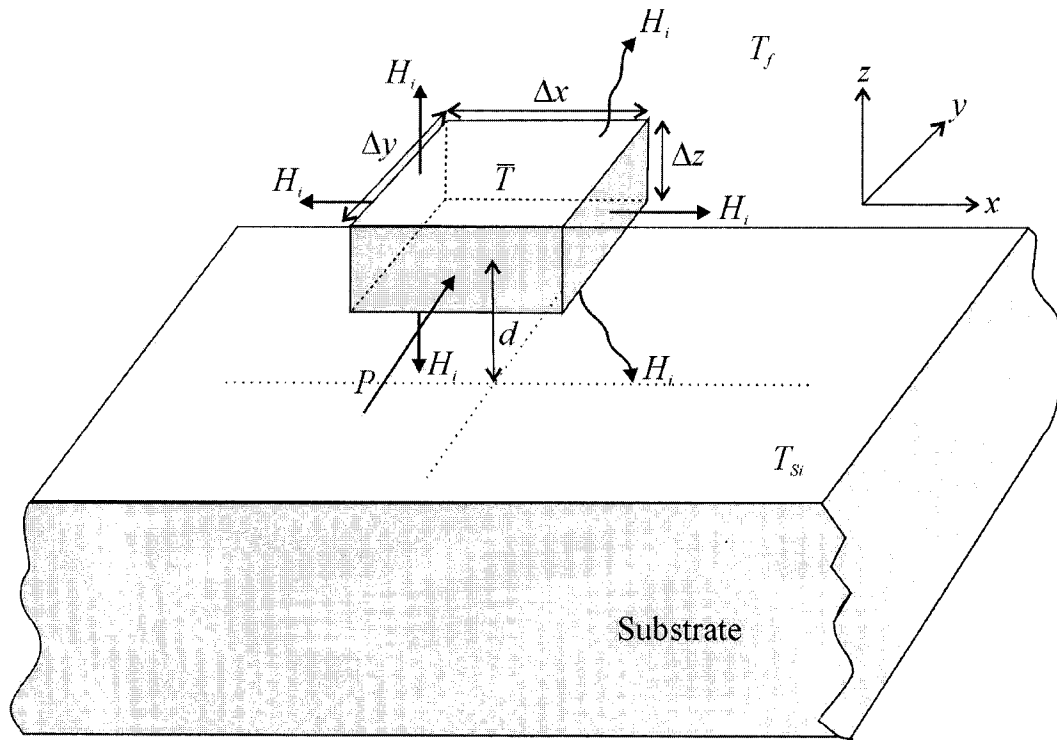
Figure 6.1 Micro-Pirani gauge platform of differential volume, $\Delta v = \Delta x \Delta y \Delta z$.

In terms of the applicable modes of heat transfer (convection is ignored for the reasons presented in Chapter 3), (6.1) can be expanded to

$$H_{total} = P + H_{\substack{conduction \\ thru\,arms}} + H_{\substack{conduction \\ thru\,medium}} + H_{radiation} . \qquad\qquad (6.2)$$

The conductive heat loss through the arms, $H_{\substack{conduction \\ thru\,arms}}$, occurs from the sides of the platform through the length of the arms, which are attached to the substrate at their ends in the y-direction (not shown in Figure 6.1). Assuming heat loss from two sides, representing the two support arms in the actual devices, and assuming the etched cavity is without undercutting, leads to the expression:

$$H_{\substack{conduction \\ thru\,arms}} = -2 \cdot k_1(T)\frac{\Delta x \Delta z}{y}(\overline{T} - T_{Si}),\qquad(6.3)$$

where $k_1(T)$ [W·m^{-1}K^{-1}] is the temperature-dependent thermal conductivity of the arm material, and y [m] is the length of the support arm. Equation (6.3) also assumes equal temperature gradients along the support arms in the positive and negative y-directions.

In terms of conductive heat loss through the gas medium, $H_{\substack{conduction \\ thru\,medium}}$, the actual physical process is very complex and has been discussed rigorously in [6, 12, 20]. In essence, only conductive heat loss to the substrate from the lower surface of the platform need be considered. This is based on the assumption that the characteristic dimension, or etch depth, is much less than the dimensions of the surrounding environment, in this case the vacuum test chamber. The expression then for this form of heat loss is

$$H_{\substack{conduction \\ thru\,medium}} = -k_g(p)\frac{\Delta x \Delta y}{d}(\overline{T} - T_{Si}),\qquad(6.4)$$

observing that the gas thermal conductivity, k_g [W·m^{-1}K^{-1}], is assumed dependent only on the pressure of the gas, as defined previously in (3.9) and (3.10).

The radiation heat loss, $H_{radiation}$, from the platform is present at the upper and lower surfaces and the edges of the platform not attached to the substrate. For the purposes of this model, only radiation loss from the upper and lower surfaces is considered. The equation describing the radiative heat loss is thus (assuming constant emissivity, ε):

$$H_{radiation} = -\varepsilon\sigma\Delta x\Delta y(\overline{T}^4 - T_f^4) - \varepsilon\sigma\Delta x\Delta y(\overline{T}^4 - T_{Si}^4)$$
$$= -2 \cdot \varepsilon\sigma\Delta x\Delta y(\overline{T}^4 - T_{Si}^4) \qquad (6.5)$$

where the temperature of the gas far from the platform is considered to be equal to that of the substrate, that is, $T_f = T_{Si}$.

Lastly, the net rate of change of the internal energy of the platform, H_{total}, can be expressed as

$$H_{total} = \rho_m c_p \Delta x\Delta y\Delta z \frac{\partial \overline{T}}{\partial t}, \qquad (6.6)$$

where the variables presented have their typical meaning as defined in Chapter 3. Substituting (6.3) through (6.6) into (6.2) produces the complete heat balance equation for a differential volume as follows:

$$P - 2k_1(T)\frac{\Delta x\Delta z}{y}(\overline{T} - T_{Si}) - k_g(p)\frac{\Delta x\Delta y}{d}(\overline{T} - T_{Si}) - 2\varepsilon\sigma\Delta x\Delta y(\overline{T}^4 - T_{Si}^4)$$
$$= \rho_m c_p \Delta x\Delta y\Delta z \frac{\partial \overline{T}}{\partial t}. \qquad (6.7)$$

At steady-state, the right-hand-side of (6.7) equals zero and the power input, P, then equals the three heat loss terms:

$$P = 2k_1(T)\frac{\Delta x\Delta z}{y}(\overline{T} - T_{Si}) + k_g(p)\frac{\Delta x\Delta y}{d}(\overline{T} - T_{Si}) + 2\varepsilon\sigma\Delta x\Delta y(\overline{T}^4 - T_{Si}^4). \qquad (6.8)$$

Applying the general platform model as described by (6.7) to the square and bridge geometries results in (6.9). The differential thickness, Δz, is replaced by z, the thickness of the combined process layers, 3.9 μm, and the etch depth, d, set to 85 μm, that of the post-processed die 5 which was used for the bulk of testing. The substrate temperature, T_{Si}, is assumed equal to room temperature, 293 K. The variable W_{arm}

represents the width of the supporting arms (21.5 and 32 μm for the small and large squares, respectively and 31 μm for both bridges), while the length of each supporting arm is represented by the variable L_{arm} (69 and 71 μm for the small and large squares respectively, and 76 μm for both bridges). The area of the suspended platform is represented by $A_{platform}$ (14 400 μm^2 for the small square, 48 400 μm^2 for the large square, and 11 466 μm^2 for the bridges).

$$P - 2k_1(T)\frac{W_{arm} \cdot z}{L_{arm}}(\overline{T} - T_{Si}) - k_g(p)\frac{A_{platform}}{d}(\overline{T} - T_{Si}) - 2\varepsilon\sigma A_{platform}(\overline{T}^4 - T_{Si}^4)$$
$$= \rho_m c_p A_{platform} \cdot z \frac{\partial \overline{T}}{\partial t},$$

$$\tag{6.9}$$

The analytical solution to (6.9) is difficult to obtain. One experimentally derived relation that ignores convection and radiation heat losses has been presented in [18]. The calculation describes the time-varying average device temperature as the exponential function

$$\frac{\partial \overline{T}}{\partial t} \propto (1 - e^{-t/\tau}),$$

$$\tag{6.10}$$

with a time constant, τ [ms], that is a function of the surrounding gas pressure. Measurements of the time constant showed a value of approximately 30 ms at 10^{-4} Torr and approximately 15 ms at one atmosphere in nitrogen [15].

A solution to the steady-state form of (6.9) has been obtained by using Matlab™ (the relevant source code is contained in Appendix D). Figure 6.2 shows the mean temperature versus pressure plot created by the Matlab program for a small square device operated at 8 and 12 mW in nitrogen and in helium. The figure shows that above 100 Torr the mean steady-state temperature is approximately independent of pressure. As the pressure decreases the temperature of the device increases, becoming nearly linear as a logarithmic function of pressure. At pressures below 0.1 Torr, when conduction through the gas becomes negligible (third term in (6.9)), the device temperature has saturated,

becoming independent of pressure. Also, for either power, the helium curves produce lower temperatures (at 1000 Torr) than the nitrogen curves, cross over the nitrogen curves at about 10 Torr, and at the low-pressure saturation, equal the nitrogen temperature at each power.
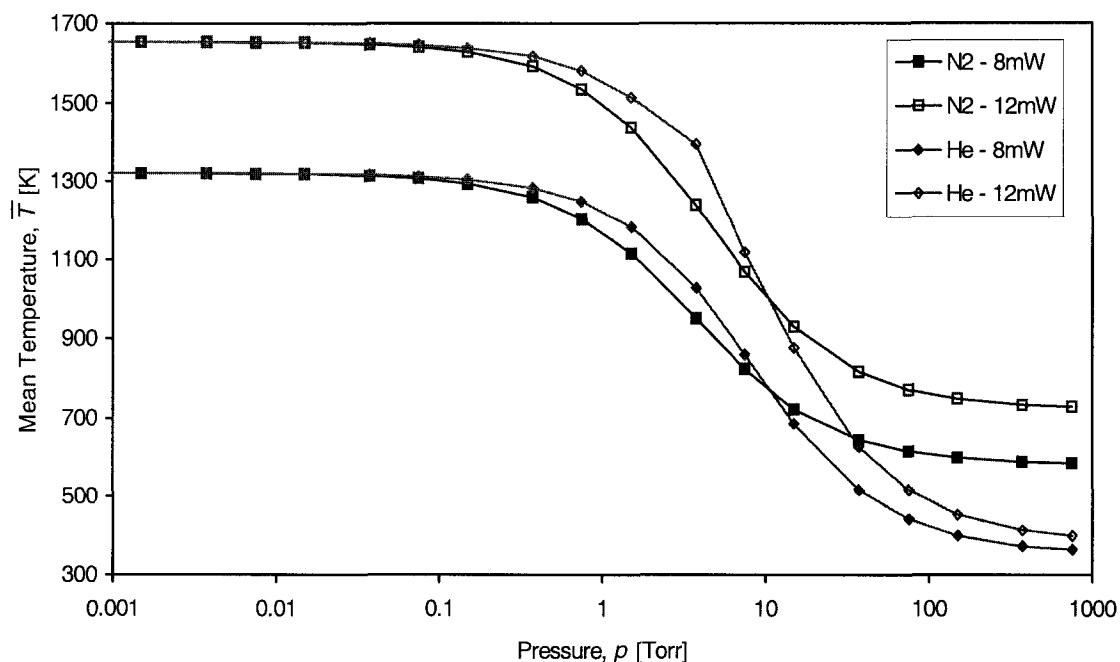
Figure 6.2 Mean device steady-state temperature versus pressure for a small square device under 8 mW and 12 mW in nitrogen and helium.

To obtain a description of the temperature profile across the device and investigate transient effects, a finite element simulation was employed and is described in the next section.

6.3 FINITE ELEMENT SIMULATION

Finite element modeling (FEM) is a numerical method of solving complex engineering and physical problems for which there often exists no closed-form analytical solution. Such problems arise in the areas of structural analysis, heat transfer, fluid flow, mass transport, and electromagnetic potential, each involving complicated geometries,

loadings, and/or material properties [98-99].

In the finite element method, a structure is divided into a system of elements interconnected at common points (nodes) in a process called discretization. Each element is described by a set of equations and, upon joining to build the entire body, contributes to the formulation of a system of simultaneous algebraic equations that describes the total structure. A computer can then be used to find approximate solutions to this set of equations and to extract estimated behaviour for individual elements. The commercial finite element software ANSYS Multiphysics 6.1™ was employed for thermal analysis of the microstructures and was made available by Swanson Software and the Mechanical Engineering Department at the University of Alberta [100, 101].

Performing a numerical simulation requires three fundamental steps. The first part consists of building the model. This includes defining the device geometry, choosing a suitable element, defining material properties, meshing or discretizing the model, and applying any additional nodes and elements. The application of additional nodes and elements is sometimes necessary as the computer-generated mesh is not always satisfactory and may need to be modified to properly describe the structure. Once the model is built, the second part involves applying constraints and loads, and solving the model. Solving the model consists of explicitly instructing the software to solve the set of simultaneous equations that define the model. The process is an iterative one in which the software will find solutions for the equations using the sparse matrix direct method and check for uniqueness of solution. The final part includes displaying and interpreting results, and refining model parameters as required. This last step is considered the most important aspect of the analysis, because the researcher is trying to understand how the applied loads affect the design and determine the accuracy of the finite element mesh.

6.3.1 Model Geometry

A three-dimensional model was initially generated for this work; this model was constructed in a manner similar to that in [20]. Preliminary models were intended to account for radiative heat transfer, provide a better approximation for the conductive heat loss to the gas, and include non-constant material properties that vary with temperature.

However, after a preliminary building of the model it was discovered that excessive amounts of computer memory, hard-drive space, and computational time would be required for the three-dimensional model. For example, obtaining a single temperature distribution at a given power and pressure for a particular gas required upwards of 10 minutes of processor time and over 100 MB of disk space. Therefore, it was decided that a two-dimensional model would be more feasible if radiation was to be accounted for.

The geometry of the two-dimensional model, as generated by the software, for the small square geometry is shown in Figure 6.3. From the figure, the device platform, support arms, and polysilicon trace can be seen along the diagonal from the upper right corner to the lower left corner. Surrounding the device platform and support arms is the open region occupied by the surrounding gas. Similar geometries for each of the other three device types (large square, single bridge, and double bridge) were also generated; the model source code for all geometries are contained in Appendix E.
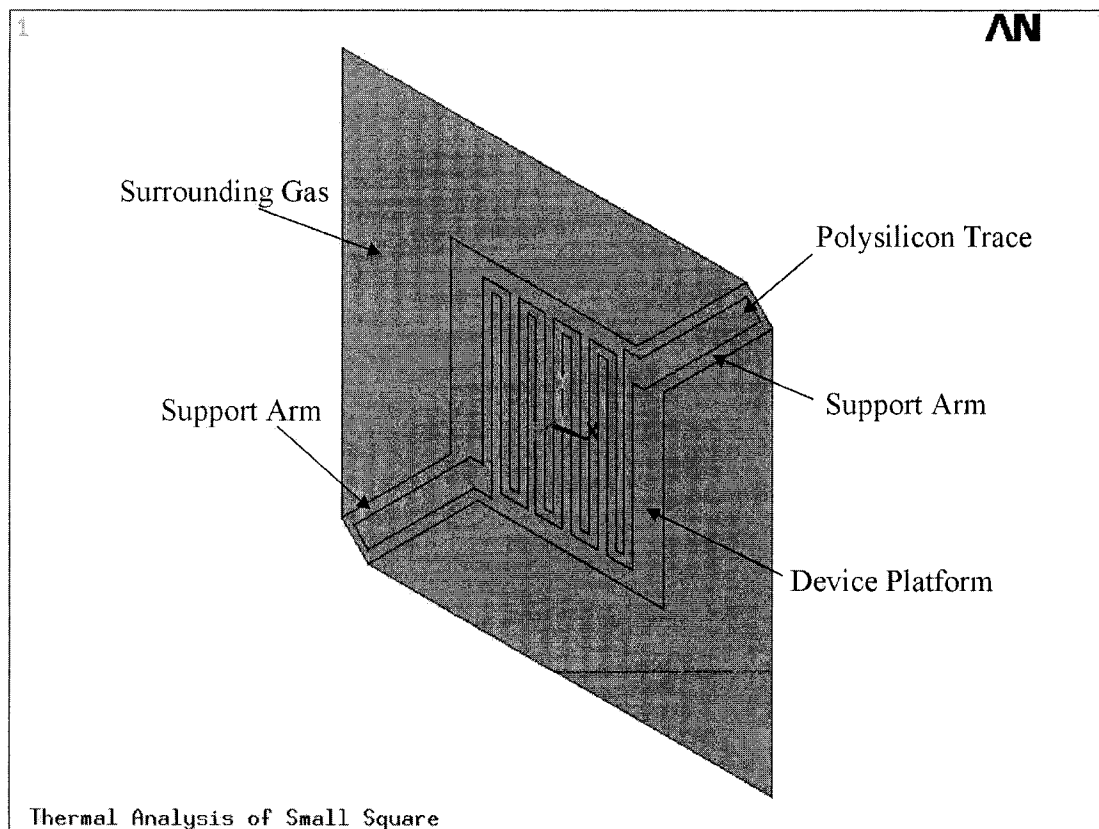
Figure 6.3 Isometric view of a two-dimensional model of a small square device.

6.3.2 Material and Gas Properties

The next step in the model building process is to specify material properties. Material properties are constrained by the software to be either constants or polynomial functions not exceeding the fourth order. Careful research must be done and due consideration given to material properties in the building of a finite element model. Justification for using constant material property values must be presented and appropriate conversions done if simulating three-dimensional effects with a two-dimensional model.

To conduct a thermal analysis, the material properties required include thermal conductivity, mass density, and specific heat, each defined as functions of temperature only. For a steady-state analysis, only the thermal conductivity is required, whereas all three material properties are required for a transient analysis. Table 6.1 lists the thermal properties for various materials used in the building of the model at standard temperature and pressure, 298 K and one atmosphere [79, 102].

Table 6.1 Selected thermo-physical material and gas properties [79, 102]*.

Material	Mass density ρ_m [kg·m⁻³]	Specific heat c_p [J·kg⁻¹K⁻¹]	Thermal conductivity k_1 [W·m⁻¹K⁻¹]
Si	2330	712	148.0
SiO$_2$	2198	745	1.4
Si$_3$N$_4$	2400	691	14.5
Al	2700	903	237.0
Polysilicon	2320	700	34.0
Air	1.137	1007	0.0263
N$_2$	1.138	1041	0.0259
He	0.163	5193	0.152
Ar	1.623	5200	0.01772
Kr	3.404	2480	0.00943
SF$_6$	5.934	665	0.0013

* Values at standard temperature and pressure: 298K, 1 atm.

6.3.2.1 Properties of Solids

The thermo-physical properties listed in Table 6.1 are dependent on both temperature and pressure. For the solid materials used in the construction of the devices, the pressure dependence can be ignored since matter in solid form is considered incompressible for pressures less than many atmospheres. Similarly, it has been common

practice to ignore temperature-induced changes since the effects tend to be small; however, the thermal properties of polysilicon should not be ignored since an increase of only 100 K leads to a 11.3% increase in electrical resistance due to the non-zero TCR, and there is a coupling between electrical conductivity and thermal conductivity.

The manner of the coupling between electrical resistance and thermal conductivity is known as the Wiedemann-Franz law [100] which states that the ratio of thermal conductivity, k_1, to electrical conductivity, g_1, is equal to a constant, L_1, known as the Lorenz number, multiplied by the temperature, T:

$$\frac{k_1}{g_1} = \frac{\pi^2 k^2}{3e^2} T = L_1 T ,$$

(6.11)

where k is the Boltzmann constant, e is the electron charge [1.60×10^{-19} C], and $L_1 =$ 2.45×10^{-8} W·Ω/K² for most metals. This law is based on the assumption that the thermal conductivity due to conduction electron mobility is much greater than that due to phonon (sound particle) mobility. This assumption is not always valid and thus deviation from the expected value of L_1 has been observed [103-104]. The Wiedemann-Franz law has also been shown to hold for non-degenerate semiconductors [103], that is, semiconductors in which there is an abundance of free electrons such that the material is prone to conduct electricity in a manner similar to a metal. The abundance of these free electrons is generated by a combination of high temperature, polycrystalline structure, and impurities (doping).

Electrical conductivity is the reciprocal of electrical resistivity, therefore substituting electrical resistivity in terms of the TCR for electrical conductivity in (6.11) produces

$$k_1 = \frac{L_1 T}{\rho_o (1 + \alpha_T (T - T_o))},$$

(6.12)

where the variables have their typical values as presented in Section 4.3.1 of Chapter 4. Using the value of thermal conductivity published by the MITEL Corporation for

polysilicon at 298 K in (6.12) results in a Lorenz number of $L_1 = 5.308 \times 10^{-7}$ W·Ω/K^2, approximately 21 times the value for metals. This suggests that in a semiconductor the thermal conductivity is at least one order of magnitude greater than the electrical conductivity when compared with a metal. A plot of the thermal conductivity versus temperature for each solid material used is shown in Figure 6.4. The data for the non-polysilicon materials is taken from tables [79, 102, 105]. In the figure, two polysilicon (poly) lines are shown - one depicting a zero TCR value and the other the experimentally found value. Over the temperature range 300 to 1000 K, the thermal conductivity of polysilicon is seen to increase by 87%. The thermal conductivity of aluminum is also shown in the figure where, having a much larger value than the other materials, its data points correspond to the vertical axis on the right-hand-side of the graph.

A plot of the specific heat versus temperature for each material (as specified in tables [79]) is shown in Figure 6.5. Again, from the figure it is easily observed that the specific heat increases over the temperature range of 300 to 1000 K.
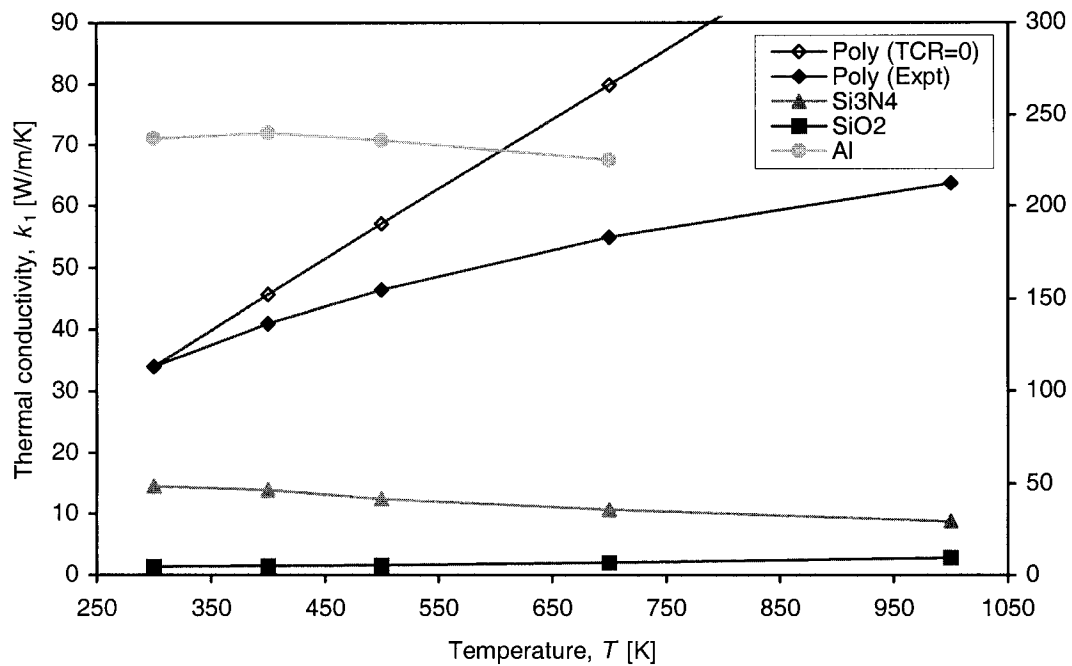
Figure 6.4 Select materials thermal conductivity as a function of temperature. The right vertical axis corresponds to the Al curve [79, 102].
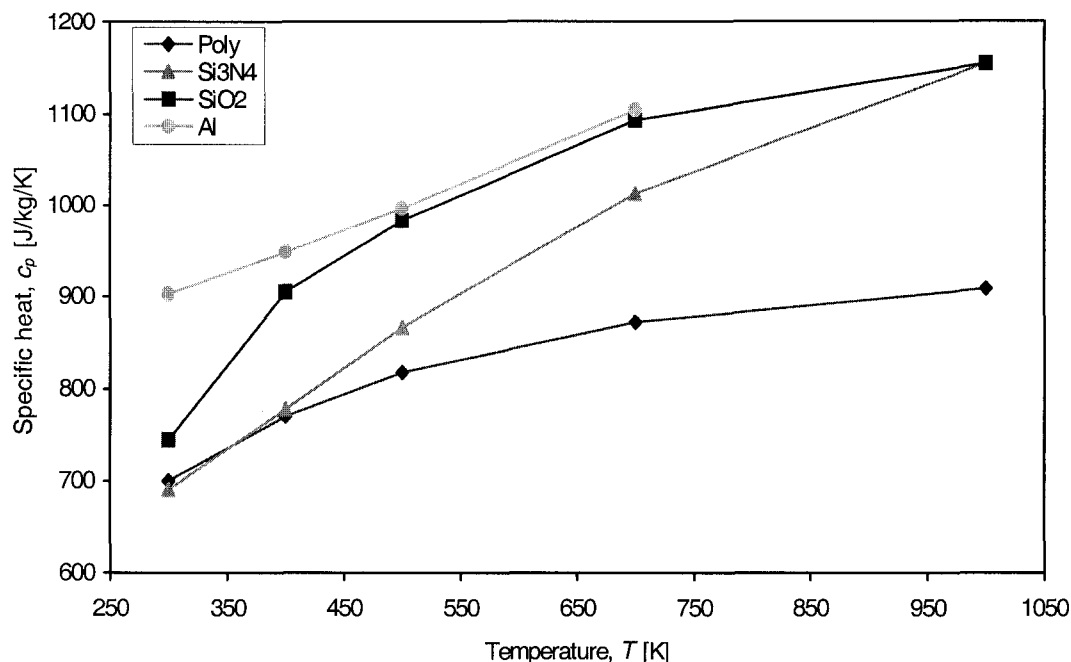
Figure 6.5 Select materials specific heat as a function of temperature [79, 102].

The change in mass density with temperature for the materials was considered zero, due to the observation that the coefficient of linear expansion for the materials is no larger than 10^{-5}. This implies that a one cubic metre block heated from room temperature to 1200 K would experience a volume, and therefore density, change of no more than 2.75%. The respective densities used for analysis in this project are: 2320, 2400, 2198, and 2700 $kg \cdot m^{-3}$ for polysilicon, silicon nitride, silicon dioxide, and aluminum, respectively.

Due to the planar, two-dimensional nature of the finite element model, the material properties require modification to their two-dimensional equivalent. The two-dimensional equivalent material property for each area was investigated and reported in [106]. In the reference, a three-dimensional thermal model was compared to a two-dimensional thermal model, and a difference in steady-state mean device temperature of 0.32% was observed. The researcher in [106] then concluded that a three-dimensional object could be accurately modeled by an equivalent two-dimensional model, thus significantly reducing the computational and time requirements necessary to produce a solution. This equivalency takes the form of an effective material property value for

regions in the device fabricated with multiple layers so that the layers could be represented by a single layer in the two-dimensional geometry. The micro-Pirani devices contain three separate regions that require this treatment. The first region is comprised of polysilicon, silicon dioxide and silicon nitride stacked layers. The second area contains only silicon dioxide and nitride, while the third area contains silicon dioxide, silicon nitride, and aluminum. Table 6.2 lists each area and its relative thickness in microns and the percentage of material per unit area in parentheses.

Table 6.2 Fabrication layers relative thickness

Material	Poly/SiO$_2$/Si$_3$N$_4$ regions [μm]	SiO$_2$/Si$_3$N$_4$ regions [μm]	Al/SiO$_2$/Si$_3$N$_4$ regions [μm]
Poly	0.3 (7.7%)	0.0 (0.0%)	0.0 (0.0%)
SiO$_2$	3.1 (79.5%)	3.1 (86.1%)	3.1 (70.5%)
Si$_3$N$_4$	0.5 (12.8%)	0.5 (13.9%)	0.5 (11.4%)
Al	0.0 (0.0%)	0.0 (0.0%)	0.8 (18.2%)
Total (μm)	3.9	3.6	4.4

Effective two-dimensional material properties, as reported in [106], are equal to the sum of each layer thickness, z_i [μm], multiplied by the thermo-physical property of each respective layer, or:

$$k_{1,effective} = \sum_{i=1}^{N} k_{1,i} \cdot z_i,$$

$$c_{p,effective} = \sum_{i=1}^{N} c_{p,i} \cdot z_i, \qquad (6.13)$$

$$\rho_{m,effective} = \sum_{i=1}^{N} \rho_{m,i} \cdot z_i.$$

Applying (6.13) to the areas defined in Table 6.2 produces the two-dimensional model, adjusted solid material properties as shown in Table 6.3. At the bottom of each section of the table, the relevant polynomial fit equations for the material properties are also displayed.

Table 6.3 Two-dimensional model, adjusted mass density, specific heat, and thermal conductivity properties for solid material fabrication layers.

T [K]	ρ_m [kg·m^{-3}]	c_p [J·kg^{-1}K^{-1}]	k_1 [W·m^{-1}K^{-1}]
		Poly/SiO$_2$/Si$_3$N$_4$ regions	
300	2233	735	21.728
400		878	23.908
500		955	25.132
700		1066	28.027
1000		1136	32.365
	$\rho_m = 2233$	$c_p = -9 \times 10^{-4}T^2 + 1.752T + 306.4$	$k_1 = 0.0148T + 17.647$
		SiO$_2$/Si$_3$N$_4$ regions	
300	2226	738	11.53
400		887	11.63
500		967	11.20
700		1082	11.55
1000		1155	13.28
	$\rho_m = 2226$	$c_p = 2 \times 10^{-6}T^3 - 3.9 \times 10^{-3}T^2 + 3.559T - 15.6$	$k_1 = 8 \times 10^{-6}T^2 - 0.0083T + 13.407$
		Al/SiO$_2$/Si$_3$N$_4$ regions	
300	2312	768	201.128
400		899	203.631
500		972	199.997
700		1086	191.550
	$\rho_m = 2312$	$c_p = 1 \times 10^{-6}T^3 - 2.9 \times 10^{-3}T^2 + 2.832T + 150.9$	$k_1 = -0.0271T + 211.95$

6.3.2.2 Properties of Gases

Unlike the solid materials used in the model, the properties of gases are heavily temperature and pressure dependent. Figure 6.6 shows a plot of thermal conductivity versus pressure for nitrogen and helium at two temperatures, namely 298 and 700 K. The plot was generated using (3.9) and (3.10) as defined in Chapter 3, gas physical properties listed in Table 6.4 [107], and an etch depth, d, of 85 μm. Below 1 Torr, both gases exhibit thermal conductivities that are essentially temperature independent. Above 10 Torr, the thermal conductivities of each gas are mostly pressure independent with changes due to temperature being relatively small. For this reason, and for simplicity, the material properties for the gases are considered as functions of pressure only. Note that the He and N$_2$ curves at 298 K cross at approximately 1 Torr. The results in Figure 6.6 show that as the gas temperature increases, the pressure at which the crossover occurs increases slightly; at 700 K the crossover is seen to occur at about 3 Torr. Figure 6.7

shows a plot of thermal conductivity at 298 K versus pressure for each of the gases used in this project.
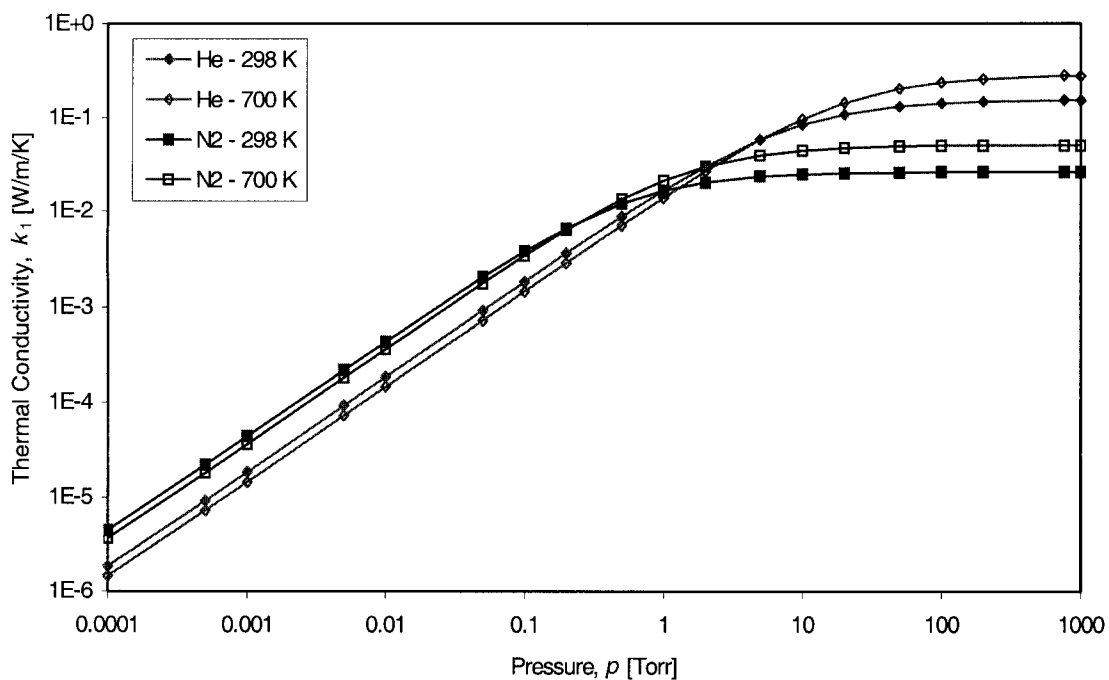
Figure 6.6 Thermal conductivity versus pressure for nitrogen and helium at 298 and 700 K.

Table 6.4 Various gas parameters at 298 K.

Gas	Mean collision diameter, a [Å]	Molar weight M_g [x10^{-3} kg·mol^{-1}]	Transition Pressure p_o [Torr]
Air	3.88	28.98	0.54
N$_2$	3.70	28.02	0.60
He	1.20	4.003	5.67
Ar	2.90	39.95	0.97
Kr	3.30	83.80	0.75
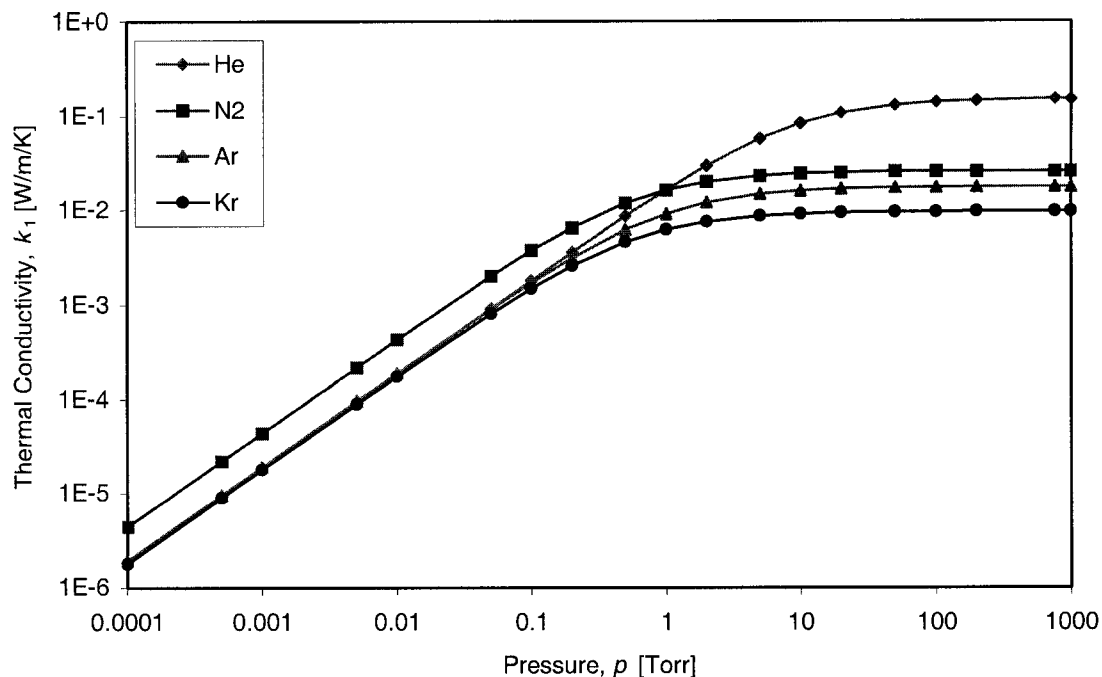
Figure 6.7 Thermal conductivity versus pressure for each gas at 298 K.

The specific heat is defined as the heat capacity at constant pressure, that is, the quantity of heat required to change one mole of gas by one degree Kelvin at a fixed pressure [108]. The quantity of heat required when the volume is fixed is referred to as the heat capacity at constant volume. Hence, the specific heat is solely referring to the heat capacity at constant pressure. Further, for a monatomic gas, whose energy is a result of translational motion, the heat capacity at constant pressure is a constant, independent of temperature. In the case of diatomic and polyatomic gases, whose energy is a result of translational, vibrational, and rotational motion, the heat capacity at constant pressure is not independent of temperature. By definition then, the specific heat of a gas is solely a function of the gas for monatomic ideal gases and a function of gas and temperature for polyatomic gases. Figure 6.8 shows the specific heat versus temperature for various gases and their respective best-fit equations [79, 107].
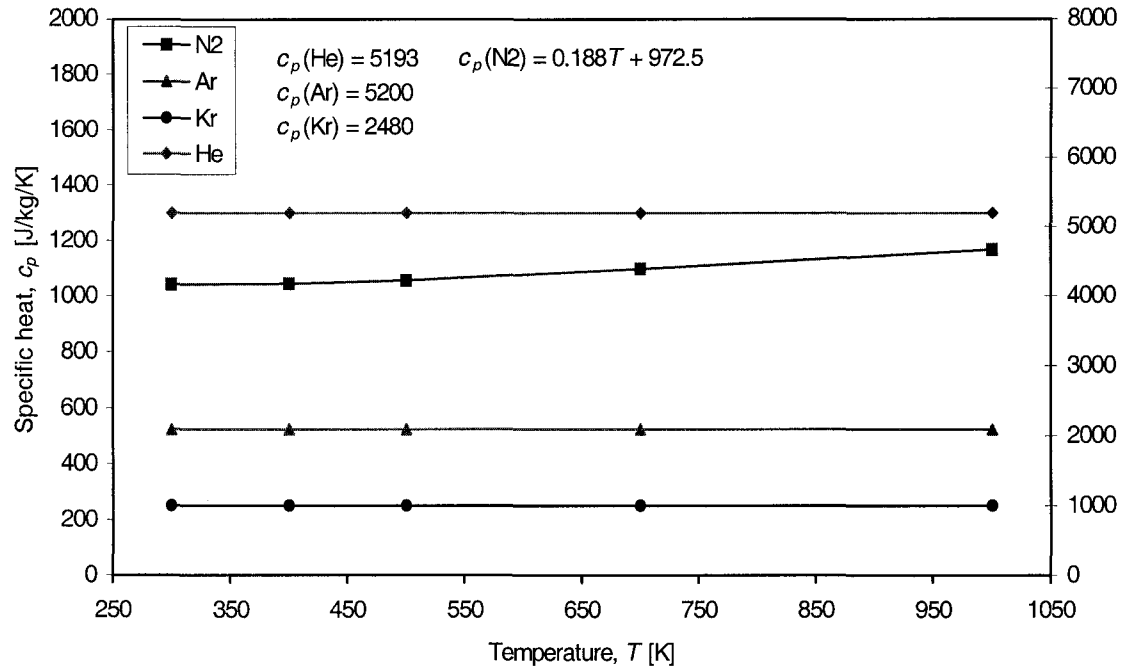
Figure 6.8 Specific heat versus temperature for various gases. The right vertical
axis corresponds to the helium curve.

The mass density of a gas can be determined by the use of the ideal gas law [108]
which states that the pressure of a gas, p [Pa], is related to its temperature, T [K], and
volume, v [m^3], by:

$$p = \frac{N\Re T}{v} = \frac{m}{v} \cdot \frac{\Re T}{M_g},$$

(6.14)

where N [mol] is the number of moles of gas equal to mass, m [kg] divided by the molar
weight, M_g [kg·mol^{-1}], and $\Re$ [8.3145 J·K^{-1}mol^{-1}] is the molar gas constant. Converting
units of pressure from Pascals (Pa) to Torr and solving for the density in (6.14) produces

$$\rho_m = 133.3224 \cdot \frac{pM_g}{\Re T},$$

(6.15)

where the pressure is now expressed in units of Torr, and of which a plot for each gas of interest as a function of pressure at 298 K is shown in Figure 6.9.
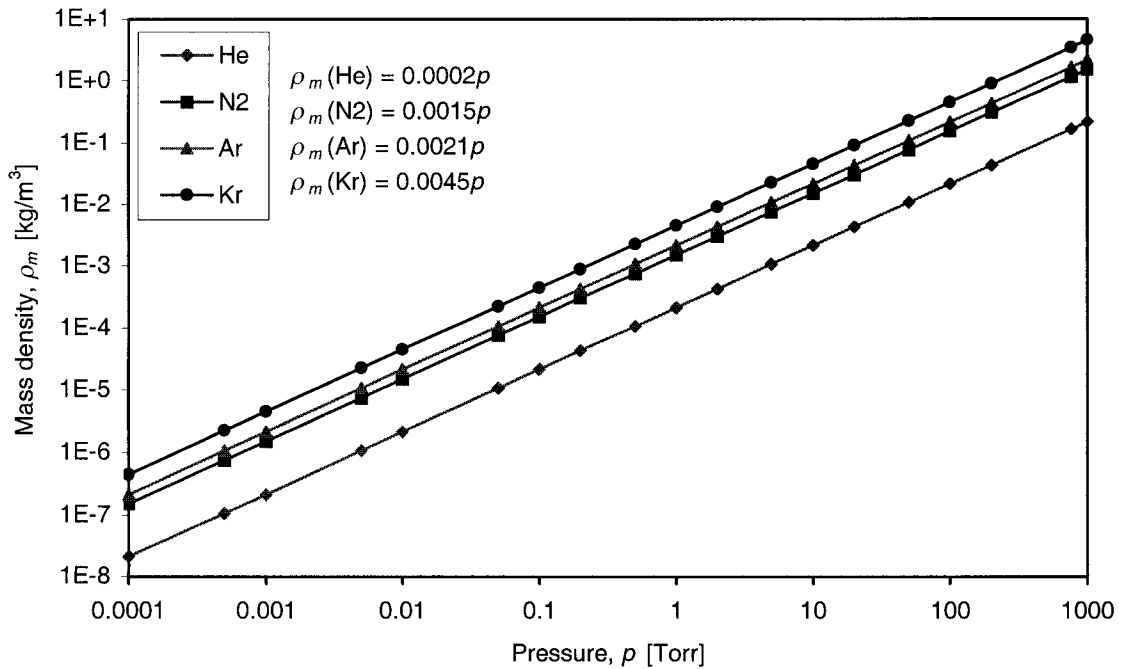
Figure 6.9 Mass density versus pressure for various gases.

Upon completion of the specification of material properties for the finite element model, the next step is to discretized or mesh the geometry and add any additional elements and nodes that may be required.

6.3.3 Meshing, Additional Nodes and Elements

The third step in completing the FEM model is the selection and application of an element to discretize or mesh the model geometry. The element selected in this project to mesh the micro-Pirani gauge model was PLANE35, a six node triangular thermal element with temperature as the singular degree-of-freedom. The six nodes of the element exist on the corners and the mid-point of each side of the triangle. Each of the four model geometries, including the surrounding open regions, was meshed using adaptive meshing, an iterative process that optimizes the size and number of elements required to discretize the structure. The number of elements used in meshing a model must be optimized to

produce accurate results. For example, the use of too few elements will not sufficiently resolve the model, while the use of too many elements may lead to large computation time and a failure to achieve convergence of solution. In the case of the four device geometries modeled here, consistent results were obtained, invariant with mesh size, when using between 1000 and 2000 elements in each model.

For our two-dimensional model, the only way to incorporate the heat loss through the gas, (6.4), and the radiative heat loss, (6.5), in ANSYS™ is to generate additional nodes and elements. Previous models for similar structures have not taken into consideration both conduction and radiation heat losses [20, 106]. To implement these losses, two sets of nodes, identical to existing nodes in the two-dimensional model (device and open regions) but displaced by 85 µm, the cavity etch depth, in the +z and −z directions, were generated, and constrained at room temperature. A set of three-dimensional conduction bar elements, LINK33, was generated between the existing nodes of the surface of the two-dimensional model and a set of nodes created in the −z direction to model the etched silicon pit. Connecting the nodes generated in the +z direction to the existing nodes on the surface of the device was a set of three-dimensional radiation bar elements, LINK31, to model the radiation loss from the surface, the length of each bar element thus being determined by the distance between its connecting nodes. Thus, the two-dimensional model is converted to a quasi three-dimensional model, the display of which is shown in Figure 6.10 for the small square device. Note that in the figure, the bars completely cover the front and back area of the plane of the device, including the open regions.

In ANSYS™, the conduction bars are modeled on the heat equation and the radiation bars on the Stefan-Boltzmann law, each bar considering the heat transfer between two nodes in space. As such, the software requires each bar element to be specified by an area and relevant material properties, such as thermal conductivity, density, specific heat, or emissivity, depending upon the application. The conduction bars were given the material properties of the surrounding gas and an area equal to the area of the model divided by the number of nodes on the surface of the two-dimensional model to completely contain the area of the two-dimensional model.

The length of the conduction bars (displacement of the nodes in the −z direction)

was later modified to 60% of the etch depth (51 μm), as suggested in [106]. This modification takes into account the increased heat loss through the gas near the ends of the support arms, below to the sidewalls of the etched cavity, and above to the surrounding die. The radiation bars were given the same area as the conduction bars to completely enclose the two-dimensional model, a form factor of one, an emissivity of 0.45, and the Stefan-Boltzmann constant value of 5.67×10^{-20} W·μm^{-2}K^{-4}. The form factor is the ratio of radiation leaving the device surface to the radiation intercepted at the other end of the radiation bar. The emissivity value of 0.45 was used as a starting point to produce a solution and chosen because of the work reported in [109], where multi-layered silicon dioxide layers, embedded with a polysilicon layer and suspended over a silicon substrate, were measured at visible and near infrared wavelengths. The emissivity was reported to vary from less than 0.05 at room temperature to 0.45 for temperatures in
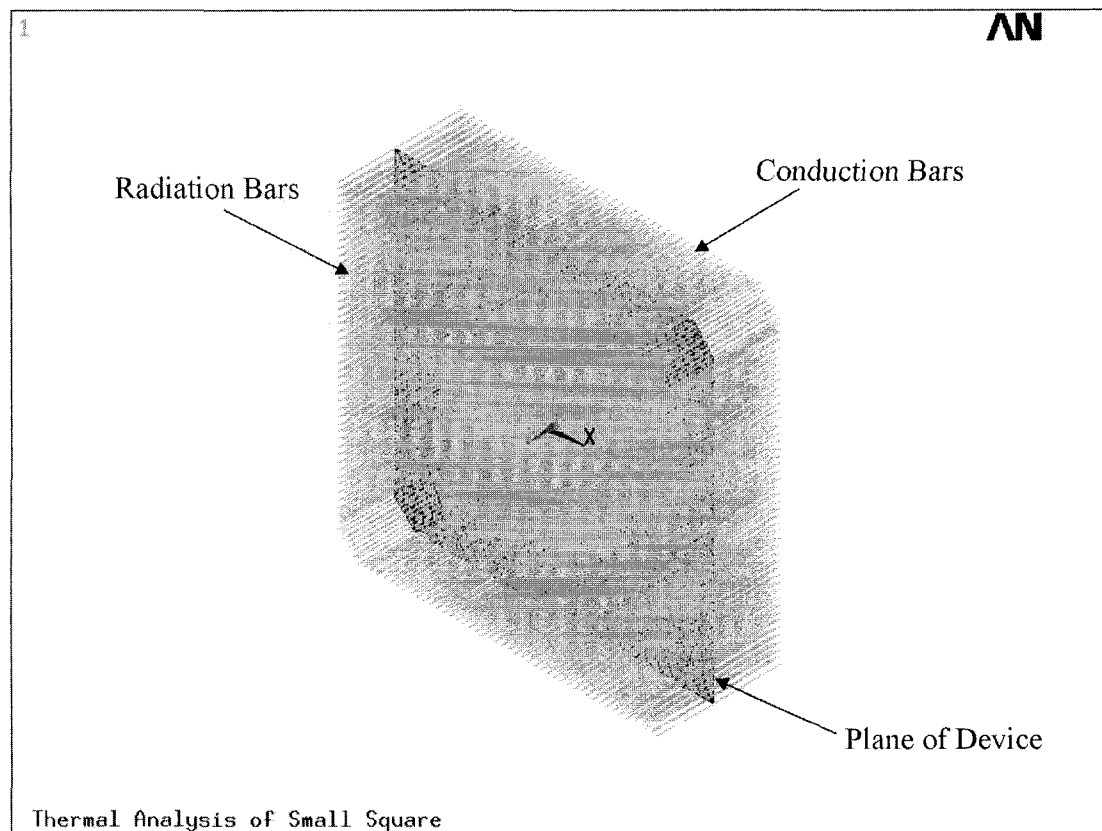
Figure 6.10 Three-dimensional model of small square device after meshing and adding conduction bars below, and radiation bars above, the plane of the device.

excess of 900 K. Note however, that the structures reported in [109] did not include a silicon nitride layer. Lastly, the length of the radiation rods (displacement of the nodes in the +z direction) was set to half that of the etch depth (43 μm) to compensate for the expected emission of radiation equally from both the upper and lower surfaces, and as denoted by the factor, 2, in (6.5).

6.3.4 Constraints, Loads, and Solving the Model

After building and meshing the model and defining material properties, the next step in the finite element process involves the application of constraints and loads. In order to constrain the model, the nodes around the perimeter of the plane of the device were set to a temperature of 293 K. Nodes at the bottom of the conduction bars and at the top of the radiation bars were also constrained to 293 K. These constraints represent the environment surrounding the device, that is, the perimeter of the device is maintained at room temperature.

For this model, the only load applied was heat generation in the area of the polysilicon, representative of the current flowing through the device. The level of heat generation was determined by dividing the amount of dissipated power by the area of the polysilicon geometry. For example, modeling an input power of 8 mW for the small square device (model polysilicon area of 6262 μm^2) requires a heat generation of 1.28×10^{-6} $W \cdot \mu m^{-2}$. The applied load can vary as a function of time, with different loads applied to various nodes and areas. The software limits each time-varying load to a polynomial function not exceeding an order of four; however, for this project the load was considered constant.

Having followed these steps, the model is ready to be solved. Obtaining a solution entails each node being assigned a set of numerical values, one for each degree-of-freedom of the node. Since the elements used in the meshing have only a single degree-of-freedom, temperature, each node will be given value representing its absolute temperature. In the solution phase, the analysis type and options must be specified. For a thermal model, only two analysis types can be specified: steady-state and transient. Analysis options include specifying the time steps to be taken at which a solution is obtained and the end time for the solution. For a steady-state analysis, only the solution

at the end time is displayed. In a transient analysis, a solution can be obtained at every time step up to and including the end time. For example, every millisecond up to a fixed time value. As stated earlier, ANSYS™ uses a sparse matrix direct numerical method for solving the simultaneous set of equations defined the model, by default.

6.3.5 Results and Interpretation

Figure 6.11 shows the contour plots of temperature for a small square device operated at 8 mW input power in two gases and for two pressures. In each of the figures, the contour colours were set to specific temperatures starting at 293 K, increasing by 120 K, and represented by nine colours. The first plot, Figure 6.11(a), shows the temperature distribution for a small square device in nitrogen at 760 Torr. The symmetry in

(a)   (b)

(c)   (d)
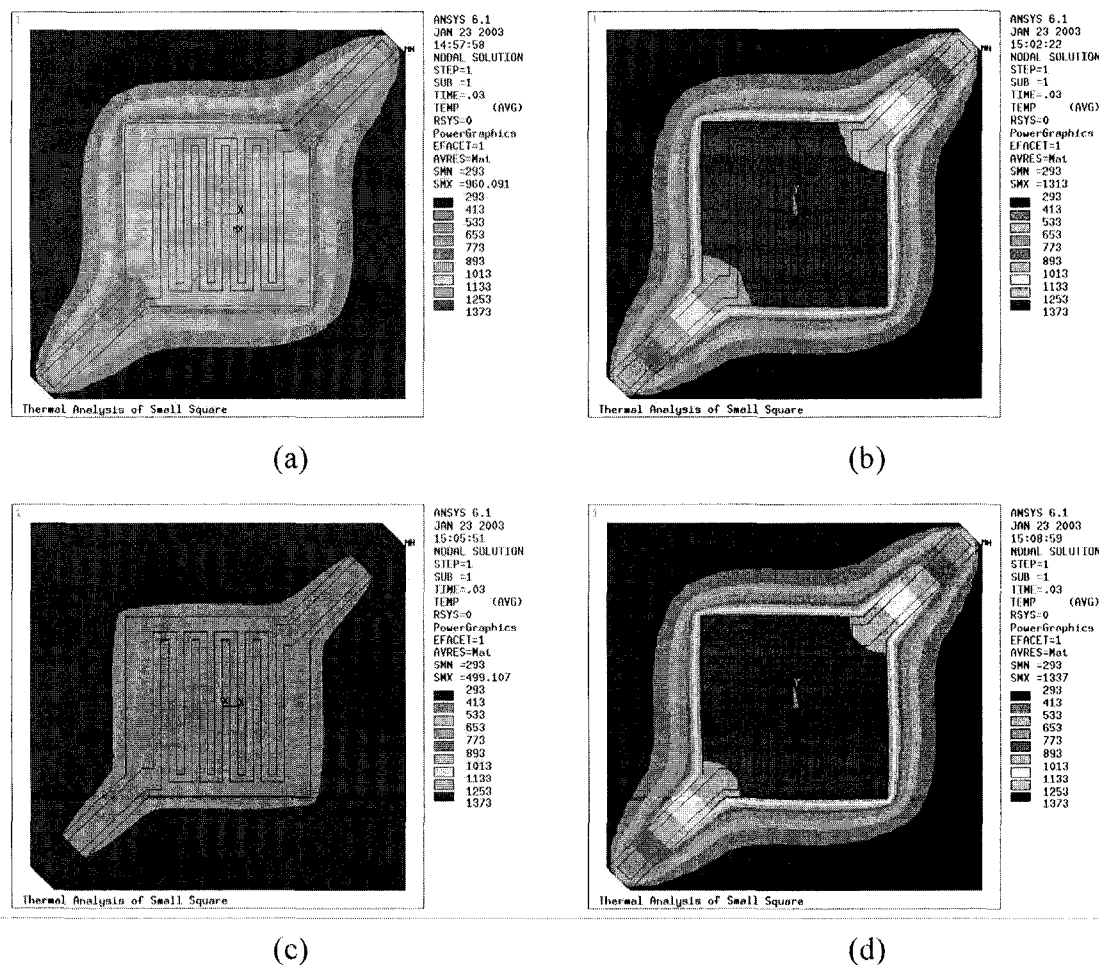
Figure 6.11 Small square operated with 8 mW in (a) nitrogen at 760 Torr, (b) nitrogen at 0.1 Torr, (c) helium at 760 Torr, and (d) helium at 0.1 Torr.

temperature across the surface of the device is evident with the center platform exhibiting the maximum temperature, 960 K. The temperature then decreases along the lengths of the arms to 293 K at the end of each arm. Also seen in the figure, is the heating of the gas occupying the open regions. Not seen in the figure is that looking edge-on, there is a bubble of heated gas enclosing the space above and below the plane of the device. The mean platform and support arm temperature for the device is 883 K. Figure 6.11(b) shows the same device at a pressure of 0.1 Torr, where the maximum temperature is 1313 K, again present across the center platform. The mean device temperature is 1201 K, an increase of 318 K from the case shown in (a). Figures 6.11(c) and (d) show the same device now in helium at 760 and 0.1 Torr, respectively. At 760 Torr in helium, the maximum temperature is 499 K and the mean device temperature is 470 K. Decreasing the pressure to 0.1 Torr in a helium environment increases the maximum temperature to 1337 K and the mean device temperature by 753 K to 1223 K.

In comparison with the Matlab generated mean device temperature under similar conditions, as shown by Figure 6.2, the finite element simulation shows relatively good agreement. Both models produce mean device temperatures within 200 K of each other at 760 Torr, and within 100 K at 0.1 Torr.

To achieve agreement between experiment and simulation, only a few parameters can reasonably be modified. For this project, these parameters are limited to the emissivity of the radiation bars and the length and area of the conduction bars. Decreasing the emissivity will increase the magnitude of the device temperature since the device becomes less efficient at emitting radiation. Increasing the length of the conduction bars will decrease the temperature gradient between the device and the room temperature substrate, resulting in an increase of the mean device temperature. Increasing the area of any of the bars will result in a decrease in mean device temperature, the decrease due to increased heat flux away from the device. Varying other parameters such as the material properties and heat generation would not be warranted, as they are well defined both by theory and by previous work [20, 106, 109]. In the next section, the results from various simulations and a comparison with experiment are presented.

6.4 SIMULATED DETECTOR RESPONSE

Solving the ANSYS model yields the temperature distribution over the surface of the device. Determination of the mean device temperature is performed by averaging the temperature of the nodes that occupy the device geometry. To compare the experimental data with the simulation requires the use of Planck's distribution, $I(\lambda,T)$, for the emission of radiation, as a function of temperature. Coupling the distribution with the responsivity of the detector, $R'(\lambda)$, and the solid angle ratio, S_{ar}, (see Chapter 3) that accounts for the detector-device arrangement, produces the following relation:

$$I_d(T) = S_{ar} \cdot \iint_{Device} \int_0^\infty \varepsilon(\lambda,T)I(\lambda,T)R'(\lambda)d\lambda dxdy .$$ (6.16)

The emissivity is assumed constant for the near-infrared wavelengths detectable by the photodetector, so integrating over the device gives a final form of

$$I_d(T) = S_{ar}\varepsilon A \cdot \int_0^\infty I(\lambda,T)R'(\lambda)d\lambda ,$$ (6.17)

where A is the area of the device and the solid angle ratio is calculated to be 16.15%. A plot of the integral of (6.17) as a function of temperature for both a silicon and germanium photodetector is shown in Figure 6.12. Also in the figure, for comparison, is a plot of the total emitted power per square millimetre from a black body, (3.14), and the resistance, (1.1), both as functions of temperature. From 300 to 1500 K, the resistance increases by less than one order of magnitude, while the total emitted power increases by approximately 3 orders of magnitude. Similarly, for the same temperature increase, the germanium detector experiences an increase in response of approximately 10 orders of magnitude and the silicon detector an increase of approximately 15 orders of magnitude. Thus, measuring the temperature change of the device from the radiation of a black body results in a significant increase in sensitivity when compared to measuring resistance changes alone, especially when considering the responsivity of the photodetector.

Therefore, combining the mean temperature of the device versus pressure produced by either the electro-thermal model or the FEM with (6.17), a plot of the detector current versus pressure can be generated for comparison with the experimental results presented in Chapter 5.
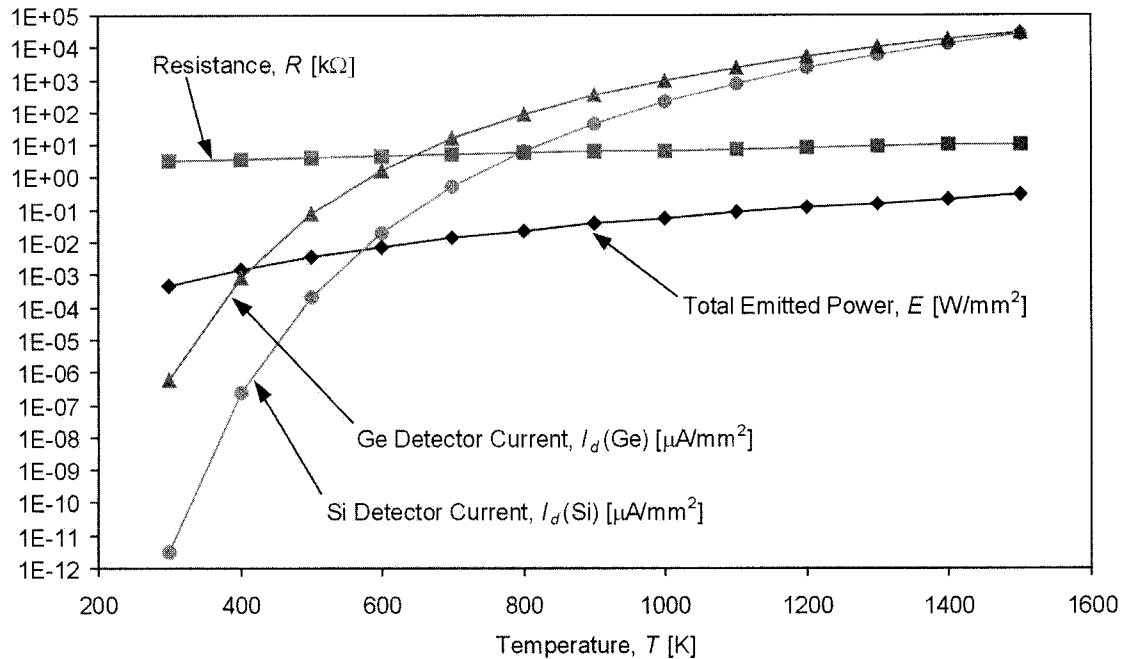
Figure 6.12 Plot of resistance, total black body emitted power, and detector current (Ge and Si) per square millimetre of black body surface versus temperature.

Figure 6.13 shows a comparison between the experiment results (Figure 5.19) and the electro-thermal model for the small square device at 8 mW in various gases. The experimental results were obtained at pressures above approximately 1.0 Torr only. Seen in the figure is that at the lowest pressure the resulting heat transfer is due solely to radiation and conduction through the supports; hence, each gas produces approximately the same detector output.
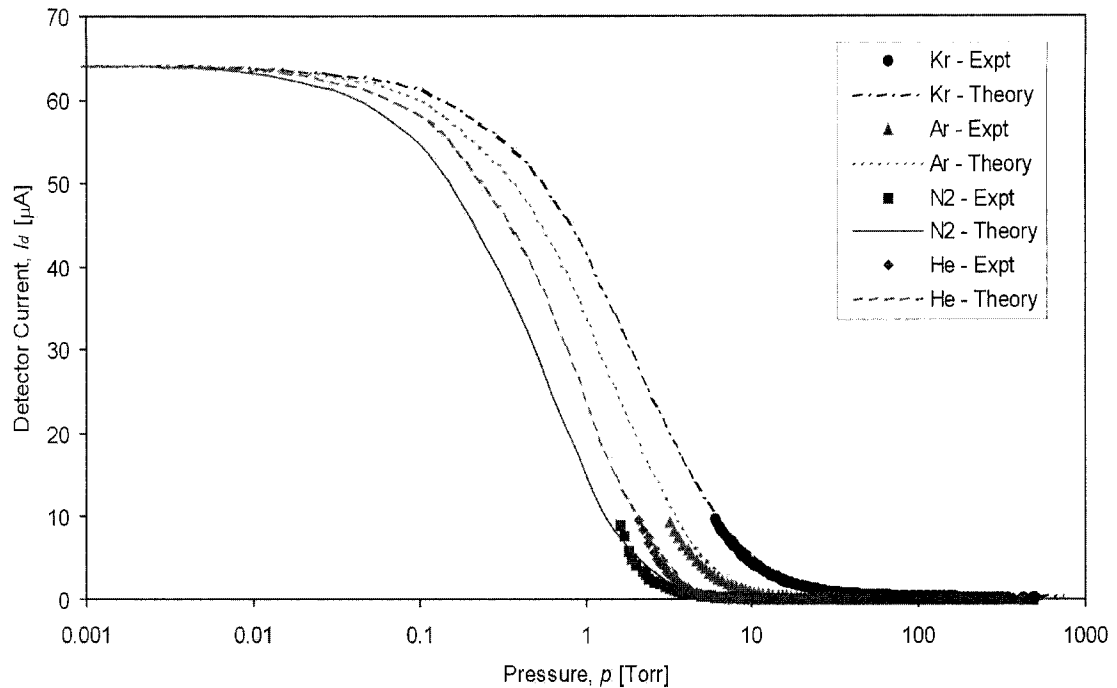
Figure 6.13 Comparison between experiment and electro-thermal model for a small square device at 8 mW in various gases.

Reasonable agreement in the trend between experiment and electro-thermal simulation can be seen in Figure 6.14, with a closer look at the results of Figure 6.13; the plots were achieved using an emissivity of only 0.05, unlike the value of 0.45 used initially, and with the use of approximation coefficients for (3.9) and (3.10). The approximation coefficient for (3.10) was required to account for any temperature-induced changes in transition pressure. The discrepancy between the initial emissivity value (0.45 as reported in [108]) and the one used here may be partially due to the addition of the silicon nitride layer, the thickness and number of silicon dioxide layers, and the different composition of the polysilicon, but is more likely a demonstration of the limitation of the electro-thermal model. The generation of the electro-thermal simulation data is relatively straightforward with modest computational time requirements needed to generate a large number of points. The main disadvantage to using the electro-thermal simulation is that only values for the mean device temperature and detector current for simple geometries can be generated. It is not possible to obtain data on the temperature distribution across the device surface or perform a transient analysis.
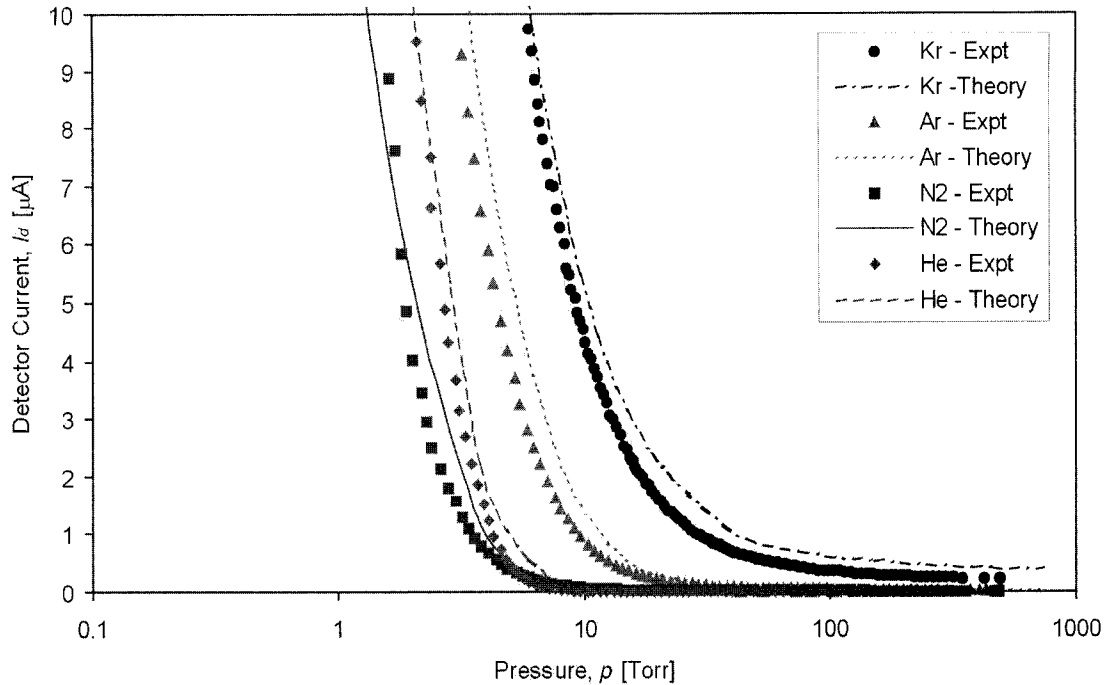
Figure 6.14 Comparison between experiment and electro-thermal model for a small square device at 8 mW in various gases.

The same experimental data was then compared with the results from the FEM simulation and is shown in Figure 6.15. Producing the FEM simulation requires a two-part process. First, the mean device temperature was extracted from the steady-state solution of the FEM. This process required substantially more computational time than the electro-thermal simulation, but with the benefit of being able to produce a temperature distribution across the surface of the device. In the figure, only a few simulation points were generated, connected by straight lines, as each point requires in excess of 10 minutes of computational time. Next, this mean temperature was entered into a Matlab program that performed the function of (6.17) to produce the photodetector current.

The FEM model parameters used include an emissivity of 0.05, conduction and radiation bar areas of 17.00 μm^2 (approximately equal to the model area divided by the number of nodes), a conduction bar length equal to 60% of the etch depth (consistent with the results in [106]), and a radiation bar length equal to 50% of the etch depth (to account for losses from top and bottom surfaces). Changing the length of the radiation
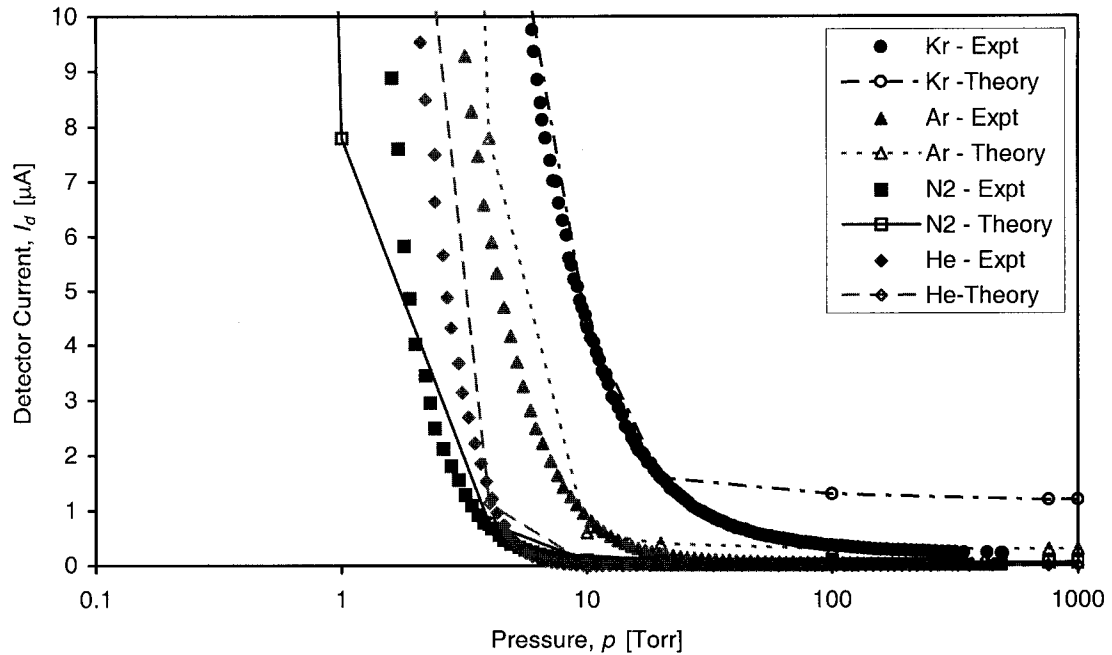
Figure 6.15 Comparison between experiment and finite element model
for a small square device at 8 mW in various gases.

bars produced a couple of degrees difference in the mean device temperature, even though this parameter has no physical meaning in a theoretical radiation treatment – an obvious demonstration of the software limitations. Reasonable agreement in the trend of the curves exists between the FEM simulation and experiment, with the FEM simulation trend appearing to be not as good as that produced by the electro-thermal model. One reason for this discrepancy is that the temperature dependence of the gas is ignored in the FEM, whereas the electro-thermal model required the use of approximation coefficients.

Figure 6.16 shows a comparison between experiment (Figure 5.23) and FEM simulation for each of the four device geometries in nitrogen and operated at a constant power of 8 mW. The manner of producing the simulated results was identical to that for producing Figure 6.15. Each of the device geometries utilized the same parameters with the exception of the area of the conduction and radiation bars being approximately equal to the model area divided by the number of nodes. These areas were 17.00, 30.00, 25.00, and 30.00 μm^2 each for the small square, large square, single bridge, and double bridge, respectively. Again, reasonable agreement in the trend between experiment and

simulation is observed, given the small number of simulation data points. Variations between experimental data and simulation are likely due to factors such as the constant emissivity used and the instability of the polysilicon when operated at a high temperature.

Lastly, one of the main advantages of the FEM simulation is the ability to produce transient thermal analyses. Figure 6.17 shows the temperature versus time curves for a single node resident in the finite element model of a small square device at 760 and 1 Torr in nitrogen, and operated at 8 mW constant power. It was assumed that all nodes on the platform would exhibit the same thermal rise-time even though they would have different steady-state temperatures. Five separate nodes were examined, each having the same temperature versus time trends for various steady-state temperatures. For the chosen node represented in the figure, the time constant is predicted to be 12 ms at 760 Torr, and 18 ms at 1 Torr. Curve fitting of the data in Figure 6.17 was attempted with the expectation that the device thermal rise-time follows an exponential function in the same manner as (6.10), which it, in fact, did. A list of the thermal time constants produced by the FEM simulation for a small square device at 8 mW in each of the gases tested as a
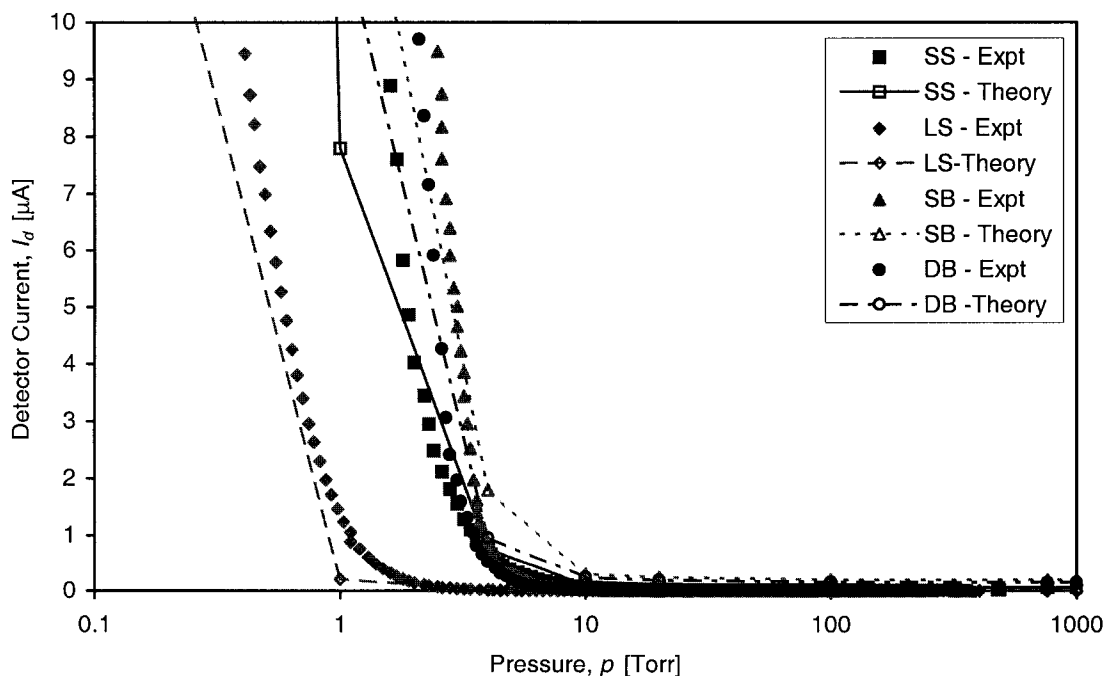
Figure 6.16 Comparison between experiment and finite element model for each device type at 8 mW in nitrogen.
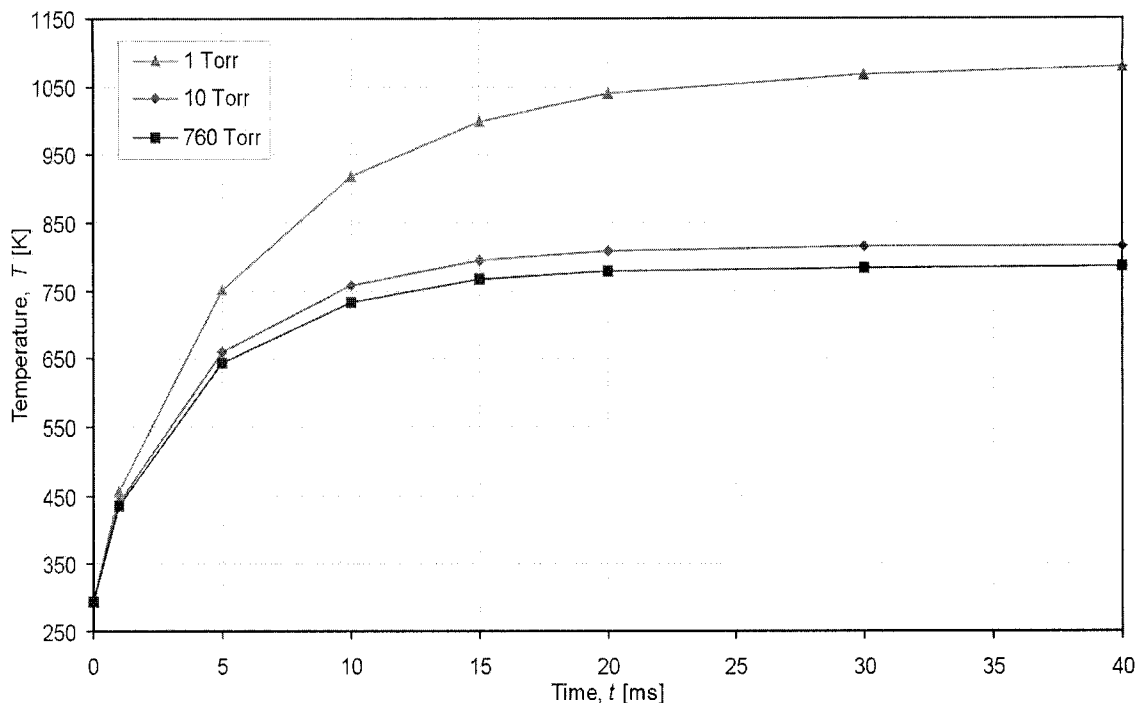
Figure 6.17 Temperature versus time for a selected node from the finite element model of a small square in nitrogen at 8 mW.

function of pressure is shown in Table 6.5. The simulated data suggests that at a given pressure, each gas can be identified by the time it takes for the device to heat to steady-state – the higher the pressure, the more significant the difference in rise-times. This is in contrast to the transient results observed in the experimental data, which suggest that the lower the pressure, the greater the difference in thermal time constant between gases. The reason for the discrepancy is that the finite element model is only an approximation of the actual devices and a model of the device thermal rise-time. In addition, in Chapter 5 the polysilicon resistance rise-time was measured (0 to 95% of the steady-state value), which is not the same parameter as the device thermal exponential time constant.

Table 6.5 Simulation small square exponential time constants in various gases at 8 mW.

Pressure,	Thermal time constant, τ [ms]			
p [Torr]	N_2	He	Ar	Kr
760	6.6	2.1	7.4	8.6
10	6.8	2.2	7.8	8.7
1	7.5	7.8	8.7	9.2

6.5 SUMMARY

This chapter has presented an analytical model describing the operation of the micro-Pirani gauge devices. A proper analytical solution to this model is difficult to obtain and only approximate solutions have been possible. Using finite element methods provides an effective manner by which to model the device behaviour and compare with experimental results. Both the electro-thermal and finite element models have generated reasonable trend comparisons with experiment and each other supporting this mathematical description as presented. Predicted transient rise-times have also been generated suggesting yet another method of identifying a gas. The next chapter discusses the feasibility of these microstructures for use as vacuum detectors and in gas analysis, and expands upon device durability and stability.

SEVEN
DISCUSSION

7.1 INTRODUCTION

Micromachined Pirani gauge structures have been investigated for a number of years with varying levels of improvement [4-10]. These projects have focused mainly on the resistive response of the devices to variations in pressure and without investigating device response to different gas environments. By focusing our attention to the radiation emission from these microstructures, a significant improvement in device sensitivity to changes in pressure has been achieved [18-20], while observing device response in the presence of various gases has resulted, with some success, in an entirely new application for these devices.

In this chapter, the experimental data presented in Chapter 5 and the significance of the finite element simulations presented in Chapter 6 will be discussed. Specific attention will be made to the effectiveness of the micro-Pirani gauges to measure vacuum and to detect a gas when operated under the modes of constant power and constant photodetector response. To begin, an examination of the observed durability problem and the repeatability of measurements for the micro-Pirani devices will be discussed.

7.2 DEVICE DURABILITY AND REPEATABILITY

7.2.1 Durability

During the testing of the micro-Pirani gauge devices, low durability was observed. In some cases, the low durability was a result of the polysilicon trace breaking down or melting, and in others, intrinsic stress causing a fracturing of the arms, in either case leading to an open circuit. These two mechanisms for device failure were termed type I (polysilicon breakdown) and type II (stress fracture) and examples of each are

shown by a microphotograph of a small square device in Figures 7.1 (a) and (b), respectively.

(a)   (b)
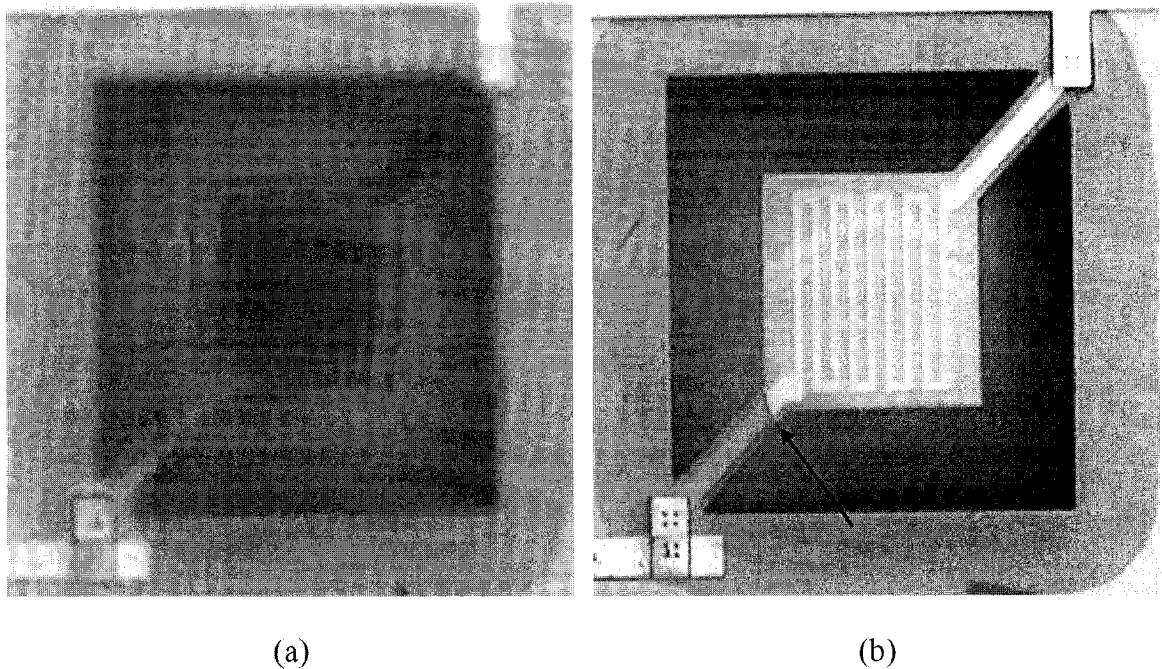
Figure 7.1 Microphotograph of a small square device with (a) type I failure (polysilicon breakdown), and (b) type II failure (stress fracture).

A type I failure is simply the result of too much current through the polysilicon producing Joule heating sufficient to cause localized melting of the polysilicon. The occurrence of type I failures can be reduced by limiting the current sourced through the device and hence, limiting the amount of power being dissipated in the structure. As described by the electro-thermal model in Chapter 6, the amount of power dissipated in the structure will be the balance between the power supplied to the device and the various heat losses by radiation and conduction. As such, the actual amount of sourced current required to cause a type I failure will vary with the environment in which the device is operated. For example, at atmospheric pressure in nitrogen as much as 30 mW can safely be dissipated in a small square device. This same power dissipated at pressure below 10 Torr, where the lack of gas molecules reduces heat transfer, will result in a device temperature sufficient to cause a type I failure.

Observations of device operation have shown that when the resistance value exceeds approximately twice the room temperature value, equivalent to an increase of about 1000 K with a TCR of 10^{-3} K^{-1}, the lifetime of the device is significantly shortened. The lifetime of the micro-Pirani devices is defined as the number of separate instances in which current is passed through a particular device. However, resistive means are not very effective for monitoring the health of a device during operation because of the instability of the polysilicon at high temperatures and the likelihood of permanent changes to the room temperature resistance. Instead, conditions in which the device resistance is twice its room temperature resistance correspond to a photodetector current of approximately 10 μA from the germanium detector when placed at a distance of 2.3 mm (the distance used for the experimental results). Therefore, the prevention of type I device failures has lead to the determination of a maximum safe photodetector current of 10 μA, valid when the germanium detector is placed 2.3 mm from the operating device. Operation of any devices under conditions that result in a photodetector current in excess of 10 μA has been avoided, resulting in a significant drop in the instances of type I device failure.

Type II failures have been observed to occur before and after device operation. Failures before operation are likely the effect of intrinsic structural stress resulting from the large amounts of undercutting required to achieve structural release from the substrate. A type II failure after device operation is believed to result from the amplification of the stresses as the device cools. For example, when the device is operating and heated, thermal expansion occurs in proportion to the degree of heating, which, as shown by the finite element simulations in Chapter 6, is not uniform across the surface of the device. Upon cessation of current passing through the polysilicon, the device will cool and contract. Differences in the amount of contraction across the device will create zones of thermal stress; the intersection of these zones with any already present intrinsic stress sites may lead to a cumulative effect sufficient to cause fracture. Only two regions of type II failures have been identified, both occurring at either end of the support arms. This leads us to believe that the majority of the intrinsic and thermal stresses are localized at the ends of the support arms. A reduction in the amount of

intrinsic stress would be achieved by reducing the thickness and number of silicon dioxide and silicon nitride layers.

Devices were also observed to fail after operation in SF_6 when operating conditions produced a photodetector response larger than approximately 3 μA. The type of failure experienced after operation in SF_6 was either type I or type II, with neither failure mechanism occurring more frequently than the other. Hence, operation in SF_6 resulted in an unpredictable, yet inevitable, device failure. It is for this reason, as previously stated in Chapter 5, that testing in SF_6 was halted. The cause of the SF_6 durability problem is believed to result from the decomposition of SF_6 at temperatures in excess of 700 K [95]. Sulfur hexafluoride is a colourless, odourless, non-toxic, non-flammable, inert, insulating gas of high dielectric strength and thermal stability. It has a molecular weight of 146.05 g/mol, about five times heavier than air, making it one of the heaviest known gases. Sulfur hexafluoride is particularly suitable for application in both high-voltage power circuit breakers and high-voltage cables, as well as transformers, transducers, particle accelerators, X-ray and ultra-high-frequency equipment. As stated in [95], SF_6 decomposes at temperatures in excess of 700 K into sulfur fluorides (SF_4) and sulfur oxyfluorides (SOF_2, SO_2F_2, SOF_4). Of notable importance is that in the presence of water and excessive temperatures, SF_6 decomposes into sulfur oxydifluoride (SOF_2) and hydrogen fluoride (HF). It is the decomposition into HF that is one of the possible occurrences that will have a detrimental effect on device operation. The HF would etch away portions of silicon dioxide, exposing the heated polysilicon to the gas which, in turn, would rapidly oxidize the polysilicon and lead to a type I failure (polysilicon breakdown). A possible cause of the type II failures (stress fracture) could be the deposition of decomposition materials to selected areas of the device leading to an increase in the amount of intrinsic stress and subsequent fracturing upon cooling.

Observed in the testing of the microstructures is a permanent deformation of the platform after operation. Once released from the substrate and during normal operation, the device is heated to temperatures in excess of 1000 K as predicted by the simulations. Such temperatures are of sufficient magnitude to anneal the composite silicon dioxide and silicon nitride layers and subsequently allow the platform to become malleable enough to be strained by intrinsic and thermal stresses between the various layers. Upon

cooling, the strained platform remains in the deformed shape. Figure 7.2 shows a microphotograph of a small square device (a) before operation, and (b) after operation, where the deformation is evident by the curling of the unsupported corners of the platform. The curling is upward, as determined by changing the focal plane of the microscope.

Temperatures high enough to produce permanent deformation of the platform during operation also have an effect on the room temperature resistance of the polysilicon trace. Just as during the XeF_2 etching to release the device from the substrate resulted in localized heating sufficient to permanently change the room temperature resistance of the polysilicon, normal device operation produces sufficient temperatures to move grain boundaries leading to grain growth or re-crystallization that will permanently decrease the room temperature resistance of the polysilicon [92, 110]. The decrease in resistance is generally considered to be attributed to a reduction in the grain boundary barrier potential that create low resistivity paths for current flow [12]. Consistently, after the devices were operated in conditions such that a photodetector current in excess of approximately 2 μA was experienced, the room temperature resistance of the polysilicon

(a)   (b)
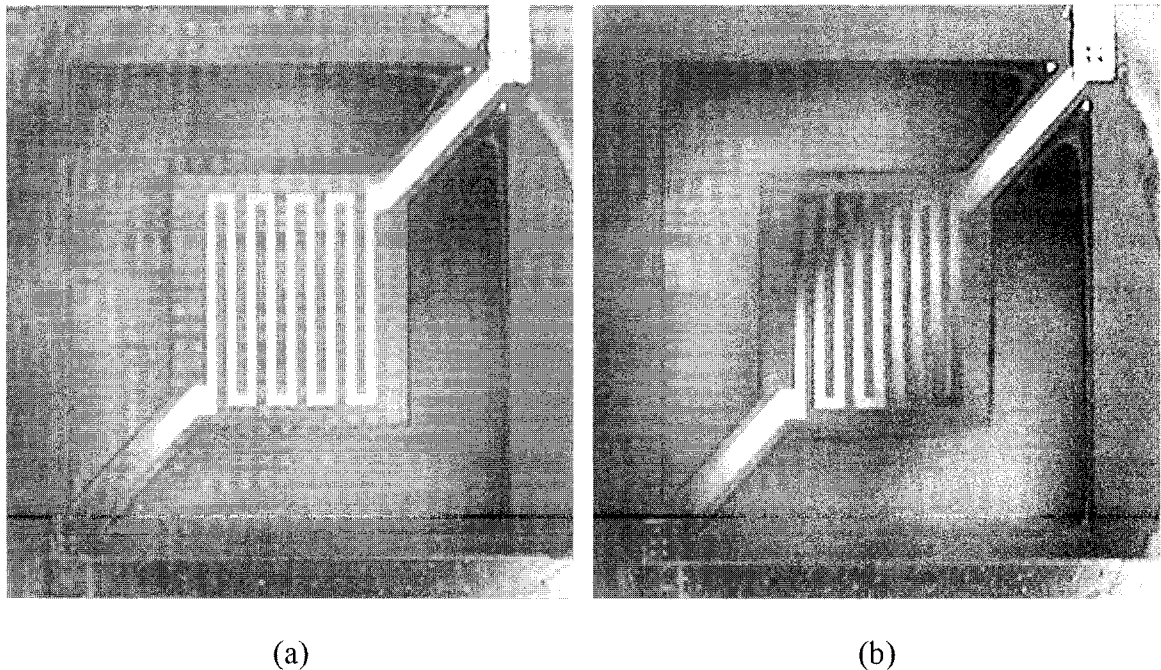
Figure 7.2 Microphotograph of a small square device
(a) before operation, and (b) after operation.

was measured to decrease by about 2.5% (100 Ω for square devices, 36 Ω for bridge devices) after the initial run. Subsequent runs failed to further change the room temperature resistance provided the device was operated such that a maximum photodetector current of 10 μA was maintained, suggesting that the first operation of a particular device annealed the polysilicon, and further annealing would require temperatures significantly higher than those experienced during normal operation. Such significantly higher temperatures would very likely lead to a type I failure.

Finally, a few devices were observed to undergo a type I (polysilicon breakdown) failure under minimal operating conditions. Upon further investigation, it was discovered that these few devices contained a fabrication defect in the polysilicon layer. Figure 7.3 (a) shows a microphotograph of one such device with the fabrication defect in two places as indicated by the arrows. Figure 7.3 (b) is a microphotograph of the same device at higher magnification of the upper left defect (see arrow). The defect takes the form of an over-etching of a portion of the polysilicon layer, most likely the result of a defect in the mask or dust on the mask creating non-conformal coverage of the photoresist during patterning of the polysilicon. The defect was not the result of post-process etching as other devices exhibited the same defect before post-process etching.

(a)   (b)
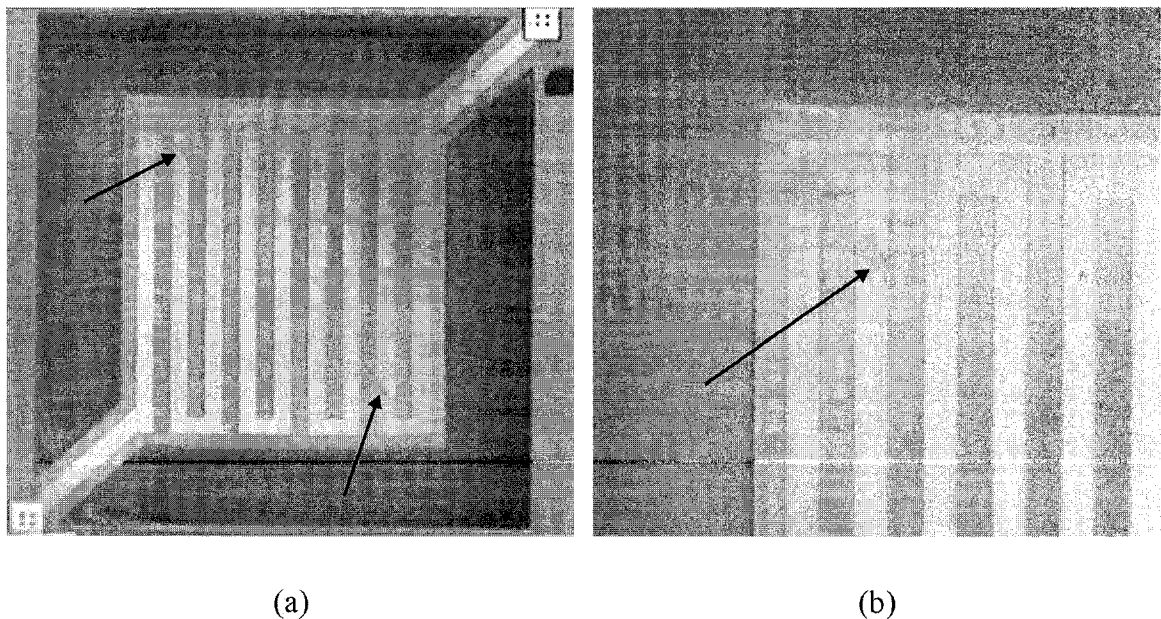
Figure 7.3 Microphotograph of a small square device (a) polysilicon fabrication problem as indicated by arrows, and (b) close-up of one of the problem areas (see arrow).

7.2.2 Repeatability

Determining the repeatability of measurements in any experiment is important. Questions such as, how does the detector response vary between different current sourcing instances with the same device, different devices residing on the same die, and different devices between separate die need to be investigated to aid in the understanding of device repeatability. Figure 7.4 shows the detector current versus pressure for three small square devices operated with 8 mW of constant power in nitrogen. The first two devices, labeled #1 (a, b), and #3 (a, b), reside on the same die. The third device, labeled #5, resides on a separate die from the first two devices. Both dice were etched at the same time and thus presumably etched the same amount. Two runs were conducted with each of the first two devices, the first run denoted by the letter, a, and the second run by the letter, b. Furthermore, each run was performed starting at 100 Torr, decreasing to 0.01 Torr, and increasing back to 100 Torr with no significant hysteresis observed. From the figure the detector response for runs performed with the same device are observed to vary by a maximum of 6.6 µA (4.9%), results between different devices residing on the same die to vary by as much as 7.2 µA (6.4%), and results between different devices residing on separate dice to vary by as much as 8.4 µA (7.2%).

To look at the long-term reliability of the devices a trial was performed by which a small square device was operated at a constant power of 8 mW in nitrogen for 32 days, 15.5 hours (2.8206×10^6 seconds). Initially, the chamber was evacuated to a pressure of 1.7 Torr and all valves closed. Over the duration of the experiment, air leaked into the system, and the pressure after 32 days increased to 5.0 Torr. Data was collected by the software every 45 minutes on various parameters such as system pressure, photodetector current, device current, and etcetera. Also, the germanium detector, placed 2.3 mm above the operating device, was used for the trial. From the initial and final chamber pressures, and the time involved, a leak rate for the system was determined to be (1.273 ± 0.039)$\times 10^{-6}$ Torr·s^{-1}. Figure 7.5 shows the detector current versus pressure for the trial, including runs performed before and after the trial for comparison. The results show good agreement before, during, and after the trial with a maximum difference between the three runs of 0.43 µA (8.5%) at 2.3 Torr, within the expected difference for multiple runs with the same device.
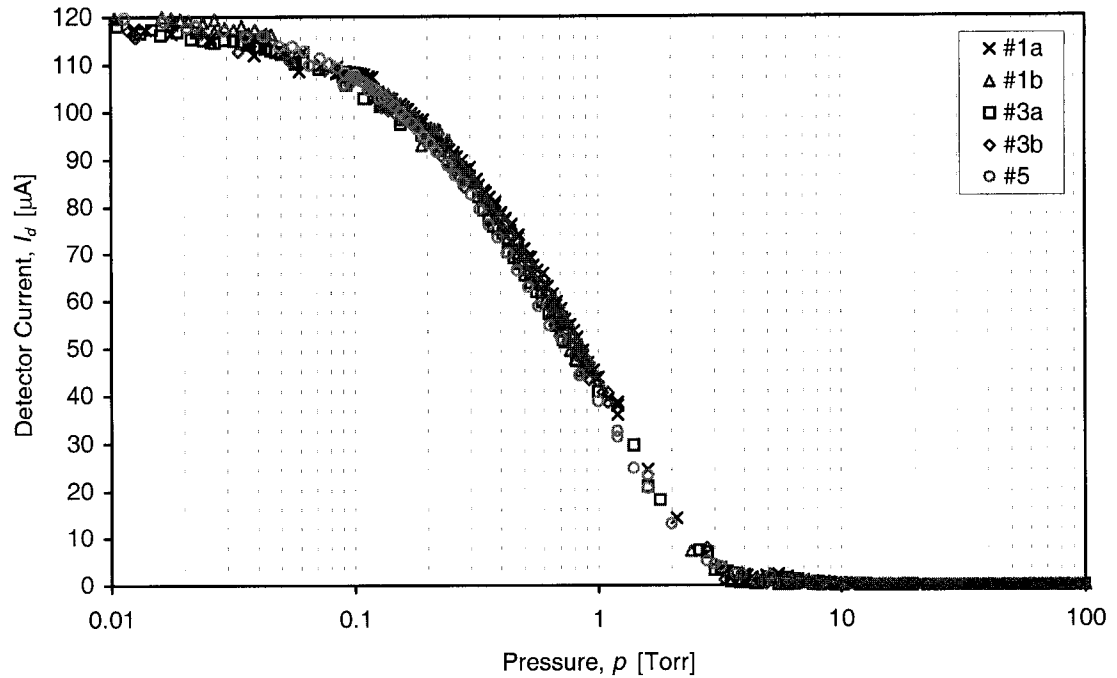
Figure 7.4 Detector current versus pressure for small square devices operating at 8 mW in nitrogen over multiple runs to determine repeatability.
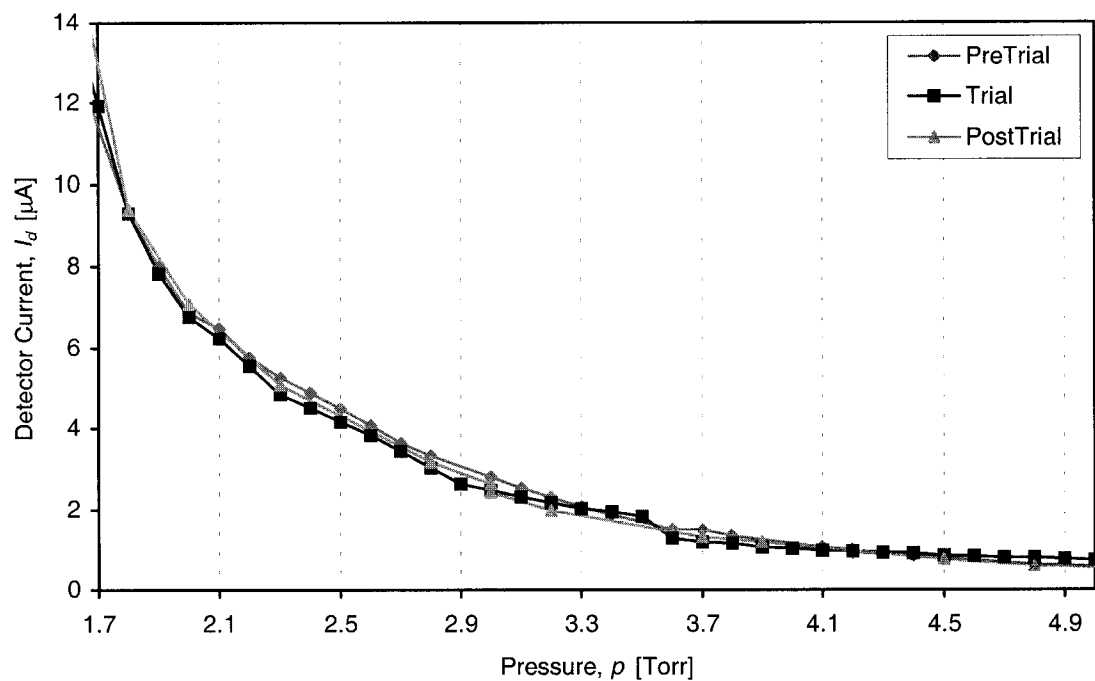
Figure 7.5 Long term trial detector current versus pressure for a small square device operated continuously with 8 mW in nitrogen for 32.6 days.

The long-term trial and repeatability experiments were conducted by sampling only a single data point at each pressure. Sample averaging would further reduce any noise-induced variations in photodetector current, possibly leading to an improvement in device repeatability. Compared to a standard, commercially available Pirani gauge whose uncertainty in measurement is typically 15% or more [3], the results discussed here demonstrate a nearly two-fold improvement, without sample averaging.

7.3 VACUUM MEASUREMENT

7.3.1 Constant Power

In terms of measuring the pressure changes of a system in nitrogen, the experimental results show that pressure from 1000 to 0.1 Torr is easily measured by operating the device at the appropriate constant power. At 0.1 Torr, smaller changes in the detector current are observed resulting in a decreasing sensitivity, as the pressure is further decreased. Operating the device at a smaller power (< 4 mW) improves the pressure-sensitive range to approximately 0.005 Torr, but detecting pressure below this value with any degree of accuracy seems unlikely [20]. The experimental results also demonstrate the typical shape for a conventional thermal-conductivity-type pressure gauge [111], but with a much larger variation in output, as predicted by the coupling of the Planck law and the detector responsivity, and shown in Figure 6.12. For example, a small square device operated with a constant power of 12 mW over the range 20 to 10^{-3} Torr will produce an increase in detector signal of more than 35 times. In comparison, a standard Pirani gauge is sensitive between 0.8×10^{-3} and 20 Torr, an uncertainty of 15 to 20%, and with a typical variation in resistance of only 33% [3, 111]. In addition, to further illustrate the advantages of using a germanium (longer-than-visible wavelength) detector, results from the use of a silicon (visible wavelength) photodetector, under similar operating conditions and with a small square device, have been reported to produce an increase in detector signal of approximately 16 times [20].

The inability to determine pressure below 0.005 Torr is a limiting factor of these devices and is a result of the lack of gas molecules and hence the negligible heat loss through the gas. At pressures of this order, the heat loss is essentially due to radiation

and conduction through the supports. For pressure above 1000 Torr, the measurements are limited by both the amount of safe current that can be passed through the device and the decreasing change in gas thermal conductivity. For example, in Figure 5.10, at 30 mW and 700 Torr the detector current is already 90% the determined maximum safe limit, and for pressure above 500 Torr, the change in thermal conductivity decreases with increasing pressure, becoming essentially constant.

As seen in Figure 5.14, considering the device temperature during operation, the large square, due to its larger size, has a lower current density for a given power and thus operates at cooler temperatures. The bridge devices behave essentially the same when compared to each other. The double bridge is consistently cooler than the single bridge, due to the effect of the second bridge acting as a heat sink, by design. Compared to the square devices, the bridge devices operate at cooler temperatures for pressures above 10 Torr, and produce larger photodetector currents for pressures below 10 Torr, especially at 4 mW. The larger detector current at lower pressure is due to the slightly smaller area of the bridge devices compared to the small square devices. As the pressure decreases, the heat loss through the gas becomes less dominant faster than it does in the case of a small square, leading to a higher mean device temperature and hence a larger detector current.

Table 7.1 lists the relative sensitivity to vacuum for each device type when operated such that the photodetector current does not exceed 10 µA (this value corresponding to a mean device temperature of approximately 1300 K). The data was derived from Figures 5.10 to 5.13 for the small and large square, single and double bridge devices, respectively. Nine pressure ranges were selected as shown with the sensitivity determined assuming device operation at an appropriate power in each range. The values were calculated by taking the inverse of the straight line slope of a selected curve at each pressure range and multiplying by the experimentally determined uncertainty in measuring the photodetector current, ±0.1 µA.

At pressure less than 1 Torr, the sensitivity to vacuum for the small and large square devices are essentially the same; the sensitivity for the bridge devices not listed as the detector response at 4 mW has exceeded the safety limit of 10 µA. At pressure ranging from 0.1 to 10 Torr, each of the four devices has nearly the same sensitivity, with the bridge devices being slightly more sensitive than the square devices. As the pressure

Table 7.1 Device sensitivity to vacuum under constant power operation in nitrogen.

Pressure, p [Torr]	Device Sensitivity, δp [Torr]			
	Small Square	Large Square	Single Bridge	Double Bridge
< 0.1	±0.01 (11%)	±0.01 (11%)	N/A	N/A
0.1 – 1	±0.04 (4.4%)	±0.02 (2.2%)	N/A	N/A
1 – 4	±0.06 (2.0%)	±0.08 (2.7%)	±0.1 (3.3%)	±0.1 (3.3%)
4 – 10	±0.39 (6.5%)	±0.32 (5.3%)	±0.1 (1.7%)	±0.1 (1.7%)
10 – 20	±1.2 (12%)	±1.1 (11%)	±0.3 (3.0%)	±0.8 (8.0%)
20 – 40	±1.5 (7.4%)	±0.7 (3.5%)	±1.4 (7.0%)	±2.9 (15%)
40 – 100	±2.5 (4.2%)	±6.4 (11%)	±5.0 (8.3%)	±6.6 (11%)
100 – 200	±22 (22%)	±54 (54%)	±6.8 (6.8%)	±11 (11%)
> 200	±20.2 (4.0%)	±455 (91%)	±109 (22%)	±170 (34%)

is further increased to between 10 and 100 Torr, the differences between device types start to show, with the small square yielding the best sensitivity and the double bridge the worst. Finally, at pressure above 100 Torr, the small square has the best sensitivity and the large square the worst when operated at 30 mW. The experimental figures suggest that the large square and bridge devices, when operated at powers greater than 30 mW, would have better sensitivities for pressure larger than 100 Torr. Operation of the devices at powers greater than 30 mW was not performed, however, due to the problem of device durability and the limited number of fabricated devices. For example, 30 mW represents a mean device temperature of approximately 1100 K at 700 Torr in nitrogen, rapidly increasing to 1300 K (the maximum determined safe mean device temperature) for a decrease in pressure of only 300 Torr. Using a better choice of powers, for example, 2 mW for pressure less than 0.1 Torr, and 25 mW for pressure from 100 to 200 Torr, would also improve the sensitivity. Overall, the single bridge device provides the largest sensitivity to pressures from 0.005 to 1000 Torr assuming the best power for each range is used. At pressures below 20 Torr, the upper limit for a standard Pirani gauge, the values listed in Table 7.1 are at least 25% better than those listed for a standard Pirani gauge [3]. Hence, detecting the thermal radiation emitted from a micro-Pirani gauge and

operating with constant power significantly improves the sensitivity to vacuum and the useful operating range.

7.3.2 Constant Response

Under constant photodetector response operation, the higher the maintained response, the higher the required power to maintain it, at any given pressure. In maintaining the photodetector response, the radiative emission from the device is considered to come directly from the surface of the device, not the polysilicon layer. The reason for this is that the temperature gradient in the z-direction is very small because of the device's large aspect ratio, as demonstrated in the finite element simulations. Hence, the temperature of the polysilicon is roughly that of the surface of the platform.

For each device type it is possible to distinguish power as a function of pressure for responses ranging from 0.5 to 50 μA, but only for pressure above 0.01 Torr, as seen in Figure 5.15. At pressure below 0.01 Torr, the change in power as a function of pressure is less than the uncertainty in measuring power, ±0.1 mW. For lower set responses, such as 0.5 μA, the power required appears to saturate once a sufficiently high pressure is reached, approximately 700 Torr in this case. The saturation is a consequence of the fact that increasing the pressure beyond 700 Torr results in a constant thermal conductivity (Figure 6.7), and hence constant heat loss, and therefore constant device temperature. Extrapolating from the data suggests that pressures above 1000 Torr, not tested as the capacitance manometers are limited to 1000 Torr, would be possible to measure, provided a response of 10 μA or higher is maintained.

Comparing device geometries (Figure 5.16), the bridge devices produce similar curves, with the double bridge consistently requiring about 4 mW less power at a given pressure than the single bridge. In this case, it was expected that the double bridge, because of the second bridge heat sink, would have required more power than the single bridge. The reason for this behaviour is likely the result of device variation, as only one device of each type was tested. The shape of the square devices curves are similar, with the small square requiring significantly less power to maintain a response of 10 μA. This large square has an area approximately three times larger than the other device geometries, resulting in three times the radiation emission and three times the conductive

heat loss through the gas, at a given temperature and pressure. Three times the radiative emission results in a larger detector signal and hence should require a lower power than the other devices. However, the dominant heat loss mechanism at pressure above 0.1 Torr is the conductive heat loss through the gas, not the radiative heat loss. Therefore, even with three times the radiative emission, the large square device produces a lower detector signal than the other devices under similar conditions due to its larger overall heat loss, and hence lower temperature, thus requiring more power to maintain a given response.

To determine device sensitivity under constant photodetector response conditions, a least squares fit was performed on the data in Figure 5.16 and derivatives of the best-fit lines calculated. The highest correlation coefficients (90 to 94%) were produced only by using a power function to produce the best-fit lines. Figure 7.6 shows the derivative formulae and a plot of the inverse of the derivatives, the inverse slope, versus pressure for the experimental data of Figure 5.16. The figure shows, as expected, that the sensitivity of each device changes over pressure, with the single bridge device exhibiting the best
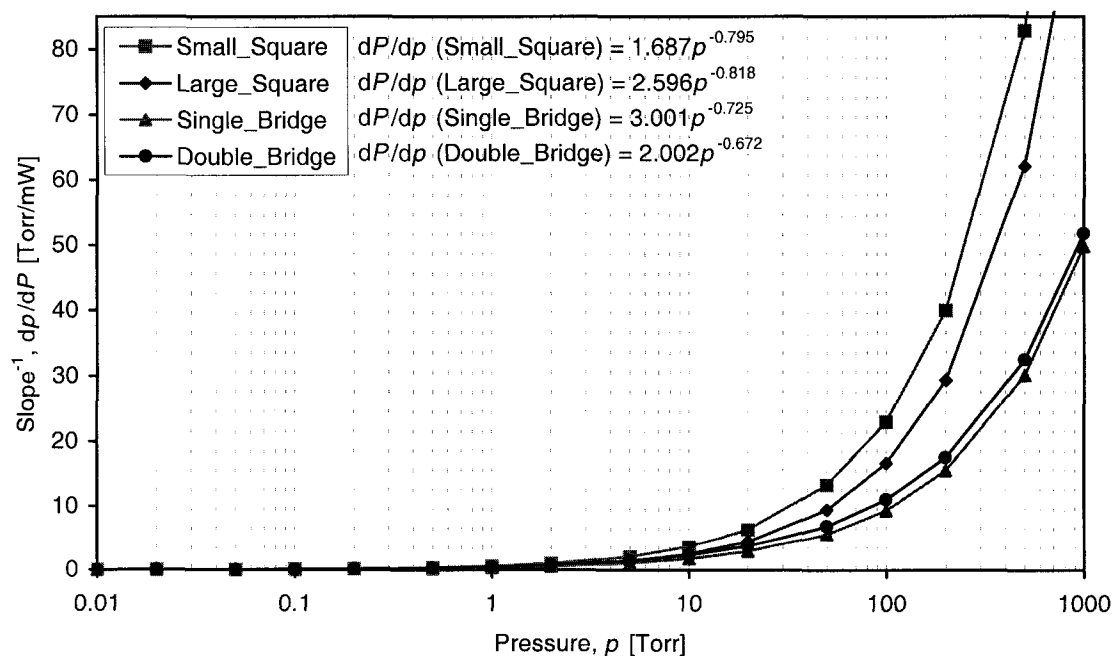
Figure 7.6 Inverse slope versus pressure for the data of each device type
operated under 10 μA constant detector response in nitrogen.

sensitivity (0.5 to 4.0%), and the small square device the worst sensitivity (1.4 to 6.8%), for pressure from 1000 to 0.2 Torr. The sensitivity is then determined by multiplying the inverse slope with the uncertainty in measuring power, assuming that the single bridge device would have produced results comparable to the double bridge device had it continued to function below 10 Torr. Below 0.2 Torr, the large square device is the most sensitive (5.2 to 8.9%) and the double bridge device (8.5 to 23%) the least sensitive. Again, compared to a standard Pirani gauge, the results shown here are at least twice as sensitive, with a substantial increase in useful operating range.

A plot of power per total device area versus pressure was produced from the data of Figure 5.16 and is shown in Figure 7.7. It was anticipated that dividing the data from each device by that device's total respective area would result in an overlap of the data. As seen in the figure, this was not the case and hence, it is not possible to strictly compare each device's response with each other. However, it should be noted that the order of appearance of the curves has changed from that of Figure 5.16. In the case of power per device area, the bridge devices require more power to heat up than the square devices, with the large square requiring the least power. The reason for the difference between the curves is directly related to the geometry of the platform and polysilicon. In the bridge devices, the polysilicon and platform exist as a single, long filament in which the heat loss occurs from the top and bottom surfaces and along the edges of the platform. In contrast, the square devices have a trace of polysilicon in the form of a serpentine path inside a square platform, where the heat loss is from the top and bottom surfaces, and only the outer trace of polysilicon experiences heat loss. To put it more clearly, the polysilicon in the center of the platform of the square devices experiences heat loss to the environment but also heat gain from the adjacent polysilicon traces, unlike the bridge devices. Therefore, the adjacent heating between the serpentine polysilicon traces in the square devices, the large square having the largest traces, results in less overall heat loss than is the case of the bridge devices where the polysilicon trace is not serpentine in shape.
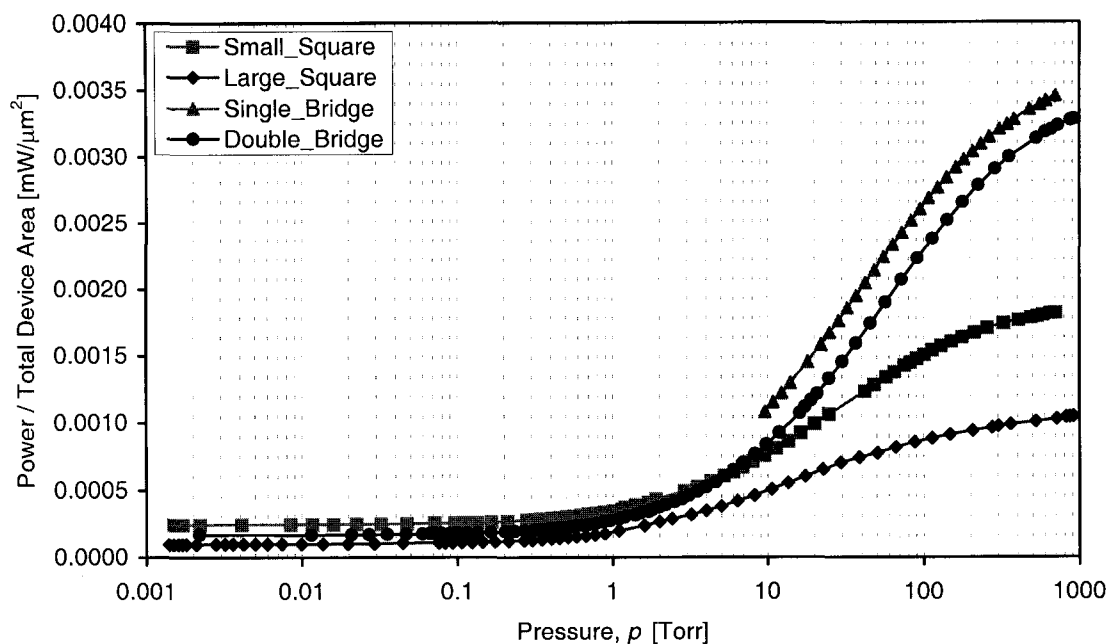
Figure 7.7 Plot of power / total device area versus pressure for each device operated at 10 μA constant detector response in nitrogen.

7.4 GAS ANALYSIS

7.4.1 Constant Power

Under constant power operation the shape of the experimental curves for each gas follow a similar pattern as those for nitrogen. The separation and positioning of the gas curves is also consistent with the relative thermal conductivity of each gas (Figure 6.7), with the exception of SF_6. The results from sulfur hexafluoride do not follow the expected pattern, as is the case with the other gases. This is, as previously suggested, likely the result of its decomposition at high temperature (leading to a durability problem), resulting in a gas or gas mixture having a different thermal conductivity than SF_6.

Further, the relative position of the gas curves is consistent among all device geometries (Figures 5.19 to 5.22), as expected, since changing the gas is an external condition that will influence the mean device temperature regardless of the device geometry. The bridge devices produce similar detector responses (with the double bridge consistently producing a lower response than the single bridge at a given pressure) for

each gas and the responses from the large square devices occur at lower pressures than those for the other devices, consistent with the results for nitrogen.

For all devices, operating at 8 mW constant power, the difference in detector current at a given pressure for each gas increases with decreasing pressure until the maximum safe detector current (10 μA) is reached. If the devices were to continue operating beyond the maximum safe detector current, the difference in detector current would continue to increase with decreasing pressure, reaching a maximum difference, and then decrease until the curves converged at approximately 0.01 Torr, as predicted by Figure 6.13. This convergence is in agreement with the predicted variation in thermal conductivity as a function of pressure (Figure 6.7) for each gas. To best distinguish between gases, the pressure at which the largest detector current difference between each gas occurs must be determined. For the gases tested here, the pressure at which the largest difference in detector signal for each gas occurs for each device type, and without exceeding the maximum safe response current, is listed in Table 7.2. The entries for the table were obtained from the data of each device type (Figures 5.19 to 5.22). The entries are limited by the endpoints of the gases not exceeding 10 μA of detector response, where the actual optimum pressure is suggested by Figure 6.13 to occur at a lower pressure than that stated in the table. The convergence of the helium and nitrogen curves needs also to be considered. In general, the gases can be easily distinguished over a range of pressure, governed by the large response region. The table also shows the optimum pressure that produces the largest difference in detector current between nitrogen and helium, as illustrated in Figure 7.8, and between nitrogen, argon, and krypton. The figure is produced from the data of Figure 5.19 with the axis scales increased to better show the crossover. The reason for distinguishing these two gases from the other gases is because, unlike the other gases, the nitrogen and helium experimental data cross each other at between 2 and 10 Torr, depending on the device type in use (5 Torr in the case of the small square as shown in Figure 7.8). This crossover is predicted by the change in thermal conductivity with pressure for each gas (Figure 6.7).

Table 7.2 Optimum pressure to distinguish between the gases tested for each device type at 8 mW constant power.

Device Type	Lowest pressure for largest difference between gases [Torr]		
	He, N₂, Ar, Kr	N₂, Ar, Kr	N₂, He only
Small Square	10.0	6.0	2.0
Large Square	1.30	1.30	0.55
Single Bridge	8.6	8.6	3.1
Double Bridge	9.6	9.6	2.7
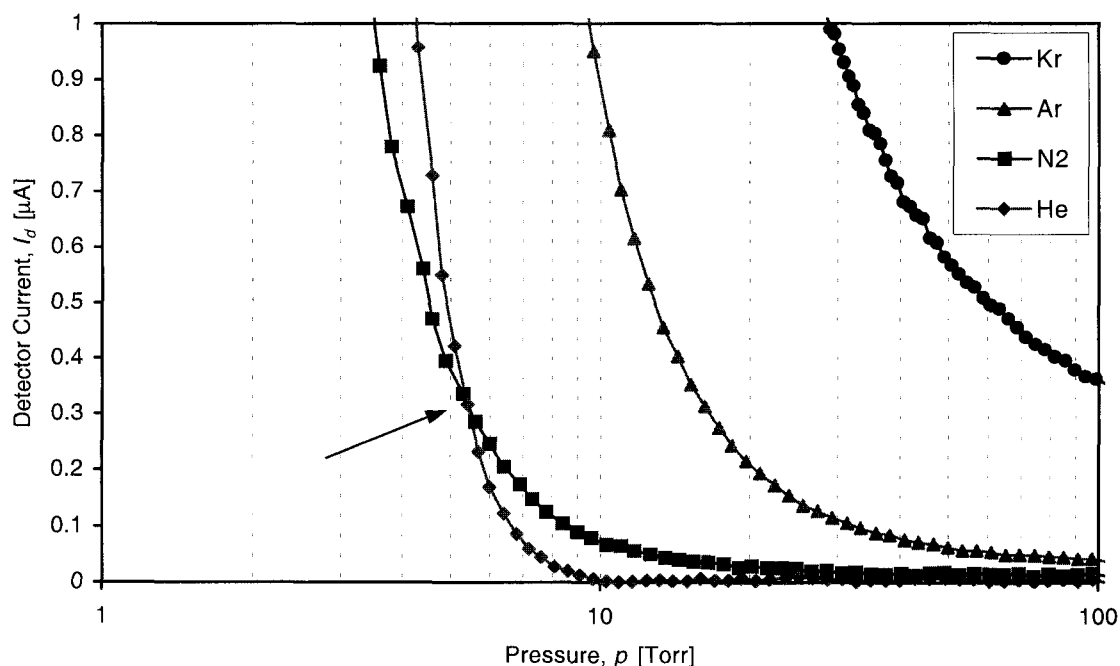
Figure 7.8 Detector current versus pressure for small square device in various gases showing crossover (arrow) between helium and nitrogen at approximately 5 Torr.

To find the smallest detectable difference in thermal conductivity we need to look at the lowest pressure at which the data is distinguishable within the uncertainty in measuring photodetector current. For each gas the pressure at which the curves could be resolved was determined and the thermal conductivity difference obtained from Figure 6.7. For constant power operation of 8 mW, the smallest detectable difference between any of the gas curves corresponds to a difference in thermal conductivity is 0.0152 W·m^{-1}K^{-1}. This means that any two known gases can be distinctly measured by operating a micro-Pirani device under 8 mW constant power and at some optimum

pressure, provided the difference in their thermal conductivities is greater than 0.0152 W·m^{-1}K^{-1}. Examples of such gases when the pressure is 700 Torr include nitrogen, hydrogen, oxygen, fluorine, bromine, helium, neon, argon, and krypton. Gases whose difference in thermal conductivities are less than 0.0152 W·m^{-1}K^{-1} and hence, could not be distinguished from each other at 700 Torr are krypton, xenon, radon, and chlorine. The disadvantage to detecting a gas in this manner is that in order to use the value of 0.0152 W·m^{-1}K^{-1}, a power of about 8 mW must be utilized. This restricts the pressure at which a significant detector response will be produced to pressure below 20 Torr.

For operation at powers less than 8 mW, as suggested by Figure 5.18, the overall response from each gas is less than that at 8 mW and the difference in detector current between the gases at a particular pressure is also smaller than that at 8 mW, suggesting that powers less than 8 mW would not distinguish between gases as effectively. At higher powers than 8 mW, as suggested by Figure 5.17, the He and N_2 curves appear to converge, the region of large increase in response shifts to higher pressure, as expected, and the separation between the curve increases. However, the useful range over which the gases can be easily detected without exceeding the maximum safe photodetector current has now decreased. Therefore, the results suggest that an optimum power, near 8 mW, will provide the maximum difference in detector current between the various gas curves, and the largest useful range for detection.

The crossover between the nitrogen and helium curves seen in the experimental figures (see Figure 7.8) occurs at a slightly higher pressure than shown in the plot of thermal conductivity versus pressure (Figure 6.6). The discrepancy is because the thermal conductivity figure is for a temperature of 700 K, whereas simulation suggests the gas temperature is over 1000 K. Higher gas temperature does shift the thermal conductivity nitrogen-helium crossover pressure closer to that shown by experiment.

A flowing gas mixture experiment was performed in which a small square device was operated at 8 mW constant power in nitrogen. Initially, the system was evacuated and a small nitrogen leak introduced such that the pressure was maintained constant at about 4 Torr. After a few minutes of operation, the nitrogen flow was replaced by an equal flow of helium gas, maintaining the system pressure at 4 Torr. The helium source

was maintained for one minute and then the system was restored to 100% nitrogen flow. Figure 7.9 shows the detector response versus time for the flowing gas mixture experiment. After two minutes of operation, at about the time of the introduction of helium, the response of the device decreases rapidly by 30%. After the helium is removed, the detector current gradually increases back to its original level as the helium leaves the system.
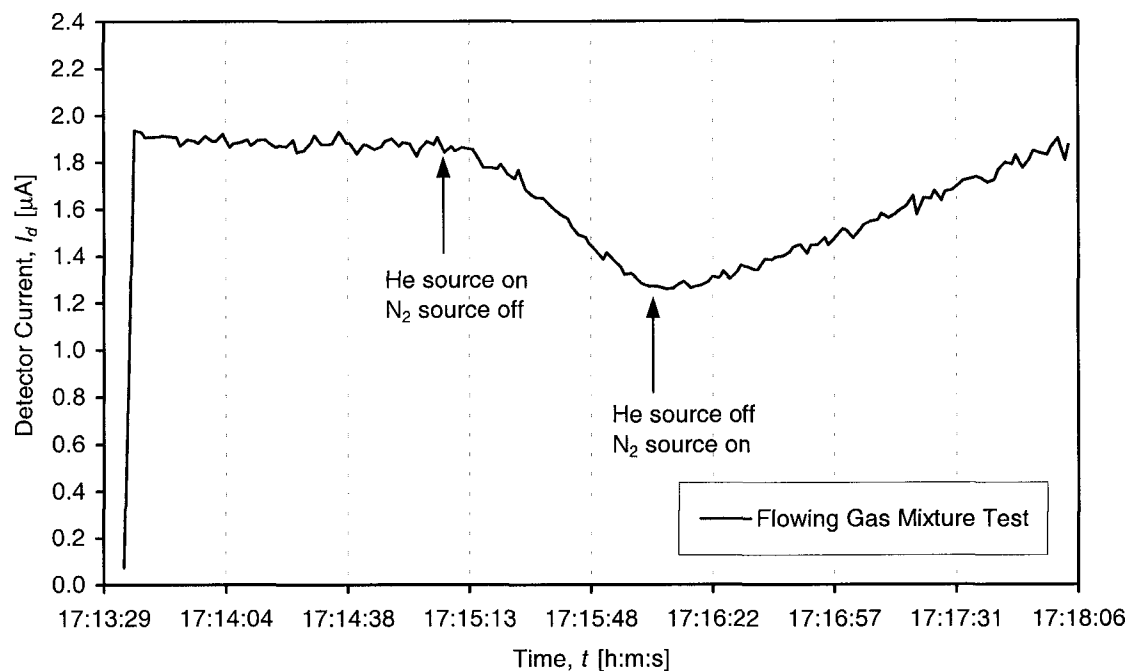
Figure 7.9 Detector current versus time for a small square device operated at 8 mW constant power in nitrogen with a helium source added and then removed.

Finally, a true test of any gas analysis system is not in the detection of a single gas, but rather in the detection of multiple gases simultaneously. That is, can a simple gas mixture be analyzed such that the percentage contribution from each gas is determined? The results from a binary combination of nitrogen with the other gases tested for a small square device operated at 8 mW constant power is shown in Figure 7.10. The system pressure was maintained at 4 Torr, and the percentage of gas mixture determined by the partial pressure of the nitrogen and other gas. For example, 1 Torr of nitrogen combined with 3 Torr of helium results in a total system pressure of 4 Torr and a

N$_2$:He gas mixture of 25:75%, respectively. For the results shown in the figure, the minimum resolvable difference in detector current was produced for mixtures A and B, namely 6.01 μA and 6.9 μA, respectively, where mixture A represents a 75:25% mixture of nitrogen to argon, and mixture B represents a 75:25% mixture of nitrogen to krypton. The effective thermal conductivity of a mixture of N gases is determined by [112]:

$$k_{g,effective} = \frac{\sum_{i=1}^{N} k_{g,i} \cdot v_i \cdot M_{g,i}^{1/3}}{\sum_{i=1}^{N} v_i \cdot M_{g,i}^{1/3}}, \tag{7.1}$$

where for each gas, $k_{g,i}$ is its thermal conductivity at the total system pressure (4 Torr), v_i is its volumetric fraction, and $M_{g,i}$ is its molar weight. For each respective chosen mixture, A and B in Figure 7.10, (7.1) produces $k_{g,effective}$ = 0.0328 W·m^{-1}K^{-1} and 0.0294 W·m^{-1}K^{-1}, for a minimum detectable difference in thermal conductivity, Δk_g, of 0.0034 W·m^{-1}K^{-1}. However, taking into consideration the error in measuring pressure for each gas results in an uncertainty in the minimum detectable thermal conductivity difference of 0.0006 W·m^{-1}K^{-1}. Therefore, a more realistic value for the minimum detectable Δk_g is 0.004 W·m^{-1}K^{-1}. At 700 Torr, this difference in thermal conductivity corresponds to a helium-nitrogen mixture, for example, of only 6%. However, operating at 8 mW produces a detector current of 0.01 μA for 100% nitrogen and 0.007 μA for 100% helium (Figure 5.19) environments, both considered un-resolvable with the uncertainty in measuring detector current, ±0.1 μA. Thus, detection of a 6% helium-nitrogen mixture would require operating the device at a higher power than 8 mW in order to produce a detector current of sufficient magnitude to be easily measured. An obvious limitation to gas analysis performed in this manner is that only binary mixtures of gases can be easily obtained. Compared to the previously determined value of 0.0152 W·m^{-1}K^{-1}, we believe that this earlier value is overly conservative due to the fixed difference in thermal conductivity for a pure gas with variation in pressure, as seen in Figure 6.13. Further work with gas mixtures was not performed due to a lack of operating devices.
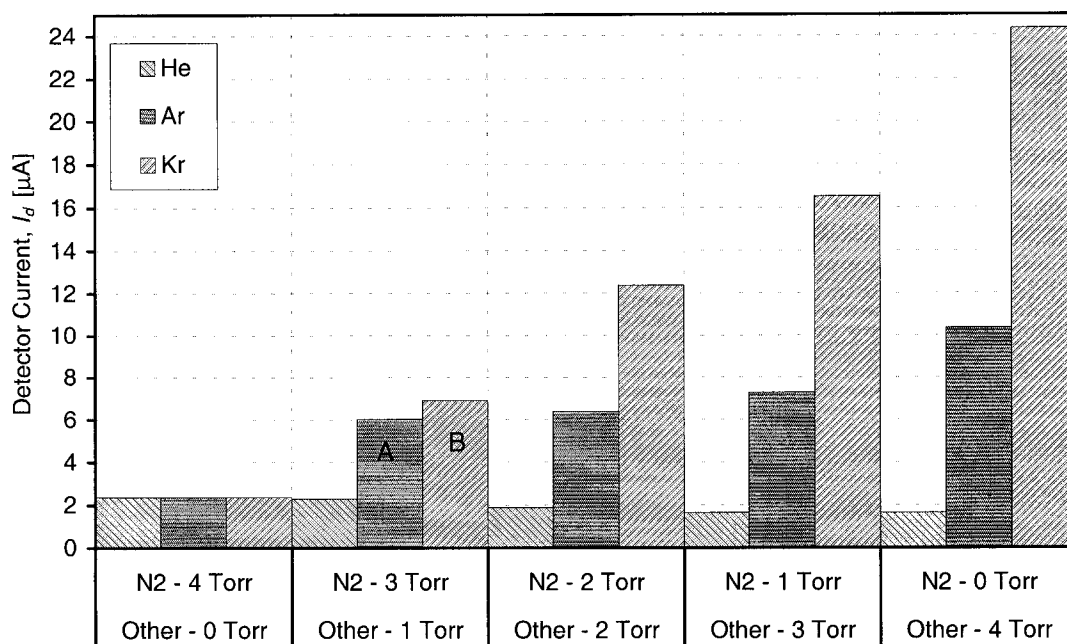
Figure 7.10 Detector current versus nitrogen-other gas mixture for a small square device operated at 8 mW constant power. Gas mixtures A and B were used in the determination of Δk_g.

7.4.2 Constant Response

The devices tested under constant photodetector response in various gases produced results in a predictable and consistent manner. The SF_6 tests, as in previous tests, did not produce results consistent with its relative value of thermal conductivity. Also, operating any device in SF_6 inevitably led to a durability problem, as mentioned before.

To distinguish the gases from each other, the largest difference in power for each device geometry occurs at 700 Torr, the highest pressure tested with the constant response mode in various gases, when operated at a constant detector current of 5 μA (Figures 5.32 to 5.35). To illustrate this difference, Figure 7.11 shows a plot of select data from Figure 5.32, where the helium curve is normalized and the other gas curves are normalized with respect to the helium curve. From the figure, the ratio of power required between each gas can then be determined. The figure shows that the greatest separation between each gas occurs at the highest pressure.

Unlike the results under constant power in various gases (Figures 5.21 and 5.22) in which the double bridge device operated at a slightly cooler temperature than the single bridge device, the single and double bridge devices (Figures 5.34 and 5.35) produced identical constant photodetector response curves. This suggests that the second bridge, designed to act as a heat sink, has only a marginal effect on the mean temperature of the heated bridge. Another possible explanation is simply that the results are within the repeatability variation of the device response.
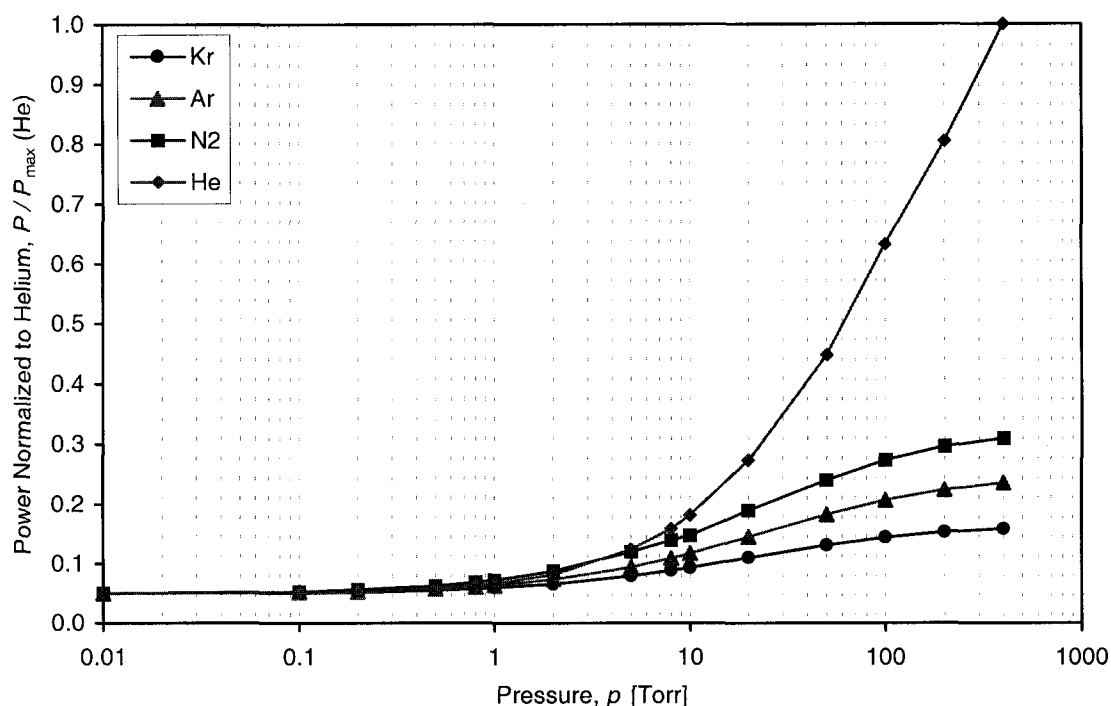
Figure 7.11 Power normalized to helium versus pressure for a small square device operated at 5 μA constant response in various gases.

For operation at constant detector response, the smallest detectable difference in thermal conductivity was determined in the same manner as done in the previous section. The lowest pressure at which the curves could be distinguished from each other within the uncertainty of calculating the input power was determined and correlated to the gas thermal conductivity (Figure 6.13) at that pressure. For a maintained detector response of 5 μA, the smallest detectable difference in gas thermal conductivity is 0.0024 $W \cdot m^{-1} K^{-1}$, similar to that determined for the gas mixtures. This suggests that operating under

constant photodetector response of 5 μA at 700 Torr, two known gases with as little as a 0.0024 W·m^{-1}K^{-1} difference in thermal conductivity could be distinctly measured. The advantage to detecting gases under constant photodetector response is that a large range of pressure can be utilized and the device operated at a temperature that maximizes device durability. Furthermore, maintaining a response greater than 5 μA and using pressure near 700 Torr produces a large separation in required power between each gas. Therefore, operation of micro-Pirani devices under these conditions should permit a large number of gases to be detected.

7.5 SUMMARY

In discussing the results of this project, a number of points have been brought forward increasing the understanding of the micro-Pirani gauge devices. The first point is that during the operation of the devices, a durability problem has been observed resulting from one of two failure mechanisms. An increase to the device life-time has been achieved by limiting the current through the structures, thus preventing type I failures. Limiting type II failure would take the form of limiting the thickness and number of silicon dioxide and silicon nitride layers or any other practice to reduce inherent stress in the devices.

The second point was that testing in sulfur hexafluoride was not feasible, possibly because of gas decomposition during operation. This resulted in inconsistent results and more importantly, short device lifetimes. In brief, the micro-Pirani gauge devices tested during this project are not electrically stable at high temperatures and should not be operated in environments that have the potential to create corrosive products upon heating.

As for the ability of the devices tested here to measure vacuum, the results show that pressure from 0.005 to 1000 Torr can be measured with high sensitivity by operating at either constant power or constant photodetector response. The single bridge device produced the best overall sensitivity to vacuum under constant power, and both the single bridge and large square devices under constant photodetector response.

In the application of gas detection, the four gases tested here can be distinguished by operating either at constant power or constant photodetector response. The pressure that best distinguishes the gases from each other varies by device for constant power. Under constant photodetector response, 700 Torr, the highest pressure tested, produces the greatest difference in required power to maintain a photodetector current of 5 μA for each gas. Application of these devices to the detection of gases is limited by the minimum detectable difference in gas thermal conductivity and operation in an explosive or flammable atmosphere is not recommended. For constant power operation, this minimum difference is 0.0152 W·m^{-1}K^{-1}, while in constant photodetector response mode the minimum difference is only 0.0024 W·m^{-1}K^{-1}.

Finally, the devices have also shown an effectiveness when used to determine a binary mixture of two known gases, distinguishing a difference in detector current for a thermal conductivity difference on the order of 0.004 W·m^{-1}K^{-1}, in general agreement with the constant detector response results, for a small square device operating at 8 mW constant power and 4 Torr.

Chapter
EIGHT
CONCLUSIONS AND FUTURE WORK

8.1 CONCLUSIONS

Four different types of optically-operated micro-Pirani gauges have been designed, fabricated, and tested for application in vacuum measurement and gas analysis. The four device types were entitled small square, large square, single bridge, and double bridge, each after their respective geometry. The devices, as received from the foundry, required post-process etching of the silicon substrate directly beneath the structures. Etched was performed with a combination of anisotropic and isotropic etchants (TMAH and XeF_2). Once post-processing was complete, the micro-Pirani structures exist as ohmically-heated, suspended platforms that emit visible radiation which is measured by a photodetector. The devices were operated in constant power and constant photodetector response modes, with both direct current and alternating current operation, for pressure ranging from 10^{-3} to 1000 Torr and in the presence of either nitrogen, helium, argon, krypton, or sulfur hexafluoride. The gases tested had a wide range of thermal conductivities to produce significant differences in detector signals. Testing in sulfur hexafluoride was halted as a result of operating temperatures in excess of its decomposition temperature, the decomposition products likely producing device failure.

The result of the vacuum measurement and gas analysis experiments show that the micro-Pirani devices, when operated such that the variation in device temperature is determined by measuring the radiation emitted, are at least twice as sensitive as standard, commercially available Pirani devices, with a two order of magnitude increase in useful pressure sensitive range. Vacuum can be measured most efficiently with the single bridge device under constant power and either the single bridge or large square devices under constant photodetector response. All four device types can detect the gases tested, with the optimum pressure to distinguish each gas under constant power varying by device. Under constant photodetector response, the optimum pressure to distinguish each

gas is at the highest pressure tested, 700 Torr. Under constant power operation, a pair of known gases whose difference in thermal conductivity is at least 0.0152 $W \cdot m^{-1} K^{-1}$ will produce distinguishable detector currents at the appropriate pressure. A thermal conductivity difference of 0.0024 $W \cdot m^{-1} K^{-1}$ is required to produce distinguishable results over a large pressure range in the case of constant photodetector response. Results from measuring the detector current for constant power operation in a nitrogen environment mixed with between 25% and 75% one of the other gases tested, confirms a minimum detectable thermal conductivity difference on the order of 0.004 $W \cdot m^{-1} K^{-1}$.

Transient response characteristics were also investigated, as well as variations in device characteristic dimension (etch depth between the device and the underlying substrate). The results of the transient response demonstrate the effectiveness of the devices to distinguish each gas at a variety of pressure.

An analytical model was described and numerical simulation results generated by finite element method. A trend comparison between the numerical simulation and experimental data was performed demonstrating good agreement, thus validating the model. A discussion of the repeatability and durability of these devices was also presented, the results of which suggest that thinner and fewer structural layers would improve device durability. This precludes the strict use of the CMOS process for device fabrication where the order, thickness, and composition of the deposited layers are fixed.

This dissertation has presented the following novel contributions to the body of knowledge concerning micro-Pirani structures:

- The analysis of heating effects observed during the isotropic, gas-phase etching of silicon by xenon difluoride.
- Significant improvement in the experimental setup and techniques for the operation and optical detection of micro-Pirani structures.
- A rigorous comparison between two photodetectors of different sizes and made from different materials.
- The analysis and detection of gas mixtures by micro-optical-Pirani devices.
- Improved and detailed modeling and simulation for these devices, most notably the inclusion of radiation considerations in the finite element model.

8.3 FUTURE WORK

It has been said that dissertation projects are never truly considered finished or complete. Therefore, regarding micro-optical Pirani devices, there are a number of areas that should be considered for further work. These include, but are obviously not limited to:

- The use of a photodetector with a (narrow) peak wavelength sensitivity beyond 1.5 μm. Such detectors include lead sulfide, indium antimony, and mercury cadmium tellurium composites, for example. Problems will arise from the high dark current, which will increase the amount uncertainty in measuring photodetector current. This issue can be improved by cooling the detector. An accurate measurement of the emissivity as a function of wavelength and temperature for these devices would help in the determination of the most effective wavelengths to monitor. Knowledge of the emissivity would also aid in the refinement of the electro-thermal model and subsequent simulations.

- Decrease photodetector-emitter separation distances to the sub-millimetre range. The advantage of this is an increase in solid angle ratio leading to a larger response. Other advantages include the detector influencing the characteristic dimension and the device heat loss by acting as a heat sink. The decrease in device-photodetector separation could be achieved by either flip-chip packaging or some other die-attach process.

- Design the micro-Pirani device with fewer process layers and thinner layers to reduce inherent stress and improve durability. For example, 0.1 μm of silicon dioxide above and below the resistive film. Such a structure would not be producible using the MITEL CMOS process, but would instead require custom fabrication. The use of a custom fabrication process usually does not allow for the integration of any electronic circuitry, such as an onboard constant power source. A solution to the problem of integration would be to fabricate the electronic circuitry on a separate die from the micro-Pirani devices, each die then being mounted within the same package.

Experimentation with other device geometries could also be investigated, including variations of the double bridge device where the second bridge heat sink is placed at various distances from the heated bridge.

- Replace the polysilicon resistive film with some other material that has a large positive TCR, but is more stable at high temperature. Two examples of the such a material include platinum oxide and tungsten oxide. Both of these high temperature stable materials are widely used in standard commercially available thermal-conductivity-type sensors because of their linear response to temperature.

- Utilize a faster response system for providing constant power or constant photodetector response feedback. This will result in better control and an improved measurement of the transient response, such as being able to accurately measure the detector rise- and fall-times over a wide range of pressures, and decreasing the current pulse width and period.

- Finally, operation of the devices in more gases, and in more gas mixtures, would confirm the minimum detectable difference in thermal conductivity as measured in this work.

REFERENCES

[1]   A. Roth, *Vacuum Technology, 3rd ed.*, Elsevier Science Publishing, New York, NY, 1990.

[2]   M. von Pirani, "Selbszeigendes vakuum-mefsinstrument", *Verhandlungen der Deutschen Physikalischen Gesellschaft*, vol. 8, 1906, pp. 686-694.

[3]   Leybold Vakuum, *Leybold vacuum products and reference book, 2001/2002 Ed.*, Cologne, Germany, pp. C16.03-C16.13.

[4]   A.M. Robinson, P. Haswell, R.P.W. Lawson, and M. Parameswaran, "A thermal conductivity microstructural pressure sensor fabricated in standard complementary metal-oxide semiconductor", *Rev. Sci. Instrum.*, vol. 63, no. 3, Mar. 1992, pp. 2026-2029.

[5]   C.H. Mastrangelo and R.S. Muller, "Microfabricated thermal absolute-pressure sensor with on-chip digital front-end processor", *IEEE J. Solid-State Circuits*, vol. 26, no.12, Dec. 1991, pp. 1998-2007.

[6]   C.H. Mastrangelo, "Thermal applications of microbridges", *Ph.D. Thesis*, University of California, Berkeley, 1991.

[7]   A.W. van Herwaarden and P.M. Sarro, "Floating-membrane thermal vacuum sensor", in *Proc. Intl. Conf. on Solid-State Sensors and Actuators (Transducers '87)*, Tokyo, 1987, pp. 287-290.

[8]   H. Baltes and D. Moser, "CMOS vacuum sensors and other applications of CMOS thermopiles", in *Proc. Intl. Conf. on Solid-State Sensors and Actuators (Transducers '93)*, Yokohama, Japan, 1993, pp. 736-741.

[9]   P.K. Weng and J.S. Shie, "Micro-Pirani vacuum gauge", *Rev. Sci. Instrum.*, vol. 65, no. 2, Feb. 1994, pp. 492-499.

[10]   J.J. van Baar, R.J. Wiegerink, T.S.J. Lammerink, G.J.M. Krijnen, and M. Elmenspoek, "Pirani pressure sensor with distributed temperature sensing", in *Proc. 2001 ASME Intl. Mech. Eng. Congr. Expo. (IMECE'01)*, New York, Nov. 2001.

[11] W. Allegretto, B. Shen, Z. Lai, and A.M. Robinson, "Numerical modeling of time response of CMOS micromachined thermistor sensor", *Sensors and Materials*, vol. 6, no. 2, Feb. 1994, pp. 71-83.

[12] N.R. Swart, "Heat transport in thermal-based microsensors", *Ph.D. Thesis*, University of Waterloo, Canada, 1994.

[13] M. Parameswaran, A.M. Robinson, Lj. Ristic, K. Chau, and W. Allegretto, "A CMOS thermally isolated gas flow sensor", *Sensors and Materials*, vol. 2, no. 1, Jan. 1990, pp. 17-26.

[14] D. Moser, R. Lenggenhager, G. Wachutka, and H. Baltes, "Fabrication and modeling of CMOS microbridge gas-flow sensors", *Sensors and Actuators B*, vol. 6, Jan. 1992, pp. 165-169.

[15] B. Shen, Z. Lai, A.M. Robinson, and W. Allegretto, "Thermal response of CMOS-micromachined thermistor sensors under constant power and constant current excitation", *Rev. Sci. Instrum.*, vol. 65, no.11, Nov. 1994, pp. 3528-3534.

[16] M. Parameswaran, A.M. Robinson, D.L. Blackburn, M. Gaitan, and J. Geist, "Micromachined thermal radiation emitter from a commercial CMOS process", *IEEE Electron Device Letts.*, vol. 12, no. 2, Feb. 1991, pp. 57-59.

[17] C.H. Mastrangelo, J.H. Yeh, and R.S. Muller, "Electrical and optical characteristics of vacuum-sealed polysilicon microlamps", *IEEE Trans. Electron Devices*, vol. 39, no. 6, June 1992, pp. 1363-1375.

[18] B. Shen, "CMOS actuators", *Ph.D. Thesis*, University of Alberta, Canada, 1996.

[19] T.C. Kleckner, R.P.W Lawson, and A.M. Robinson, "Constant power operation of incandescent micromachined polysilicon microresistors for use as vacuum pressure sensors", *J. Vac. Sci. Technol. A*, vol. 15, no. 5, Sep./Oct. 1997, pp. 2812-2815.

[20] Y. Ma, "CMOS optical micro-radiator vacuum sensor", *Ph.D. Thesis*, University of Alberta, Canada, 2002.

[21] H. Baltes and O. Brand, "CMOS-based microsensors", in *Proc. 14th European Conf. Solid-State Trans. (Eurosensors XIV)*, Copenhagen, sec. M1-1, Aug. 2000, pp. 1-8.

[22] Y. Matsuoka, Y. Yamamoto, K. Yamada, S. Shimada, M. Tanabe, A. Yasukawa, and H. Matsuzaka, "Characteristic analysis of a pressure sensor using the silicon

piezoresistance effect for high-pressure measurements", *J. Micromech. Microeng.*, vol. 5, no. 1, Mar. 1995, pp. 25-31.

[23] D. Briand, B. van der Schoot, N.F. de Rooij, H. Sundgren, and I. Lundström, "A low-power micromachined MOSFET gas sensor", *IEEE/ASME J. MEMS*, vol. 9, no. 3, Sep. 2000, pp. 303-308.

[24] A.V. Chavan and K.D. Wise, "Batch-processed vacuum-sealed capacitive pressure sensors", *IEEE/ASME J. MEMS*, vol. 10, no. 4, Dec. 2001, pp. 580-588.

[25] W.D. Jones, "Building safer cars", *IEEE Spectrum*, vol. 39, no. 1, Jan. 2002, pp. 82-85.

[26] J.S. Suehle, R.E. Cavicchi, M. Gaitan, and S. Semancik, "Tin oxide gas sensor fabricated using CMOS micro-hotplates and in-situ processing", *IEEE Electron Device Letts.*, vol. 14, no. 3, Mar. 1993, pp. 118-120.

[27] NEXUS, "Market analysis for microsystems 1996-2002" [online], Grenoble, France: NEXUS, May 2000 [cited Sept. 2001], available from World Wide Web: http://www.nexus-emsto.com/market-analysis/1-2.html. Link no longer active.

[28] NEXUS, "2002 Market analysis for microsystems" [online], Grenoble, France: NEXUS, April 2002, available from World Wide Web: http://www.nexus.emsto.com.

[29] K.B. Brown, Y. Ma, R.P.W. Lawson, W. Allegretto, F.E. Vermeulen, and A.M. Robinson, "Gas mixture analysis and vacuum measurement using a CMOS micromachined optical Pirani gauge", *IEEE Can. J. Elect. Comput. Eng.*, vol. 27, no. 1, Jan. 2002, pp. 27-31.

[30] N. Maluf, *An Introduction to Microelectromechanical Systems Engineering*, Artech House, Inc., Norwood, MA, 2000.

[31] M. Sadiku, "MEMS", *IEEE Potentials*, vol. 21, no.1, Feb./Mar. 2002, pp. 4-5.

[32] M. Madou, *Fundamentals of Microfabrication*, CRC Press LLC, Boca Raton, FL, 1997.

[33] S. Esteves, "Micromachining: An Overview of Techniques and MEMS Applications", *EE 601 Report*, University of Alberta, Canada, 1999.

[34] Lj. Ristic, ed., *Sensor Technology and Devices*, Artech House, Inc., Boston, 1994.

[35] S. Esteves, "CMOS Micromachined Devices for Application in Fluids", *M.Sc. thesis*, University of Alberta, Canada, 2000.

[36] T. Zhou, "CMOS Cantilever Microresonator", *M.Sc. thesis*, University of Alberta, Canada, 2000.

[37] B. Yu, "Large Deflections of a Magnetically Actuated Microcantilever with an On-Chip Permalloy Layer", *M.Sc. thesis*, University of Alberta, Canada, 2000.

[38] S.B. Fuller, E.J. Wilhelm, and J.M. Jacobson, "Ink-jet printed nanoparticle microelectromechanical systems", *J. MEMS*, vol. 11, no. 1, Feb. 2002, pp. 54-60.

[39] J. Bryzek, "Little ventured, less gained", *IEEE Spectrum*, vol. 33, no. 6, Jun. 1996, p. 8.

[40] K. Brown, "Gas Pressure Measurements with Cantilever-in-Cantilever Micro-structures", *M.Sc. thesis*, University of Alberta, Canada, 1999.

[41] D.P. Askeland, *The Science of Engineering Materials*, 2nd ed., Chapman & Hall, London, 1990.

[42] L.M. Landsberger, S. Naseh, M. Kahrizi, and M. Paranjape, "On hillocks generated during anisotropic etching of Si in TMAH", *J. MEMS*, vol. 5, no. 2, June 1996, pp. 106-116.

[43] J.M. Bustillo, R.T. Howe, and R.S. Muller, "Surface micromachining for micro mechanical systems", in *Proc. IEEE*, vol. 86, no. 8, Aug. 1998, pp. 1552-1574.

[44] M.A. Northrup, M.T. Ching, R.M. White, and R.T. Wastson, "DNA amplification with a microfabricated reaction chamber", in *Proc. 7th Int. Conf. on Solid-State Sensors and Actuators*, Yokohama, Japan, Jun. 1993, pp. 924-926.

[45] A.T. Woolley and R.A. Mathies, "Ultra-high speed DNA sequencing using capillary electrophoresis chips", *Anal. Chem.*, vol. 67, 1995, pp. 3676-3680.

[46] C. Rogers, "Intelligent materials", *Sci. American.*, vol. 273, no. 3, Sep. 1995, pp. 154-157.

[47] M.J. Daoura and D.R. Meldrum, "Precise automated control of fluid volumes inside glass capillaries", *J. MEMS*, vol. 8, no.1, Mar. 1999, pp. 71-77.

[48] S. Constantin, R. Freitag, D. Solignac, A. Sayah, and M.A.M. Gijs, "Capillary electrochromatography chip integrated in cartridge", in *Proc. 14th European Conf. on Solid-State Transducers*, Copenhagen, Denmark, Aug. 2000, pp. 287-290.

[49] J. Gutierrez-Monreal and C.M. Mari, "The use of polymer materials as sensitive elements in physical and chemical sensors", *Sensors and Actuators A*, vol. 12, no. 2, Aug./Sept. 1987, pp. 129-144.

[50] I. Strawbridge and P.F. James, "Glass formation from gels", in *High Performance Glasses*, M. Cable and J.M. Parker (eds.), Blackie Publishing, London, England, 1992, pp. 20-49.

[51] G.T.A. Kovacs, N.I. Maluf, and K.E. Peterson, "Bulk micromachining of silicon", in *Proc. IEEE*, vol. 86, no. 8, Aug. 1998, pp. 1536-1551.

[52] W. Kern and C.A. Deckert, "Chemical etching", in *Thin Film Processes*, J.L. Vossen and W. Kerns (eds.), Academic Press, Orlando, 1978.

[53] A. Reismann, M. Berkenblit, S.A. Chan, F.B. Kaufman, and D.C. Green, "The controlled etching of silicon in catalyzed ethylenediamine-pyrocatechol-water solutions", *J. Solid State Sci. and Techn.*, vol. 126, 1979, pp. 1406-1415.

[54] M. Vangbo and Y. Bäcklund, "Precise mask alignment to the crystallographic orientation of silicon wafers using wet anisotropic etching", *J. Micromech. Microeng.*, vol. 6, no. 2, June 1996, pp. 279-284.

[55] I.W.T. Chan, K.B. Brown, R.P.W. Lawson, A.M. Robinson, Y. Ma, and D. Strembicke, "Gas phase pulse etching of silicon for MEMS with xenon difluoride", in *IEEE Can. Conf. Elect. and Comp. Eng.*, Edmonton, 1999, pp. 1637-1642.

[56] X. Wang, X. Yang, K. Walsh, and Y. Tai, "Gas-phase silicon etching with bromine trifluoride", in *Int. Conf. on Solid-State Sensors and Actuators; Transducers '97*, Chicago, 1997, pp. 1505-1508.

[57] K.M. Striny, "Assembly techniques and packaging of VLSI devices", in *VLSI Technology*, 2nd ed., S.M. Sze (ed.), McGraw-Hill, New York, 1988.

[58] A.F. Flannery, N.J. Mourlas, C.W. Storment, S. Tsai, S.H. Tan, and G.T.A. Kovacs, "PECVD silicon carbide for micromachined transducers", in *Int. Conf. on Solid-State Sensors and Actuators; Transducers '97*, Chicago, 1997, pp. 217-220.

[59] W.F. Beach, T.M. Austin, and R. Olson, "Parylene coatings", in *Electronic Materials Handbook: Volume I, Packaging*, M.L. Minges, C.A. Dostal, and M.S. Woods (eds.), ASM International, Ohio, 1989.

[60] S. Cass, "Large Jobs for little Devices", *IEEE Spectrum*, vol. 38, no. 1, Jan. 2001, pp. 72-74.

[61] Y. Bäcklund, "Micromechanics in optical Microsystems-with focus on telecom systems", *J. Micromech. Microeng.*, vol. 7, no. 3, Sept. 1997, pp. 93-98.

[62] S. Cass, "MEMS In Space", *IEEE Spectrum*, vol. 38, no. 7, Jul. 2001, pp. 56-61.

[63] A. Martínez de Aragón, "Space application of micro/nano technologies", *J. Micromech. Microeng.*, vol. 8, no. 2, June 1998, pp. 54-56.

[64] J.W. Gardner, *Microsensors Principles and Applications*, John Wiley & Sons Ltd, Chichester, UK, 1995.

[65] W.S. Czarnocki and J.P. Schuster, "The evolution of automotive pressure sensors", *Sensors*, vol. 16, no. 5, May 1999, pp. 52-65.

[66] Lucas NovaSensor, "NPC-107 data sheet" [online], California, USA, June 2002, available from World Wide Web: http://www.novasensor.com.

[67] G.R. Fowles and G.L. Cassiday, *Analytical mechanics, 5th ed.*, Saunders College Publishing, New York, 1993.

[68] J. Söderkvist, "Micromachined gyroscopes", *Sensors and Actuators*, vol. A43, May 1994, pp. 65-71.

[69] P.F. Van Kessel, L.J. Hornbeck, R.E. Meier, and M.R. Douglass, "A MEMS-based projection display", in *Proc. IEEE*, vol. 86, no. 8, Aug. 1998, pp. 1687-1704.

[70] R.C. Anderson, G.J. Bogdan, A. Puski, and X. Su, "Genetic analysis systems: improvements and methods", *IEEE Tech. Digest Solid-State Sensor and Actuator Workshop*, Hilton Head Island, SC, Jun. 1998, pp. 7-10.

[71] C.C. Beatty, "A chronology of thermal ink-jet structures", *IEEE Tech. Digest Solid-State Sensor and Actuator Workshop*, Hilton Head, SC, Jun. 1996, pp. 200-204.

[72] R.S. Muller and K.Y. Lau, "Surface-micromachined microoptical elements and systems", in *Proc. IEEE*, vol. 86, no. 8, Aug. 1998, pp. 1705-1720.

[73] C.H. Mastrangelo, M.A. Burn, and D.T. Burke, "Microfabricated devices for genetic diagnostics", in *Proc. IEEE*, vol. 86, no. 8, Aug. 1998, pp. 1769-1787.

[74] C.T.C. Nguyen, "Frequency-selective MEMS for miniaturized communications devices", in *Proc. IEEE Aerospace Conf.*, vol. 1, Snowmass, Colorado, Mar. 1998, pp. 445-460.

[75] D.M. Bloom, "The grating light valve: revolutionizing display technology", in *Proc. SPIE, Projection Displays III*, vol. 3013, San Jose, CA, Feb. 1997, pp. 165-171.

[76] C. Marxer, C. Thio, M.A. Grétillat, N.F. de Rooij, R. Bättig, O. Anthamatten, B. Valk, and P. Vogel, "Vertical mirrors fabricated by deep reactive ion etching for fiber-optic switching applications", *J. MEMS*, vol. 6, no. 3, Sep. 1997, pp. 277-285.

[77] R. Zengerle, S. Kluge, M. Richter, and A. Richter, "A bi-directional silicon micropump", in *Proc. IEEE MEMS*, Amsterdam, The Netherlands, Jan. 1995, pp. 19-24.

[78] B.W. Chui, T.D. Stowe, T.W. Kenny, H.J. Mamin, B.D. Terris, and D. Rugar, "Low stiffness silicon cantilevers for thermal writing and piezoresistive readback with the atomic force microscope", *Applied Physics Letters*, vol. 69, no. 18, Oct. 1996, pp. 2767-2769.

[79] F.P. Incropera and D.P. DeWitt, *Introduction to heat transfer*, John Wiley & Sons, Inc., Toronto, 1996.

[80] J.F. O'Hanlon, *A user's guide to vacuum technology, 2nd ed.*, John Wiley & Sons, Inc., New York, 1989.

[81] C.M. Van Atta, *Vacuum science and engineering*, McGraw-Hill Book Co., New York, 1965.

[82] G.J. Van Wylen, R.E. Sonntag, and C. Borgnakke, *Fundamentals of classical thermodynamics, 4th ed.*, John Wiley & Sons, Inc., New York, 1994.

[83] M.J. Clugston, ed., *The new penguin dictionary of science*, Penguin Publishing, London, 1998.

[84] M.A. Pinsky, *Partial differential equations and boundary-value problems with applications, 2nd ed.*, McGraw-Hill, Inc., New York, 1991.

[85] G.A. Bird, *Molecular gas dynamics*, Oxford University Press, England, 1976.

[86] F. Reif, *Fundamentals of statistical and thermal physics*, McGraw-Hill, Inc., New York, 1965.

[87] M. Zeilik, S.A. Gregory, and E.v.P. Smith, *Introductory astronomy and astrophysics, 3rd ed.*, Saunders College Publishing, London, 1992.

[88] R.A. Serway, C.J. Moses, and C.A. Moyer, *Modern physics*, Saunders College publishing, London, 1989.

[89] Canadian Microelectronics Corporation, An introduction to micromachining: results of projects using Mitel's 1.5-micron CMOS technology to develop a Canadian MEMS process, report IC95-08, Queen's University, Canada, 1995.

[90] D. Johns and K. Martin, Analog integrated circuit design, John Wiley and Sons, Inc., New York, 1997.

[91] F.I. Chang, R. Yeh, G. Lin, P.B. Chu, E. Hoffman, E.J.J. Kruglick, K.S.J. Pister, and M.H. Hecht, "Gas-phase silicon micromachining with xenon difluoride", in *Proc. SPIE*, vol. 2641, Austin, TX, Oct. 1995, pp. 117-128.

[92] G.R. Hueckel, "Conduction and stability aspects of heavily doped polycrystalline silicon thin films", *Ph.D. Thesis*, Cornell University, New York, 1991.

[93] K. Ramkumar and M. Satyam, "Negative-resistance characteristics of polycrystalline silicon resistors", *J. Appl. Phys.*, vol. 62, no. 1, Jul. 1987, pp. 174-176.

[94] S. Das and S.K. Lahiri, "Electrical trimming of ion-beam-sputtered polysilicon resistors by high current pulses", *IEEE Trans. Electron Devices*, vol. 41, no. 8, Aug. 1994, pp. 1429-1434.

[95] E. Hecht, *Optics, 2nd ed.*, Addison-Wesley Publishing Co., Ontario, 1990.

[96] J. Singh, *Semiconductor Optoelectronics: Physics and Technology*, McGraw-Hill, Inc., New York, 1995.

[97] Solvay Fluor und Derivate GmbH, "Sulfur Hexafluoride", http://www.solvay-fluor.com/docroot/fluor/static_files/attachments/sf6_e.pdf, Germany, 2001.

[98] B. Sunden and M. Faghri, ed., *Modeling of Engineering Heat Transfer Phenomena, vol. 2*, Computational Mechanics Publications, UK, 1999.

[99] C.L. Tien, A. Majumdar, and F.M. Gerner, ed., *Microscale Energy Transport*, Taylor & Francis, UK, 1998.

[100] Ansys documentation is available from ANSYS, Inc., [online], Pennsylvania, USA, April 2003, available from World Wide Web: http://www.ansys.com.

[101] University of Oulu, "ANSYS 6.1 Documentation", [online], Oulun Yliopisto, Finland, April 2003, available from World Wide Web: http://www.oulu.fi/atkk/tkpalv/unix/ansys-6.1/content/.

[102] Y.S. Touloukian and T. Makita, *Thermophysical Properties of Matter*, Purdue Research Foundation, New York, 1970.

[103] J.R. Hook and H.E. Hall, *Solid State Physics*, 2nd ed., John Wiley & Sons, Ltd., England, 1994.

[104] K. Ng, *Complete Guide to Semiconductor Devices*, McGraw-Hill, Inc. New York, 1995.

[105] J.R. Welty, *Engineering Heat Transfer, SI Version*, John Wiley & Sons, Inc., New York, 1978.

[106] P.P.S. Juneja, "A Micromachined Wide-Range Vacuum Sensor Employing Phase-Sensitive Detection", *M.Sc. Thesis*, Simon Fraser University, Canada, 1993.

[107] N.B. Vargaftik, *Tables of Thermophysical Properties of Liquids and Gases*, 2nd ed., Nauka Press, Moscow, 1975.

[108] G. Carrington, *Basic Thermodynamics*, Oxford University Press, USA, 1995.

[109] H. Tada, "Novel Microelectromechanical Systems for the Study of Thin Film Properties and Measurement of Temperatures During Thermal Processing", *M.Sc. Thesis*, Tufts University, USA, 1999.

[110] H. Akimori, N. Owada, T. Taneoka, and H. Uda, "Reliability study of polycrystalline silicon thin film resistors used in LSIs under thermal and electrical stress", in *Proc. IEEE Int. Reliability Phys. Symp.*, Mar. 1990, pp. 276-280.

[111] W. Allegretto, B. Shen, P. Haswell, Z. Lai, and A.M. Robinson, "Numerical modeling of a micromachined thermal conductivity gas pressure sensor", *IEEE Trans. Computer-Aided Design of Integrated Circuits and Systems*, vol. 13, no. 10, Oct. 1994, pp. 1247-1256.

[112] R.C. Reid, J.M. Prausnitz, and T.K. Sherwood, *The Properties of Gases and Liquids*, 3rd ed., McGraw-Hill, Inc. New York, 1977.

EFFECTIVE REFLECTANCE CALCULATION

In this appendix, we detail the method used to determine the effective reflectance of light incident onto an absorbing surface, $R_{e,effective}$, as described by (5.9). Consider a flat, circular, absorbing surface of radius, r_d, placed directly above and centered at a distance s_1 from a diffuse point source emitter of light (Figure A.1). The light will intersect the surface of the disk at a distance r from its center and at an incident angle θ, after traveling a distance r', where the distance from the point source to the edge of the disk is represented by d. Therefore:

$$r' = \sqrt{s_1^2 + r^2} ,$$

(A.1)

$$d = \sqrt{s_1^2 + r_d^2} , \text{and}$$

(A.2)

$$\sin\theta = \frac{r}{\sqrt{s_1^2 + r^2}} \Rightarrow \theta = \sin^{-1}(\frac{r}{\sqrt{s_1^2 + r^2}}) .$$

(A.3)
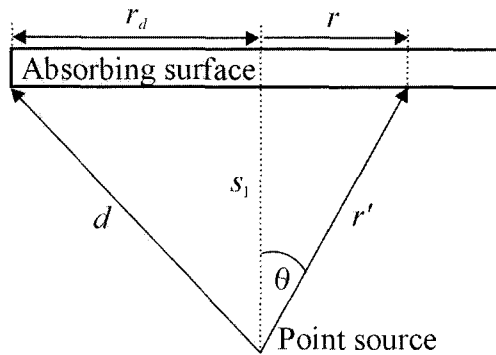
Figure A.1 Light path from a diffuse point source emitter to a flat surface.

The total power incident on the surface at distance r' is equal to the total emitted power times the area of the spherical surface intersected by the entire disk, divided by the area of the spherical surface intersected by the disk at distance r', or:

$$I_o(r') = \frac{I_o(d) \cdot 4\pi d^2}{4\pi(r')^2} = \frac{I_o(d) \cdot d^2}{(r')^2} .$$

(A.4)

Looking now at the surface of the disk from above (Figure A.2), the light incident at radius r may occur at any polar angle over the surface. To determine the overall

reflectance at any radius r, and for all polar angles, we define a differential radius, dr, on the surface as shown by the figure.
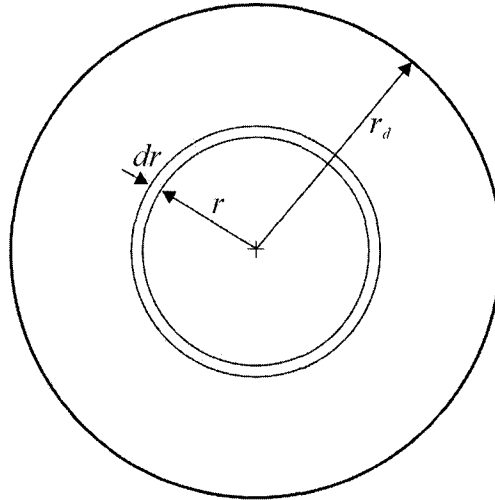
Figure A.2 Light incident over a differential radius, dr, and at any polar angle, as viewed from above the absorbing surface.

The incident power on the surface is then described by

$$I_i = \int_0^{r_d} I_o(r') \cdot 2\pi r \sin\theta dr . \qquad (A.5)$$

Substituting (A.4) into (A.5) yields

$$I_i = 2\pi \cdot I_o(d)d^2 \cdot \int_0^{r_d} \frac{r\sin\theta}{(r')^2} dr . \qquad (A.6)$$

The effective reflected power from the surface is:

$$I_{r,effective} = \int_0^{r_d} R_e(\theta) \frac{I_o(d)d^2 \cdot 2\pi r \sin\theta}{(r')^2} dr \text{ , or} \qquad (A.7)$$

$$I_{r,effective} = 2\pi \cdot I_o(d)d^2 \int_0^{r_d} R_e(\theta) \frac{r\sin\theta}{(r')^2} dr . \qquad (A.8)$$

The effective reflectance is produced by the ratio of reflected to incident powers, as described by (5.5). That is, (A.8) divided by (A.5), or:

$$R_{e,effective} = \frac{I_i}{I_{r,effective}} = \frac{\int_0^{r_d} R_e(\theta) \cdot \frac{r\sin\theta}{(r')^2} dr}{\int_0^{r_d} \frac{r\sin\theta}{(r')^2} dr}. \tag{A.9}$$

Substituting (A.1) and (A.3) into (A.9) results in

$$R_{e,effective} = \frac{\int_0^{r_d} R_e(\sin^{-1}(\frac{r}{(s_1^2 + r^2)^{1/2}})) \cdot \frac{r^2}{(s_1^2 + r^2)^{3/2}} dr}{\int_0^{r_d} \frac{r^2}{(s_1^2 + r^2)^{3/2}} dr}, \tag{A.10}$$

where the reflectance in the numerator is described by (5.7) and (5.8), namely

$$R_{e,\perp} = \Gamma_\perp^2 = \left\{ \frac{\cos\theta_i - \sqrt{\frac{n_2^2}{n_1^2} - \sin^2\theta_i}}{\cos\theta_i + \sqrt{\frac{n_2^2}{n_1^2} - \sin^2\theta_i}} \right\}^2, \tag{5.7}$$

$$R_{e,//} = \Gamma_{//}^2 = \left\{ \frac{\frac{n_2^2}{n_1^2}\cos\theta_i - \sqrt{\frac{n_2^2}{n_1^2} - \sin^2\theta_i}}{\frac{n_2^2}{n_1^2}\cos\theta_i + \sqrt{\frac{n_2^2}{n_1^2} - \sin^2\theta_i}} \right\}^2, \tag{5.8}$$

for s- and p-polarized light, respectively. In the case of un-polarized light the mean value of (5.7) and (5.8) is used for R_e. Given the form of the integral in the numerator in (A.10), an analytical solution is not feasible. Hence, the use of a numerical method is required to estimate the effective reflectance.

VACUUM MEASUREMENT FIGURES

The following figures provide more detail on the experimental data not shown in Chapter 5. Curves are labeled as XX_YY_ZZmW or XX_YY_ZZuA, corresponding to device YY, residing on die XX, and operated either at power ZZ in milliwatts or with a constant photodetector response of ZZ μA. All curves are from experimental trials while sourcing direct current in nitrogen.
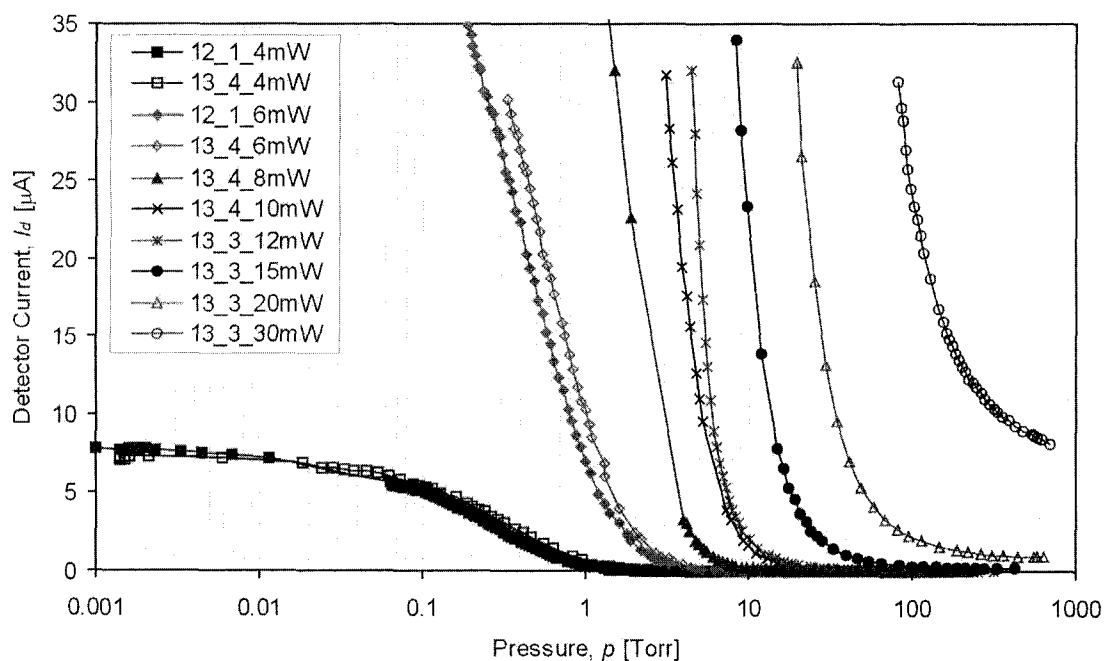
Figure B.1 Detector current versus pressure for small square devices operating under various constant powers in nitrogen.
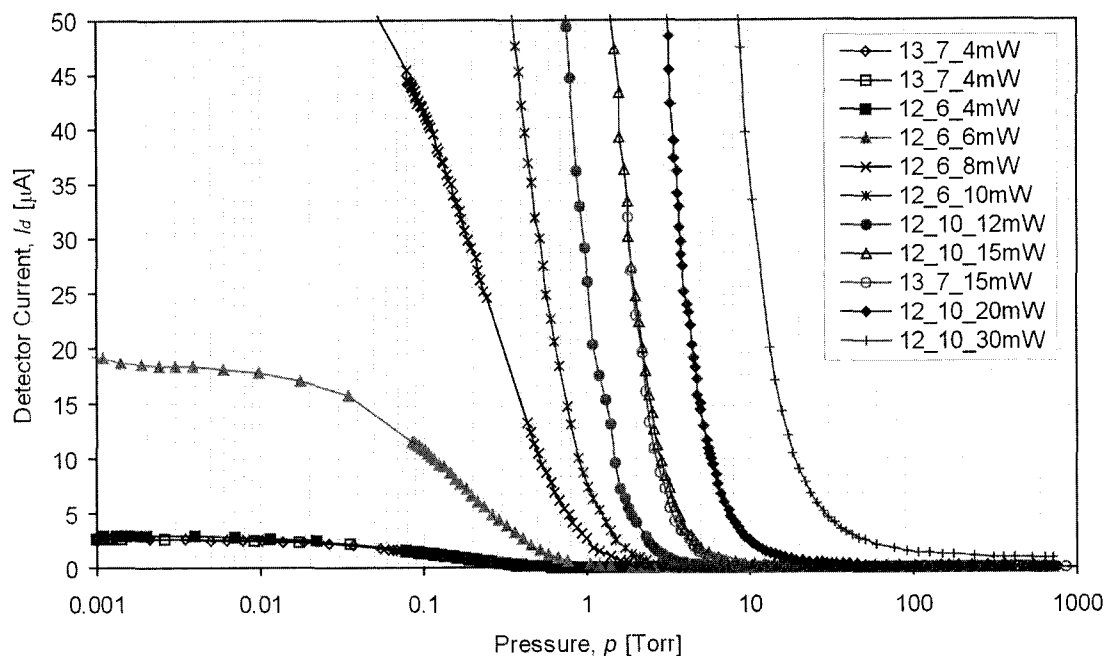
Figure B.2 Detector current versus pressure for large square devices operating under various constant powers in nitrogen.
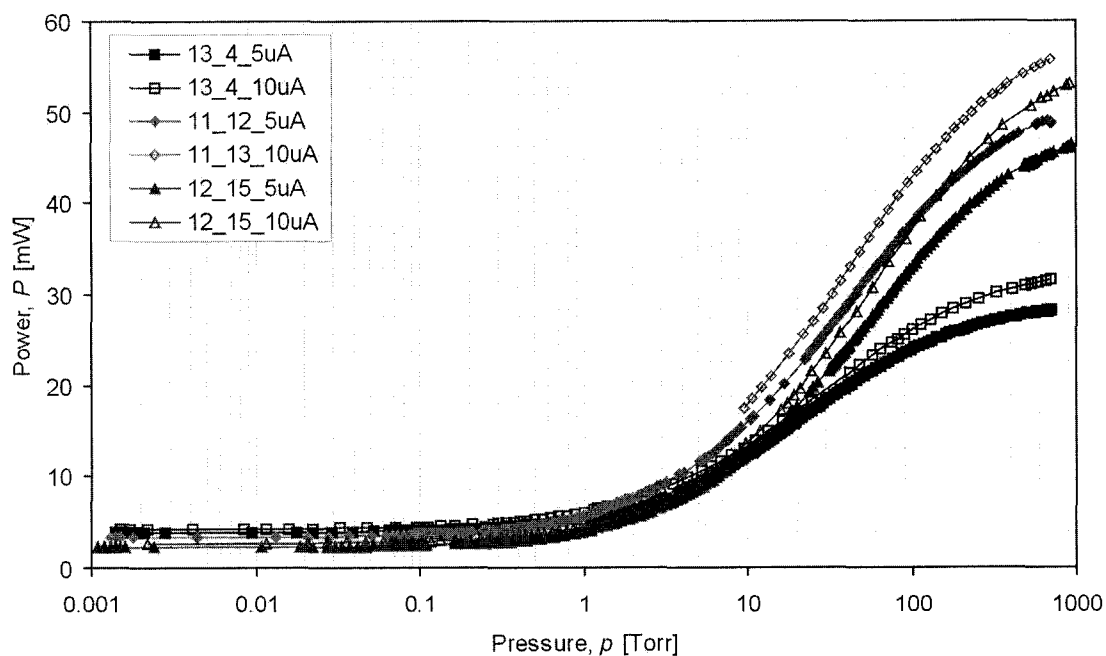
Figure B.3 Power versus pressure for small square, single bridge, and double bridge devices operating under a constant detector response of 5 and 10 μA in nitrogen.

GAS ANALYSIS FIGURES

The following figures provide more detail on the experimental data not shown in Chapter 5. Curves are labeled as XX_YY_ZZmW_GG or XX_YY_ZzuA_GG, corresponding to device YY, residing on die XX, and operated either at power ZZ in milliwatts or with a constant photodetector response of ZZ μA. The notation, GG, corresponds to the gas used (N_2, He, Ar, Kr, or SF_6). All figures are for devices under direct current source.
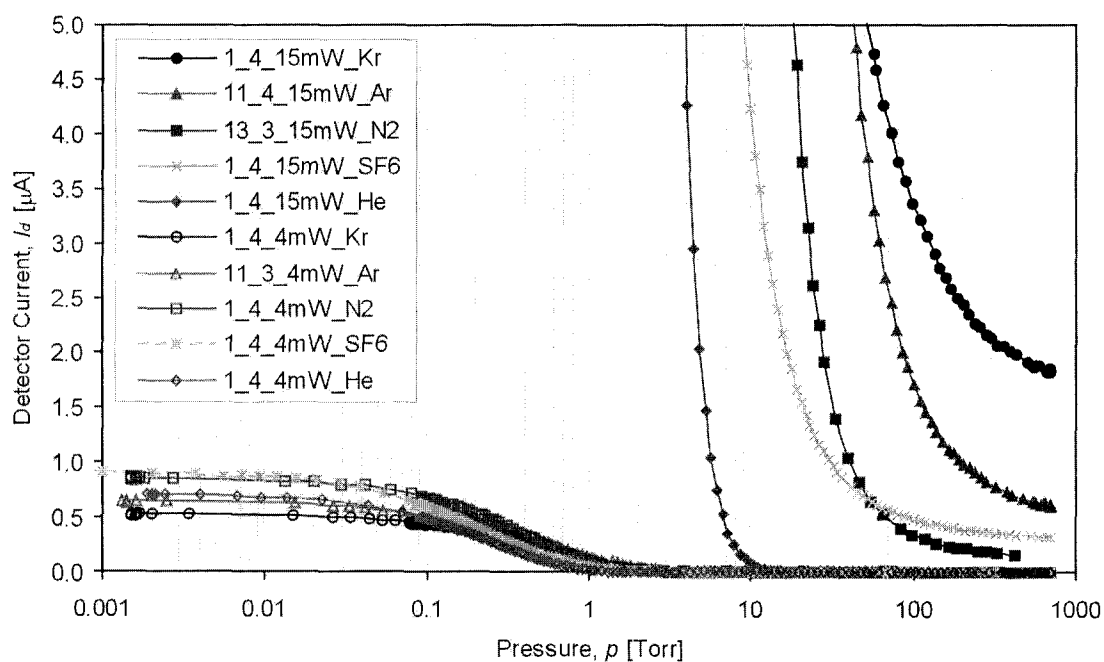
Figure C.1 Detector current versus pressure for small square devices in various gases under constant power operation.
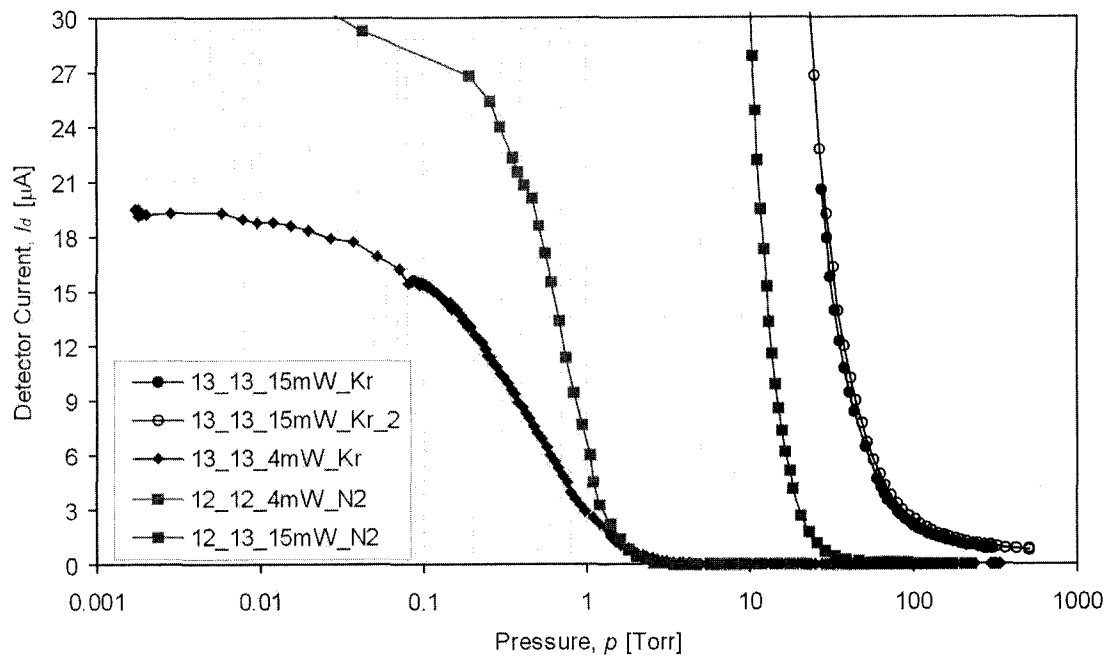
Figure C.2 Detector current versus pressure for single bridge devices in various gases under constant power operation.
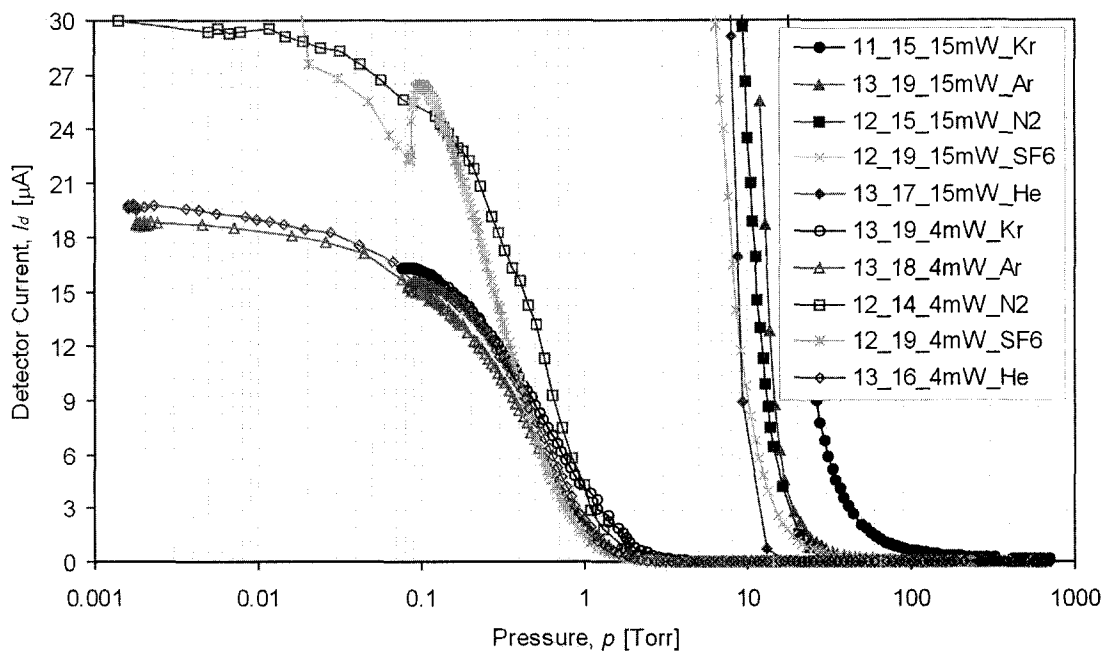
Figure C.3 Detector current versus pressure for double bridge devices in various gases under constant power operation.
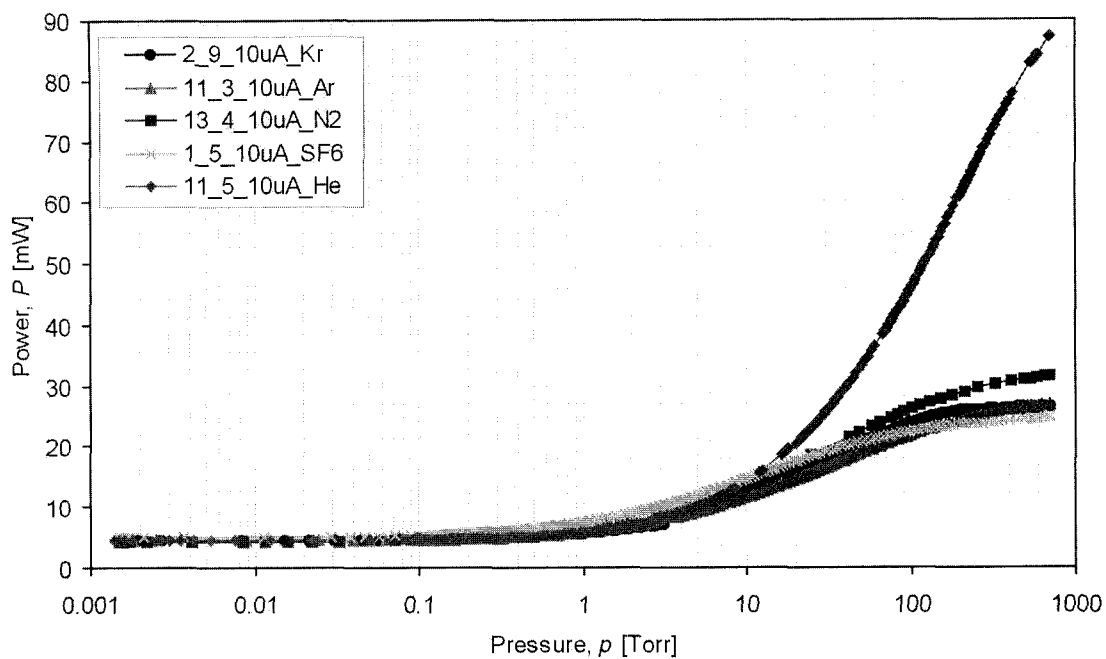
Figure C.4 Power versus pressure for small square devices
in various gases under constant response operation.
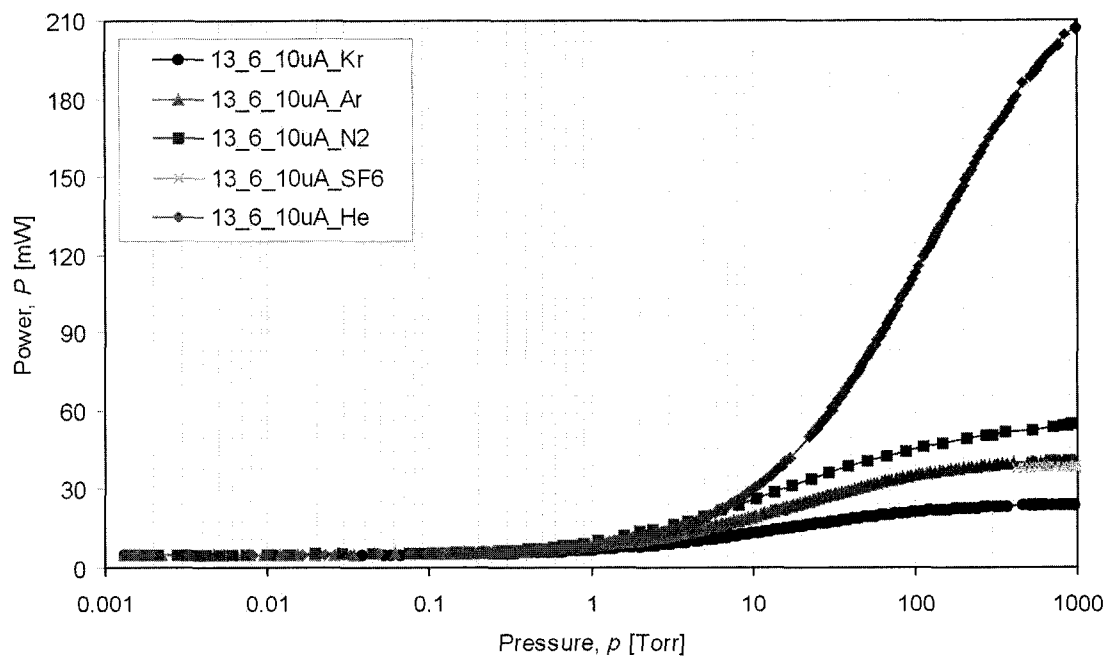
Figure C.5 Power versus pressure for large square devices
in various gases under constant response operation.
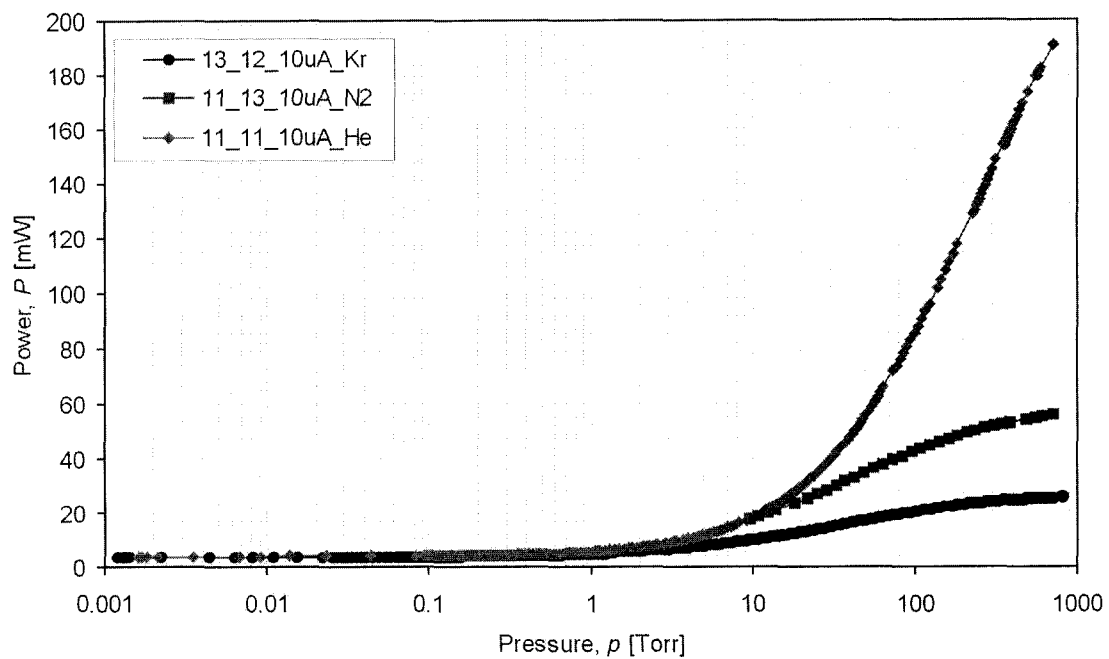
Figure C.6 Power versus pressure for single bridge devices
in various gases under constant response operation.

MATLAB™ SOURCE CODE

D.1 The following code simulates the steady-state photodetector current versus pressure for a small square device using the electro-thermal model as described by (6.9):

```
%*****************************************************
%Micro-optical Pirani gauge electro-thermal model
%-plots the detector current versus pressure curve
%-for various input powers based on the mean
%device temperature.
%*****************************************************
k=1.38e-23;   %Boltzmann constant
tg=293;       %room temperature (K)
x=120e-6;     %micro-radiator surface dimension (m)
y=x;
L=69e-6;      %supporting arm length (m)
W=21.5e-6;    %supporting arm width (m)
z=3.7e-6;     %supporting arm thickness (m)
d=85e-6;      %etch depth (m)
n=4.8;          %approximation coefficient
v=17;           %transition coefficient
e=0.05;        %emissivity, 0 to 1.0
sar=0.1615;   %solid angle ratio Ge
%experiment
press=[484.6 203.2 103.7 49.2 20.2 10.3 5.3 4.1 3 2 1.6];
expt=[0.0088 0.0119 0.0124 0.0186 0.0289 0.0677 0.3354 0.6724 1.5635
4.0285 8.8855];
pressh=[451.6 136.8 49.3 20.6 9.7 8.1 6 4.8 3.9 3 2.6 2.1];
expth=[0.0026 0.0037 0.0078 0.0037 0.0062 0.0279 0.169 0.5489 1.5294
3.6728 5.6649 9.5347];
pressa=[430 199.7 103.6 53.4 21 10.4 8 6.2 4.9 4.1 3.2];
expta=[0.0212 0.0269 0.0378 0.0574 0.1944 0.8089 1.4271 2.4929 4.1733
5.9058 9.2861];
pressk=[493 220.8 109 50.7 33 25.1 19.9 15 11 8.9 7.1 6];
exptk=[0.2243 0.2631 0.3535 0.566 0.8549 1.2053 1.6131 2.4706 3.8734
5.2147 7.3902 9.759];
%---------------------------------------------------
for Pin = [0.008]% 0.012] %input power(s) in W
  for p=[1 2 5 10 20 50 100 200 500 1e3 2e3 5e3 1e4 2e4 5e4 1e5]
%pressure (Pa)
      %Nitrogen parameters
      kg=0.0259;     %conductivity at 1 atm and 298 K
      a=3.70e-10;    %molecular collision diameter
      po=v*k*tg/sqrt(2)/pi/a^2/d;
      %Helium parameters
      kgh=0.152;     %conductivity at 1 atm and 298 K
      ah=1.20e-10;   %molecular collision diameter
      poh=v*k*tg/sqrt(2)/pi/ah^2/d;
```

```
%Argon parameters
kga=0.01772;    %conductivity at 1 atm and 298 K
aa=2.90e-10;    %molecular collision diameter
poa=v*k*tg/sqrt(2)/pi/aa^2/d;
%Krypton parameters
kgk=0.00943;    %conductivity at 1 atm and 298 K
ak=3.30e-10;    %molecular collision diameter
pok=v*k*tg/sqrt(2)/pi/ak^2/d;
%-------------------------------------------------
%radiation heat loss
A=x*y;                   %area of platform
ste=5.67e-8;            %Stefan-Boltzmann constant
delta=2*e*ste*A;        %radiation term
%conduction through arms
k1=1.4*0.96+34*0.04;    %thermal conductivity
beta=2*k1*W*z/L;        %cond eqn
%conduction through gas
alpha=kg*n*p*A/d/po/(1+p/po);    %loss to substrate
alphah=kgh*n*p*A/d/poh/(1+p/poh);
alphaa=kga*n*p*A/d/poa/(1+p/poa);
alphak=kgk*n*p*A/d/pok/(1+p/pok);
%-------------------------------------------------
gamma=delta*tg^4+(beta+alpha)*tg+Pin;
gammah=delta*tg^4+(beta+alphah)*tg+Pin;
gammaa=delta*tg^4+(beta+alphaa)*tg+Pin;
gammak=delta*tg^4+(beta+alphak)*tg+Pin;
epsilon=alpha+beta;
epsilonh=alphah+beta;
epsilona=alphaa+beta;
epsilonk=alphak+beta;
%-------------------------------------------------
%solving equations...
%-------------------------------------------------
T=[delta 0 0 epsilon -gamma];
Th=[delta 0 0 epsilonh -gammah];
Ta=[delta 0 0 epsilona -gammaa];
Tk=[delta 0 0 epsilonk -gammak];
t=roots(T);th=roots(Th);ta=roots(Ta);tk=roots(Tk);
t=t(4);
th=th(4);
ta=ta(4);
tk=tk(4);
Idg=quadl('bbody2',500,2200,[],[],t)*sar*(A+2*L*W)*1e6;
Idgh=quadl('bbody2',500,2200,[],[],th)*sar*(A+2*L*W)*1e6;
Idga=quadl('bbody2',500,2200,[],[],ta)*sar*(A+2*L*W)*1e6;
Idgk=quadl('bbody2',500,2200,[],[],tk)*sar*(A+2*L*W)*1e6;
%plot the results
%-------------------------------------------------
% Detector response vs pressure
semilogx(p*7.5e-3,Idg,'bs',p*7.5e-3,Idgh,'gd',p*7.5e-
3,Idga,'r^',p*7.5e-3,Idgk,'ko');
%semilogx(p*7.5e-3,t,'bs',p*7.5e-3,th,'gd');
hold on;
end
semilogx(press,expt,'bx',pressh,expth,'gx',pressa,expta,'rx',pressk,exp
tk,'kx');
xlabel('Pressure, p [Torr]');
```

```
    ylabel('Detector Current, Id [uA]');
    %ylabel("Mean Temperature, T  [K]');
    legend('N2','He','Ar','Kr');
    axis([0.001,1000,0,70]);
end
```

D.2 The following code performs the function of integrating the spectral emission and germanium photodetector response over the specified wavelengths as described by (6.17). This function is called upon in the electro-thermal model source code to produce the photodetector response when given the mean device temperature:

```
function [Id,E]=bbody2(l,T);
%finds emissive power in W/m^2/m
%input wavelength (l) in nm, temperature (T) in K
ll=l*1e-9;
El=3.747e-16./ll.^5./(exp(0.0144./ll./T)-1);
E=El*1e-9; %emissive power in W/m^2/nm
if l<1513
    R=8e-8*l.^2+7e-4*l-0.5134;
else
    R=3e-6*l.^2-0.012*l+11.918;
end
Id=E.*R;   %detector response in A/m^2/nm
```

D.3 The following code performs the same function as the previous code (C.2) but for the silicon photodetector:

```
function [Id,E]=bbody(l,T);
%finds emissive power in W/m^2/m
%input wavelength (l) in nm, temperature (T) in K
ll=l*1e-9;
El=3.747e-16./ll.^5./(exp(0.0144./ll./T)-1);
E=El*1e-9; %emissive power in W/m^2/nm
if l<991
    R=2e-9*l.^3-5e-6*l.^2+0.005*l-1.342;
else
    R=-2e-5*l.^2+0.046*l-21.838;
end
Id=E.*R;   %detector response in A/m^2/nm
```

ANSYS™ SOURCE CODE

E.1 The following code is the input file for building the numerical model in ANSYS for simulating the thermal response of the small square geometry:

```
/PREP7
/TITLE, Thermal Analysis of Small Square
/UNITS, SI

! Define model geometry with keypoints (k,keypt #,x,y,z) &
! create areas (A,keypt1,...,keypt8)

k,1,-60,60,0          ! Inner platform
k,2,60,60,0
k,3,60,-60,0
k,4,-60,-60,0
A,1,2,3,4

k,5,45,60,0                    ! Arms that extend from inner platform to
k,6,60,45,0                    ! surrounding 'L-shaped' regions
k,7,122,107,0
k,8,107,122,0
A,5,6,7,8

k,9,-45,-60,0
k,10,-60,-45,0
k,11,-122,-107,0
k,12,-107,-122,0
A,9,10,11,12

k,13,-42,-50,0    ! Polysilicon serpentine sections
k,14,-42,50,0
k,15,-27,50,0
k,16,-27,-50,0
k,17,-32,-50,0
k,18,-32,45,0
k,19,-37,45,0
k,20,-37,-50,0
A,13,14,15,16,17,18,19,20

k,21,-22,-50,0
k,22,-22,50,0
k,23,-7,50,0
k,24,-7,-50,0
k,25,-12,-50,0
k,26,-12,45,0
k,27,-17,45,0
k,28,-17,-50,0
```

```
A,21,22,23,24,25,26,27,28

k,29,-2,-50,0
k,30,-2,50,0
k,31,13,50,0
k,32,13,-50,0
k,33,8,-50,0
k,34,8,45,0
k,35,3,45,0
k,36,3,-50,0
A,29,30,31,32,33,34,35,36

k,37,18,-50,0
k,38,18,50,0
k,39,33,50,0
k,40,33,-50,0
k,41,28,-50,0
k,42,28,45,0
k,43,23,45,0
k,44,23,-50,0
A,37,38,39,40,41,42,43,44

k,45,38,-50,0
k,46,38,50,0
k,47,43,50,0
k,48,43,-50,0
A,45,46,47,48

k,49,-32,-45,0
k,50,-17,-45,0
A,17,49,50,28

k,51,-12,-45,0
k,52,3,-45,0
A,25,51,52,36

k,53,8,-45,0
k,54,23,-45,0
A,33,53,54,44


k,55,28,-45,0
k,56,43,-45,0
A,41,55,56,48

k,57,38,55,0          ! Polysilicon arm
k,58,47,55,0
k,59,107,115,0
k,60,115,107,0
k,61,49,41,0
k,62,38,41,0
A,57,58,59,60,61,62

k,63,-37,-55,0        ! Polysilicon arm
k,64,-47,-55,0
k,65,-107,-115,0
k,66,-115,-107,0
```

```
k,67,-49,-41,0
k,68,-37,-41,0
A,63,64,65,66,67,68

AADD,4,5,6,7,8,9,10,11,12,13,14
AADD,1,2,3
AOVLAP,ALL

k,79,122,122,0            ! Open regions
k,80,122,-122,0
k,81,-122,-122,0
k,82,-122,122,0
A,79,80,81,82

AOVLAP,ALL
ADELE,3,4,1,              ! Delete extraneous areas
AGLUE,ALL
!---------------------------------------------------------------
! Define material properties

MPTGEN,1,18,273,100       ! temp table for non-linear mat. prop.
TOFFST,0.1

! Density (defined in units of kg/micron^3)
MP,DENS,1,2233e-18        ! poly/oxide/nitride
MP,DENS,3,2226e-18        ! oxide/nitride

! Specific Heat (defined in units of J/kg/K)
MP,C,1,306.41,1.752,-9e-4       ! poly/oxide/nitride
MP,C,3,-15.60,3.56,-3.9e-3,2e-6  ! oxide/nitride

! Thermal conductivity (defined in units of W/micron/K)
MP,KXX,1,17.647e-6,1.48e-8       ! poly/oxide/nitride
MP,KXX,3,13.407e-6,-8.3e-9,8e-12    ! oxide/nitride

! Gas properties
MP,C,2,2480           ! Specific heat of open region gas
MP,DENS,2,2.15e-21        ! Density of open region gas
MP,KXX,2,9.00e-9         ! Therm cond of open region gas
!---------------------------------------------------------------
! Meshing

SMRTSIZE,0.5
ET,1,PLANE35          ! PLANE35 = 2-D 6 node triangular plane
ET,2,LINK33           ! 3-D Conduction bar
ET,3,LINK31          ! Radiation link

TYPE,1
MAT,1
AMESH,15           ! Mesh polysilicon

TYPE,1
MAT,3
AMESH,1                 ! Mesh oxide

TYPE,1
MAT,2
```

```
AMESH,5                             ! Mesh right open region

TYPE,1
MAT,2
AMESH,6                             ! Mesh left open region
!----------------------------------------------------------------
! Generate conduction and radiation rods

R,1,17.00            ! Bars area = 59300 um^2/3461 nodes
R,2,17.00,1,0.05,5.67e-20! Rad. area,form factor,emissivity,sbc

NGEN,2,3461,ALL,,,,,-51   ! Generate cond. nodes, depth = 0.6*85um
TYPE,2
MAT,2
REAL,1
E,1,3462                           ! Generate first element
EGEN,3461,1,1683                   ! More elements

NGEN,2,6922,1,3461,,,,43 ! Generate rad. nodes, height = 0.5*85um
TYPE,3
MAT,2
REAL,2
E,1,6923             ! Generate first element
EGEN,3461,1,5144     ! More elements
!----------------------------------------------------------------
! Clean up model

NUMMRG,ALL
NUMCMP,ALL
WSORT,ALL
!----------------------------------------------------------------
! Apply constraints, loads, and obtain solution

/SOLUTION

!ANTYPE,STATIC              ! Steady-state analysis type
ANTYPE,TRANS               ! Transient analysis type
TUNIF,293            ! All nodes at uniform starting temp

D,3462,TEMP,293,,10383,1 ! Set all selected nodes to temp of 293K
!D,1048,TEMP,293,,1049,1   ! Constraint at end of right arm
!D,1052,TEMP,293,,1053,1   ! Constraint at end of left arm
D,1786,TEMP,293,,1876,1
D,2626,TEMP,293,,2716,1

TIME,0.001           ! Set time at end of load step
KBC,1                ! Stepped load step
BFA,4,HGEN,1.28e-6,,,      ! Power/poly area: 8 mW/6262 um^2
LSWRITE

TIME,0.005           ! Set time at end of load step
KBC,1                ! Stepped load step
BFA,4,HGEN,1.28e-6,,,      ! Power/poly area: 8 mW/6262 um^2
LSWRITE

TIME,0.010           ! Set time at end of load step
KBC,1                ! Stepped load step
```

```
BFA,4,HGEN,1.28e-6,,,      ! Power/poly area:  8 mW/6262 um^2
LSWRITE

TIME,0.015              ! Set time at end of load step
KBC,1                   ! Stepped load step
BFA,4,HGEN,1.28e-6,,,      ! Power/poly area:  8 mW/6262 um^2
LSWRITE

TIME,0.020              ! Set time at end of load step
KBC,1                   ! Stepped load step
BFA,4,HGEN,1.28e-6,,,      ! Power/poly area:  8 mW/6262 um^2
LSWRITE

TIME,0.030              ! Set time at end of load step
KBC,1                   ! Stepped load step
BFA,4,HGEN,1.28e-6,,,      ! Power/poly area:  8 mW/6262 um^2
LSWRITE

TIME,0.040              ! Set time at end of load step
KBC,1                   ! Stepped load step
BFA,4,HGEN,1.28e-6,,,      ! Power/poly area:  8 mW/6262 um^2
LSWRITE

TIME,0.050              ! Set time at end of load step
KBC,1                   ! Stepped load step
BFA,4,HGEN,1.28e-6,,,      ! Power/poly area:  8 mW/6262 um^2
LSWRITE

AUTOTS,ON               ! Use auto time stepping
!DELTIM,0.005,0.005,0.05,ON ! Set time step sizes,first,min,max

LSSOLVE,01,08,1
FINISH
!--------------------------------------------------------------
! Display results

!/POST1
!/CONT,ALL,9,293,145,
!/PLOPTS,INFO,ON
!PLNSOL,TEMP,,0,1
!ANTIME
/POST26
NSOL,2,1,TEMP,,
```

E.2 The following code is the input file for building the numerical model in ANSYS for simulating the thermal response of the large square geometry:

```
/PREP7
/TITLE, Thermal Analysis of Large Square
/UNITS, SI

! Define model geometry with keypoints (k,keypt #,x,y,z) &
! create areas (A,keypt1,...,keypt8)

k,1,-93.7,109.9,0        ! Inner platform
k,2,96.3,109.9,0
```

```
k,3,96.3,-110,0
k,4,-93.7,-110,0
A,1,2,3,4

k,5,-79.5,-110,0          ! Arms that extend from inner platform to
k,6,-129.6,-160,0         ! surrounding 'L-shaped' regions
k,7,-143.7,-129.9,0
k,8,-93.7,-79.9,0
A,5,6,7,8

k,9,82.1,109.9,0
k,10,132.2,160,0
k,11,146.3,129.8,0
k,12,96.3,79.8,0
A,9,10,11,12

k,13,-83.7,-100.1,0       ! Polysilicon serpentine sections
k,14,-83.7,99.9,0
k,15,-53.9,99.9,0
k,16,-53.9,-100.1,0
k,17,-63.9,-100.1,0
k,18,-63.9,89.9,0
k,19,-73.7,89.9,0
k,20,-73.7,-100.1,0
A,13,14,15,16,17,18,19,20

k,21,-43.8,-100.1,0
k,22,-43.8,99.9,0
k,23,-13.8,99.9,0
k,24,-13.8,-100.1,0
k,25,-23.8,-100.1,0
k,26,-23.8,89.9,0
k,27,-33.8,89.9,0
k,28,-33.8,-100.1,0
A,21,22,23,24,25,26,27,28

k,29,-4.2,-100.1,0
k,30,-4.2,99.9,0
k,31,26.2,99.9,0
k,32,26.2,-100.1,0
k,33,16.2,-100.1,0
k,34,16.2,89.9,0
k,35,6.2,89.9,0
k,36,6.2,-100.1,0
A,29,30,31,32,33,34,35,36

k,37,36.2,-100.1,0
k,38,36.2,99.9,0
k,39,66.2,99.9,0
k,40,66.2,-100.1,0
k,41,56.2,-100.1,0
k,42,56.2,89.9,0
k,43,46.2,89.9,0
k,44,46.2,-100.1,0
A,37,38,39,40,41,42,43,44

k,45,76.2,-100.1,0
```

```
k,46,76.2,99.9,0
k,47,86.2,99.9,0
k,48,86.2,-100.1,0
A,45,46,47,48

k,49,-63.9,-90.1,0
k,50,-33.8,-90.1,0
A,17,49,50,28

k,51,-23.8,-90.1,0
k,52,6.2,-90.1,0
A,25,51,52,36

k,53,16.2,-90.1,0
k,54,46.2,-90.1,0
A,33,53,54,44

k,55,56.2,-90.1,0
k,56,86.2,-90.1,0
A,41,55,56,48

k,57,76.2,83.9,0          ! Polysilicon arm
k,58,132.5,147.2,0
k,59,138,135.7,0
k,60,86.2,83.9,0
A,57,46,47,58,59,60

k,61,-83.7,-84.1,0        ! Polysilicon arm
k,62,-73.7,-84.1,0
k,63,-130,-146.4,0
k,64,-135.5,-135.9,0
A,61,62,20,13,63,64

AADD,4,5,6,7,8,9,10,11,12,13,14
AADD,1,2,3
AOVLAP,ALL

k,79,146.3,160,0          ! Open regions
k,80,146.3,-160,0
k,81,-143.7,-160,0
k,82,-143.7,160,0
A,79,80,81,82

AOVLAP,ALL
ADELE,3,4,1,              ! Delete extraneous areas
AGLUE,ALL
!-------------------------------------------------------------------
! Define material properties

MPTGEN,1,18,273,100       ! temp table for non-linear mat. prop.
TOFFST,0.1

! Density (defined in units of kg/microns^3)
MP,DENS,1,2233e-18        ! poly/oxide/nitride
MP,DENS,3,2226e-18        ! oxide/nitride

! Specific Heat (defined in units of J/kg/K)
```

```
MP,C,1,306.41,1.752,-9e-4          ! poly/oxide/nitride
MP,C,3,-15.60,3.56,-3.9e-3,2e-6   ! oxide/nitride

! Thermal conductivity (defined in units of W/micron/K)
MP,KXX,1,17.647e-6,1.48e-8         ! poly/oxide/nitride
MP,KXX,3,13.407e-6,-8.3e-9,8e-12 ! oxide/nitride

! Gas properties
MP,C,2,972.5,0.188            ! Specific heat of open region gas
MP,DENS,2,1.51e-20           ! Density of open region gas
MP,KXX,2,2.59e-8             ! Therm cond of open region gas
!---------------------------------------------------------------
! Meshing

SMRTSIZE,0.6
ET,1,PLANE35               ! PLANE35 = 2-D 6 node triangular plane
ET,2,LINK33               ! 3-D Conduction bar
ET,3,LINK31          ! Radiation link

TYPE,1
MAT,1
AMESH,15              ! Mesh polysilicon

TYPE,1
MAT,3
AMESH,1                   ! Mesh oxide

TYPE,1
MAT,2
AMESH,5                   ! Mesh right open region

TYPE,1
MAT,2
AMESH,6                   ! Mesh left open region
!---------------------------------------------------------------
! Generate conduction and radiation rods

R,1,30.00          ! Cond. bars area = 92289 um^2/2937 nodes
R,2,30.00,1,0.05,5.67e-20! Rad. area,form factor,emissivity,sbc

NGEN,2,2937,ALL,,,,,-51  ! Generate cond. nodes, depth = 0.6*85um
TYPE,2
MAT,2
REAL,1
E,1,2938                 ! Generate first element
EGEN,2937,1,1421         ! More elements

NGEN,2,5874,1,2937,,,,43 ! Generate rad. nodes, height = 0.5*85um
TYPE,3
MAT,2
REAL,2
E,1,5875          ! Generate first element
EGEN,2937,1,4358  ! More elements
!---------------------------------------------------------------
! Clean up model

NUMMRG,ALL
```

```
NUMCMP,ALL
WSORT,ALL
!-----------------------------------------------------------------
! Apply constraints, loads, and obtain solution

/SOLUTION

ANTYPE,STATIC          ! Steady-state analysis type
!ANTYPE, TRANS         ! Transient analysis type
TUNIF,293        ! All nodes at uniform starting temp

D,2938,TEMP,293,,8811,1  ! Set all selected nodes to a temp of 293K
!D,1062,TEMP,293,,1063,1  ! Constraint at end of left arm corners
!D,1066,TEMP,293,,1067,1  ! Constraint at end of right arm corners
D,1706,TEMP,293,,1794,1
D,2322,TEMP,293,,2410,1

BFA,4,HGEN,3.93e-7,,,     ! Power/poly area: 8 mW/20333 um^2

TIME,0.05                ! Set time at end of load step
!KBC,1                        ! Stepped load step
DELTIM,0.005,0.005,0.05,ON ! Set time step sizes,first,min,max
AUTOTS,ON             ! Use auto time stepping
!OUTRES,all,all,
SOLVE
FINISH
!-----------------------------------------------------------------
! Display results

/POST1
/CONT,ALL,9,293,145,
/PLOPTS,INFO,ON
PLNSOL,TEMP,,0,1
!ANTIME
```

E.3 The following code is the input file for building the numerical model in ANSYS for simulating the thermal response of the single bridge geometry:

```
/PREP7
/TITLE, Thermal Analysis of Single Beam
/UNITS, SI

! Define model geometry through keypoints (k,keypt #,x,y,z) &
! create areas (A,keypt1,...,keypt8)

k,1,-293.4,-41.3,0        ! Define open regions
k,2,-328.6,-6.1,0
k,3,-260,62.5,0
k,4,181.3,62.5,0
k,5,217.8,99,0
k,6,253,63.8,0
k,7,202.1,12.9,0
k,8,-239.2,12.9,0
A,1,2,3,4,5,6,7,8

k,9,273.3,40.2,0
```

```
k,10,308.5,5,0
k,11,239.9,-63.6,0
k,12,-201.4,-63.6,0
k,13,-237.9,-100.1,0
k,14,-273.1,-64.9,0
k,15,-222.2,-14,0
k,16,219.1,-14,0
A,9,10,11,12,13,14,15,16

A,6,7,8,1,14,15,16,9       ! Define the oxide regions

k,17,207.6,3.5,0           ! Define polysilicon trace
k,18,270.1,66,0
k,19,278.1,58,0
k,20,215.6,-4.5,0
k,21,-226.1,-4.5,0
k,22,-288.6,-67,0
k,23,-296.6,-59,0
k,24,-234.1,3.5,0
A,17,18,19,20,21,22,23,24

AOVLAP,3,4           ! Delete extraneous areas
ADELE, 5,6,1,1
AGLUE,ALL
!-----------------------------------------------------------------
! Define material properties

MPTGEN,1,18,273,100     ! temp table for non-linear mat prop.
TOFFST,0.1

! Density (defined in units of kg/micron^3)
MP,DENS,1,2233e-18      ! poly/oxide/nitride
MP,DENS,3,2226e-18      ! oxide/nitride

! Specific Heat (defined in units of J/kg/K)
MP,C,1,306.41,1.752,-9e-4        ! poly/oxide/nitride
MP,C,3,-15.60,3.56,-3.9e-3,2e-6 ! oxide/nitride

! Thermal conductivity (defined in units of W/micron/K)
MP,KXX,1,17.647e-6,1.48e-8         ! poly/oxide/nitride
MP,KXX,3,13.407e-6,-8.3e-9,8e-12   ! oxide/nitride

! Gas properties
MP,C,2,972.5,0.188      ! Specific heat of open region gas
MP,DENS,2,1.51e-20      ! Density of open region gas
MP,KXX,2,3.70e-9        ! Therm cond of open region gas
!-----------------------------------------------------------------
! Meshing

SMRTSIZE,0.5
ET,1,PLANE35           ! PLANE35 = 2-D 6 node triangular plane
ET,2,LINK33            ! 3-D Conduction bar
ET,3,LINK31        ! Radiation link

TYPE,1
MAT,1
AMESH,9               ! Mesh polysilicon
```

```
TYPE,1
MAT,3
AMESH,7                         ! Mesh oxide

TYPE,1
MAT,3
AMESH,8                         ! Mesh oxide

TYPE,1
MAT,2
AMESH,1                         ! Mesh upper open region

TYPE,1
MAT,2
AMESH,2                         ! Mesh lower open region
!-----------------------------------------------------------------
! Generate conduction and radiation rods

R,1,25.00          ! Cond. bars area = 74437 um^2/2911 nodes
R,2,25.00,1,0.05,5.67e-20! Rad. area,form factor,emissivity,sbc

NGEN,2,2911,ALL,,,,,,-51   ! Generate cond. nodes, depth = 0.6*85um
TYPE,2
MAT,2
REAL,1
E,1,2912                    ! Generate first element
EGEN,2911,1,1391            ! More elements

NGEN,2,5822,1,2911,,,,43 ! Generate rad. nodes, height = 0.5*85um
TYPE,3
MAT,2
REAL,2
E,1,5823              ! Generate first element
EGEN,2911,1,4302      ! More elements
!-----------------------------------------------------------------
! Clean up model

NUMMRG,ALL
NUMCMP,ALL
WSORT,ALL
!-----------------------------------------------------------------
! Apply constraints, loads, and obtain solution

/SOLUTION

ANTYPE,STATIC            ! Steady-state analysis type
!ANTYPE,TRANS            ! Transient analysis type
TUNIF,293               ! All nodes at uniform starting temp

D,2912,TEMP,293,,8733,1   ! Set all selected nodes to temp of 293K
!D,788,TEMP,293,,791,1     ! Constraint at upper corners
!D,1848,TEMP,293,,1851,1   ! Constraint at lower corners
D,1852,TEMP,293,,1970,1
D,792,TEMP,293,,910,1
!D,336,TEMP,293,,,1
!D,339,TEMP,293,,,1
```

```
!D,562,TEMP,293,,,1
!D,565,TEMP,293,,,1

BFA,5,HGEN,1.52e-6,,,      ! Power/poly area: 8 mW/5276 um^2

TIME,0.05                  ! Set time at end of load step
!KBC,1                     ! Stepped load step
DELTIM,0.005,0.005,0.05,ON ! Set time step sizes,first,min,max
AUTOTS,ON                  ! Use auto time stepping
!OUTRES,all,all,
SOLVE
FINISH
!----------------------------------------------------------------
! Display results

/POST1
/CONT,ALL,9,293,145,
/PLOPTS,INFO,ON
PLNSOL,TEMP,,0,1
!ANTIME
```

E.4 The following code is the input file for building the numerical model in ANSYS for simulating the thermal response of the double bridge geometry:

```
/PREP7
/TITLE, Thermal Analysis of Double Beam
/UNITS, SI

! Define model geometry with keypoints (k,keypt #,x,y,z) &
! create areas (A,keypt1,...,keypt8)

k,1,-309,-3.6,0            ! Define open regions
k,2,-344.4,31.8,0
k,3,-274.5,101.7,0
k,4,165.6,101.7,0
k,5,187.4,123.5,0
k,6,223.5,87.4,0
k,7,188.2,52.1,0
k,8,-253.3,52.1,0
A,1,2,3,4,5,6,7,8

k,9,273.3,40.2,0
k,10,308.5,5,0
k,11,239.9,-63.6,0
k,12,-201.4,-63.6,0
k,13,-226.8,-89,0
k,14,-262,-53.8,0
k,15,-222.2,-14,0
k,16,219.1,-14,0
A,9,10,11,12,13,14,15,16

k,17,-290.6355339,-24.4644661,0
k,18,-243.6355339,24,0
k,19,198.1644661,24,0
k,20,244.764461,69.1355339,0
k,21,251.8355339,62.0644661,0
```

```
k,22,205.2355339,14,0
k,23,-236.5644661,14,0
k,24,-283.5644661,-31.5355339,0
A,17,18,19,20,21,22,23,24

A,6,7,8,1,14,15,16,9     ! Define the oxide around open regions

k,25,-312.528427,-21.071573,0 ! Define polysilicon trace
k,26,-250.828427,41.8,0
k,27,190.371573,41.8,0
k,28,242.571573,92.828427,0
k,29,248.228427,87.171573,0
k,30,196.028427,33.8,0
k,31,-245.171573,33.8,0
k,32,-306.871573,-26.728427,0
A,25,26,27,28,29,30,31,32

k,33,207.6,3.5,0             ! Define aluminum trace
k,34,270.1,66,0
k,35,278.2,58,0
k,36,215.7,-4.5,0
k,37,-226.1,-4.5,0
k,38,-288.6,-67,0
k,39,-296.6,-59,0
k,40,-234.1,3.5,0
A,33,34,35,36,37,38,39,40

AOVLAP,3,4,5,6
ADELE,7,12,1,1
AGLUE,ALL
!----------------------------------------------------------------------
! Define material properties

MPTGEN,1,18,273,100        ! temp table for non-linear mat prop.
TOFFST,0.1

! Density (defined in units of kg/micron^3)
MP,DENS,1,2233e-18         ! poly/oxide/nitride
MP,DENS,3,2226e-18         ! oxide/nitride
MP,DENS,4,2312e-18         ! aluminum/oxide/nitride

! Specific Heat (defined in units of J/kg/K)
MP,C,1,306.41,1.752,-9e-4           ! poly/oxide/nitride
MP,C,3,-15.60,3.56,-3.9e-3,2e-6   ! oxide/nitride
MP,C,4,150.9,2.832,-2.9e-3,1e-6   ! aluminum/oxide/nitride

! Thermal conductivity (defined in units of W/micron/K)
MP,KXX,1,17.647e-6,1.48e-8           ! poly/oxide/nitride
MP,KXX,3,13.407e-6,-8.3e-9,8e-12 ! oxide/nitride
MP,KXX,4,211.95e-6,-2.71e-8 ! aluminum/oxide/nitride

! Gas properties
MP,C,2,972.5,0.188          ! Specific heat of open region gas
MP,DENS,2,1.15e-20          ! Density of open region gas
MP,KXX,2,2.59e-8            ! Therm cond of open region gas
!----------------------------------------------------------------------
! Meshing
```

```
SMRTSIZE,0.5
ET,1,PLANE35              ! PLANE35 = 2-D 6 node triangular plane
ET,2,LINK33              ! 3-D Conduction bar
ET,3,LINK31      ! Radiation link

TYPE,1
MAT,1
AMESH,18          ! Mesh polysilicon

TYPE,1
MAT,2
AMESH,15          ! Mesh middle open region

TYPE,1
MAT,4
AMESH,19          ! Mesh aluminum

TYPE,1
MAT,3
AMESH,13,14          ! Mesh oxide

TYPE,1
MAT,3
AMESH,16,17          ! Mesh oxide

TYPE,1
MAT,2
AMESH,1                   ! Mesh upper open region

TYPE,1
MAT,2
AMESH,2              ! Mesh lower open region
!------------------------------------------------------------------
! Generate conduction and radiation rods

R,1,30.00          ! Cond. bars area = 95418 um^2/3095 nodes
R,2,30.00,1,0.05,5.67e-20! Rad. area,form factor,emissivity,sbc

NGEN,2,3095,ALL,,,,,-51   ! Generate cond. nodes, depth = 0.6*85um
TYPE,2
MAT,2
REAL,1
E,1,3096                   ! Generate first element
EGEN,3095,1,1487          ! More elements

NGEN,2,6200,1,3095,,,,43 ! Generate rad. nodes, height = 0.5*85um
TYPE,3
MAT,2
REAL,2
E,1,6201          ! Generate first element
EGEN,3095,1,4582    ! More elements
!------------------------------------------------------------------
! Clean up model

NUMMRG,ALL
NUMCMP,ALL
```

```
WSORT,ALL
!------------------------------------------------------------------
! Apply constraints, loads, and obtain solution

/SOLUTION

ANTYPE,STATIC            ! Specify steady-state analysis type
!ANTYPE,TRANS            ! Transient analysis type
TUNIF,293          ! All nodes at uniform starting temp

D,3096,TEMP,293,,9285,1  ! Set all selected nodes to temp of 293K
D,1539,TEMP,293,,1542,1  ! Constraint at upper corners
D,2307,TEMP,293,,2310,1  ! Constraint at lower corners
D,1543,TEMP,293,,1645,1
D,2311,TEMP,293,,2413,1
D,504,TEMP,293,,505,1

BFA,8,HGEN,1.52e-6,,,      ! Power/poly area: 8 mW/5276 um^2

TIME,0.05               ! Set time at end of load step
!KBC,1                      ! Stepped load step
DELTIM,0.005,0.005,0.05,ON ! Set time step sizes,first,min,max
AUTOTS,ON               ! Use auto time stepping
!OUTRES,all,all,
SOLVE
FINISH
!------------------------------------------------------------------
! Display results

/POST1
/CONT,ALL,9,293,145,
/PLOPTS,INFO,ON
PLNSOL,TEMP,,0,1
!ANTIME
```